TU Clausthal

Clausthal University of Technology

Improving Reservoir Characterization using the Adjoint Method in History Matching

A Doctoral Thesis

By

Daniel Dare Awofodu

Submitted in partial fulfilment of the requirements for the degree of Doktor-Ingenieur (Dr.-Ing.)

First Reviewer: Prof. Dr. Leonhard Ganzer

Second Reviewer: Prof. Dr.-Ing Mohammed M. Amro

External Advisor: Assoc. Prof. Hussein Almuallim

Faculty of Energy and Management Science

Institute of Petroleum Engineering

Clausthal University of Technology

Date: 11th October, 2019

Declaration

I confirm that I have prepared this doctoral thesis independently by myself. All information taken from other sources are clearly referenced.

Clausthal-Zellerfeld, 11th October 2019 ……

Daniel Dare Awofodu (M.Sc)

Abstract (English)

With globally rising demand for fossil fuels and the continuous maturation of oil and gas fields worldwide, reservoir characterization is becoming increasingly important in reservoir management studies for the successful development of realistic reservoir models. Most reservoir models constructed from cores, logs, seismic data etc. are only satisfactory replica of subsurface reservoirs in best case scenarios. This is so because data acquired at various scales are only sufficient to estimate reservoir size, structure, massive faults and petrophysical properties at well locations. Information on inter-well permeability/porosity are unknown thus leading to the omission of inter-well flow barriers and channels. In other cases, oil and gas companies build reservoir models using sparse data either due to time or budget constraints. The consequences of building subpar reservoir models is that they never reproduce measured data even after spending considerable efforts in history matching.

State-of-the-art methods available today for improving reservoir characterization in reservoir models are mostly data-driven methods that use only measured injection and production data to infer hidden reservoir features like faults and channels. These methods suffer from major limitations such as the lack of support for simulation models with constant injection rates, poor support for simulation models undergoing significant changes in flow patterns over time (e.g. introducing an infill well), satisfactory support for aquifer-dominated reservoirs, limitations on well architectures supported and the inability to actually reveal hidden reservoir features in reservoir models.

This dissertation introduces a proposed method for improving reservoir characterization using a history matching method that utilizes the adjoint method which is a powerful method for computing sensitivities. These sensitivities are needed to fit reservoir simulation models to measured data through unconstrained history matching (UHM) for the purpose of revealing hidden reservoir features like faults, channels etc. The term "unconstrained" means that model parameters such as permeability and/or porosity are allowed to vary from zero to their default maximum value or possibly higher. Subsequently, developed detection algorithms are applied directly on best-case permeability and/or porosity arrays obtained from UHM in order to reveal the location, shape and other essential properties of hidden reservoir features. Finally, classical history matching (CHM) is performed on the improved model (new base model containing revealed reservoir features) with the original or geologically constrained permeability and/or porosity distribution respected and other model parameters included.

The proposed method is evaluated with a handful of synthetic and real field reservoir simulation models in order to ascertain its effectiveness in revealing hidden reservoir features under various practical reservoir settings. Results obtained show that the

proposed method outperforms other methods existing in literature. In addition, the proposed method does not suffer from aforementioned limitations. It is also discovered that production noise greater than ±15% as well as numerical noise can have a detrimental impact on the performance of the proposed method. Finally, the capability of the proposed method in revealing certain types of reservoir features during UHM is heavily dependent on the model parameters defined.

Zusammenfassung

Der weltweite Bedarf an fossilen Treibstoffen steigt, während ein Großteil der Öl- und Gasproduktion aus Lagerstätten gedeckt wird, die bereits ihre maximale Förderung überschritten haben. Unter diesen Bedingungen wird eine verbesserte Reservoircharakterisierung immer wichtiger. Herkömmliche Reservoirmodelle basieren auf Kernflutversuchen, Logdaten, seismischen Untersuchungen etc. Nur im Falle optimalen Voraussetzungen lassen sich Lagerstätten mit Hilfe dieser Modelle zufriedenstellend abbilden. Die gewonnenen Daten ermöglichen lediglich eine Abschätzung von Reservoirgröße, Struktur, großen Verwerfungen und petrophysikalischer Eigenschaften im Bereich der Bohrlöcher. Es sind keine Informationen über Barrieren und hochpermeable Kanäle zwischen den Bohrlöchern bekannt. Des Weiteren werden aus Kosten- und Zeitgründen Reservoirmodelle mit unzureichender Datenlage erstellt. Als Konsequenz können unzureichende Modelle nie das beobachtete Verhalten eines Reservoirs simulieren, obwohl signifikante Ressourcen für den Historymatch aufgebracht werden.

Moderne Methoden zur Verbesserung der Reservoircharakterisierung sind meist datengetrieben. Sie nutzen Produktions- und Injektionsdaten, um Störungen oder hochpermeable Kanäle zu entdecken. Diese Methoden haben in der Anwendung erhebliche Nachteile. Beispielhaft sind Simulationsmodelle mit konstanten Injektionsraten, Modelle mit sich ändernden Strömungsverläufen (z.B. Infill-Bohrungen), Aquifer-dominierte Modelle, spezielle Bohrlocharchitekturen sowie die Unfähigkeit verborgene Reservoir Features zu identifizieren.

Diese Dissertation stellt eine Methode zur verbesserten Reservoircharakterisierung vor. Diese basiert auf dem sog. Adjoint-State-Verfahren, welches zur Ermittlung von Sensitivitäten genutzt wird. Sensitivitäten werden benötigt, um während des „unconstrained“ Historymatch (UHM) das Simulationsmodell an die Produktionsdaten anzupassen und versteckte Reservoireigenschaften zu ermitteln. Beim „unconstrained“ Historymatch können Zelleigenschaften wie Porosität und/ oder Permeabilität zwischen Null und einem Vorgabewert variiert werden. Anschließend werden Detektionsalgorithmen direkt auf Best-Case-Permeabilitäts- und/ oder Porositäts-Arrays aus dem UHM angewandt. Dies ermöglicht Lage, Form und weitere essentielle Eigenschaften von verborgenen Reservoirmerkmalen zu ermitteln. Zum Schluss wird ein klassischer Historymatch (CHM) mit dem optimierten Reservoirmodell durchgeführt (neues Basismodell mit den ermittelten Reservoir Features). Hierbei werden die ursprünglichen oder geologischen Randbedingungen bezüglich Permeabilität und/ oder Porosität eingehalten und die zusätzlichen Modellparameter in das Modell eingefügt.

Die vorgestellte Methode wird anhand von künstlichen und echten Reservoirmodellen untersucht, um die Effizienz bei der Identifikation von versteckten Reservoirmerkmalen zu ermitteln. Die Ergebnisse übertreffen andere Methoden aus der Literatur. Des Weiteren besitzt diese Methode im Gegensatz zu anderen nicht die oben genannten Nachteile. Es wurde entdeckt, dass Produktionsschwankungen größer ±15 % sowie numerische Schwankungen einen nachteiligen Einfluss auf die Performance der vorgestellten Methode haben kann. Schließlich wird gezeigt, dass die Fähigkeit zur Detektion von versteckten Reservoireigenschaften während des UHM stark von den definierten Modellparametern abhängig ist.

Dedication

I dedicate this thesis to my Mom, Dad, Dayo, Lola, Jason and my sweetheart Odile ☺. I love you all!

Acknowledgement

First and foremost, I would like to thank God Almighty for his divine guidance and protection. It is by His grace that we are able to flourish and succeed and all glory and honour go to Him.

I would like to express my most profound gratitude to Prof. Dr. Leonhard Ganzer for giving me the opportunity to pursue a PhD programme at the Reservoir Engineering Department of the Institute of Petroleum Engineering at TU Clausthal. Prof. Ganzer went the extra-mile to ensure that the research proposal for the DGMK 742-2 research project was accepted with sufficient funding. Before and even after the commencement of my PhD programme, Prof. Ganzer was always there to help me bypass barriers. Prof. Ganzer has been an awesome supervisor and he helped me shaped the way I see things, including research and science in general. Thank you Prof. Ganzer for all the support you gave me during my PhD adventure. Thank you for helping me learn how to work independently and be productive. Thank you for providing insightful comments and direction on my work. I feel very privileged to have worked with you. Thank you so much!

I am also grateful to Prof. Dr.-Ing Mohammed M. Amro for taking time out to review this thesis and provide insightful comments. I truly appreciate it.

I would also like to say a big thank you to Assoc. Prof. Hussein Almuallim for the productive discussions we had regarding the use of SenEx in this research project. Thank you for trusting me with the hidden tricks and secrets of SenEx. Thank you for providing a plethora of SenEx licenses whenever I needed them. Thank you for providing invaluable assistance whenever I ran into SenEx-related issues and got stuck with hard-to-interpret error messages. I appreciated every moment working with you. You're the best!

Special thanks go to the project sponsors Wintershall Dea GmbH, Neptune Energy, RAG Rohoel-Aufsuchungs Aktiengesellschaft and the coordinator DGMK (Deutsche Wissenschaftliche Gesellschaft für Erdöl, Erdgas und Kohle e.V) for fully funding this research work within the framework of the DGMK 742 research project.

I will like to specially thank Jim Schellinger for his support in helping me prepare most of the MATLAB codes used in this work. Jim also assisted me with testing which was a major stress relief for me. Thanks Jim!

I will be remiss if I do not say a big thank you to Dr. Ralf Schulze-Riegert for introducing me to history matching, optimization methods, uncertainty quantification and other related concepts. Without him, I probably wouldn't be in the position to write this thesis. Thanks a lot Ralf!

Many thanks go to my friends and family for their unquantifiable support throughout my academic career. I consider myself lucky to be surrounded by great friends and colleagues who have supported me in ways that they might not even know. Of special mention are Richard, Ugo 1 of Texas, BomBom, Somebody, Hakam, Dr. Ajala, Dr. Bello, Dr. Hincapie, Chief Elvis, Chief Ugo, Ini, Faith, Femi, Helen, Calvin, Abdul, Benjamin, Paschal, Rasoul, Davin and many others. It has really been a blessing having all these people consider me as a friend and brother and I would like to acknowledge them all as having played a major role in my PhD and my life and helping me grow into the person I am today.

I am indebted to all PhD colleagues and staffs of the Institute of Petroleum Engineering for their encouragement and advice provided during the PhD seminar. Thanks guys!

Table of Contents

List of Figures

List of Tables

List of Symbols

Symbols	Description
UP	Uncertain parameter
Q, $Q(x)$	Objective function
i	Well of interest
α	Weighting factor
β	Normalization term (Variance)
t	Time at which measurements are available
sim	Simulated data
obs	Observed or measured data
q_{oR}, q_{wR}, q_{gR}	Oil, water & gas production rate computed from Darcy's law
Subscript R	Reservoir conditions
B_o, B_w, B_g	Oil, water and gas formation volume factor
c_f	Pore volume or formation compressibility
V_b	Bulk volume
S_o, S_w, S_g	Oil, water & gas saturation
p_o, p_w, p_g	Oil, water & gas phase pressure
q_{op}, q_{wp}, q_{gp}	Surface oil, water & gas production rate
$\emptyset_{orig}$	Original porosity at initialization
$\emptyset$	Porosity
R_s	Gas dissolved in oil
R_{sw}	Gas dissolved in water
Δx, Δy, Δz	Grid size in the X, Y and Z direction
$p_{c_{ow}}$	Oil-water capillary pressure
$p_{c_{go}}$	Gas-oil capillary pressure
A	Cross-sectional area
k, K	Permeability
k_{ro}, k_{rw}, k_{rg}	Oil, water & gas relative permeability
h	Thickness
ρ_o, ρ_w, ρ_g	Oil, water and gas density
μ_o, μ_w, μ_g	Oil, water and gas viscosity
f	Simplified term for fluid flow simulator equations
y	Vector of state variables
x	Vector of model parameters
l	Time step
L	Last time step from forward simulation run
N	Total number of active grid blocks
N_w	Total number of wells
T	Transpose

P_{wf}	Flowing well pressure
m	Phases
n	Active grid block number
o, w, g	Oil, water & gas
f_o, f_w, f_g	Flow simulator equations for oil, water & gas
f_{pwf}	Simulator pressure equation
w	Well number
J	Term for adjoining simulator and objective function equation
λ	Adjoint variable
∇	First-order partial differential or gradient notation
Nx	Number of model parameters
d	Mismatch parameter
k	Iteration number
d^k	Direction of search
μ	Step size
$f(X)$, $f(X')$	Solution space
N_o, N_w, N_g	Corey oil, water & gas exponents
S_{wi}	Initial water saturation
S_{or}	Residual oil saturation
Kro_{max}	Maximum oil relative permeability
Krw_{max}	Maximum water relative permeability
ith	Data point number
Sim_{mean}	Mean value of simulated data
Obs_{mean}	Mean value of observed data
γ_{fault}	Threshold value that reveals a fault location and shape
$\gamma_{channel}$	Threshold value that reveals a channel location and shape
$\gamma_{fracture}$	Threshold value that reveals fracture location
$\gamma_{vert.comm.}$	Threshold value that reveals vertical communication between layers
$f_{i,j}$	Connectivities estimated for each injector-producer pair
τ_j	Time constant for each producer
J_j	Productivity index for each producer
$T_{i,1}, T_{i,2}, T_{i,3}$	Transmissibility between well pairs
$V_{p_{i,1}}, V_{p_{i,2}}, V_{p_{i,3}}$	Pore volume between well pairs
$\gamma_{aquifer}$	Threshold value that reveals the existence of an aquifer/water body
$\gamma_{non-vert.comm.}$	Threshold value that reveals non-vertical communication between layers
Krg_{max}	Maximum gas relative permeability

Chapter 1

"Where oil is first found is in the minds of men"

Wallace Pratt (1885-1981)

1. Introduction

1.1 The Value of Hydrocarbons

Crude oil and natural gas will remain a dominant source of energy for a larger part of this century in spite of fluctuating oil prices and a fast-growing renewable energy niche. According to the United States Energy Information Administration (US-EIA) [1], petroleum consumption in the United States alone is expected to remain relatively constant from 2019 to 2035 and then increase by 9% from 2035 to 2050 in spite of volatile oil prices and regardless of the Clean Power Plan (CPP) compliance. US-EIA also predicts that petroleum and natural gas liquids will remain the largest source of energy in the world through 2050. In addition, the International Energy Agency (IEA) [2] forecasts that between the year 2019 and 2024, global oil demand is expected to rise at an average annual growth rate of 1.2% which translates to an annual average increase of 191,000 m^3 per day. In order to meet this ever-growing energy needs, it is important for the oil and gas industry to invest in new technologies that can contribute significantly to the improvement of recovery factor in both new and existing oil fields. Having said that, the potential for an enormous investment rests strongly on crude oil and natural gas prices.

1.2 Reservoir Characterization and its Shortcomings

According to Kelkar [3], reservoir characterization is a multidisciplinary task which involves the integration of various qualitative and quantitative data in a consistent manner in order to build reservoir models. These data typically include seismic data (2-D, 3-D and 4-D), outcrops, well logs, routine and special core analysis, fluid data, well test data and production data. With these data, an approximate 3-D representation of

the spatial distribution of the petrophysical properties of a reservoir (such as permeability, porosity and saturation) can be constructed and used to predict future reservoir performance. Figure 1-1 describes a generic reservoir characterization workflow.

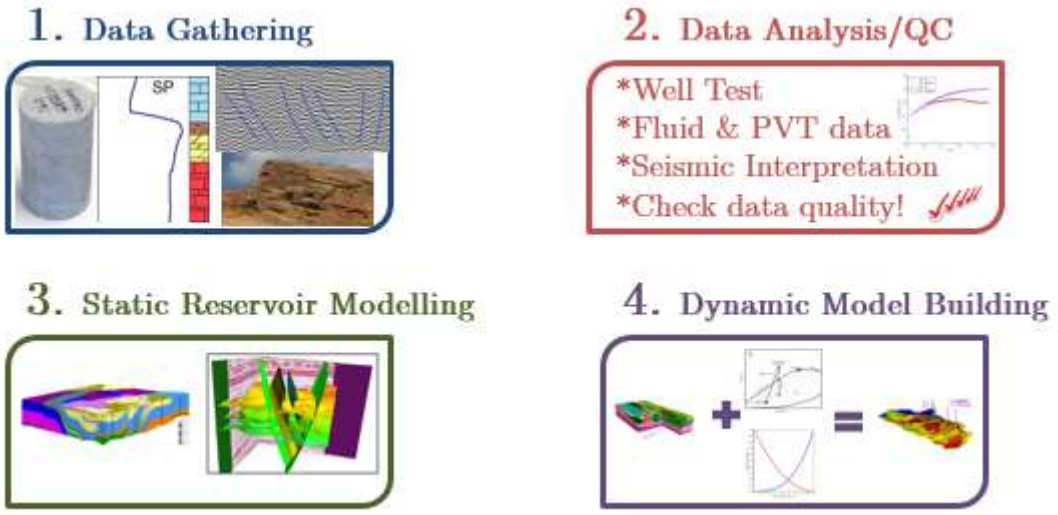

Figure 1-1: A Generic Reservoir Characterization Workflow.

Over the years, research has shown that reservoir models constructed even from detailed reservoir characterization studies are satisfactory representation of the true reservoirs existing deep beneath the surface in best case scenarios. The reasons for this can be attributed to several factors. The first factor is related to the random distribution of petrophysical properties at inter-well locations. Core and log data extracted at respective well locations have a radius of investigation which is typically a few metres away from these wells. This means that the petrophysical properties derived from them are only accurately suited to the neighbourhood of these wells. The use of advanced geostatistical and geophysical methods [4], [5], [6] can be employed to estimate (typically using random-based method) the petrophysical properties at inter-well locations. Imagine having a thief zone (a small area with high permeability streak) existing in reality between two wells with available core and log data measurements, the likelihood of being aware of the existence of the thief zone and capturing them in the final reservoir model through random distribution of inter-well petrophysical properties is very small.

The second factor is related to the level of heterogeneity that characterizes the reservoir in question. Compared to siliciclastic reservoirs (e.g. sandstone reservoirs), carbonate reservoirs are difficult to characterize because of their extreme geological and petrophysical heterogeneity [7]. In other cases, constructing representative reservoir models of fractured reservoirs can be very complex and is still an area of ongoing research.

The last factor is related to the quality and amount of data available prior to reservoir characterization. Most times, the data collected are usually not 100% exact and sometimes only a few are available due to time and budget constraints. For example,

failure to perform rigorous analysis of the seismic data can lead to the omission of key reservoir faults, uncertainties in fault locations and information about the size, shape and bed thickness of reservoir compartments [8]. After all, reservoir models are only as good as the data used to construct them.

In an attempt to mitigate the aforementioned factors, history matching is performed on reservoir models resulting from reservoir characterization with the aim of reducing permeability and/or porosity uncertainty. This process is expected to increase confidence in the reservoir models for prediction purposes if the estimated permeabilities and porosities provide a better description of the true properties in the reservoir. Of course, the level of success attainable is dependent on the history matching technique and parameterization approach.

1.3 What is History Matching?

History matching sometimes referred to as "model validation", "model conditioning" or "inverse estimation" is the process of fitting simulation results from a reservoir model to available measured data. It requires a great deal of model adjustment in order to ensure consistency with reservoir performance and it can take up to 80% of the total reservoir management study time [9]. Some professional experience helps in minimizing the amount of time required for history matching. The term "experience" describes increased understanding of reservoir mechanics. Reservoir models that reproduces well and field measurements after history matching are more likely to give accurate predictions. Besides conditioning models to available measured data, history matching can also be used to validate other data. For instance, pressure response from well test analysis may indicate the possibility of the existence of a fault which may not have been confirmed from seismic data due to resolution issues. In such a case, fault realizations of different transmissibility multipliers across each fault can be defined as an uncertainty and then history matching can be used to provide more evidence about the existence of the fault.

In order to successfully perform a realistic history matching task, Carlton [10] defined 4 key guidelines that must be followed by reservoir engineers. They are:

1. The engineer must have a fundamental grasp of reservoir engineering.
2. Knowledge and extent of accuracy of the data source is very crucial.
3. Expertise in reservoir simulation is necessary and history matching must consider modelling limitations.
4. Knowledge of the model geology is important to modify them either directly or indirectly.

Prior to the commencement of any history matching task, a clear list of known uncertain (input) parameters and model responses must be specified. Model responses are

expectations from history matching that reservoir engineers will like to observe e.g. simulated cumulative oil production rate vs. measured cumulative oil production rate. Following the definition of input parameters and model responses, sensitivity studies must be conducted to rank each input parameter according to their influence and screen out those with little or no influence on selected model responses. In doing so, only key input parameters with defined uncertainty ranges are retained and modified in the history matching stage.

From a mathematical standpoint, history matching is an inverse problem with non-unique solutions. The term "non-unique" means that there are usually equiprobable best-case models (or multiple history-matched model realizations) that fit available measured data. History matching is an inverse problem in the sense that field measurements are used to estimate input parameter values that reproduces these measurements. Typically one or more reservoir models are calibrated with available observed data in an attempt to perform an extensive reservoir uncertainty assessment. Despite this, the quality of history-matched results obtained may only be satisfactory if these sets of models do not fully capture the true reservoir behaviour [11]. This is particularly the case when the reservoir models in question overlooks important mechanisms, omits key reservoir features or the model is just too simple (poor reservoir characterization).

To demonstrate the impact of deficient reservoir characterization on history matching, two scenarios typical for any reservoir characterization study are briefly discussed with illustrations presented in Figure 1-2. Scenario 1 describes a case where all existing reservoir behaviour are wholly captured in the reservoir model prior to history matching. The known input parameters are the inter-well permeability and porosity, rock compressibility, fault structure and fault transmissibility multiplier. Since the reservoir model is a very good representation of reality, we will expect that history matching delivers excellent history-match quality for all or most model responses defined.

Scenario 2 describes a slightly different case. Here, not all existing reservoir behaviour are fully captured in the reservoir model. Known input parameters are the inter-well permeability, inter-well porosity and the rock compressibility. The unknown input parameter is the existence of a fault and its transmissibility multiplier. The input parameter is termed "unknown" because the reservoir characterization study is assumed to not consider the possibility of the existence of the fault. In such a situation, it is obvious that it will be very difficult to match certain model responses irrespective of the type of history matching technique employed.

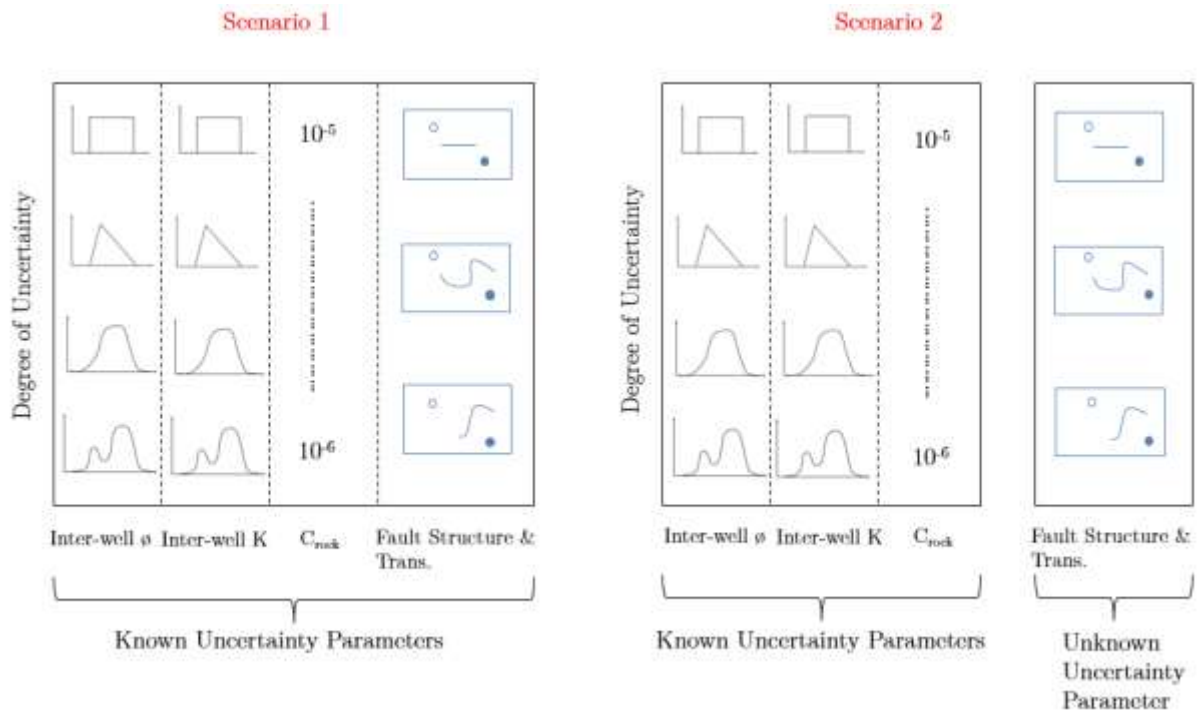

Figure 1-2: Impact of deficient reservoir characterization on history matching.

From the illustration provided in Figure 1-2, it is clear that despite years of innovative development and advancement in assisted history matching (AHM) techniques, they often fail to deliver excellent history-match results because of unaccounted reservoir uncertainties. Well-built reservoir models are meant to be an accurate representation of subsurface reservoirs – unfortunately they often fall short of being a complete replica of reality. It is the "unknown unknowns" (dominating features in reservoir systems whose existence we have no knowledge of) that present the greatest challenge to improving reservoir characterization and understanding reservoir behaviour.

Developing an adjoint-based reservoir characterization improvement workflow that can reveal hidden reservoir features not captured in reservoir simulation models during history matching is the main focus area of this thesis. It is expected that the workflows and algorithms proposed in this thesis will identify model deficiencies (e.g. reveal the existence of hidden reservoir features) and other essential characteristics of these hidden reservoir features.

1.4 Previous work done on Project DGMK 742

In an attempt to investigate ways of developing advanced technologies for increasing confidence in the predictive capability of reservoir simulation models, the Institute of Petroleum Engineering at Clausthal University of Technology in collaboration with participants from the oil and gas industry created the Joint Industry Project DGMK 742 in the year 2011. The Joint Industry Project DGMK 742 was supported by Neptune Energy, DEA Deutsche Erdoel AG and RAG Rohoel-Aufsuchungs Aktiengesellschaft

through the Deutsche Wissenschaftliche Gesellschaft für Erdöl, Erdgas und Kohle e.V (DGMK). Other research and development partners include FirmSoft Technologies Inc. and Schlumberger Information Solutions AS.

The first phase of the DGMK 742 research project titled "Adjoint method used in History Matching and Optimization Workflows" focused on the development of an integrated workflow using state-of-the-art optimization techniques in combination with the adjoint method for history matching. In order to achieve this deliverable, SenEx, an advanced history matching tool based on the adjoint method which is capable of performing analytical sensitivity-based parameter modifications at grid block level, was linked to an existing and robust optimization framework, MEPO. The model parameters employed for any history matching problem were permeability and porosity. The hotlink which is presently referred to as MEPO-tSenEx has been tested with a plethora of history matching problems with many success counts recorded. Oil, water and gas production rates matching as well as pressure and formation pressure (RFT) matching delivered excellent results. In addition, the developed history matching workflow (MEPO-tSenEx) delivered acceptable history-match results with only small parameter modifications made to permeability and porosity at grid block level. This approach ensured that the final history-matched model remained geologically sensible.

Some of the benefits of using the adjoint method implemented in SenEx are listed below:

1. Model parameter modifications are based on analytical sensitivity calculations compared to tedious and painstaking traditional history matching approaches that require repeated modification of model parameters on a trial-and-error basis.
2. Can be used with complex reservoir simulation models (e.g. models with local grid refinements, dual porosity and dual permeability models etc.)
3. The introduction of a weighting scheme allows reservoir engineers to prioritize model responses with the most mismatch during history matching.
4. Supports a broad range of model parameters like permeability, porosity, fault transmissibility multipliers, relative permeability curves, aquifer properties, fluid contacts, fracture porosity and permeability etc.
5. A history match is typically achieved with less number of iterations when compared to other existing methods in literature.

Most limitations of the adjoint method implemented in SenEx which were mentioned in the first phase of the DGMK 742 research project have been tackled over the years. In spite of that, a few limitations exist which are:

1. Only supports black-oil model formulations.
2. Sometimes, history matching is not achieved for some reservoir simulation models despite analytical sensitivity-based modifications made to the most uncertain model parameters due to poor reservoir characterization study or the omission of key reservoir features.

Investigating ways to tackle the second limitation paved the way for a new research project (DGMK 742-2). This thesis summarizes findings and results obtained from research project DGMK 742-2.

1.5 Who are the Beneficiaries of this Thesis?

This thesis focuses on improving reservoir characterization with the adjoint method used in history matching. This research aims to make a significant contribution to the existing body of knowledge by developing an effective method to reveal hidden reservoir features ("unknown unknowns") not captured in reservoir simulation models using the adjoint method. The beneficiaries of this thesis are the reservoir management teams of oil and gas companies who crave to enhance reservoir understanding in virgin and mature oil and gas fields, reveal hidden reservoir features not captured into reservoir simulation models and improve history matching results for better prediction of future reservoir performance. These steps have a strong impact on the financial performance of oil and gas companies. It is hoped that the proposed method for improving reservoir characterization in reservoir simulation models surpasses existing methods available in literature. The development of an adjoint-based reservoir characterization improvement workflow for revealing hidden reservoir features (e.g. fault, channel, vertical communication, fractures etc.) not captured in reservoir models and the formulation of hidden reservoir feature detection algorithms forms the backbone of this research. In addition, a fault shape detection algorithm is developed to minimize human intervention or any form of subjective bias that may occur when estimating the shape of revealed fault(s) in form of fault lines. Furthermore, channels and other area-based reservoir features can be revealed using a modified Canny edge-detection method.

1.6 Thesis Objectives

In this thesis, we aim to:

- Develop an adjoint-based reservoir characterization improvement workflow for revealing hidden reservoir features (e.g. faults, channels, fractures etc.) not captured in reservoir simulation models (could also be the result of incomplete Petrel models).
- Formulate specific feature detection algorithms by studying numerous signature patterns and model parameters unique to each reservoir feature.
- Compare the performance of the proposed method with renowned state-of-the-art methods existing in literature.
- Objectively estimate the shape of revealed fault(s) using a developed fault shape detection algorithm and also detect channels and other area-based reservoir features using a modified Canny edge-detection method.

- Observe the influence of erroneous production data and numerical noise on the proposed method.
- Validate the effectiveness of the proposed method with real field cases (e.g. field-scale heterogeneous models).

1.7 Thesis Structure

This thesis entails improving reservoir characterization with the adjoint method used in history matching. The main goal is to reveal hidden reservoir features not captured in reservoir simulation models. The adjoint method is implemented into a so-called "Adjoint-based reservoir characterization improvement workflow" which is described later on in this thesis. This thesis is divided into 6 chapters and 3 appendices. The background and motive behind this research is given in Chapter 1.

Chapter 2 reviews the art and history of history matching over the last 6 decades. The latter part of this chapter reviews prominent methods existing in literature that have been applied to improve reservoir characterization in reservoir simulation models during history matching.

Chapter 3 is divided into five sections. The first section provides a brief description of the linear least squares objective function equation employed. The second section succinctly describes the reservoir simulator used with emphasis on the flow and pressure equations solved by the simulator. The third section describes the principle and mathematical background of the adjoint method used in this work. Here, we begin with an overview of the theoretical background of the adjoint method which is then followed by the formulation of the adjoint system of equations and how the adjoint variables and sensitivities are determined. Highlights of the merits and demerits of using the adjoint method are also provided. Also, an explanation on what adjoint sensitivities are and how they are computed are provided. The penultimate section presents a brief mathematical description showing how model parameter updates are guided by computed adjoint sensitivities using the steepest-descent algorithm. The last section provides a detailed explanation of what the adjoint-based reservoir characterization improvement workflow is, how it works and the number of stages involved.

Chapter 4 presents the evaluation of the proposed method with numerous examples. Also, test models experiencing significant changes in flow patterns which is typical in many practical reservoir settings are evaluated with the proposed method. Events that can induce changes in flow pattern over time such as injector-to-producer conversion and vice versa, shutting-in well(s) that have been online for a while and the introduction of an infill well are incorporated into each test model evaluated. Thereafter, the performance of the proposed method in revealing hidden reservoir features is compared with prominent state-of-the-art methods. This is then followed by the description of the reservoir feature detection algorithms formulated in this research work. In addition, a proposed catalogue

for improving reservoir characterization in reservoir simulation models is presented here. The steps required to validate the shape and location of hidden reservoir features using adjoint-derived sensitivities are also discussed. Afterwards, the use of the developed pattern detection algorithms for revealing line-based (e.g. sealing faults) and area-based (e.g. channels) reservoir features are discussed. Examples are also presented to demonstrate how these pattern detection algorithms work. Subsequently, the influence of numerical and production noise on the proposed method is evaluated using a synthetic and a semi-synthetic (PUNQ-S3) model respectively. The concluding section highlights the benefits in performing constrained and unconstrained history matching. The final section discusses some limitations of the proposed method.

The application of the proposed method to a real field case provided by one of the project sponsors is captured in Chapter 5. A detailed description of the reservoir simulation model is not provided since the model is constructed from a field that is still in production till today. In addition, the effectiveness of the proposed method in revealing hidden faults in an ensemble of field-scale heterogeneous models is also evaluated and results are discussed in this chapter.

Chapter 6 provides key conclusions and recommendations for future work.

In Appendix A, we present the improved MEPO-tSenEx command scripting used in this research project. Appendix B renders the lines of MATLAB code for interpreting adjoint-derived sensitivities. Appendix C renders the lines of MATLAB code for the modified Canny edge-detection method and the fault shape detection algorithm.

Chapter 2

> "Progress, far from consisting in change, depends on retentiveness....Those who cannot remember the past are condemned to repeat it"
>
> George Santayana (1863-1952)

2. State-of-the-Art and Literature Review

For a brief moment, imagine that you are a member of a reservoir management team and you have been entrusted with some information about a field. With this information, you are required to make a decision about strategies for maximizing production from this field. Typically, the very first thing to do is to start a field study. Upon the availability of seismic data, core and log data, fluid data, petrophysical data etc., a detailed reservoir and fluid characterization study is performed by members of your team. Based on this study, a reservoir model is constructed and you are expected to perform history matching to fit the reservoir model to measured data. Despite your efforts to fit all model responses of interest to you to their corresponding measured data, you find out that only a handful of these model responses yield acceptable matches. Using the history-matched model you got, you are also expected to make prediction runs to ascertain the future performance of the field. Based on your final results, you will then suggest a strategy to improve current production from the field.

When making decisions bordering around reservoir management, we can always be certain that *there will always be uncertainty*. For example, using the anecdote in the previous paragraph, the main uncertainty is the correctness of the reservoir model prior to history matching. It is very much possible to expect a different field response in the future as compared to what was predicted by your study because of the satisfactory level of history-matched model realised.

In this chapter, the art and history of history matching will be reviewed succinctly. Also, different approaches that have been applied till date for improving reservoir characterization in reservoir simulation models will be focused on in this chapter.

2.1 The Art of History Matching

As mentioned earlier in Chapter 1, history matching is a crucial part of any field study. In this stage, the initially developed reservoir model is updated using measured data obtained from field measurements. Such measured data include production data etc. History matching is a process of reducing the misfit between model responses and measured data until a perfect fit is achieved. The goal of performing a history match is to obtain more information about defined uncertain (input) parameters. The ultimate goal however is to update the model in a geologically consistent manner in order to make reliable prediction runs. Some examples of typical reservoir parameters defined and modified during history matching are described in Figure 2-1. Also, Figure 2-2 shows a typical history matching workflow applied today in many field studies.

There are very few books [9], [10], [12], [13], [14], [15] available that describe in some details what history matching is, typical uncertain parameters that can be modified during history matching and a step-by-step guide on how history matching should be performed for various reservoir situations. It may interest the reader to know that of these few books available, only Oliver et al. [14] and Ozgen & Gilman [15] focuses deeply on the art of history matching using different optimization techniques available in literature. This reveals that there is still not enough work done on educating reservoir engineers on the importance of performing fast, realistic and geologically sensible history matching for better reservoir performance prediction. On the contrary, many journal and conference papers exists on history matching and a huge percentage of them will be used to review history matching practices performed on reservoir models over the last 6 decades.

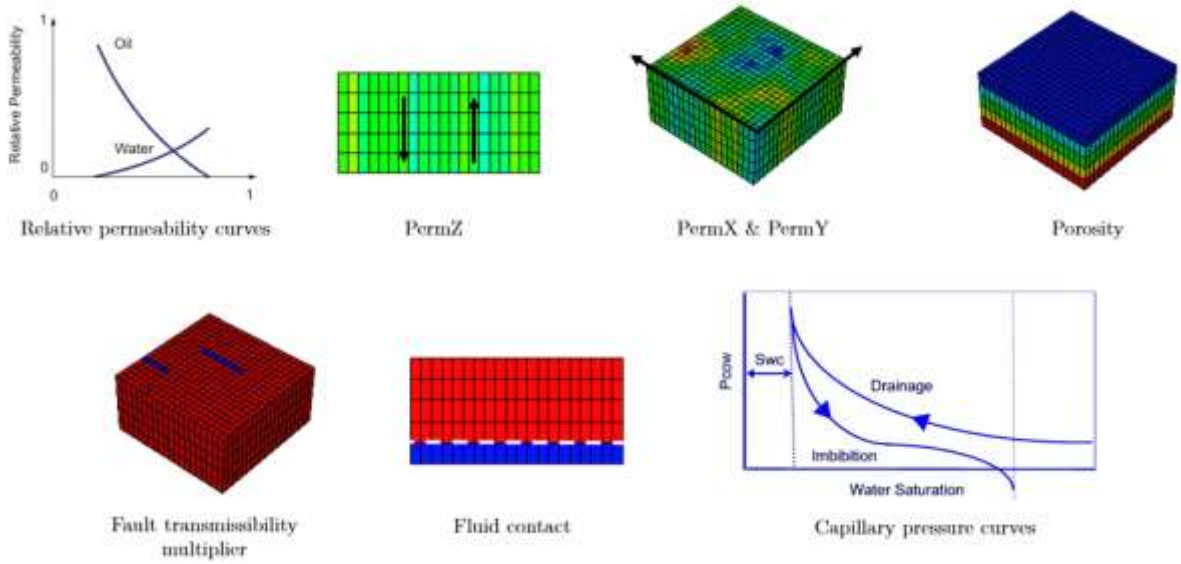

Figure 2-1: Typical reservoir parameters modified during history matching.

2.1.1 History of History Matching

The earliest known recorded case of history matching was performed by Kruger [16]. In his study, he pointed out the need to have an agreement between calculated and measured data. Using a numerical method for a mathematical model of a reservoir, he defined the areal permeability distribution as an uncertain parameter and adjusted it in order to match past reservoir conditions and obtain reliable prediction of future reservoir performance. From his study, a crucial conclusion was made. He emphasized on the importance of validating reservoir models by fitting them to measured data.

Few years after, other authors (Coats [17], Slater and Durrer [18] and Thomas [19]) confirmed Kruger's assertion and pointed out the importance of uncertain parameter definition and their respective degree of uncertainty in history matching.

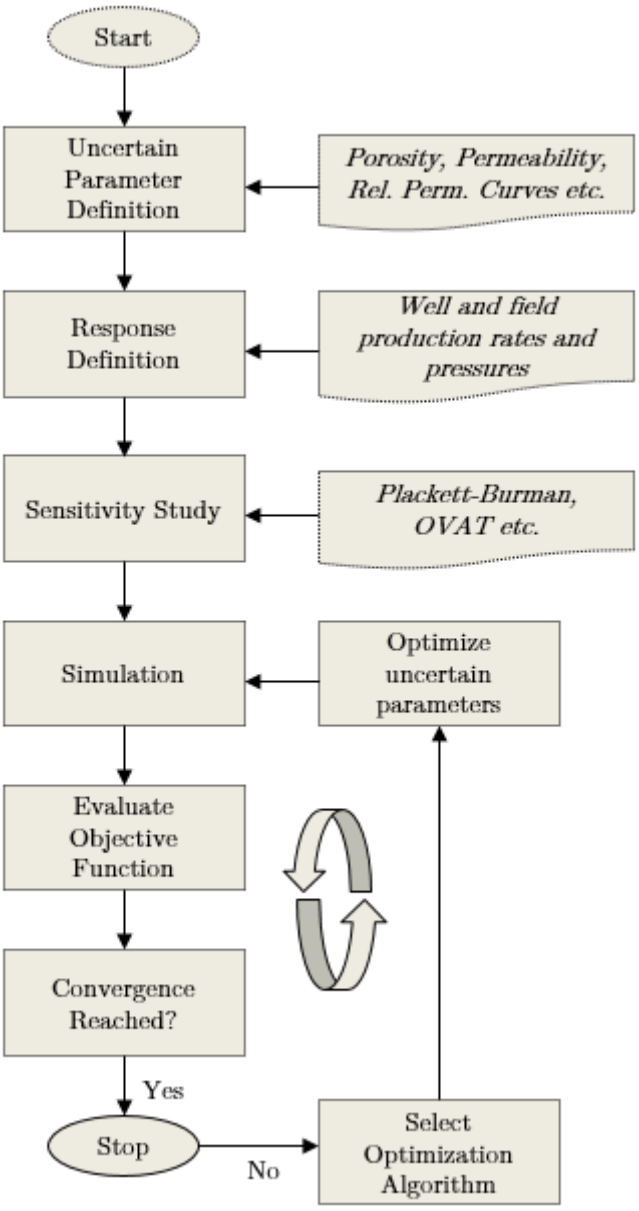

Figure 2-2: Typical history matching workflow applied today in many field studies.

In the 70-ies, optimal control theory became an in-demand technique for conditioning models to measured data and it was first implemented by Chavent [20] and Chen [21]. They both used optimal control theory for assisted history matching of a reservoir characterized by single-phase flow. Other authors leveraged the optimal control theory concept for other types of reservoir models. Dougherty and Khairkhah [22] applied the optimal control theory to real-gas reservoir systems and concluded that values obtained for defined uncertain parameters are not unique and that changing the initial uncertain parameter values results in different final realized values.

Over the years, history matching experienced a paradigm shift in change-of-concept from the optimal control theory to the Bayesian framework. Gavalas [23] was the first to introduce the Bayesian framework concept into history matching. He applied the

Bayesian method to a one-dimensional one-phase reservoir to estimate reservoir porosity and permeability. From his study, he concluded that the accuracy of Bayesian estimates are heavily dependent on the reliability of the prior statistics used.

In 1980, Pruess [24] used a numerical simulator (SHAFT79) developed by Lawrence Berkeley Laboratory for history matching of a geothermal reservoir. Although, he adopted the trial-and-error approach to adjust uncertain parameters like permeabilities, results obtained showed semi-quantitative agreement with measured data. His work is considered to be the first reported case where history matching is performed in combination with a numerical reservoir simulator.

Few year after, Watson and Lee [25] presented a new algorithm for assisted history matching capable of handling a moderate number of uncertain parameters. The algorithm was based on Marquardt's modification of the Gauss-Newton method. Later on, Zuber [26] determined key coalbed methane reservoir properties using history matching. He concluded that in order to leverage the full advantage of history matching in determining reservoir parameters that are difficult to measure in a laboratory, it is important to minimize unknown uncertainties and ensure accurate measurement of field and laboratory data.

While researchers continued to test new algorithms in an effort to improve assisted history matching techniques, Watkins [27] emphasized on the importance of not completely neglecting reservoir engineering experience while performing assisted history matching. He stressed the need for good user input in reservoir history matching especially when an optimization framework is adopted. Based on his idea, many commercial assisted history matching tools were created with an option for reservoir engineers to define uncertain parameters and their corresponding extent of uncertainties.

In the 90-ies, the use of experimental design and response surface methods in history matching of reservoir models began to gain popularity. Experimental design is a technique used to generate a set of simulation runs that provide inter-relationship between uncertain parameters and model responses. The earliest attempt to incorporate experimental design into assisted history matching was performed by Damsleth [28]. He applied experimental design to a North Sea field development study to obtain the relationship between uncertain parameters and model responses. In his work, he approximated the relationship between uncertain parameters and model responses with a smooth parametric function. He concluded that experimental design can give the same information as the One-Variable-At-a-Time (OVAT) method with 30% to 40% fewer simulation runs.

By the end of the mid 90-ies, assisted history matching had become a necessary concept in the oil and gas industry for enhancing reservoir understanding. Towards the very end of the 90-ies, a generic framework for history matching had been established. Additional research work carried out till date have focused mainly on improving reservoir

characterization, ensuring geologically consistent history matching and improving optimization algorithms applied to history matching (making them fast and more accurate [29]).

The modern age of history matching commenced in the early 20th century. During this period, a handful of optimization algorithms were developed and the importance of generating multiple history-matched models in an attempt to quantify uncertainty in prediction runs became more pronounced [30]. Most of the optimization algorithms developed in the modern age have been stochastic-based methods with many application to history matching available in literature. These algorithms do not require the computation of the gradient of the objective function with respect to uncertain (input) parameters to determine optimization direction. The genetic algorithm (GA) which is a stochastic-based method belongs to the group of evolutionary algorithms and it was first applied to history matching by Sen [31] to a set of outcrop and tracer flow data. He compared results obtained with the GA with other evaluated algorithms. Other notable applications of the GA in assisted history matching frameworks can be found in Romero [32] and Ballester and Carter [33]. Other stochastic-based methods applied to history matching include the evolution strategy (ES) [34], particle swarm optimization (PSO) [35] and scatter search (SS) [36].

One unique stochastic-based method applied in history matching in the modern age is the ensemble Kalman filter (EnKF). Unlike other methods that utilizes a single model, EnKF utilizes an ensemble of models. Its uniqueness is born from its ability to assimilate data in a sequential manner, forward in time (see Figure 2-3). It is appraised to be very promising because of its flexibility in supporting real-time data assimilation from new field measurements. The first recorded application of the EnKF to history matching was carried out by Liu and Oliver [37]. They used the EnKF for history matching facies boundaries and compared their results with a gradient-based minimization method. Although both methods performed similarly in terms of computational effort required and history matching results obtained, coding the EnKF was substantially less complex. Other examples where the EnKF has been successfully applied to history matching can be found in Naevdal [38], Bianco [39] and Schulze-Riegert [40].

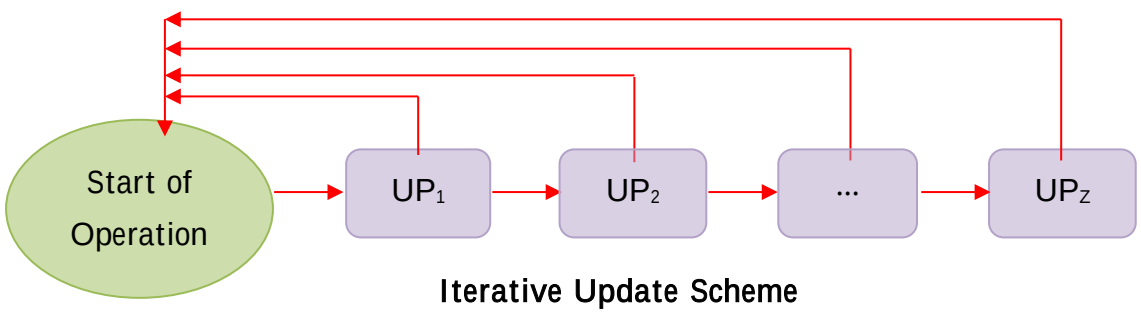

Iterative Update Scheme

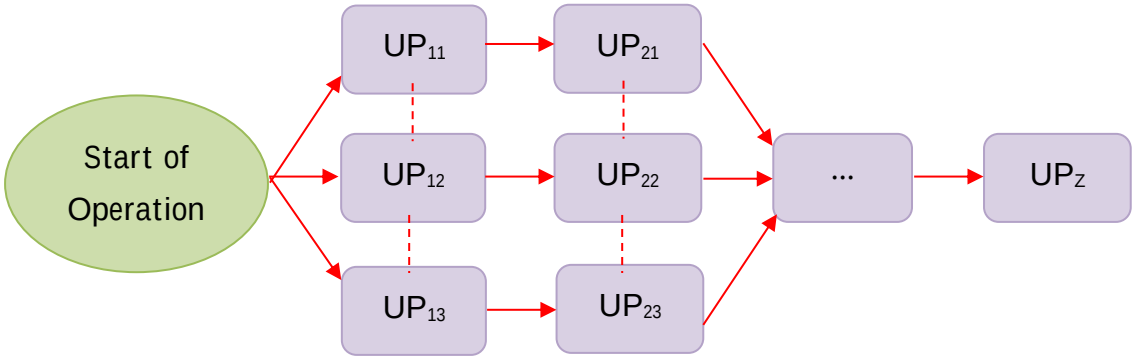

Figure 2-3: Update scheme for iterative (e.g. adjoint method) and sequential (e.g. EnKF) optimization algorithms.

In the 20th century, the idea of substituting actual simulation models with proxy models took flight and its very first application to history matching and uncertainty quantification was carried out by Mohaghegh [41]. He used a surrogate reservoir model (SRM) to mimic the performance of a large full field model to accelerate simulation run time. This allowed for hundreds of Monte Carlo simulations to be performed within seconds to ascertain the impact of uncertain parameters on the objective function. Another application of proxy modelling methodology in assisted history matching framework was carried out by Zubarev [42]. He presented a comparative study of proxy modelling methodologies applied to history matching and compared their performance to full field simulation models of different model structures and different number of uncertain parameters. He concluded that proxy models are not recommended for history matching especially for cases where the uncertainty domain is so large and complex. Proxy models cannot replace reservoir simulators. The accuracy of results obtained from proxy models depends mainly on the extent of proxy training and validation of the models used in creating the proxies.

If the reader recalls vividly, the last time gradient-based optimization methods were applied in history matching was in the 70-ies and it was the optimal control theory. Despite its exactness in computing gradient of objective function with respect to uncertain parameters, the reason why they were not used for such a very long time had to do with the complexity of coding the adjoint method (a sensitivity-based method). Besides, it is extremely important to know the inner workings of the reservoir simulator so that the coding of the adjoint method can be tailored accordingly. This made the implementation of the adjoint method physically demanding. Researchers sort for easier ways of coupling gradient-based methods with reservoir simulators for application in history matching. An example of a cost-effective gradient-based method that can be easily coupled to a reservoir simulator is the simultaneous perturbation stochastic approximation (SPSA).

Gao [43] coupled the modified version of the SPSA algorithm with a commercial reservoir simulator to history match multiphase flow production data. As the name implies, the SPSA uses simultaneous stochastic perturbation of all uncertain parameters to generate a search direction (down-hill) at each iterative step. Despite modifications made to the convergence behaviour of the SPSA, Gao [43] concluded that the adjoint method delivers better history-match results than the SPSA algorithm when applied to assisted history matching.

In an attempt to improve the uniqueness of reservoir models obtained from history matching using gradient-free algorithms, Rafiee [44] formulated a penalized objective function which avoids over-parameterization and seeks the most suitable unique solution. Their work aimed at delivering a single best-case history match model using gradient-free algorithms which are stochastic-based in nature. Their research was performed and funded under project DGMK 681.

For many years, researchers around the globe experimented with gradient-free algorithms because of the difficulty of coupling gradient-based algorithms with reservoir simulators. In 2010, Almuallim et al. [45] developed a commercial gradient-based assisted history matching tool which utilized the adjoint method for computing gradients of the objective function with respect to uncertain parameters. In his work, he rigorously computed the Jacobian of model responses (which are part of the objective function) with respect to defined model parameters. This information was then used to analyse how each model parameter affects the model responses, and hence, decide how each model parameter should be updated (at grid block level) to minimize the objective function (or the overall model error). Model parameters are analogous to uncertain parameters. He applied his sensitivity-based parameter modification tool to a three-phase reservoir with lengthy production history and more than 40 wells. Using an already matched case achieved by manual history matching, he showed that the adjoint-based history matching tool can achieve very significant reduction in overall model error by executing only a few simulation runs. In addition, the final history-matched case remained geologically consistent since minimal changes were made to grid block model parameters. Other instances where his adjoint-based history matching tool was applied to history matching problems include Ajala [46], Schulze-Riegert [40], Lind [47], Schulze-Riegert [48], Ajala [49] and Ajala [50].

Till today, research remains ongoing on ways to improve reservoir characterization through history matching, achieve geologically consistent history matching, improve the effectiveness of gradient-based or gradient-free algorithms in handling ill-posed minimization problems and making the history matching process faster. Figure 2-4 captures growing interest and development in history matching from 1990 to 2010.

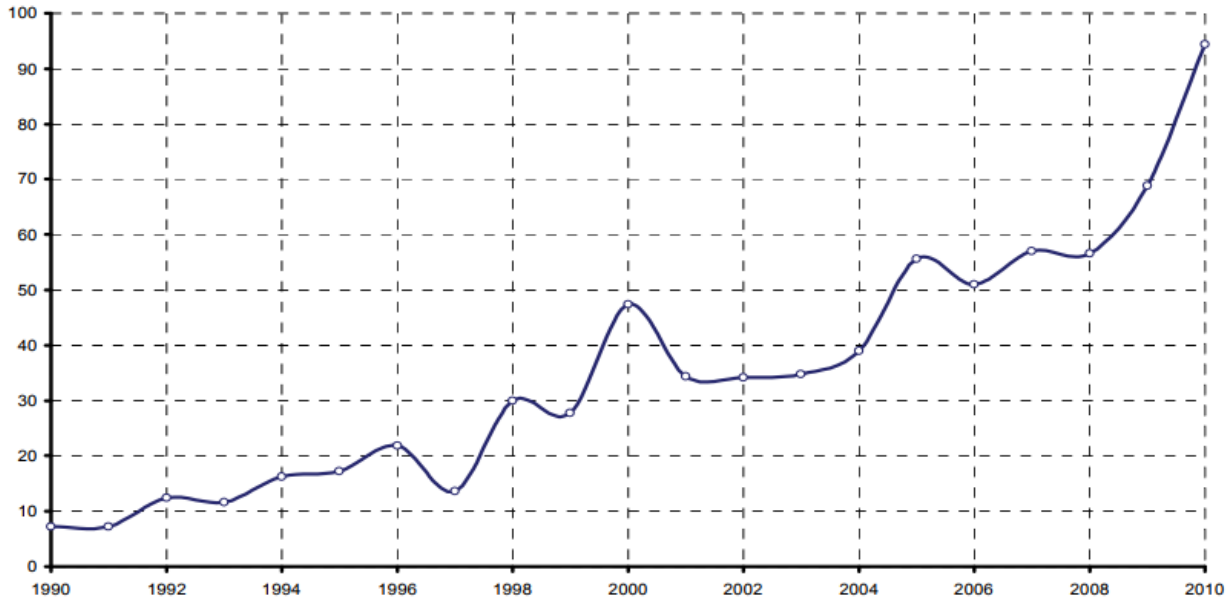

Figure 2-4: Approximate number of papers presented on history matching every year to journals and conferences around the world (Rwechungura [51]).

2.2 State-of-the-Art Methods for Improving Reservoir Characterization in Reservoir Simulation Models during History Matching

There is a strong need to develop reservoir models that capture essential reservoir behaviour in order to capture past, model present and predict future hydrocarbon flow in reservoirs. Usually, a team of geoscientists and engineers work together to create these reservoir models, despite this, the complexity of petroleum reservoirs itself makes the construction of representative reservoir models particularly very challenging. While a handful of reservoir properties are directly measured, many more are inferred (typically based on experience or smart-guesses) leading to the frequent generation of reservoir models with huge uncertainty. Moreover, data acquisition and analysis can be quite expensive and time consuming and since oil and gas companies are required to make important decisions daily with scanty resources at their disposal, the chances of developing reservoir models that omit important reservoir features can be quite high. In this section and other subsequent sections, the term "improving reservoir characterization" and "revealing hidden reservoir features" are used interchangeably. From the author's point of view, both terms are similar.

Determination of the existence of these hidden reservoir features during history matching requires the availability of field measurements (measured injection and production data). These data are typically the most available in any waterflooding project. A good initial guess of the reservoir rock properties (e.g. grid block permeabilities and porosities) is very much important in improving reservoir characterization. The combination of reservoir permeability with injection and production data gives insight into the direction

of fluid flow in a reservoir which is needed to properly characterize reservoirs and estimate the location of most hidden reservoir features.

A handful of techniques exists in literature that utilize injection data, production data and a good initial guess of the reservoir permeability to infer the existence and possibly provide an approximate location of hidden reservoir features in reservoir models. Prior to the 90-ies, numerical simulation had been the most widely used method for improving reservoir characterization through the determination of injector-producer interactions. Results obtained from numerical simulations were then used to infer the existence of hidden reservoir features. Since simulators require an abundance of reservoir data in order to make accurate predictions, the provision of limited reservoir data made the use of simulators alone insufficient in revealing hidden reservoir features. It became paramount to either supplement numerical simulation with other specialized techniques or replace them with methods that do not require the construction of reservoir simulation models in order to effectively reveal hidden reservoir features.

In the mid 90-ies, statistics-based approaches like the Spearman rank correlation [52], [53] and wavelet transformation combined with the Spearman rank correlation [54] were used to visually cross-correlate injection and production rates for different well pairs in an attempt to reveal hidden reservoir features (see Figure 2-5).

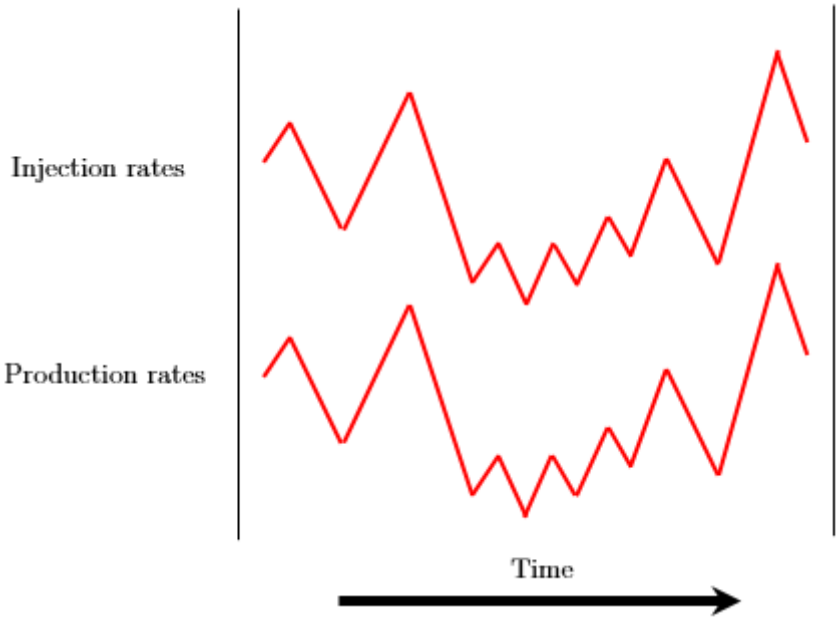

Figure 2-5: Cross-correlation of injection and production rates with the Spearman rank correlation.

This methods however suffered from two main limitations: firstly, the cross-correlation results were lacking in distinction (results were non-unique) and secondly, the entire process was time consuming. In the late 90-ies, Panda and Chopra [55] came up with an inexpensive and less time consuming approach for quantifying injector-producer interactions. Their approach could be considered as the first data-driven and automated

approach for estimating injector-producer interactions. In their approach, they trained an artificial neural network (ANN) with a set of multi-variate data consisting of injection, production, well location, sand/shale and petrophysical information in order to estimate injection-producer interactions and infer the location of hidden reservoir features such as faults, pinch-outs, thief zones etc. To quantify injector-producer interactions, an adequate permeability field capturing the measured permeability at respective well locations and the thickness of the surrounding wells were used as input for the ANN. The key idea behind the determination of injector-producer interactions through their use of the ANN could be found in the fluctuations present in the injection and production data. If these fluctuations are non-existent, they prohibited the use of their method in inferring hidden reservoir features.

Earlier on in the 20th century, Albertoni and Lake [56] presented the idea of combining constrained multi-variate linear regression with diffusivity filters to infer the location of hidden reservoir features between injector-producer pairs. In their work, injector-producer interactions is viewed as synonymous to interference well testing. In other words, a stimulus at the injector returns a response at the producer. The relationship between these input/output signals are described by weighting coefficients. These weighting coefficients quantify connectivity between injector-producer pairs and infer hidden reservoir features like faults, channels etc. Injection and production data were the only inputs required to generate these weighting coefficients. Connectivity between wells described by these weighting coefficients depends only on the location of the well and the field geology. Similar to other existing methods, it is imperative for the injection and production rates to fluctuate for proper estimation of the weighting coefficients.

Inspired by the concept proposed by Albertoni and Lake [56], Yousef et al. [57] developed the capacitance model (CM) for characterizing reservoirs based on fluctuations in injection and production rates. They determined two main parameters for each injector-producer pair. One parameter accounts for connectivity between injector-producer pairs and the other quantitatively describes fluid storage in inter-well regions. Some years later, Sayarpour [58] made some improvements to the capacitance model (CM) developed by Yousef et al. [57]. The improved model was called the capacitance-resistance model (CRM) and it became the most widely used data-driven model in the 20th century. The key difference between the CRM and the model developed by Albertoni and Lake [56] lies in the capability of the CRM in accounting for compressibility and transmissibility effects. The model developed by Albertoni and Lake [56] only accounts for transmissibility effects. Furthermore, the CRM utilizes fluctuation in flow rates and flowing pressure data to quantitatively infer hidden reservoir features in reservoir models during history matching.

In the year 2010, Kaviani et al. [59] developed a multi-well productivity index-based method capable of inferring the existence of hidden reservoir features in reservoir models. In their approach, by separating the effects of skin factors, well locations, injection rates

and producers' flowing pressures from estimated connectivity, a heterogeneity matrix is obtained which represents the field heterogeneity and anisotropy. Few years after, Gherabati et al. [60] developed a network model approach which utilizes well location information, injection and production rate data for estimating conductance values between well pairs. These conductance values, which is determined from the average permeability between injector-producer pair, area open to flow between pairs, distance between wells and the average fluid viscosity can quantitatively infer the existence of hidden reservoir features. Their method was basically the first reported approach in literature to support changes in flow pattern due to injector-producer conversion and vice versa, shutting-in a producer that has been operating for a while or the inclusion of a new well (e.g. an infill well). Furthermore, their approach was the first to handle constant rate injectors and producers - an injection strategy that is difficult to handle for well-rate-fluctuation-based data-driven methods (Panda and Chopra [55], Albertoni and Lake [56], Yousef et al. [57], Sayarpour [58]) and correlation-based methods (Heffer et al. [61], Jansen and Kelkar [62]). The model parameter defined for their minimization problem which is the problem of estimating connectivity between well pairs is the conductance. Like with many other existing methods ([56], [57], [58]), Kaviani et al. [59] and Gherabati et al. [60] used connectivity maps to infer the existence of hidden reservoir features in reservoir models but failed to explicitly determine the exact location, shape and other essential properties of these reservoir features.

In the year 2016, another class of data-driven and model-free reservoir characterization method was developed. Tian and Horne [63] used the modified Pearson's correlation coefficient method to estimate connectivity between injector-producer pairs and provided a validation to the estimated connectivities by applying a machine learning based multi-well testing tool. Connectivity between well pairs were estimated by comparing injection and production rate measurements to a reference state rates obtained by running simulation for a case where zero injection rates are specified. For a completely homogeneous system without any hidden reservoir feature, connectivity using their approach was determined by the distance between injector-producer pairs. The degree of accuracy of estimated connectivity depended slightly on fluctuations in injection rates.

Recently, Guo and Reynolds [64] improved the inter-well numerical simulation model (INSIM) earlier developed by Zhao et al. [65]. The improved method called the inter-well numerical simulation model with front tracking (INSIM-FT) solves for pressure implicitly and computes water saturation explicitly using the Buckley-Leverett equation [66]. Saturation profiles along connections between well pairs were computed analytically by a front-tracking method [67] which eliminated deficiencies experienced when a change in flow pattern is encountered in INSIM such as handling injector-to-producer conversion and vice versa, long well shut-in period and the addition of a new well. Imaginary wells placed between well pairs increased the number of possible flow paths travelled by the injected water and prevented direct injector-injector and producer-producer connections. These imaginary wells are neither injectors nor producers and thus their total flow rate

is always zero. The inclusion of the front-tracking method ensured improved inter-well connectivity estimation and support for reservoir without injectors (aquifer-dominated reservoirs). Similar to other existing approaches, injection and production data were required to estimate model parameters such as transmissibilities, pore volume and relative permeability curves. The transmissibility and pore volume between well pairs is analogous to inter-well permeability and porosity. A connectivity map is designed a priori describing how wells are connected to one another before history matching commences. Wells not connected in the connectivity map are not considered in the history matching phase. Only producers are history-matched since the true water injection rates and pressures are specified in INSIM-FT for all injectors. Furthermore, Guo and Reynolds [64] performed history matching using the ensemble smoother with multiple data assimilation [68] starting typically with hundreds of prior model parameters, consequently no prior knowledge of reservoir geology is required.

Awofodu et al. [69] evaluated different optimization algorithms applied to history matching workflows at grid block level for the purpose of revealing hidden reservoir features not captured in reservoir models during history matching. They defined a history matching problem with a base model lacking in channel information that was captured in the true model used for generating measured data. In order to compound the minimization problem, they generated measured data from a heterogeneous true model solution and specified these measurements for an equivalent homogeneous base model. Starting with an initial homogeneous base model, they applied the Plackett-Burmann method [70] to generate initial ensembles for the evaluated optimization methods. From their work, they deduced that gradient-free methods like the Covariance Matrix Adaptation Evolution Strategy (CMA-ES) [71] and proxy modelling methods [72] coupled with neural networks cannot reveal hidden reservoir features despite the application of the Plackett-Burmann to speed up the development of satisfactory base models.

So far, the methods developed by Gherabati et al. [60] and Guo and Reynolds [64] surpasses the CRM [58] in the sense that they can be applied to reservoir models with constant and fluctuating injection rates and models experiencing changes in flow patterns over time (e.g. shutting-in wells that have been operating for a long time, injection-to-producer conversion or vice versa and the addition of a new well). Despite that, the location and shape of hidden reservoir features are not revealed by these methods but rather their existence is inferred from connectivity maps ([56], [57], [58], [59], [60], [64], [65]). Finally, in most reported application of these state-of-the-art methods in history matching problems, they have only been extensively used to improve inter-well connectivity by inferring the presence of hidden faults and channels in base models. To the best of the author's knowledge, no method exists in literature or in the market that can be used to reveal the approximate location and shape of hidden channels, faults, fractures and vertical or non-vertical communication in reservoir models.

In this thesis, we developed an adjoint-based reservoir characterization improvement workflow that can be used to reveal the approximate location, shape and other essential characteristics of hidden reservoir features not captured in reservoir simulation models. In addition, we show that the proposed method is able to reveal the approximate location and shape of hidden reservoir features regardless of whether the injection rates are constant or varying. Furthermore, reservoir feature detection algorithms tailored specifically to each reservoir feature to be revealed are formulated from rigorous case studies highlighting model parameters that are influential in revealing specific types of reservoir features. Also, in an attempt to minimize human bias when determining the shape of revealed faults, a fault shape detection algorithm that estimates revealed fault shape in form of a line is developed. Unlike other aforementioned methods earlier described in literature, our approach requires the use of a commercial reservoir simulator to predict fluid flow and pressure changes across the reservoir.

In the next chapter, the working principle of the adjoint-based reservoir characterization improvement workflow is discussed. First, a brief description of the objective function equation is provided. Afterwards, a detailed mathematical description of the adjoining of the fluid flow and pressure equations solved by the simulator to the objective function equation in order to obtain the adjoint system of equations, adjoint variables and adjoint sensitivities is presented. Thereafter, an explanation on what adjoint sensitivities are and how they are computed from calculated adjoint variables are provided. Subsequently, a succinct mathematical description is presented showing how model parameter updates are guided by computed adjoint sensitivities using the steepest-descent algorithm. Finally, a detailed explanation on what the adjoint-based reservoir characterization improvement workflow is, how it works, and the number of stages involved is covered in the next chapter.

Chapter 3

> "The significant problems we have cannot be solved at the same level of thinking with which we created them"
>
> Albert Einstein (1879-1955)

3. A Reservoir Characterization Improvement Workflow Utilizing the Adjoint Method

This chapter introduces the methods and algorithms used in this thesis. We review the linear least squares objective function equation, fluid flow and pressure equations solved by most commercial finite difference reservoir simulators, the adjoint method, the steepest-descent algorithm and finally provide a detailed explanation of the fundamental working principle of the adjoint-based reservoir characterization improvement workflow.

3.1 Objective Function Formulation

In Chapter 2, some references were made to the term "objective function". In this section, a detailed explanation on what the objective function is and why it is important to formulate it for any history matching task is discussed here.

In history matching or minimization problems, the objective function term (or overall model error), Q, quantitatively describes the quality of a reservoir simulation model. In theory, Q is minimized per iteration run until $Q \to 0$ is reached. In practice, getting $Q \to 0$ is not feasible in history matching so we try to minimize Q as best as we can. In addition, it may be worthwhile to mention that Q is a dimensionless entity. In this thesis, the linear least squares objective function for a three-phase reservoir as formulated by Almuallim et al. [45] can be written as:

$$Q = \sum_{t}^{steps} \left[\frac{\alpha_{o,i}\left(O_{i,t}{}^{sim} - O_{i,t}{}^{obs}\right)^2}{\beta_{o,i}} + \frac{\alpha_{w,i}\left(W_{i,t}{}^{sim} - W_{i,t}{}^{obs}\right)^2}{\beta_{w,i}} + \frac{\alpha_{g,i}\left(G_{i,t}{}^{sim} - G_{i,t}{}^{obs}\right)^2}{\beta_{g,i}} + \frac{\alpha_{p,i}\left(p_{i,t}{}^{sim} - p_{i,t}{}^{obs}\right)^2}{\beta_{p,i}} + \frac{\alpha_{RFT,i}\left(RFT_{i,t}{}^{sim} - RFT_{i,t}{}^{obs}\right)^2}{\beta_{RFT,i}} \right] \quad (1)$$

where i is the well of interest. α represents the positive weighting factors for each model response defined e.g. fluid and gas production rates, water-cut, pressures (flowing/shut-in) and RFT (Repeated Formation Tester) data. O, W, G, p, RFT denotes oil, water, gas, well bottom-hole flowing pressures and RFT respectively. β is a variance (normalization term) for specifying user-defined tolerance for each model response (or mismatch parameter) defined for well i. t represents the time at which measurements are available and also the time for which model responses are computed and outputted by the reservoir simulator. This guarantees accurate calculation of error between the calculated and measured data. sim represents the simulated or calculated data obtained from the reservoir simulator while obs represents the measured or observed data.

Most of the model responses defined in this thesis are limited to injection and production rates, water-cut and flowing bottom-hole pressures for the injectors and producers. Consequently, the RFT terms in Equation (1) are neglected.

3.2 The Reservoir Simulator

In order to compute saturation and pressure changes in time across grid blocks in our reservoir models, we utilized a commercial finite difference reservoir simulator. The equation solved by reservoir simulators can be derived by combining the law of force, law of conservation of mass and the thermodynamic connections that illustrate the pressure-volume-temperature behaviour of oil, water and gas [73]. According to Breitenbach et al. [73], the fundamental flow equations for oil, water and gas for simple black oil formulations are:

For Oil (in Volume/Time)

$$\frac{\partial}{\partial x}\left(\frac{q_{oR}}{B_o}\right)\Delta x + \frac{\partial}{\partial y}\left(\frac{q_{oR}}{B_o}\right)\Delta y + \frac{\partial}{\partial z}\left(\frac{q_{oR}}{B_o}\right)\Delta z + q_{op} + \left[\frac{\emptyset_{orig} c_f}{B_o} + \emptyset \frac{\partial}{\partial p_0}\left(\frac{1}{B_o}\right)\right] V_b S_o \frac{\partial p_o}{\partial t} = -\frac{V_b \emptyset}{B_o}\frac{\partial S_o}{\partial t} \quad (2)$$

For Water (in Volume/Time)

$$\frac{\partial}{\partial x}\left(\frac{q_{wR}}{B_w}\right)\Delta x+\frac{\partial}{\partial y}\left(\frac{q_{wR}}{B_w}\right)\Delta y+\frac{\partial}{\partial z}\left(\frac{q_{wR}}{B_w}\right)\Delta z+q_{wp}+\frac{V_bS_w\emptyset_{orig}c_f}{B_w}\frac{\partial p_o}{\partial t}+V_bS_w\emptyset\frac{\partial}{\partial p_w}\left(\frac{1}{B_w}\right)\frac{\partial p_w}{\partial t}=-\frac{V_b\emptyset}{B_w}\frac{\partial S_w}{\partial t} \quad (3)$$

For Gas (in Volume/Time)

$$\begin{aligned}&\frac{\partial}{\partial x}\left(\frac{q_{gR}}{B_g}+\frac{q_{oR}R_s}{B_o}+\frac{q_{wR}R_{sw}}{B_w}\right)\Delta x+\frac{\partial}{\partial y}\left(\frac{q_{gR}}{B_g}+\frac{q_{oR}R_s}{B_o}+\frac{q_{wR}R_{sw}}{B_w}\right)\Delta y\\&+\frac{\partial}{\partial z}\left(\frac{q_{gR}}{B_g}+\frac{q_{oR}R_s}{B_o}+\frac{q_{wR}R_{sw}}{B_w}\right)\Delta z\\&+\left(q_{gp}+q_{op}R_s+q_{wp}R_{sw}\right)\\&+\left[\emptyset_{orig}V_bc_f\left(\frac{S_g}{B_g}+\frac{S_oR_s}{B_o}+\frac{S_wR_{sw}}{B_w}\right)+\emptyset V_bS_o\frac{\partial}{\partial p_o}\left(\frac{R_s}{B_o}\right)\right]\frac{\partial p_o}{\partial t}\\&+\emptyset V_bS_w\frac{\partial}{\partial p_w}\left(\frac{R_{sw}}{B_w}\right)\frac{\partial p_w}{\partial t}+\emptyset V_bS_g\frac{\partial}{\partial p_g}\left(\frac{1}{B_g}\right)\frac{\partial p_g}{\partial t}\\&=-\emptyset V_b\left(\frac{1}{B_g}\frac{\partial S_g}{\partial t}+\frac{R_s}{B_o}\frac{\partial S_o}{\partial t}+\frac{R_{sw}}{B_w}\frac{\partial S_w}{\partial t}\right)\end{aligned} \quad (4)$$

where q_{oR}, q_{wR} and q_{gR} are oil, water and gas production rates computed from Darcy's law. The subscript R denotes reservoir conditions. B_o, B_w and B_g are the formation volume factor for oil, water and gas respectively. c_f is the pore volume or formation compressibility, V_b is the bulk volume and S_o, S_w and S_g are oil, water and gas saturation. p_o, p_w and p_g are the oil phase, water phase and gas phase pressure. q_{op}, q_{wp} and q_{gp} denotes oil, water and gas production rates at the surface. $\emptyset_{orig}$ connotes original porosity at initialization and $\emptyset$ is the new porosity after pore pressure drop. $\emptyset_{orig}$ and $\emptyset$ are usually approximately the same because of the extremely small c_f in reservoirs. t represents time, R_s is the gas dissolved in oil and R_{sw} is the gas dissolved in water. Δx, Δy and Δz represents the differential element in X, Y and Z direction.

Conversion factors in Equations (2) to (4) are neglected. Nowadays, most commercial reservoir simulators express the computed oil, water or gas production rates in kg/day or moles/day. The fundamental pressure equation can be obtained by combining Equations (2) to (4) with pressure defined as the only dependent variable. This means that terms like $\frac{\partial p_w}{\partial t}$, $\frac{\partial p_g}{\partial t}$, q_{oR}, q_{wR} and q_{gR} becomes

$$\frac{\partial p_w}{\partial t}=\frac{\partial p_o}{\partial t}-\frac{\partial p_{c_{ow}}}{\partial t} \quad (5)$$

$$\frac{\partial p_g}{\partial t} = \frac{\partial p_o}{\partial t} + \frac{\partial p_{c_{go}}}{\partial t} \tag{6}$$

$$q_{oR} = -\frac{A_x k_x k_{ro}}{\mu_o}\left(\frac{\partial p_o}{\partial x} + \rho_{oR}\frac{\partial h}{\partial x}\right) \tag{7}$$

$$q_{wR} = -\frac{A_x k_x k_{rw}}{\mu_w}\left(\frac{\partial p_o}{\partial x} - \frac{\partial p_{c_{ow}}}{\partial x} + \rho_{wR}\frac{\partial h}{\partial x}\right) \tag{8}$$

$$q_{gR} = -\frac{A_x k_x k_{rg}}{\mu_g}\left(\frac{\partial p_o}{\partial x} + \frac{\partial p_{c_{go}}}{\partial x} + \rho_{gR}\frac{\partial h}{\partial x}\right) \tag{9}$$

In Equations (7) to (9), q_{oR}, q_{wR} and q_{gR} are expressed in the X direction only. Similar expressions can be written as well for them in the Y and Z directions.

For simplicity purposes, the fundamental flow equation solved by most simulators can be written as

$$f(y, x) = 0 \tag{10}$$

where f denotes the fluid flow simulation equations solved for oil, water, gas and the flowing wellbore pressure. y expressed in Equation (11), is a vector of state variables (e.g. grid block pressure and saturation) computed for every specified time step and x is a vector of model parameters typically modified during history matching (e.g. grid block permeability and porosity).

$$y = \begin{bmatrix} y^0 \\ y^1 \\ y^2 \\ \vdots \\ y^L \end{bmatrix} \tag{11}$$

y^0 denotes predetermined initial reservoir conditions. Besides, for each grid block, y^l can be expressed as

$$y^l = \left[p_1^l, \cdots, p_N^l, S_{o,1}^l, \cdots S_{o,N}^l, S_{w,1}^l, \cdots S_{w,N}^l, \cdots, P_{wf,1}^l, \cdots, P_{wf,N_w}^l\right]^T \tag{12}$$

where p, S_o, S_w and P_{wf} denotes pressure, oil saturation, water saturation and flowing well pressure at each grid block. $l = 0,1,2,3, \cdots, L$ represents the time step index and L signifies the last time step. N is the total number of active grid blocks and N_w is the total number of wells. T indicates that the vector y^l is transposed.

If the vector of model parameters x consists of only permeability in the X direction and porosity (K_x & $\emptyset$) for all active grid blocks, then x for porosity and permeability in the X direction can be expressed as

$$x_{\emptyset} = \emptyset = [\emptyset_1, \emptyset_2, \emptyset_3, \cdots, \emptyset_N]^T \tag{13}$$

$$x_{K_x} = K_x = \left[K_{x,1}, K_{x,2}, K_{x,3}, \cdots, K_{x,N}\right]^T \tag{14}$$

Taking Equation (12) into account, Equation (10) for a reservoir system with phases m at grid block n can be expressed as

$$f_{m,n}^{l+1}(y^{l+1}, y^l, x) = 0 \tag{15}$$

where $m = o, w, g$ and $n = 1,2,3, \cdots, N$. o, w, g denotes oil, water and gas respectively. Similarly for the flowing wellbore pressure, Equation (10) can be expressed as

$$f_{Pwf,w}^{l+1}(y^{l+1}, y^l, x) = 0 \tag{16}$$

where $w = 1,2,3, \cdots, N_w$.

A simplified form of the complete simulator equations expressed in Equations (15) and (16) can be written as

$$f^{l+1} = f(y^{l+1}, y^l, x) = \begin{bmatrix} f_{o,1}^{l+1} \\ f_{w,1}^{l+1} \\ f_{g,1}^{l+1} \\ \vdots \\ f_{g,N}^{l+1} \\ f_{Pwf,1}^{l+1} \\ \vdots \\ f_{Pwf,N_w}^{l+1} \end{bmatrix} = 0 \tag{17}$$

In most reservoir simulators available today, the Newton-Raphson method [74] is used to solve Equation (17) using the fully implicit approach [75]. Once Equation (17) is solved, information necessary to formulate and solve the adjoint equations becomes available.

3.3 Formulation of the Adjoint Equations and Sensitivities

Fichter et al. [76] described the adjoint method as an efficient and powerful gradient-based tool for computing first-order derivatives of the objective function with respect to

desired model parameters (uncertain parameters). Similarly, in history matching and optimization problems, the adjoint method can be applied to compute sensitivities. These sensitivities are the first-order derivatives of objective function (overall model error) with respect to model parameters like porosity and permeability at every grid block. Sensitivities of the objective function to virtually any type of model parameter (local- or global-based) can be obtained using the adjoint method. Using any minimization algorithm of choice, these first-order derivatives can be used to minimize the objective function Q.

Sensitivity calculations using the adjoint method warrants three main steps as described by Zhang et al. [77]. These principal steps (arranged in the order of their execution) are: the forward model formulation, solving the adjoint system of equations and the sensitivity calculations. The forward model formulation, which is the first task executed, can be performed by any available commercial reservoir simulator (e.g. ECLIPSE E100, tNavigator, CMG IMEX etc.). Outputs from the forward model run typically stored in a restart file required for solving the adjoint equations and sensitivity calculations include pressure, oil, water and gas saturations at each grid block for each time step. In addition, the flowing bottom-hole pressures (BHP) for wells at each time step is often required.

Following the successful execution of a simulation run, the pressure and saturation results are saved for each grid block at each time step in a restart file which can be very large depending on the number of active grid blocks in the reservoir model. Thereafter, solving of the adjoint system of equations commences. According to Oliver et al. [14], in order to formulate the adjoint equations, it is necessary to adjoin the simulator equations to the objective function equation by defining a connecting term J as shown in Equation (18).

$$J = Q(y,x) + \lambda^T f(y,x) \tag{18}$$

where λ is a multiplier that satisfies Equation (18). Expressing J in differential form, Equation (18) becomes

$$dJ = (\nabla_y Q)^T dy + \lambda^T (\nabla_y f^T)^T dy + (\nabla_x Q)^T dx + \lambda^T (\nabla_x f^T)^T dx \tag{19}$$

To solve for λ, dy must be eliminated in Equation (19). To achieve this, we define the condition that

$$(\nabla_y Q)^T = -\lambda^T \left(\nabla_y f^T\right)^T \tag{20}$$

Taking the transpose of Equation (20), we obtain an expression presented in Equation (21) that can be used to solve for λ.

$$\nabla_y Q = -\lambda \left(\nabla_y f^T\right) \tag{21}$$

As described by Oliver et al. [14], Equation (21) is regarded as the adjoint equation that must be solved backwards in time in order to obtain the multiplier λ. Hereinafter, we will refer to λ as the "adjoint variable".

Figure 3-1 presents typical minimum and maximum values for λ (lambda) over a 50 time step period for an especially well formulated history matching problems with numerical-noise-free simulation results. Note that the adjoint variables are computed for each active grid block in a reservoir model at each time step. The computed adjoint variables from Equation (21) are listed out in a row vector of λ called an adjoint vector. In Figure 3-1, the minimum and maximum adjoint variables in a reservoir model at each time step is plotted. In most practical applications, the larger the adjoint variables computed (e.g. -1.67, -16.13, 2.56, 10.51 etc.), the less meaningful they become and consequently the less likely a good history match is achieved. The stability of the adjoint variables computed is heavily dependent on the accuracy of the simulator results [78].

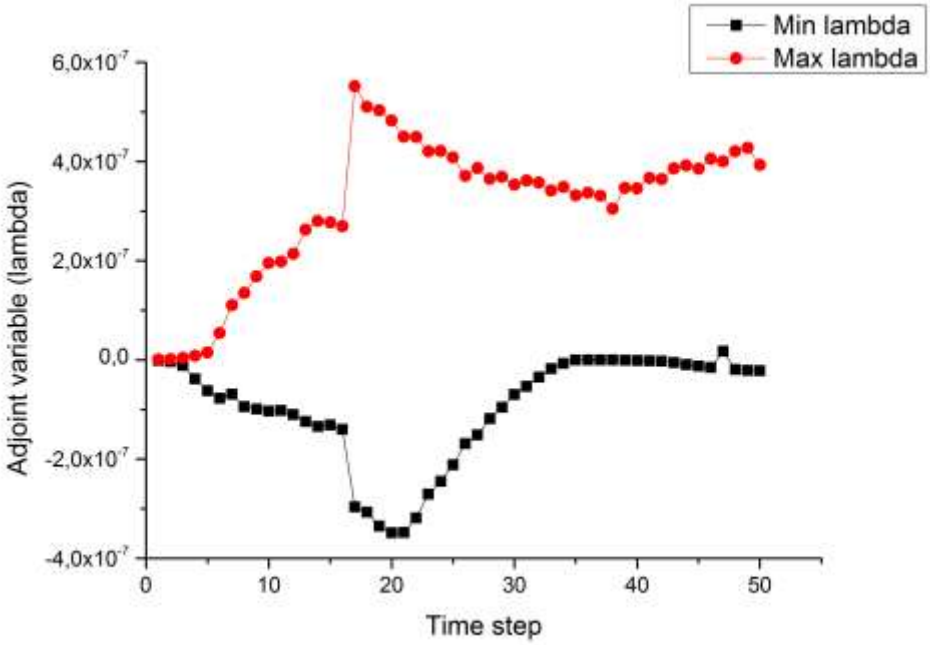

Figure 3-1: A typical adjoint variable (λ) vs. time step plot

Once again, computation of the adjoint variable λ is only possible if a forward model run $\nabla_y f^T$ has already been executed. Unlike the adjoint equation, the simulator equations must be solved forward in time. Taking the time step index into account, the linearized form of the adjoint equation described in Equation (21) can be expressed as

$$\left[\nabla_{y^l}(f^l)^T\right]\lambda^l + \left[\nabla_{y^l}(f^{l+1})^T\right]\lambda^{l+1} = -\nabla_{y^l}Q \qquad (22)$$

where $\nabla_{y^l}Q$, expressed in Equation (23), is the derivative of the objective function Q with respect to simulator primary variables y^l (pressure, oil, water and gas saturation) at

every grid block at time step l. $\nabla_{y^l}(f^l)^T$, expressed in Equation (24), is the transpose of the Jacobian matrix of the complete simulator equations evaluated at y^l.

$$\nabla_{y^l} Q = \left[\frac{\partial Q}{\partial p_1^l}, \frac{\partial Q}{\partial S_{o,1}^l}, \frac{\partial Q}{\partial S_{w,1}^l}, \frac{\partial Q}{\partial S_{g,1}^l}, \cdots, \frac{\partial Q}{\partial p_N^l}, \frac{\partial Q}{\partial P_{wf,1}^l}, \cdots, \frac{\partial Q}{\partial P_{wf,N_w}^l}\right]^T \tag{23}$$

$$\nabla_{y^l}(f^l)^T = \begin{bmatrix} \frac{\delta f_{o,1}^l}{\delta p_1^l} & \frac{\delta f_{w,1}^l}{\delta p_1^l} & \cdots & \frac{\delta f_{g,N}^l}{\delta p_1^l} \\ \frac{\delta f_{o,1}^l}{\delta S_{w,1}^l} & \frac{\delta f_{w,1}^l}{\delta S_{w,1}^l} & \cdots & \frac{\delta f_{g,N}^l}{\delta S_{w,1}^l} \\ \frac{\delta f_{o,1}^l}{\delta S_{g,1}^l} & \frac{\delta f_{w,1}^l}{\delta S_{g,1}^l} & \cdots & \frac{\delta f_{g,N}^l}{\delta S_{g,1}^l} \\ \frac{\delta f_{o,1}^l}{\delta p_2^l} & \frac{\delta f_{w,1}^l}{\delta p_2^l} & \cdots & \frac{\delta f_{g,N}^l}{\delta p_2^l} \\ \vdots & \vdots & \cdots & \vdots \\ \frac{\delta f_{o,1}^l}{\delta S_{g,N}^l} & \frac{\delta f_{w,1}^l}{\delta S_{g,N}^l} & \cdots & \frac{\delta f_{g,N}^l}{\delta S_{g,N}^l} \end{bmatrix} \tag{24}$$

When Equation (22) is written out for each state variable, the combination of all equations is referred to as the "adjoint system of equations". The adjoint equation described in Equation (22) is solved for oil, water, gas and flowing wellbore pressure under the conditions that

$$\lambda_o^{L+1} = \lambda_w^{L+1} = \lambda_g^{L+1} = \lambda_{Pwf}^{L+1} = 0 \tag{25}$$

$$\lambda_o^{l=0} = \lambda_w^{l=0} = \lambda_g^{l=0} = \lambda_{Pwf}^{l=0} = 0 \tag{26}$$

where L is the last time step for the forward simulation run and the first time step for the backward adjoint run. Equations (25) precludes the calculation of λ for time steps greater than L. Furthermore, Equation (26) ensures that initial reservoir conditions are fixed. When Equation (22) is expressed in terms of oil, water or gas, the unit of λ is $\frac{day}{m^3}$. On the contrary, when Equation (22) is expressed in terms of pressure, the unit of λ is bar^{-1}.

In order to solve the adjoint equation presented in Equation (22), the solution of $\nabla_y f^T$ obtained after the forward run is stored at each defined time step. The final task to be executed after successful forward simulation run and solving of adjoint system of equations is the sensitivity calculations. The computation of model parameter sensitivity is performed by combining Equations (19) and (20) and then transposing to obtain

$$dJ = (\nabla_x Q)dx + \lambda(\nabla_x f^T)dx \tag{27}$$

A Jacobian matrix similar to that shown in Equation (24) can also be written for the derivative of the complete simulator equations with respect to model parameters $\nabla_x f^T$. In discretized form and with the inclusion of the time stepping index, Equation (27) can be written as

$$\nabla_x J = \nabla_x Q + [\nabla_x (f^l)^T](\lambda^l) \tag{28}$$

where $\nabla_x J$ is the model parameter adjoint sensitivity. The presence of the derivative of the objective function with respect to model parameters $\nabla_x Q$ in Equation (28) ensures that complete information on model parameter sensitivities are obtained. For typical history matching problems, $\nabla_x Q$ can be written as

$$\nabla_x Q = \frac{\partial Q}{\partial x} = [\frac{\delta Q}{\delta \emptyset}, \frac{\delta Q}{\delta K}, \dots, \frac{\delta Q}{\delta x_{Nx}}]^T \tag{29}$$

where $\emptyset$ and K are the porosities and permeabilities (K_x, K_y, K_z) in every grid block. Nx denotes the number of model parameters to be modified during history matching. Equation (28) written with respect to K_x becomes

$$\nabla_{K_x} J = \frac{dJ}{dK_x} = \nabla_{K_x} Q + \sum_{l=1}^{L} \left[\nabla_{K_x} (f^l)^T\right](\lambda^l) \quad for\ l = 1,2,3 \dots, L \tag{30}$$

A similar expression can be written for K_y, K_z, $\emptyset$ and other model parameters of interest (e.g. relative permeability parameters). The unit of $\nabla_x J$ and $\nabla_x Q$ is dependent on the unit of the model parameter. For example, $\nabla_{K_x} J$ and $\nabla_{K_x} Q$ both have a unit of mD^{-1} while $\nabla_{\emptyset} J$ and $\nabla_{\emptyset} Q$ is dimensionless.

In order to compute adjoint sensitivities with Equation (28), vector $\nabla_x Q$ must first be evaluated. Q is considered as the whole data mismatch part of the objective function. Subsequently, $\nabla_x Q$ is given by

$$\nabla_x Q = \nabla_x Q(x) = \nabla_x \left[\sum_i \frac{\left(d_i^{sim}(x) - d_i^{obs}\right)^2}{\beta_i^2}\right] \tag{31}$$

The expression provided for $Q(x)$ in Equation (31) is a simplified form of the objective function equation previously described in Equation (1). The choices of Q are restricted to well oil production rate, well water-cut, well gas production rate, flowing/shut-in pressures etc. particularly at time steps where measurements exist. If one wishes to use an easy-to-implement first-order iterative optimization algorithm like the steepest

descent [79], then only $\nabla_x Q$ needs to be computed in the adjoint procedure. By doing so, Equation (22) only needs to be solved once and the resulting adjoint solutions are substituted into Equation (28) to determine the gradient. Consequently, Equation (28) can be rewritten as

$$\frac{dQ}{dx} = \nabla_x Q + [\nabla_x (f^l)^T](\lambda^l) \tag{32}$$

It is quite common to write the left-hand size of Equation (28) as the gradient of J, or the gradient of Q with respect of x and this depends strongly on the iterative optimization algorithm employed [80].

In order to familiarize the reader with what typical adjoint sensitivity plots look like, examples are presented. Figure 3-2 presents the sensitivity of the objective function Q to K_x ($\frac{dQ}{dK_x}$) at last time step (reserve direction of forward model time step) for a 20 x 20 x 1 reservoir model after history matching. Similar to the adjoint variables, adjoint sensitivities are typically of very low values. As seen in Figure 3-2, adjoint sensitivities can be positive, negative or zero. A grid block with a negative sensitivity value suggests an increase in the grid block property value (e.g. increasing K_x for that grid block) in order to reduce the objective function. On the other hand, a grid block with a positive sensitivity value suggests a decrease in the grid block property value (e.g. decreasing K_x for that grid block) in order to reduce the objective function. A grid block with zero sensitivity means that the (present) grid block property value has no influence on the objective function (e.g. keep K_x unchanged for that grid block).

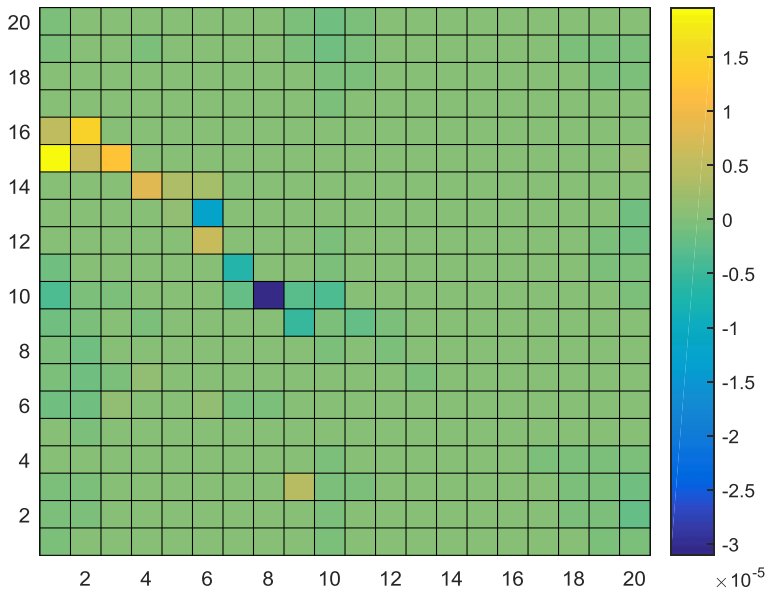

Figure 3-2: Sensitivity of Q to K_x for a 20 x 20 x 1 reservoir model

Figure 3-3 and Figure 3-4 show 2-D and 3-D plots for the sensitivity of the objective function to permeability in the X-direction ($\frac{dQ}{dK_x}$) at last time step for a 39 x 39 x 1 reservoir model. It is important to note that sensitivities changes per time step. This means that the sensitivity map for the 1st time step is not the same as the sensitivity map for the 20th time step and so on.

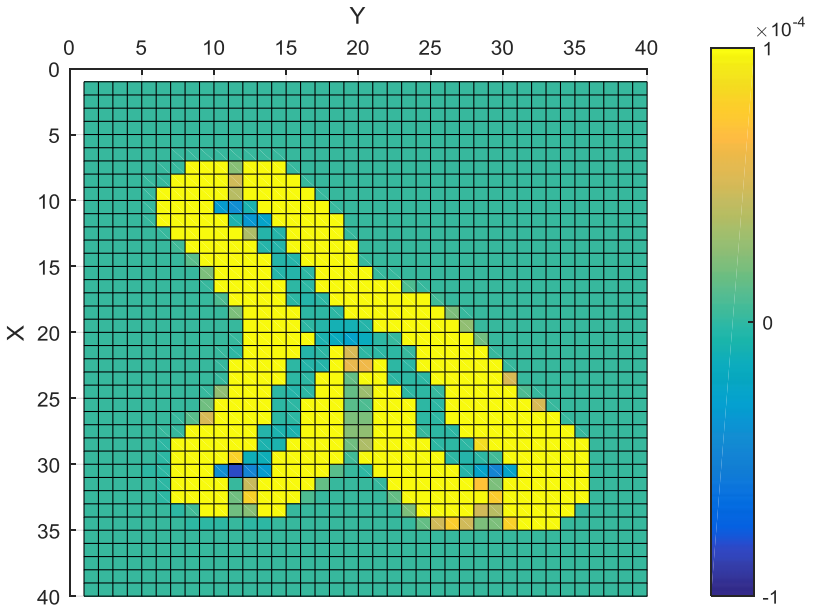

Figure 3-3: 2-D sensitivity plot of Q to K_x for a 39 x 39 x 1 reservoir model

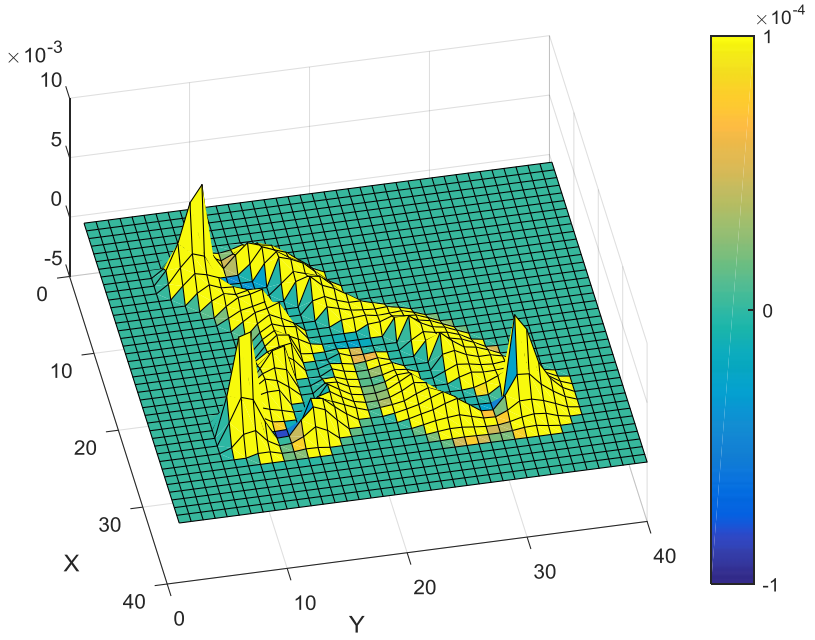

Figure 3-4: 3-D sensitivity plot of Q to K_x for a 39 x 39 x 1 reservoir model

3.3.1 Merits of the Adjoint Method

A handful of advantages in using the adjoint method for history matching and optimization problems include:

1. It is possible to generate as much analytical model parameter sensitivities as required from a single forward simulation run.
2. Since model parameter modification per iteration is based on analytically computed sensitivities, minimal human involvement is required.
3. Small modifications to model parameters like porosity and permeability are performed on a grid cell-by-cell basis around the neighbourhood of injectors and producers.
4. No need for the use of box multipliers.
5. Only a relatively small number of simulations are required to achieve practically acceptable history-match results when compared to other history matching techniques.
6. Final model after history matching is very much similar to the starting model thus maintaining some degree of geological consistency.
7. Reservoir models with large number of wells and long production history do not pose a significant threat to the adjoint method.

3.3.2 Demerits of the Adjoint Method

The adjoint method suffers from some limitations which are:

1. The CPU time for sensitivity calculation is largely dependent on the number of time steps.
2. For a reservoir model with hundreds of thousands of active grid blocks, a large amount of memory is required to store grid block pressure and saturation values per time step at the end of each forward simulation run.

3.4 Model Parameter Update using the Steepest Descent Algorithm

Updates made to model parameters in an iterative approach are performed by analyzing sensitivities of the objective function computed for each model parameter as shown in Equations (32). The process of updating these model parameters is performed through the use of steepest descent algorithm [79] which is an efficient algorithm for determining the minima of any function. The steepest descent algorithm minimizes $Q(x)$ by computing d^k at point x that sets $Q(x) \to 0$. In other words, the steepest descent algorithm seeks to find the minimum of the objective function i.e. $\frac{dQ}{dx} = 0$. Linearization of $Q(x)$ is crucial for model parameter updating. The steepest descent algorithm which is based on the Newton-Raphson method [74] can be expressed as

$$x^{k+1} = x^k + \mu d^k \tag{33}$$

where μ, the step size, is a small positive constant ($\mu > 0$) that determines the speed of convergence of the history matching problem to an acceptable $Q(x)$. In other words, the number of iterations k required to reach $Q(x) \to 0$ is determined by the step size (μ). μ has a dimension of x^2. Its unit depends on the unit of the model parameter updated. When μ is set too high, $Q(x)$ overshoots or diverges away from an optimal $Q(x)$. Also, when μ is set too low, convergence to $Q(x) \to 0$ becomes extremely slow. The typical solution path for the steepest descent algorithm is shown in Figure 3-5. $f(X)$ describes the solution space and X_1 and X_2 are defined model parameters. On each elliptical curve represented by $f(X)$, the objective function value is constant. The minimum (or minimizing model) lies at the centre of concentric ellipses. Note that in Figure 3-5, the initial guess (indicated by the red circle) and the results of the first 11 iterations proceeds in a zig-zag path towards the minimum. This is the standard operation of the steepest descent algorithm.

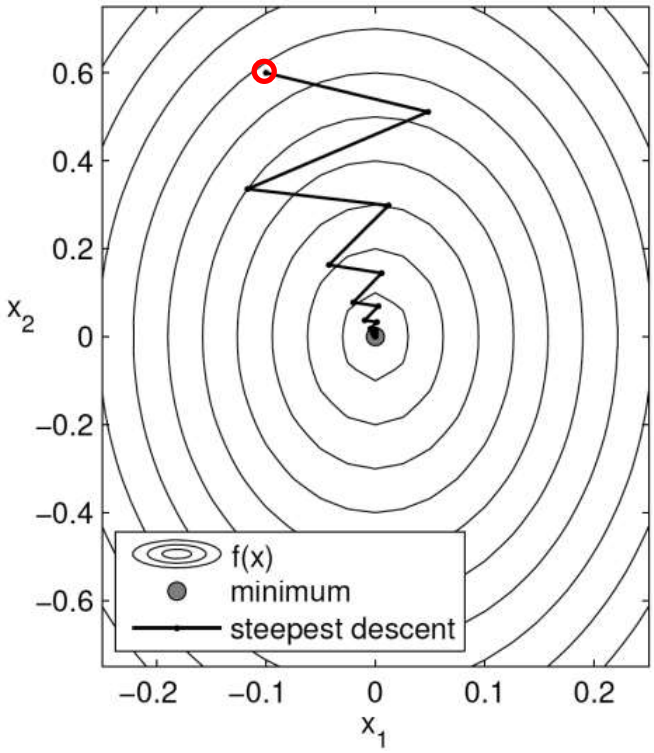

Figure 3-5: Typical solution path of the steepest descent algorithm.

In this thesis, the step size (μ) is fixed per iteration for each model parameter defined. Furthermore, depending on the degree of overshoot of $Q(x)$ experienced per iteration k, we introduced a maximum ratio value which halves the step size and recomputes d^k at previous best point until $Q(x)$ is minimized. d^k is the direction of search and it can be expressed as

$$d^k = -\frac{dQ(x)}{dx} \tag{34}$$

The negative sign in Equation (34) indicates the direction of descent. In a typical minimization problem, our goal is to minimize $Q(x)$. In this thesis, Q and $Q(x)$ are used interchangeably and both connote the objective function. The combination of Equation (33) and (34) yields

$$x^{k+1} = x^k - \mu \frac{dQ(x)}{dx} \tag{35}$$

Using Equation (35), model parameter updates can be performed per iteration using the sensitivity of the objective function to each model parameter defined.

The strategy adopted by the steepest descent algorithm is outlined as follows:

1. Evaluate d^k at an initial guess x^k.
2. Compute the direction for x^k from the first derivatives of d^k.
3. Proceed to new position x^{k+1} so that $d^k(x^{k+1}) < d^k(x^k)$.
4. Repeat (2) to (3) with x^k replaced with x^{k+1}.

3.5 The Adjoint-based Reservoir Characterization Improvement Workflow

Inspired by the adjoint method developed by Almuallim et al. [45] and evaluated by Ajala [78] with numerous reservoir simulation models of various types, we developed an adjoint-based reservoir characterization improvement workflow that can be used to reveal the location, shape and other essential properties of hidden reservoir features not captured in reservoir simulation models. These hidden features are revealed through the formulation of reservoir feature detection algorithms which are discussed in the next chapter. An improved version of the MEPO-tSenEx hotlink developed in DGMK 742-1 is used in this research work. The lines of Windows batch commands required for the hotlink is available in Appendix A.

The proposed method accounts for weighting at well level for different model responses to be matched. In other words, the adjoint-based reservoir characterization improvement workflow allows weighting of wells and their respective model responses ($\alpha_o, \alpha_w, \alpha_g$ & α_p) as shown in Equation (1). For instance, a higher weight can be assigned for water-cut matching of well X while simultaneously assigning a lower weight for flowing pressure matching of well X if the water-cut error is significantly larger than the flowing pressure error. Also, the proposed method makes it possible to assign weights to wells (either injectors or producers) based on their mismatch score prior to a history match run. The introduction of a weighting scheme ensures that wells with the highest mismatch scores are given higher emphasis in the history matching process.

In order to prevent the formulation of a strongly weighted minimization problem when using the adjoint-based reservoir characterization improvement workflow [81], weight values greater than 1.0 are assigned only to model responses with high mismatch scores. Other model responses with low or fairly low mismatch scores are assigned weight values

of 1.0. A weight value of 1.0 signifies that a model response should be history-matched as is without strong emphasis on it. Although not encouraged, weight values of 0.0 can be assigned to eliminate model responses from the objective function equation. Based on a rigorous evaluation of the effect of implementing weighting, it is observed that if weight values are not defined for model responses with the highest mismatch scores, we are unable to clearly reveal hidden reservoir features since all model responses are treated equally. Consequently, history matching or minimization problems formulated as input for the proposed method using the adjoint technique are somewhat always weakly weighted in order to stabilize the problem and improve the accuracy of results obtained.

In addition, localized model parameter modifications are performed at grid block level within the vicinity of each well thus reducing the degree of freedom of the so-called "exhaustive" minimization problem. This action ensures that hidden reservoir features existing between injector-producer pairs are captured much better for more complex reservoir settings. Furthermore, this approach minimizes model parameter update problems that may occur when wells are situated very close to one another. Moreover, besides permeability and porosity modification at grid block level, the proposed method supports the inclusion of global and regional relative permeability curves as a model parameter using the Corey relative permeability model. Resulting adjoint-derived sensitivities for the Corey parameters ($\frac{\delta Q}{\delta N_o}, \frac{\delta Q}{\delta N_w}, \frac{\delta Q}{\delta S_{wi}}, \frac{\delta Q}{\delta S_{or}}, \frac{\delta Q}{\delta Kro_{max}}$ & $\frac{\delta Q}{\delta Krw_{max}}$) are used to update the relative permeability curves per iteration and improve history matching results. Finally, where necessary, a combination of reservoir feature indicator maps and the adjoint-derived sensitivities can be used to reveal and validate the existence of hidden reservoir features.

3.5.1 The Proposed Workflow

The adjoint-based reservoir characterization improvement workflow consists of five key stages which are:

1. Simulation case definition.
2. Unconstrained history matching (UHM) using the adjoint method.
3. Revealing hidden reservoir features using formulated reservoir feature detection algorithms based on knowledge of key model parameters that reveal these features.
4. Guided feedback implementation of the revealed hidden reservoir feature back into the starting or base model resulting in the creation of an "improved model".
5. Constrained or classical history matching (CHM) on the improved model also using the adjoint method.

Figure 3-6 provides a brief summary of the adjoint-based reservoir characterization improvement workflow. Each stage of the proposed workflow is discussed in details in the following sub-sections.

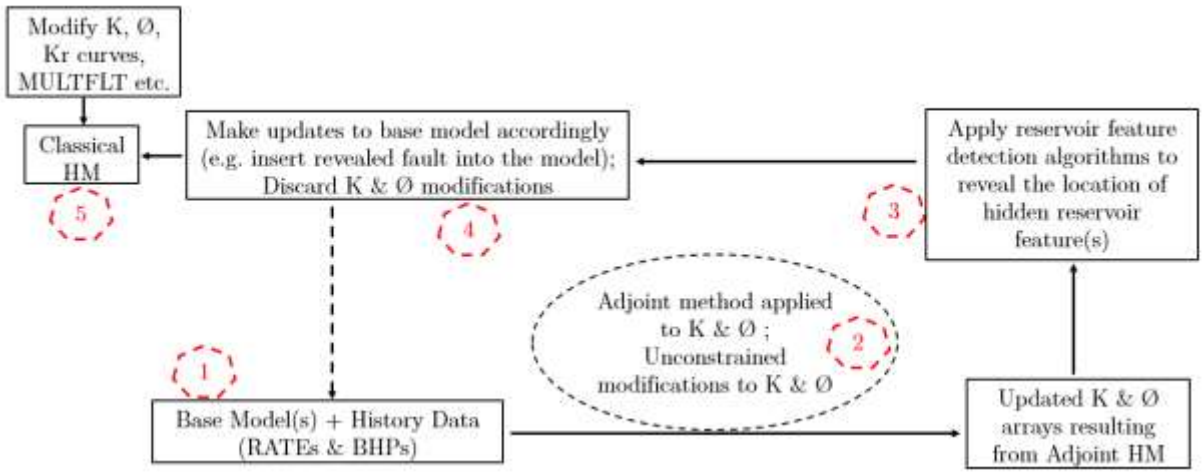

Figure 3-6: The adjoint-based reservoir characterization improvement workflow.

3.5.1.1 Simulation Case Definition

The simulation case definition entails the creation of a full-field reservoir simulation models. A reservoir simulation model is created when a static model and a dynamic or flow model are combined together. For research purposes, small-scale synthetic reservoir simulation models were constructed in-house to evaluate the proposed method. Each reservoir simulation model contains one or more geological features like fault, channels, fractures etc. Reservoir simulation models with geological features present in them are termed "true models" and the solution of these true models are defined as measured data for the base models. The "base models" contains no information about these geological features. The measured data specified can be fluid production rates (oil, water & gas), flowing bottom-hole pressures or both. For a real field case, the reservoir simulation model and measured data will suffice.

3.5.1.2 Unconstrained History Matching (UHM) with the Adjoint Method

Unlike classical history matching practices where model parameters are modified and constrained to known uncertainty ranges, unlimited degree of model parameter modification is permitted in this stage. The uncertainty range definition for model parameters have a significant impact on the performance of the adjoint method in matching reservoir simulation models. When UHM is executed using the adjoint method, model parameters are specified and their uncertainty limits are defined in an unconstrained manner. The term "unconstrained" means that model parameters like permeability and/or porosity are allowed to vary from as low as zero to their default maximum value or possibly higher.

The concept of UHM can also be explained mathematically using the formulation of the solution space similar to Figure 3-5. In Figure 3-7, two different solution spaces are presented. $f(X)$ and $f(X')$ describes the solution space for a constrained and unconstrained minimization problem respectively. Like with most constrained minimization or history matching problems, it is typical to specify the uncertainty limits of the defined model parameters. Here, the model parameters are porosity (X_1) and

permeability (X_2). From Figure 3-7, the uncertainty limits for porosity and permeability for the CHM problem are 0.1 - 0.2 and 200 mD - 800 mD respectively. The minimum point (otherwise known as the point where overall model error or objective function value is lowest) is located outside the solution space of $f(X)$. For a poorly constructed reservoir model deficient in relevant reservoir features like faults, channels etc., performing CHM in an attempt to seek the minimum point will only yield sub-optimal results in best-case scenarios.

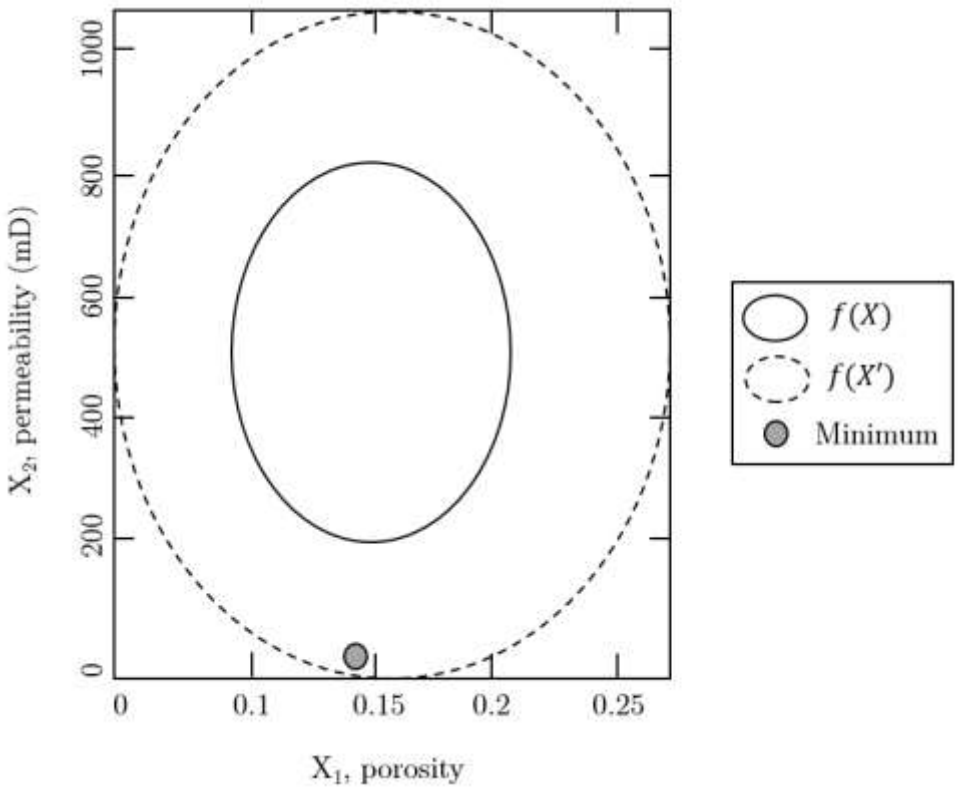

Figure 3-7: Solution space for constrained and unconstrained history matching.

In order to find the minimum point in Figure 3-7 which is located in the $f(X')$ domain, it becomes necessary to extend the uncertainty limit beyond that specified for $f(X)$. In this case, the uncertainty limits for porosity and permeability becomes 0.0 - 0.27 and 0.0 mD - 1050 mD respectively. Of course, retaining the uncertainty limit for porosity between 0.1 - 0.2 while specifying that for permeability between 0.0 mD - 1050 mD can also enable us to find the minimum point in this example. The act of extending the uncertainty limits or model parameter constraints in order to seek out the minimum point is termed "unconstrained history matching (UHM)".

Performing UHM using the adjoint method results in the fitting of simulation results to measured data despite unrealistic updates made to permeability and/or porosity. The final permeability and/or porosity arrays resulting from UHM are used to render insights to hidden reservoir features not captured in reservoir simulation models. Also, resulting permeability and/or porosity arrays are not used directly for prediction runs. Once

information on the location, shape and other intrinsic properties of the hidden features are revealed, the permeability and/or porosity arrays resulting from UHM are discarded.

It is worthwhile to mention that weighting of model responses plays a huge role in achieving acceptable history-match results. UHM performed without the implementation of weights on model responses yield fairly good history-match results. As mentioned earlier, weight values greater than 1.0 are used to signify emphasis on matching selected model responses. A positive weight value equal to or lower than 1.0 denotes that the model response should be given normal or low treatment. Weight values of 0.0 exempt the model response from been history-matched. Negative weight values are not permitted as they alter the form of the objective function equation and this is not desired. Table 3-1 presents a typical weight matrix that can be explicitly specified for different model responses.

Table 3-1: An example showing the weight matrix for different model responses.

Well Name	BHP Weight	Gas Weight	Oil Weight	Water Weight
P1_Prod	1	1	1	5
P2_Prod	1	1	10	1
P3_Prod	10	1	1	5
P4_Prod	1	1	1	10
INJ1_Inj	1	0	0	1
INJ2_Inj	1	0	0	1
INJ3_Inj	20	0	0	5

3.5.1.3 Recognition/Interpretation of Hidden Reservoir Features

Recognizing indications of hidden reservoir features is relatively easy; capturing them objectively is the challenge. The most demanding part of the adjoint-based reservoir characterization improvement workflow is revealing the location, shape and other important characteristics of hidden reservoir features from best-case permeability and/or porosity arrays resulting from UHM with minimal human intervention.

Permeability maps are a good choice for revealing hidden reservoir features like faults, channels, fractures etc. in reservoir simulation models because permeability in itself is a strong indicator of fluid flow in porous media. On the contrary, porosity maps which is typically an indication of storage or volume, are better candidates for revealing hidden features like structure-related issues. Reservoir features such as aquifers require the combination of permeability and porosity maps to infer the presence.

In this thesis, reservoir feature detection algorithms are formulated specifically for different reservoir features we want to reveal. The structure of each algorithm is different because some model parameters are more likely to reveal certain reservoir features better than others. These algorithms are directly executed on best-case permeability and/or porosity maps in order to reveal hidden reservoir features. In addition, a catalogue

highlighting key model parameters that strongly influence these features is provided. Also, validation of the existence of these features is often possible from adjoint-derived sensitivity maps. All hidden reservoir features in a reservoir simulation model are often revealed after performing one complete cycle of the adjoint-based reservoir characterization improvement workflow.

3.5.1.4 Guided Feedback Implementation into Base Model(s)

In this stage, revealed reservoir features are implemented back into the base model. The updated base model is termed an "improved model". Depending on the reservoir feature revealed, it is quite possible to have more than one distinct reservoir feature shapes proffered as alterative solutions. This can result in the generation of more than one improved model. For instance, if more than one fault shape is revealed and they all lie somewhat within the same vicinity, each fault shape may be taken into account resulting in the creation of multiple improved models. Alternatively, a developed fault shape detection algorithm which is discussed in the next chapter can be used to estimate the potential fault shape in form of a line. In the case of revealing channels or other area-based features like fractures etc., a modified Canny edge-detection method [82] can be used to map out the potential channel shape while dampening noise from the best-case permeability array obtained from UHM.

Furthermore, updates of such nature performed on the base model are restricted to the underlying geological knowledge. Unless for cases where there are reasons to doubt the original permeability and porosity distributions, geological consistency is maintained across the improved model.

3.5.1.5 Constrained History Matching (CHM) on Improved Base Model(s)

Upgrades made to the base model result in the creation of an improved model. Improved models with a tolerable degree of omitted reservoir features are good candidates for CHM. Here, uncertainty ranges for several model parameters of interest (e.g. permeability, porosity, relative permeability curves, fault transmissibility multipliers etc.) are specified and respected. For instance, when Corey relative permeability parameters are defined as model parameters, their uncertainty limits are constrained to a range defined by the user. The term "constrained" implies that uncertainty ranges are respected as expected in classical history matching.

In addition, other characteristics of the revealed reservoir features can be accurately estimated from CHM performed on the improved model. For example, after a fault is revealed and its transmissibility multiplier (MULTFLT) is estimated using the fault detection algorithm, the transmissibility multiplier of the revealed fault can be specified as a model parameter when executing CHM on the improved model. This approach ensures accurate determination of the approximate true value of the revealed fault transmissibility multiplier (MULTFLT).

Chapter 4

> "All prospects look good until drilled"
>
> Anadarko (1994)

4. Revealing Hidden Reservoir Features not captured in Reservoir Simulation Models

In Chapter 3, we introduce the adjoint-based reservoir characterization improvement workflow for revealing hidden reservoir features in reservoir simulation models. In this chapter, several case examples are presented for homogeneous and heterogeneous synthetic models which are used to evaluate the effectiveness of the proposed method. The main goals of this chapter are to:

1. Demonstrate the feasibility of using the proposed method in revealing hidden reservoir features in 2-D and 3-D simplistic reservoir models under different injection strategies, events leading to changes in flow patterns over time and with different well architectures.
2. Compare the performance of the proposed method with notable state-of-the-art methods.
3. Formulate reservoir feature detection algorithms based on key model parameters that reveals these reservoir features. In addition, present a catalogue that shows the relationship between certain model parameters and some reservoir features.
4. Validate the location and shape of revealed features using adjoint-derived sensitivities obtained from UHM.
5. Objectively estimate potential shapes of hidden faults and identify channels using a developed fault shape detection algorithm and the modified Canny edge-detection method respectively.
6. Observe the influence of simulator solver settings and noisy production data on the proposed method and finally perform a complete cycle of the adjoint-based

reservoir characterization improvement workflow on a heterogeneous synthetic model.

4.1 Evaluated Injection Strategies

The effect of 4 injection strategies on the proposed method were evaluated with synthetic reservoir simulation models. Each injection strategy is quantified using the voidage replacement ratio (VRR). These injection strategies are:

1. Over-injection strategy (VRR > 1)
2. Under-injection strategy (VRR < 1)
3. Par-injection strategy (VRR = 1)
4. Varying-injection strategy (0.025 < VRR < 1.875)

VRR > 1 signifies an over-injection strategy. Here, the injected fluid volume is greater than the volume produced. VRR < 1 signifies that an under-injection strategy is implemented. Here, the injected fluid volume is less than the volume produced. In a par-injection strategy, VRR = 1. This indicates that we are injecting and producing the same fluid volume. The final injection strategy tested is the varying-injection strategy. The varying-injection strategy incorporates the combination of all other injection strategies mentioned. The VRR range for the varying-injection strategy is set to 0.025 < VRR < 1.875. Figure 4-1 presents a plot capturing the VRR for each injection strategy vs. production time.

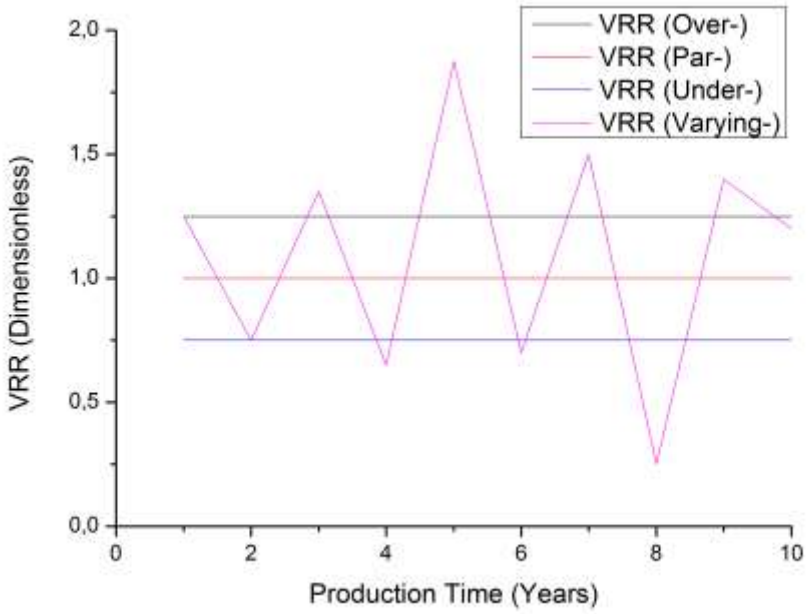

Figure 4-1: VRR vs. production time plot for all injection strategies evaluated.

4.2 R-squared Value Determination

R-squared is a mathematical means of determining the fit between simulated and measured data for any defined model responses. Mathematically, R-squared (R^2) is calculated using the formula stated in Equation (36).

$$R^2 = \left[\frac{\sum[(Sim_{ith} - Sim_{mean}) * (Obs_{ith} - Obs_{mean})]}{\sqrt{\sum(Sim_{ith} - Sim_{mean})^2 * \sum(Obs_{ith} - Obs_{mean})^2}}\right]^2 \quad (36)$$

where Sim_{mean} and Obs_{mean} are the mean value of the simulated and measured data respectively. ith indicates the data point number. The number of data points for the simulated and measured data must be the same in order to prevent errors in R-squared calculations. In addition, the simulated and measured data must be available for the same time step. By plotting the simulated data against measured data, a regression line can be drawn to determine the fit between both data [83]. R-squared values are always between 0% and 100%. A value of 0% indicates that there is no correlation between simulated and measured data while a value of 100% indicates that the simulated and measured data are exactly the same.

Figure 4-2 presents the simulated and measured well oil production rate (WOPR) for two producers over a period of 1 year. The image to the left of Figure 4-2 clearly shows a poor fit between simulated WOPR and measured WOPR while the image to the right of Figure 4-2 shows an excellent fit between simulated WOPR and measured WOPR.

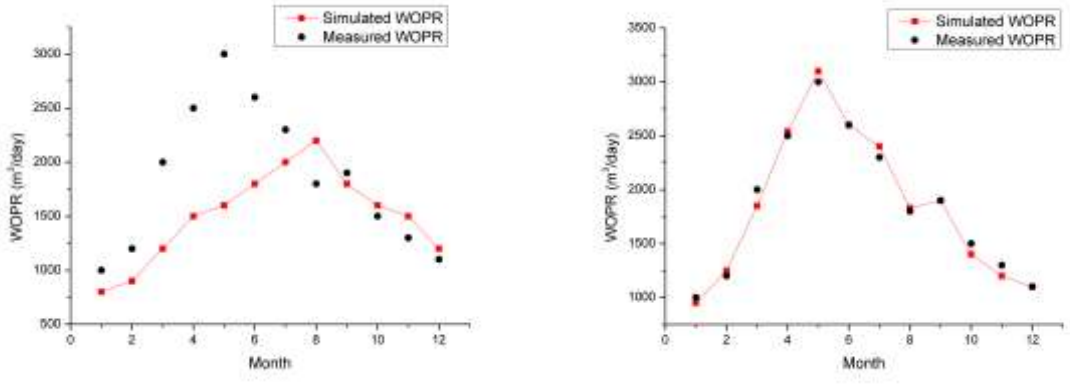

Producer-A *Producer-B*

Figure 4-2: Simulated vs. measured WOPR for two different producers.

The R-squared values generated for both model responses (WOPR@Producer-A and WOPR@Producer-B) are shown in Figure 4-3 respectively. The image to the left of Figure 4-3 has an R-squared value of 24%. This is as a result of the poor fit between the simulated and measured WOPR for Producer-A. On the other hand, the image to the right of Figure 4-3 has an R-squared value of 99% which is indicative of an excellent fit between simulated and measured WOPR for Producer-B as seen in Figure 4-2.

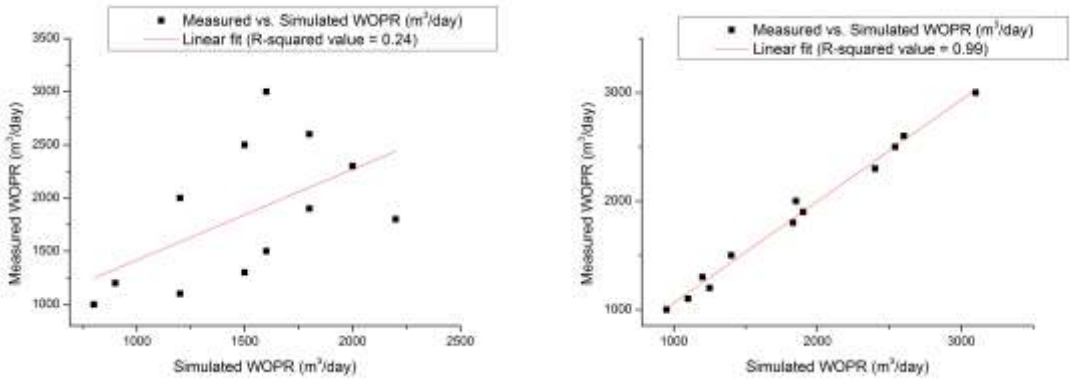

Producer-A *Producer-B*

Figure 4-3: R-squared plots generated for both model responses.

In scenarios where the model response values are very small (e.g. water-cut values), generated R-squared values do not necessarily indicate poor fit between measured and simulated data. In other words, it is possible to have a low R-squared value for water-cut (WWCT) and still visually observe an acceptable match between simulated WWCT and measured WWCT. Figure 4-4 presents a case where the simulated and measured well water-cut (WWCT) over a period of 1 year appears good enough visually but have a low R-Squared value. The image to the left of Figure 4-4 clearly shows an acceptable match between the simulated and measured WWCT while the image to the right of Figure 4-4 presents the generated R-squared value for the water-cut mismatch plot. Most reservoir engineers will accept the image to the left of Figure 4-4 as an acceptable history-match result because the water production recorded for the 6th month is very small.

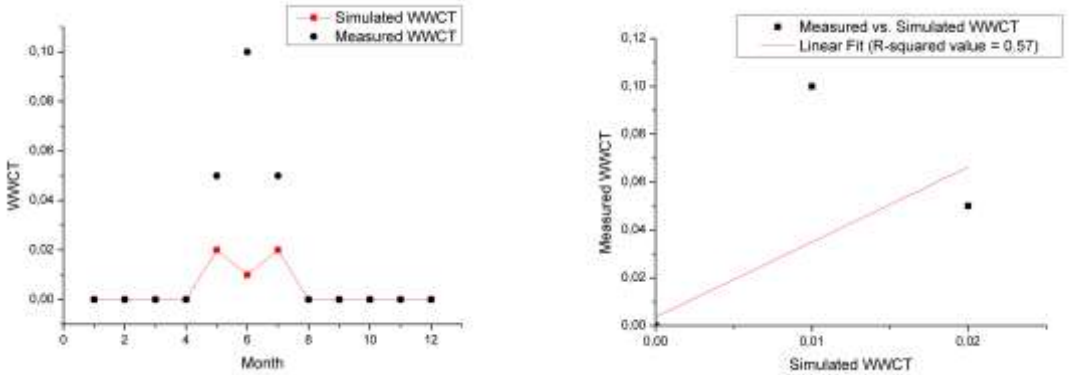

Figure 4-4: Simulated vs. measured WWCT and equivalent R-squared plot generated for WWCT.

4.3 Synthetic Case Examples

A handful of synthetic reservoir simulation models with different inherent reservoir features were constructed in order to evaluate the proposed method under varying conditions. Also, additional tests were performed to test the proposed method with different injection strategies and with different well architectures (vertical or horizontal producers). The final series of tests conducted were focused on models experiencing changes in flow pattern over time. In addition, some tests were performed to observe the influence of noisy production data and simulator solver settings on the proposed method.

4.3.1 Case Example 1: Revealing Hidden Faults

A simple 2-D reservoir model with 1 vertical injector and 2 vertical producers is constructed as a proof-of-concept model to test the effectiveness of the proposed method. The model dimensions are 10 x 10 x 1 in the X, Y and Z directions and all grid blocks are active. The size of each grid block in the X and Y direction is 500 ft (152 metres). In the Z direction, the grid block size is 50 ft (15.2 metres). The model contains predominantly oil and water. No free gas evolved during the 5-year production period. A porosity value of 20% and a horizontal permeability of 275 mD is assigned to every grid block in the model. The vertical permeability is 27.5 mD in every grid block. The water and oil viscosity are set at 0.3 cp and 1.3 cp respectively. The relative permeability curve for the entire field is shown in Figure 4-5.

The injector ("INJECTOR") is controlled by its injection rates (RATE-controlled) while the producers ("PRODUCER" and "Obs 1") are controlled by their combined oil and water production rates (LRAT-controlled). An under-injection waterflooding strategy with a VRR < 1 is implemented. The injector injects 7000 barrels of water per day (approximately 1110 m^3/day) while each producer produces a combined oil and water rate of 8000 barrels of liquid per day (approximately 1270 m^3/day). One sealing fault (coloured in blue) and two non-sealing faults (coloured in green) are introduced into the model as shown in Figure 4-6. This is the true model. The transmissibility multiplier of the sealing fault (MULTFLT) is set to 0.0 while that of the non-sealing faults are set to 1.0. In the base model, all three faults are completely removed meaning that no flow barriers exists in the base model. The solution of the true model derived from running a commercial reservoir simulator (i.e. ECLIPSE) is defined as measured data in the base model. No Gaussian noise is added to the measured data.

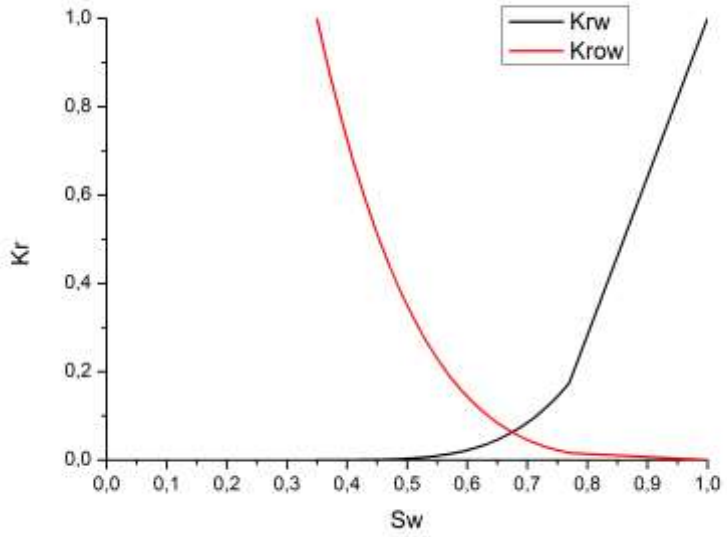

Figure 4-5: Relative permeability curve for the entire model.

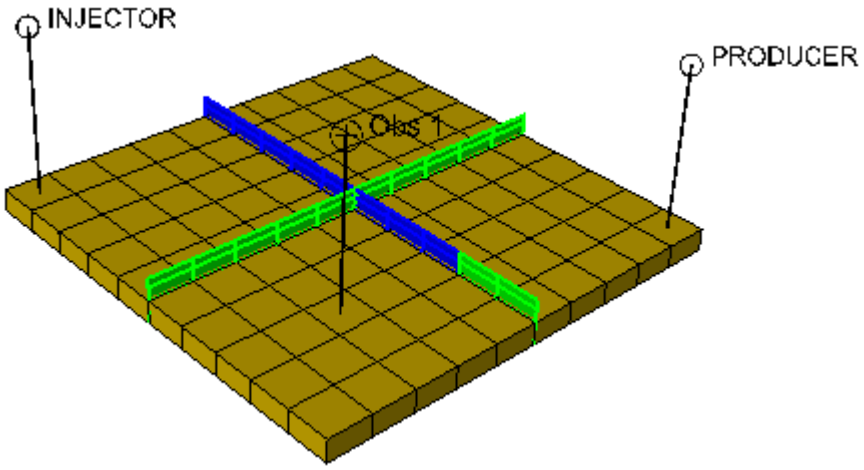

Figure 4-6: 1-injector and 2-producer homogeneous model showing the location of sealing fault (coloured in blue) and non-sealing faults (coloured in green) in the true model.

Horizontal permeabilities (K_x & K_y) were defined as model parameters prior to performing UHM using the adjoint method. The uncertainty limits for the horizontal permeabilities are defined as

$$0.0 \leq K_x, K_y \leq K_{x_{max}}, K_{y_{max}} \tag{37}$$

where $K_{x_{max}}$ & $K_{y_{max}}$ represents the original or default maximum values for permeability in the X and Y direction which are $K_{x_{max}} = K_{y_{max}} = 275$ mD. In other instances, the uncertainty limit for permeability and/or porosity can vary from zero to a very large number which is denoted by infinity (∞) in Equation (38).

$$0.0 \leq K_x, K_y, K_z, \emptyset < K_{x_\infty}, K_{y_\infty}, K_{z_\infty}, \emptyset_\infty \quad (38)$$

As might be expected, one should not confuse UHM with CHM. UHM is only a means to reveal hidden reservoir features not captured in reservoir simulation models by exploiting the effectiveness of the adjoint method in making modifications to model parameters particularly at grid block level. CHM is a conventional and acceptable history matching practice that respects model parameter uncertainty limits.

The initial assumptions employed prior to performing UHM are:

1. No prior information about the presence of hidden reservoir feature(s).
2. Base model is considered "good enough" so no need for the generation of geostatistical ensembles.
3. Core data is available for each well hence changes to grid block permeability and porosity values in each well is not permitted.

By employing Equation (37) in the UHM stage, the progression of the objective function (Q) with increasing number of iterations is presented in Figure 4-7. The objective function (Q) is a measure of the simulation model quality. The lower Q gets, the better the history-matched results. A total of 130 iterations were executed in order to reach an optimal Q. This is so because μ_{K_x,K_y}, the step sizes for K_x and K_y, is set to 3.5 mD^2. In the early stage of the UHM process, Q is reduced significantly over the first 90 iterations. As the points at each iteration of $\nabla_x Q$ approaches the neighbourhood of minimum Q, the rate of error reduction slows down tremendously as expected. The 115th iteration was selected as our best-case since it delivered the lowest Q with an overall model error reduction value of 97.8%.

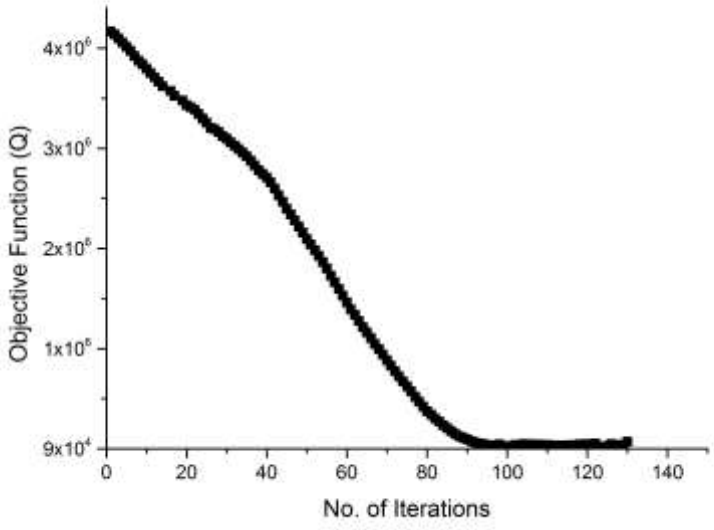

Figure 4-7: Progression of the objective function (Q) vs. number of iterations for case example 1.

The model responses defined for this problem are well water-cut (WWCT), well oil production rate (WOPR) and well bottom-hole flowing pressure (WBHP). Best-case results for the most offending model responses (model responses with the worst history-match results) from UHM are shown in Figure 4-8. All model responses are in field units (unfortunately ☹). WOPR is in STB/day (stock tank barrels per day), WWCT is unitless, TIME is in days and WBHP is in psia (psi absolute).

In this thesis, R-squared values are used to describe the match quality of model responses. An R-squared value equal to or greater than 97% describes model responses with excellent matching. On the other hand, an R-squared value less than 97% describes model responses with satisfactory or poor matching. We adopted the R-squared approach as an alternative to showing all mismatch plots because of the large number of wells and model responses per well. The R-squared values for all model responses generated for the best-case result obtained from UHM is presented in Table 4-1.

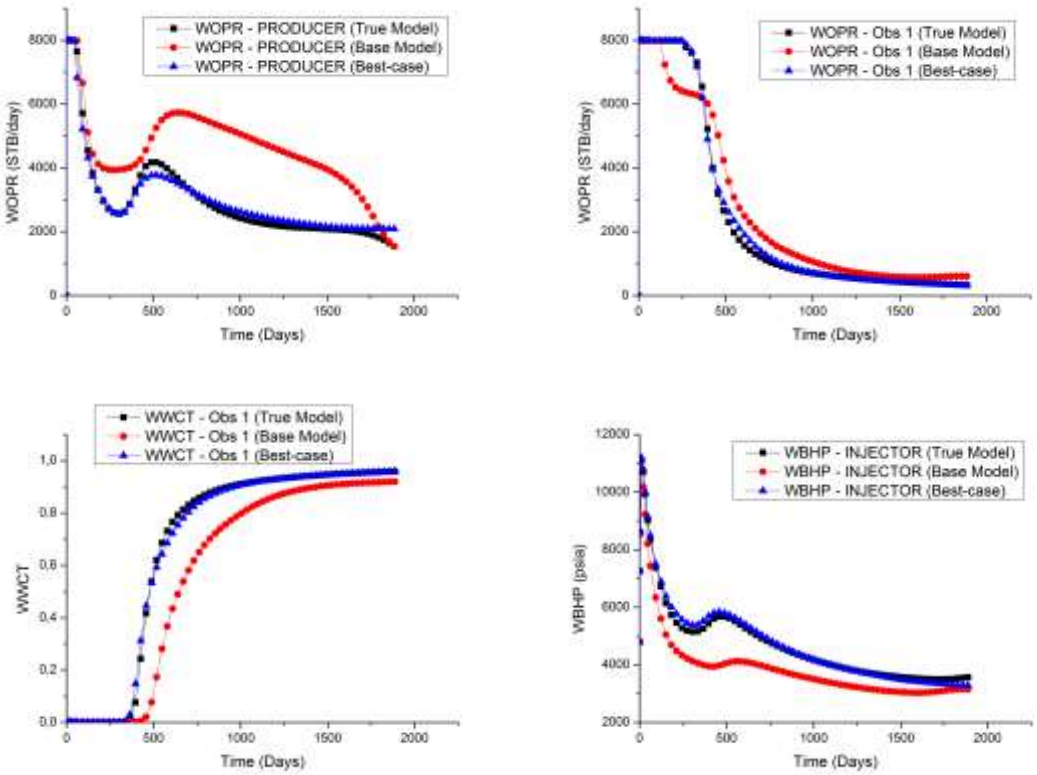

Figure 4-8: Best-case results for the most offending model responses after performing UHM for case example 1.

Table 4-1: R-squared values for the best-case result from UHM for case example 1.

Well Name	WBHP	WWCT	WOPR
PRODUCER	99.9%	99.8%	99.7%
Obs 1	99.6%	99.7%	99.8%

INJECTOR	99.7%	–	–
$R^2 \geq 97\%$; $R^2 < 97\%$			

In order to reveal the location of the hidden faults, a permeability ratio map is generated which requires the availability of best-case K_x and K_y arrays resulting from UHM. As described in Equation (39), the permeability ratio map is calculated by dividing the product of the best-case K_x and K_y arrays by the product of the base-case K_x and K_y arrays.

$$PERM\ Ratio\ Map = \frac{(Kx * Ky)_{best\ case}}{(Kx * Ky)_{base\ case}} \tag{39}$$

K_z is not included in Equation (39) because it has practically negligible influence on revealing fault location. This is proven from in-depth in-house tests performed for numerous problems with single or multiple layer reservoir models that relates to revealing hidden fault location. Figure 4-9 shows the permeability ratio map obtained. The white-coloured regions represents grid blocks with little or no change in permeability. In other words, the base-case permeability is virtually equal to the best-case permeability after UHM. These grid blocks have values of 1.0. Grid blocks with colours varying from light-yellow to purple identifies regions with extreme permeability reduction (by a factor of 0.1 or lower).

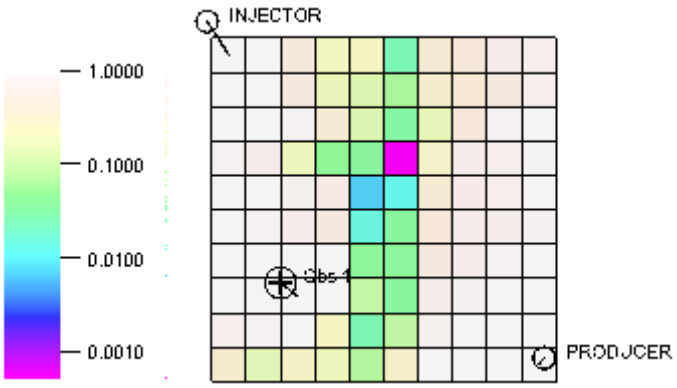

Figure 4-9: Permeability ratio map generated for case example 1.

The expression provided in Equation (40) is used to generate the fault indicator map from the permeability ratio map. The expression "return (1.0)" in Equation (40) assigns a value of 1.0 to grid blocks that are less likely to be potential fault blocks.

$$Fault\ Indicator\ Map = if\ (PERM\ Ratio\ Map > \gamma_{fault});\ return\ (1.0);\ else\ return\ (\gamma_{fault}) \tag{40}$$

Figure 4-10 presents the fault indicator map capturing the location and shape of the revealed fault in purple-coloured grid blocks. The threshold value of the fault, γ_{fault}, is a positive value that filters out regions of permeability reduction that are highly unlikely to contain the hidden fault(s). In this case example, the threshold value that reveals the location of the hidden fault is $\gamma_{fault} = 6\times10^{-2}$. Below this threshold value, we start to lose information about the existence of the hidden fault. The revealed fault lies in an identical location as the sealing fault in the true model which is shown in Figure 4-6.

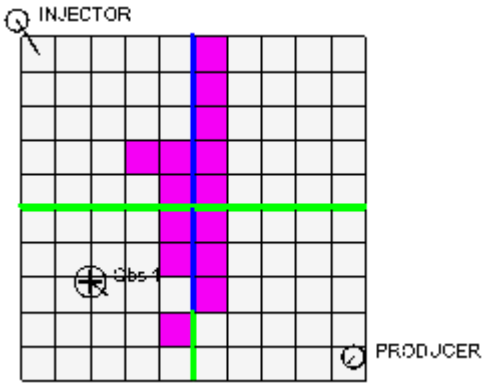

Figure 4-10: Fault indicator map for case example 1 generated at $\gamma_{fault} = 6\times10^{-2}$.

As seen from the fault indicator map (Figure 4-10), only the location of the sealing fault (blue fault line) is revealed precisely. The non-sealing faults (green fault lines) are not revealed since they do not impede fluid flow in the reservoir.

4.3.2 Case Example 2: Revealing Hidden Channels

Compared to Case Example 1 discussed earlier, the second case example is designed to show that the proposed method can also be used to reveal hidden channels. To demonstrate this, we constructed a synthetic model with 4 vertical injectors and 9 vertical producers. The model dimensions are 40 x 40 x 1 in the X, Y and Z directions and all grid blocks are active. The size of each grid block in the X and Y direction is fixed at 500 ft (152 metres). In the Z direction, the grid block size is 20 ft (6 metres). The model contains mainly oil and water with no free gas evolving over a 10-year production period. In order to create channels in the homogenous model with a constant porosity value set at 20%, two different permeability values were assigned in the model. A low horizontal permeability value of 2 mD represents the non-channelized zones while a high horizontal permeability value of 500 mD represents the channelized zones (see Figure 4-11). This is the true model. Each channel connects all 4 injectors (INJ1, INJ2, INJ3 and INJ4) to producer P5. The horizontal permeability values in every grid block are the same (i.e. $K_x = K_y$). On the other hand, the vertical permeability in every grid block is 10% of the horizontal permeability.

The water and oil viscosity are retained at 0.3 cp and 1.3 cp respectively. Also, the relative permeability curve for the entire model is similar to that shown in Figure 4-5. All 4 vertical injectors are controlled by their water injection rates while all 9 vertical

producers are controlled by their combined liquid rates. An over-injection waterflooding strategy with a VRR > 1 is implemented in this example. Each injector injects 10000 barrels of water per day (approximately 1590 m^3/day) while each producer produces a combined oil and water rate of 7000 barrels of liquid per day (approximately 1110 m^3/day). In the base model, all channels are removed completely, however, the permeability of the grid block housing each injector and producer P5 are retained since we assume that core data are available for these wells. Figure 4-12 presents the permeability distribution of the base model. The solution of the true model is defined as measured data in the base model and no Gaussian noise is added to the measured data.

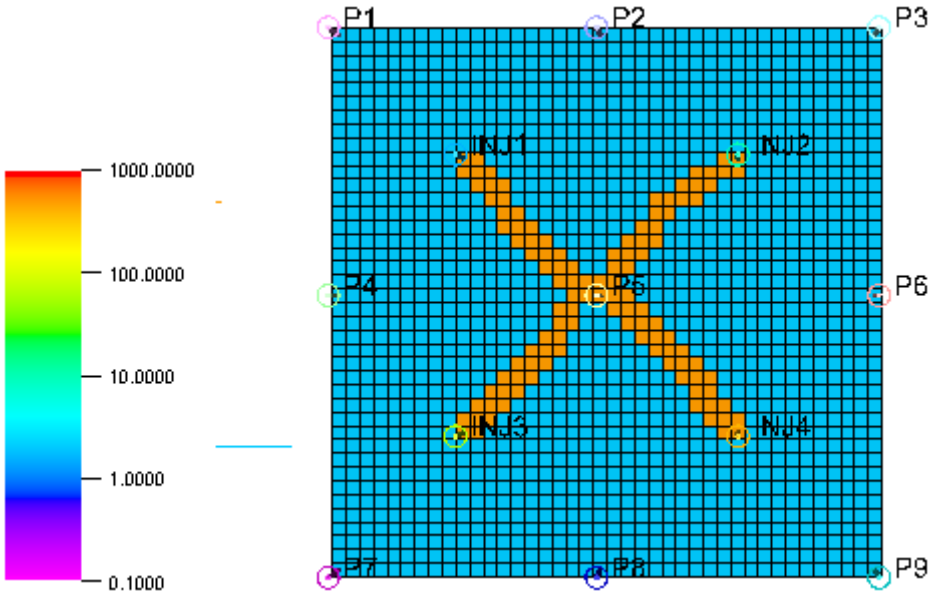

Figure 4-11: True model (K_x) for case example 2 capturing channel locations.

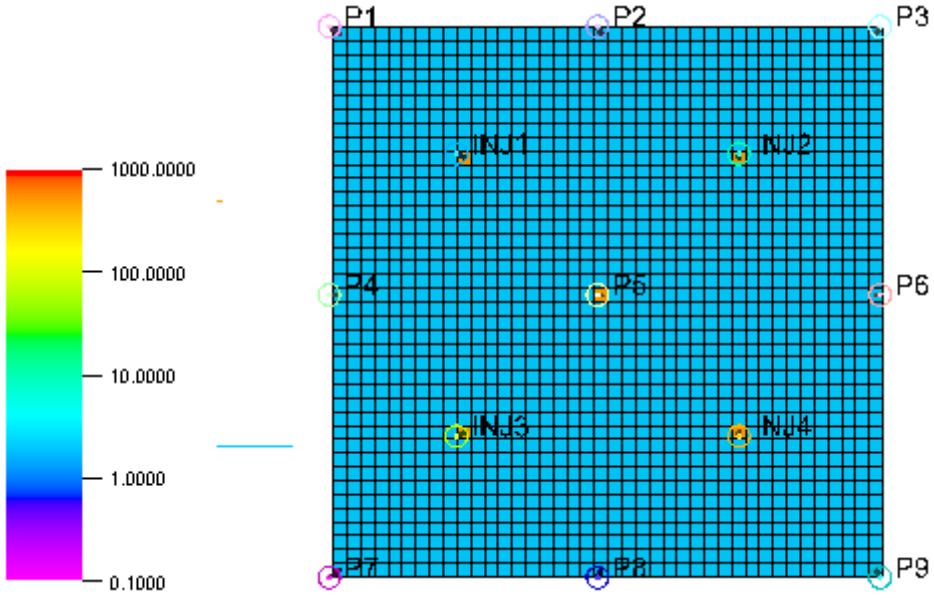

Figure 4-12: K_x distribution for the base model for case example 2.

Compared to Case Example 1 where we reveal the location and shape of a hidden sealing fault, horizontal and vertical permeabilities (K_x, K_y & K_z) were defined as model parameters prior to performing UHM using the adjoint method in order to reveal the hidden channels in the base model. The uncertainty limits for the horizontal and vertical permeabilities are defined as

$$0.0 \leq K_x, K_y, K_z \leq K_{x_{max}}, K_{y_{max}}, K_{z_{max}} \tag{41}$$

where $K_{x_{max}}, K_{y_{max}}$ & $K_{z_{max}}$ represents the original or default maximum values for permeability in the X, Y and Z direction. The initial assumptions employed in Section 4.3.1 are retained. Changes to grid block permeability and porosity in each well is not permitted since we assume core data is available for each well.

By employing Equation (41) in the UHM stage utilizing the adjoint method, the objective function progression (Q) with increasing number of iterations is presented in Figure 4-13. A total of 350 iterations were executed in order to reach an optimal Q. This is so because the step size, μ_{K_x,K_y,K_z} = 2.0 mD^2, is utilized. As seen in Figure 4-13, the objective function value drops smoothly all through to the last iteration. The 350th iteration was selected as our best-case since it delivered the lowest Q with an overall model error reduction value of 99.9%.

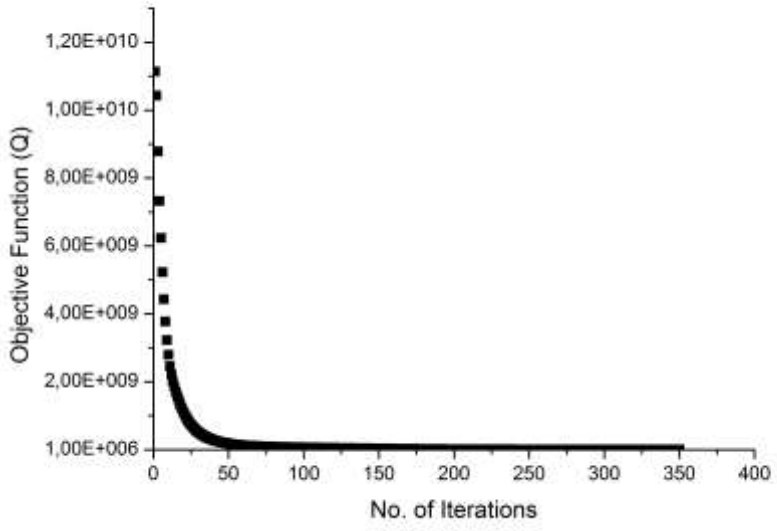

Figure 4-13: Progression of the objective function (Q) vs. number of iterations for case example 2.

The model responses defined for this problem are similar to those of Case Example 1. Best-case results for the most offending model responses are presented in Figure 4-14. Also, the R-squared values for all model responses generated for the best-case result obtained from UHM is presented in Table 4-2.

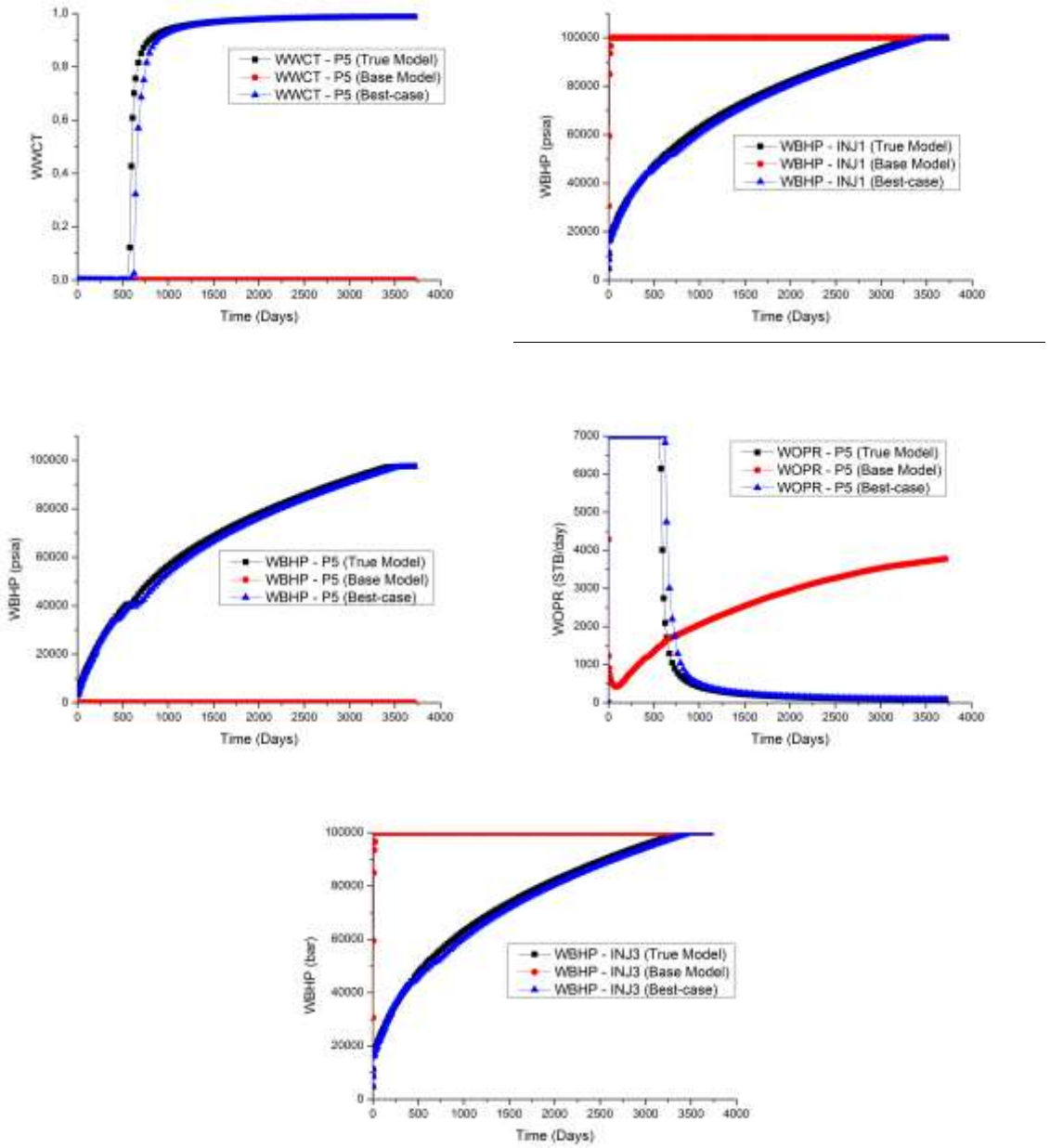

Figure 4-14: Best-case results for the most offending model responses after performing UHM for case example 2.

Table 4-2: R-squared values for the best-case result from UHM for case example 2.

Well Name	WBHP	WWCT	WOPR
P1	100.0%	100.0%	99.9%
P2	100.0%	100.0%	99.9%
P3	100.0%	100.0%	99.9%
P4	100.0%	100.0%	99.9%
P5	99.7%	99.8%	99.8%
P6	100.0%	100.0%	99.8%
P7	100.0%	100.0%	99.9%
P8	100.0%	100.0%	99.8%

P9	100.0%	100.0%	99.9%
INJ1	99.8%	—	—
INJ2	99.8%	—	—
INJ3	99.8%	—	—
INJ4	99.7%	—	—
$R^2 \geq 97\%$; $R^2 < 97\%$			

In order to reveal the location of the hidden channels, the permeability ratio map is generated which requires the availability of best-case K_x, K_y and K_z arrays resulting from UHM. As described in Equation (42), the permeability ratio map is calculated by dividing the product of the best-case K_x, K_y and K_z arrays by the product of the base-case K_x, K_y and K_z arrays.

$$PERM\ Ratio\ Map = \frac{(Kx * Ky * Kz)_{best\ case}}{(Kx * Ky * Kz)_{base\ case}} \tag{42}$$

Unlike Case Example 1 where we excluded K_z from the permeability ratio map formula, here K_z is included in Equation (42) because it plays a significant role in revealing the location of channels especially for cases where the reservoir model in question is multi-layered. Figure 4-15 shows the permeability ratio map obtained for Case Example 2. The white-coloured region represents grid blocks with little or no change in permeability. Grid blocks coloured in purple identifies regions with extreme permeability increase (by a factor of approximately 250).

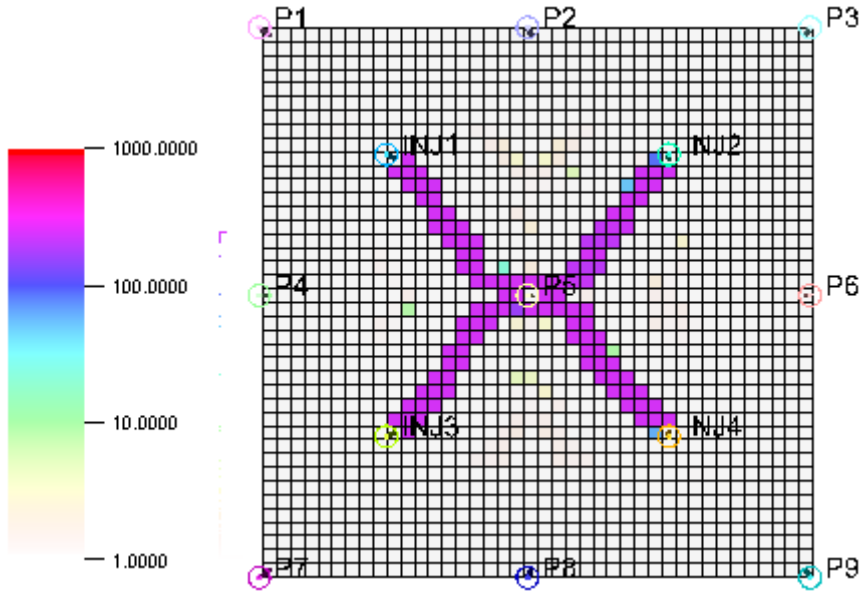

Figure 4-15: Permeability ratio map generated for case example 2.

The expression provided in Equation (43) can be used to generate a channel indicator map from the permeability ratio map especially for cases where more than one hidden

reservoir features exist in the reservoir model. The expression "return (max. of PERM Ratio Map)" in Equation (43) highlights regions in the permeability ratio map that are very likely to be high permeability zones or channels while the expression "return (1.0)" in Equation (43) assigns a value of 1.0 to grid blocks that are less likely to be potential high permeability zones or channels.

$$Channel\ Indicator\ Map = if\ (PERM\ Ratio\ Map > \gamma_{channel});\ return\ (max.\ of\ PERM\ Ratio\ Map);\ else\ return\ (1.0) \quad (43)$$

Figure 4-16 presents the channel indicator map capturing the shape of the revealed channels in purple-coloured grid blocks. The channel threshold value, $\gamma_{channel}$, is a positive value that filters out regions of permeability increase that are highly unlikely to be channels or high permeability zones. In this case example, the threshold value that reveals the location of the channels is $\gamma_{channel}$ = 200. Above this threshold value, we start to lose information about the existence of the hidden channels as shown in Figure 4-17.

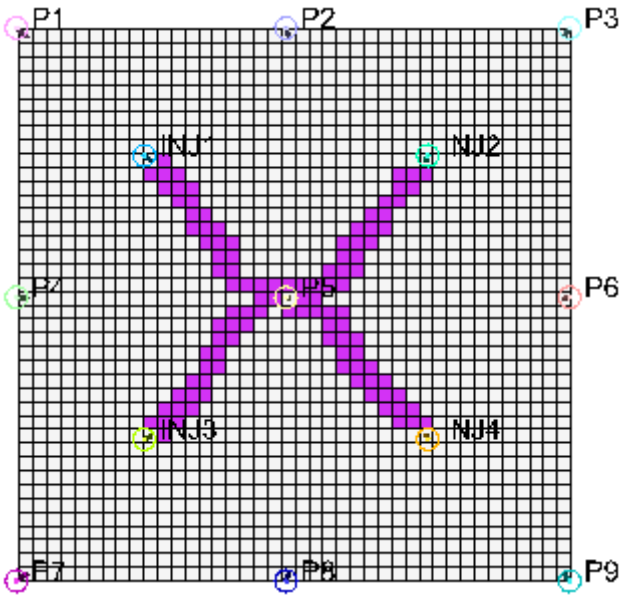

Figure 4-16: Channel indicator map for case example 2 generated at $\gamma_{channel}$ = 200.

By setting $\gamma_{channel}$ = 240, one can observe that the channel connecting injector INJ2 to producer P5 is no longer fully visible in Figure 4-17. Also, it may be worthwhile to mention that the revealed channels in Figure 4-16 shares a striking resemblance with the channels in the true model which is shown in Figure 4-11. Finally, a close observation of Figure 4-15 shows that the permeabilities in the grid blocks housing all 4 injectors and producer P5 are unchanged. This is indicated by the white-coloured grid blocks with a value of 1.0 inferring that the base-case and best-case permeability values for these grid blocks after UHM are the same.

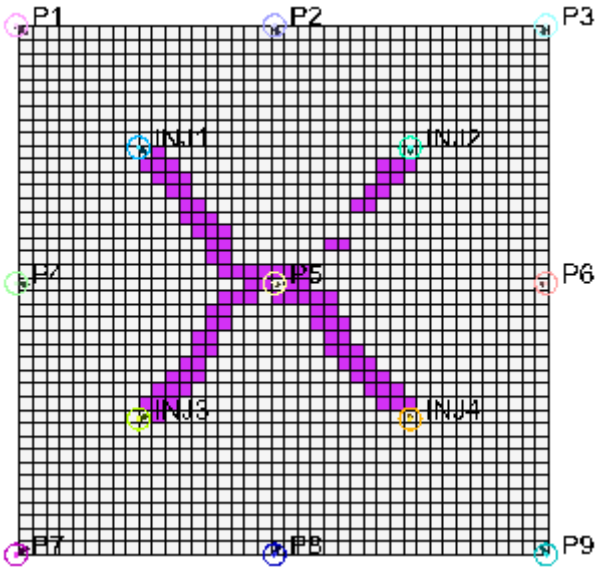

Figure 4-17: Channel indicator map for case example 2 generated at $\gamma_{channel}$ = 240.

4.3.3 Case Example 3: Revealing Hidden Fractures

An interesting problem is formulated in this case example. Here, we evaluated the effectiveness of the proposed method in revealing fractures assumed to be induced by high pressure water injection using a small-scale 3-D heterogeneous synthetic model. The heterogeneous test model contains 1 vertical injector and 3 vertical producers. The model dimensions are 10 x 10 x 3 in the X, Y and Z directions and all grid blocks are active. The size of each grid block in the X and Y direction is 500 ft (152 metres). In the first layer, ΔZ is 20 ft (6 metres). In the second layer, ΔZ is 30 ft (9.1 metres) and in the third layer, ΔZ is 50 ft (15.2 metres). The model contains predominantly oil and water. No free gas evolved during the 16-year production period. The porosity and permeability distribution are generated using the sequential Gaussian simulation method. Porosity values ranges from 10% to 30% while the horizontal permeability values ranges from 0.77 mD to 1000 mD. The vertical permeability is 10% of the horizontal permeability. The relative permeability curve for the entire field is shown in Figure 4-5.

The injector ("INJECTOR") is controlled by its injection rate while the producers ("PRODUCER", "Obs 1" and "Obs 2") are controlled by the combined oil and water production rates. An over-injection waterflooding strategy with a VRR > 1 is implemented. The injector injects 10000 barrels of water per day (approximately 1590 m^3/day) while each producer produces a combined oil and water rate of 8000 barrels of liquid per day (approximately 1270 m^3/day). All wells are perforated in all 3 layers. The permeability (K_x) distribution in the 1st, 2nd and 3rd layer are shown in Figure 4-18 and Figure 4-19 respectively. The permeability area (square) close to the injector represents the fractured area which is assumed to be induced by high pressure water injection. The horizontal permeability in the fractured area ranges from 600 mD to 1000 mD while the horizontal permeability in other parts of the reservoir ranges from 0.77 mD to 5 mD. This is the true model.

In the base model, the horizontal and vertical permeability distribution is virtually the same as that of the true model. Besides that, the fractured area in the true model is omitted from the base model (see Figure 4-20 and 4-21). In addition, in order to compound the problem, we assume that core data exist and is known for all wells irrespective of the differences in horizontal and vertical permeability observable between the true model and the base model for the well "INJECTOR". This means that the core data for well "INJECTOR" in the base model is respected regardless. Figure 4-20 and Figure 4-21 presents the K_x distribution for the base model in the 1st, 2nd and 3rd layer respectively. The solution of the true model is defined as measured data in the base model. No Gaussian noise is added to the measured data.

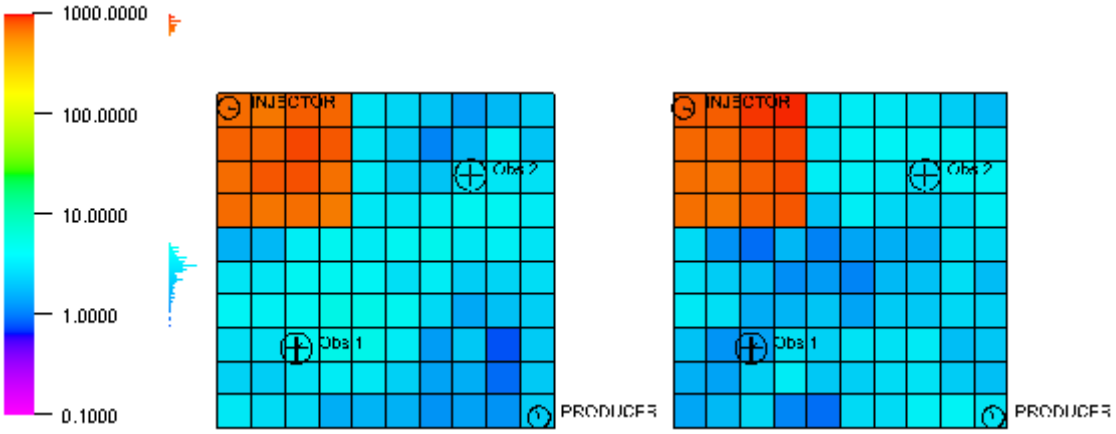

Figure 4-18: True model capturing K_x distribution in 1st and 2nd layer respectively.

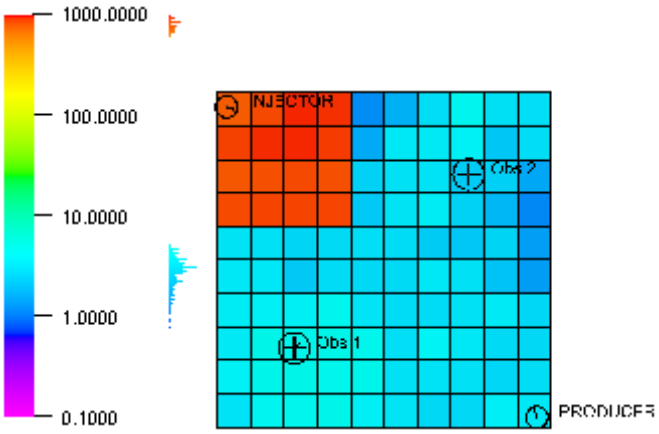

Figure 4-19: True model capturing K_x distribution in 3rd layer.

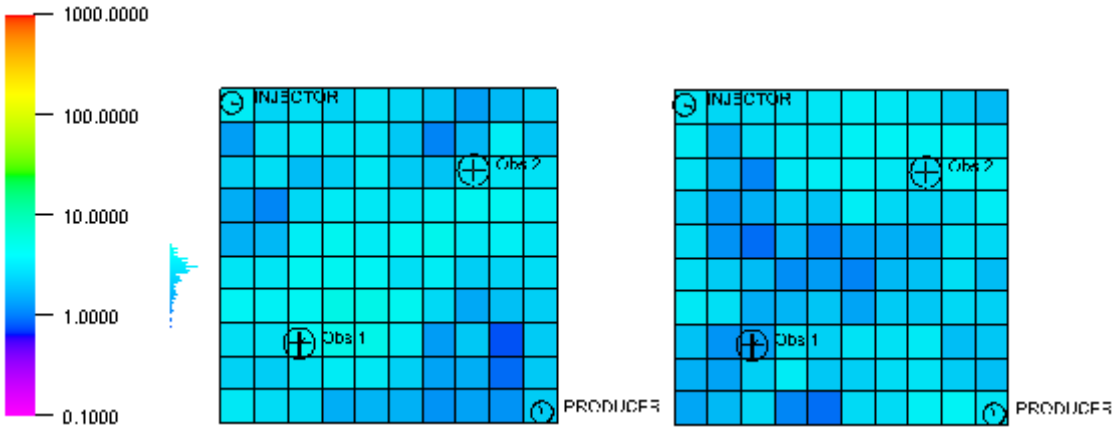

Figure 4-20: Base model capturing K_x distribution in 1st and 2nd layer.

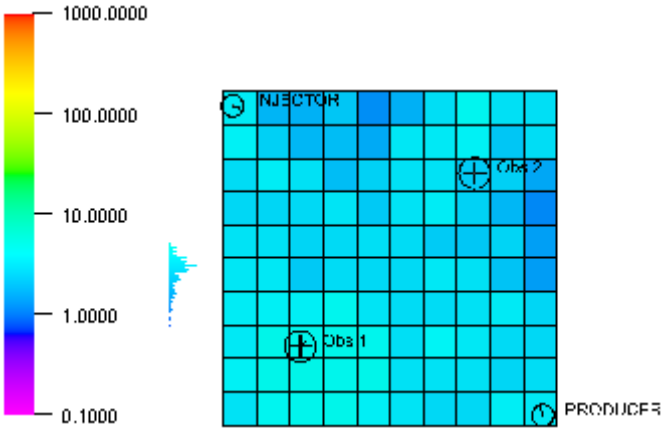

Figure 4-21: Base model capturing K_x distribution in 3rd layer.

In order to reveal hidden fractures in the base model, it is crucial to specify horizontal and vertical permeabilities (K_x, K_y & K_z) as model parameters prior to performing UHM using the adjoint method. The uncertainty limits for K_x, K_y & K_z are defined as

$$0.0 \leq K_x, K_y, K_z < K_{x_\infty}, K_{y_\infty}, K_{z_\infty} \tag{44}$$

where $K_{x_\infty}, K_{y_\infty}$ & K_{z_∞} represents values that are larger than the original or default maximum values for permeability in the X, Y & Z direction. In this case example, K_{x_∞} & K_{y_∞} are set to 1 Darcy while K_{z_∞} is set to 100 mD. The initial assumption described in Section 4.3.1 are retained.

Using Equation (44) in the UHM stage with the adjoint method, the objective function progression (Q) with increasing number of iterations is presented in Figure 4-22. A total of 230 iterations were executed in order to reach an optimal Q. This is so because the step size, μ_{K_x,K_y} = 20 mD^2 and μ_{K_z} = 10 mD^2, are utilized. As seen in Figure 4-22, the objective function value drops smoothly all through to the last iteration. The 230th iteration was selected as our best-case since it delivered the lowest Q with an overall model error reduction value of 74.2%.

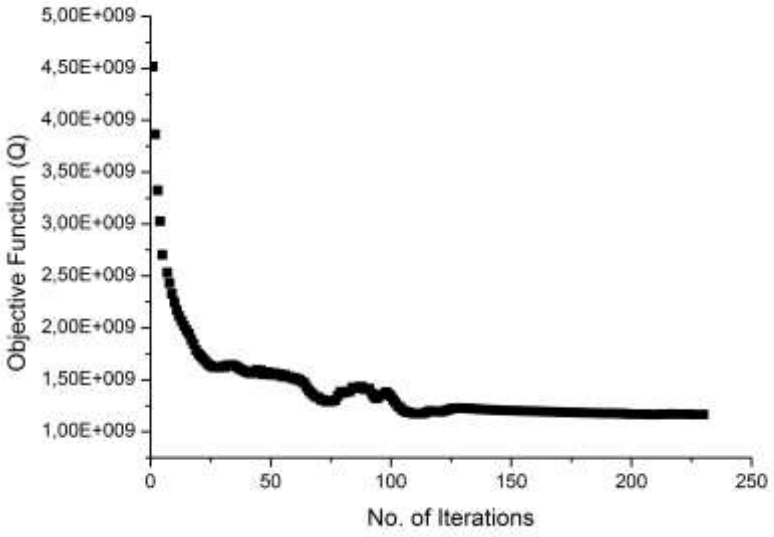

Figure 4-22: Progression of the objective function (Q) vs. number of iterations for case example 3.

The model responses defined for this problem are similar to those of the previous two case examples. Best-case results for the most offending model responses are presented in Figure 4-23. Also, the R-squared values for all model responses generated for the best-case result obtained from UHM is presented in Table 4-3.

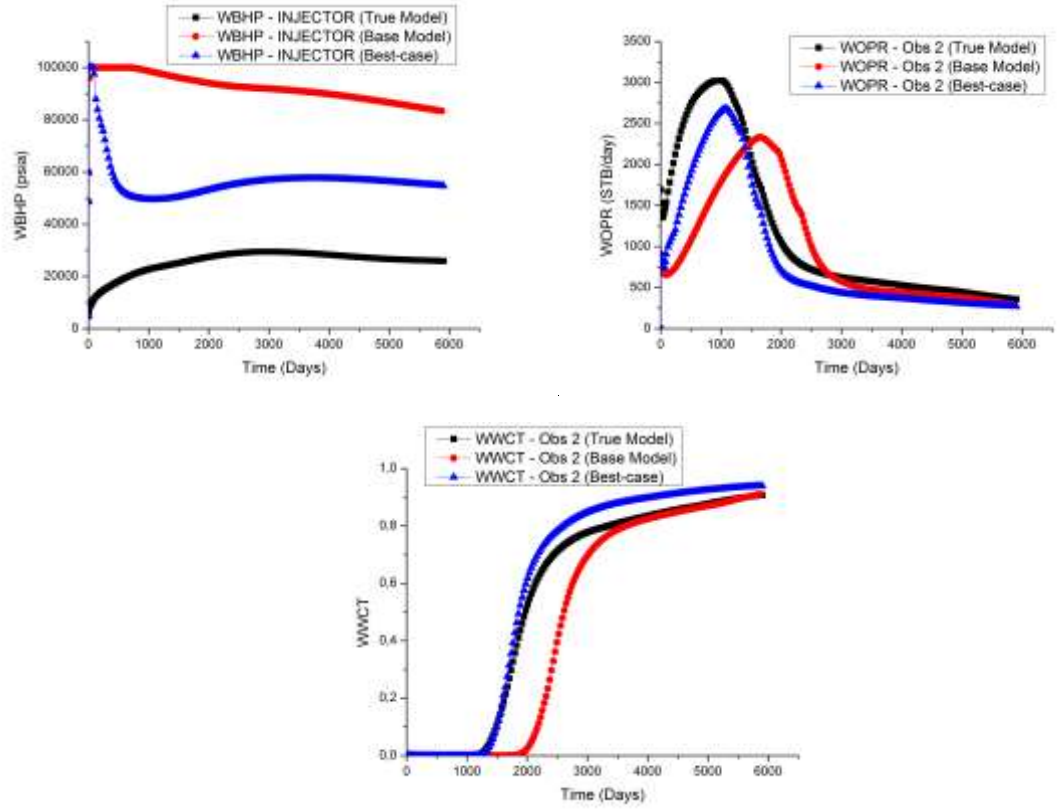

Figure 4-23: Best-case results for the most offending model responses after performing UHM for case example 3.

Table 4-3: R-squared values for the best-case result obtained from UHM for case example 3.

Well Name	WBHP	WWCT	WOPR
PRODUCER	100.0%	98.5%	98.1%
Obs 1	100.0%	98.8%	98.2%
Obs 2	100.0%	91.8%	85.6%
INJECTOR	60.1%	–	–
$R^2 \geq 97\%$; $R^2 < 97\%$			

In order to reveal the location of the hidden fractures, Equation (42) is used to generate the permeability ratio map for the best-case result from UHM. Figure 4-24 and Figure 4-25 shows the permeability ratio map obtained for Case Example 3 for the 1st, 2nd and 3rd layer respectively. Blue-coloured grid blocks in Figure 4-24 and Figure 4-25 with a value of 1.0 represents grid blocks with little or no change in permeability. Grid blocks with purple colouration identifies regions with permeability reduction. On the other hand, grid blocks with red colouration identifies regions with extreme permeability increase. The reason for such disproportionate increase and reduction in permeability which is noticeable in the permeability ratio maps (see Figure 4-24 and Figure 4-25) can be attributed to reservoir model heterogeneity.

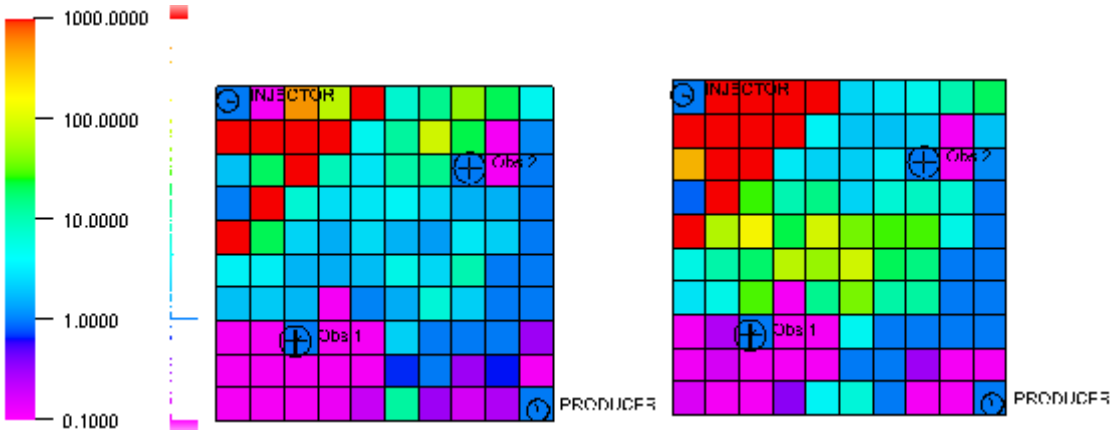

Figure 4-24: Permeability ratio maps generated for case example 3 for the 1st and 2nd layer respectively.

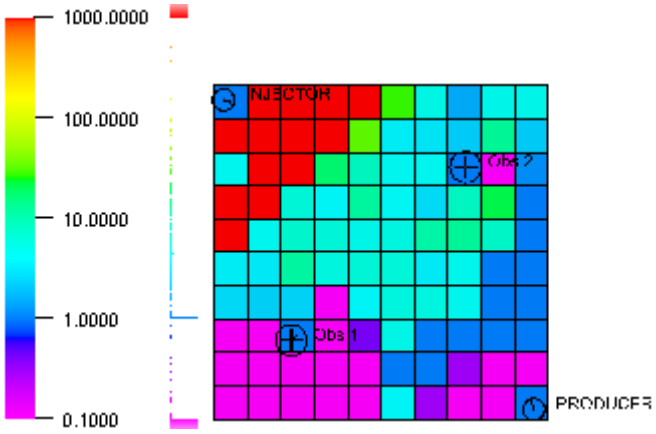

Figure 4-25: Permeability ratio map generated for case example 3 for the 3rd layer.

The fracture indicator maps can be generated from the permeability ratio maps using the same expression required for generating the channel indicator maps (see Equation (43)). This is so because channels and fractures are permeability-dependent and can easily be identified from best-case permeability arrays from UHM. Figure 4-26 and Figure 4-27 presents the fracture indicator maps capturing the location of the revealed fractures in red-coloured grid blocks for the 1st, 2nd and 3rd layer respectively. The threshold value that reveals the location of the fractures is $\gamma_{fracture}$ = 500. Above this threshold value, we start to lose information about the existence of the hidden fractures.

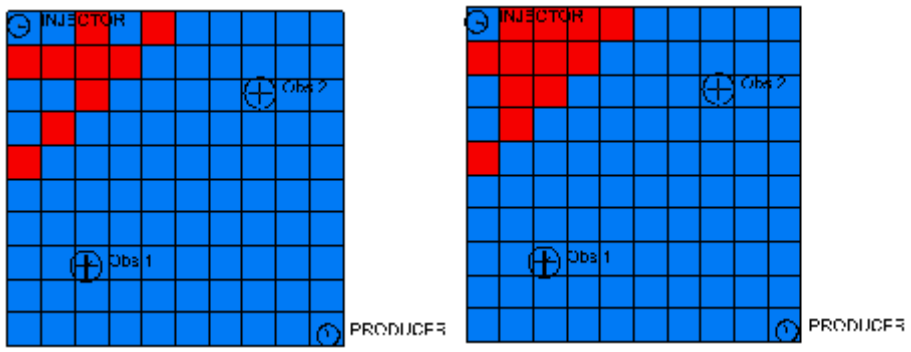

Figure 4-26: Fracture indicator maps for case example 3 generated at $\gamma_{fracture}$ = 500 for the 1st and 2nd layer respectively.

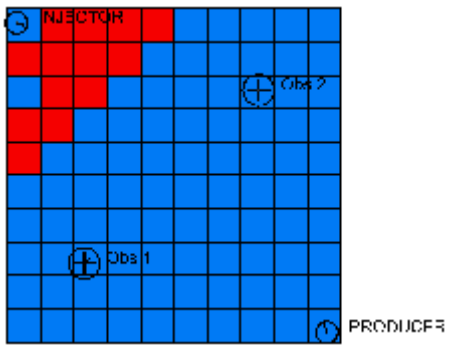

Figure 4-27: Fracture indicator map for case example 3 generated at $\gamma_{fracture}$ = 500 for the 3rd layer.

Despite not being able to attain a match quality of 97% or greater for all model responses defined, the revealed fractures in Figure 4-26 and Figure 4-27 are similar in location and probably shape to the fractures in the true model which are shown in Figure 4-18 and Figure 4-19. As seen in Figure 4-26 and Figure 4-27, the permeability values of the grid blocks housing the injector are unchanged. This attests to the fact that the proposed method can be used to reveal hidden reservoir features in reservoir simulation models regardless of whether core data exists for wells or not.

4.3.4 Case Example 4: Identification of Vertical Communication

The effectiveness of the proposed method in revealing the degree of vertical communication or connectivity between reservoir layers especially for cases where reservoir heterogeneity issues abound in the reservoir model is evaluated using a 3-D heterogeneous synthetic model. The test model used is similar to the model used in Case Example 3 with 300 active grid blocks (10 x 10 x 3), 1 vertical injector and 3 vertical producers. The model contains predominantly oil and water and no free gas evolved during the 16-year production period. The porosity and permeability distribution are generated using the sequential Gaussian simulation method. Porosity values ranges from 3% to 27% while the horizontal permeability ranges from 0.0 mD to 415 mD. The vertical permeability ranges from 0.0 mD to 1530 mD. The relative permeability curve for the entire field is shown in Figure 4-5.

The injector ("INJECTOR") is controlled by its injection rate while the producers ("PRODUCER", "Obs 1" and "Obs 2") are controlled by the combined oil and water production rates. An over-injection waterflooding strategy with a VRR > 1 is implemented. The injector injects 10000 barrels of water per day (approximately 1590 m^3/day) while each producer produces a combined oil and water rate of 8000 barrels of liquid per day (approximately 1270 m^3/day). All wells are perforated in all 3 layers. Of particular importance to us is the permeability distribution in the Z direction (K_z) for all layers which are shown in Figure 4-28 and Figure 4-29 respectively. From Figure 4-28 and Figure 4-29, one can see that K_z values are mostly large in the 1st and 3rd layer. In the 2nd layer, only a few grid blocks (8 in total) have large K_z values (between 200 mD and 1280 mD). The K_z values for most grid blocks (92 in total) in the 2nd layer are very small (bordering around 0.005 mD on the average). This is based on the assumption that some degree of vertical communication exists between the 1st and 3rd layer through the 2nd layer. This is the true model. Figure 4-30 presents the histogram for K_z values in the 2nd layer for the true model.

In the base model, the horizontal permeability distribution is virtually the same as that of the true model. On the contrary, the vertical permeability ranges from 0.0 mD to 415 mD. Also the range of vertical permeability distribution in the 2nd layer is from 0.0002 mD to 0.0009 mD suggesting virtually no vertical communication between the 1st and the 3rd layer. Figure 4-31 and Figure 4-32 shows the K_z distribution for the base model

in all 3 layers. The solution of the true model is defined as measured data in the base model. No Gaussian noise is added to the measured data.

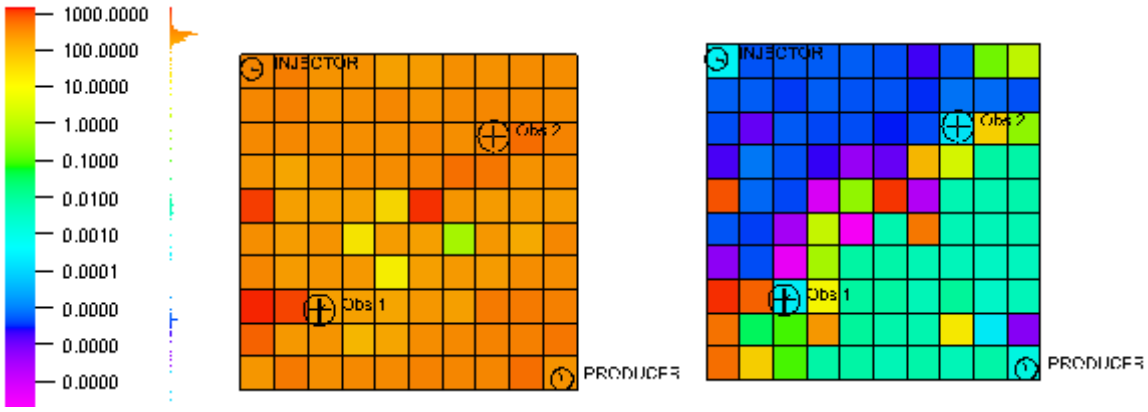

Figure 4-28: True model capturing K_z distribution in 1st and 2nd layer respectively.

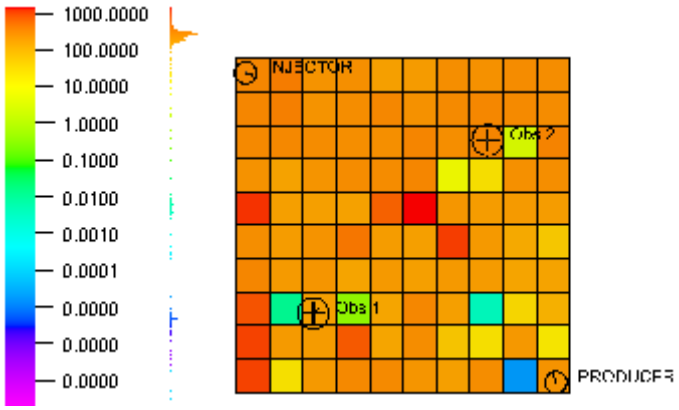

Figure 4-29: True model capturing K_z distribution in the 3rd layer.

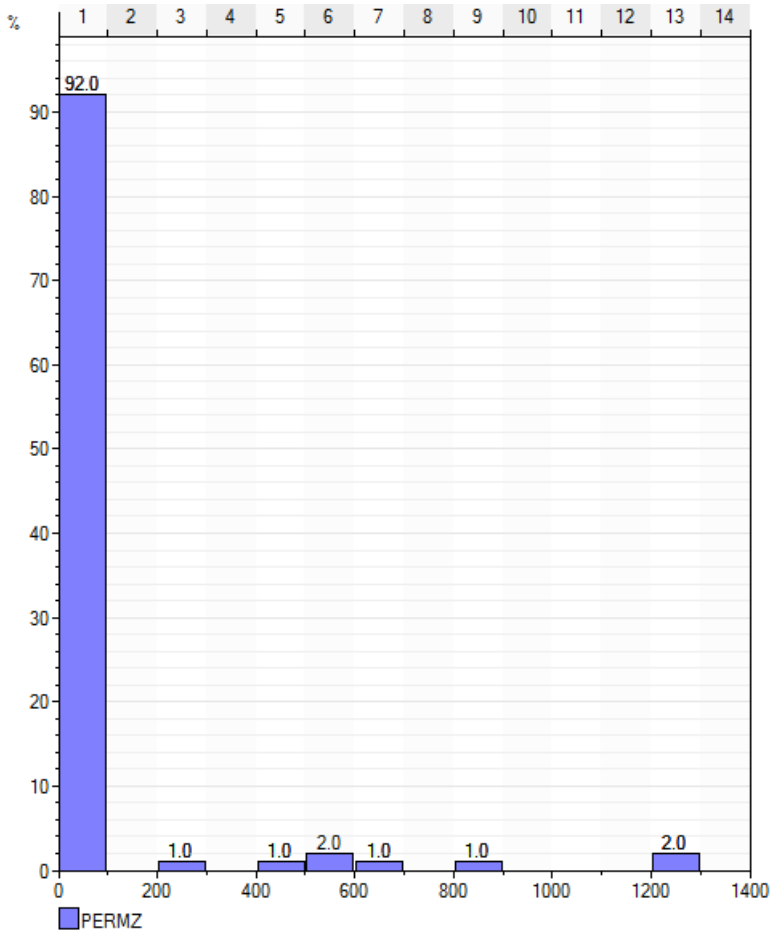

Figure 4-30: Histogram of K_z values in the 2nd layer for the true model.

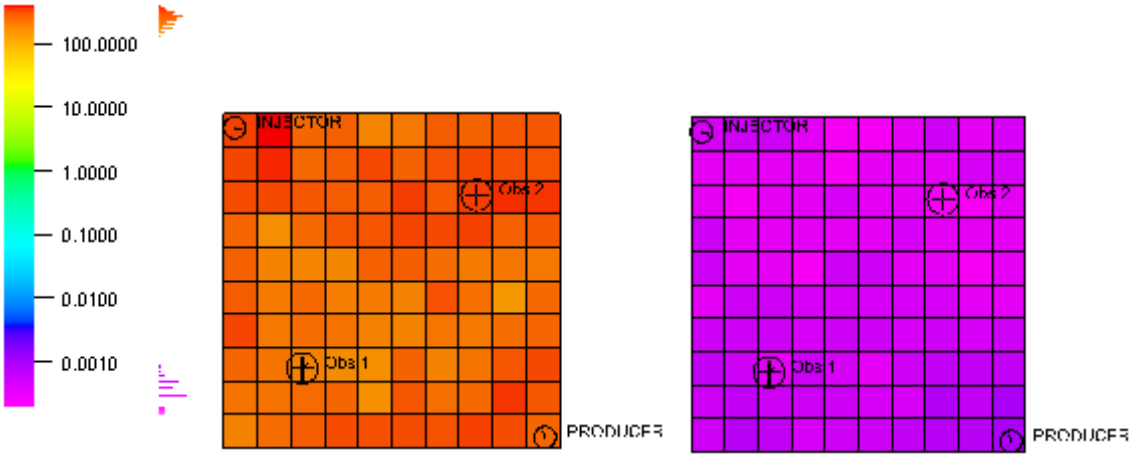

Figure 4-31: Base model capturing K_z distribution in 1st and 2nd layer respectively.

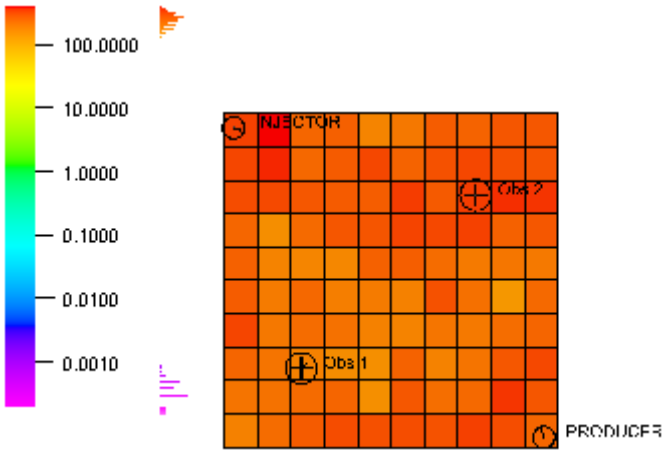

Figure 4-32: Base model capturing K_z distribution in the 3rd layer.

In order to reveal hidden vertical communication between reservoir layers in the base model, it is crucial to specify vertical permeability (K_z) as a model parameter prior to performing UHM using the adjoint method. The uncertainty limit for K_z is defined as

$$0.0 \leq K_z < K_{z_\infty} \tag{45}$$

where K_{z_∞} represents values that are larger than the original or default maximum values for permeability in the Z direction. In this case example, K_{z_∞} is set to 2 Darcy. The initial assumption described in Section 4.3.1 are retained.

Using Equation (45) in the UHM stage with the adjoint method, the objective function progression (Q) with increasing number of iterations is presented in Figure 4-33. A total of 70 iterations were executed in order to reach an optimal Q. This is so because the step size, μ_{K_z} = 10 mD^2, is utilized. At the 8th and 31th iteration (indicated by red circles in Figure 4-33), the objective function experiences a sudden jump which is then followed by a rapid decline in objective function value. This phenomenon is called "destabilization". The destabilization process typically kick in after a "stagnation region" is reached during optimization. The stagnation region is a region of fairly constant Q which may or may not be the optimal Q. Whenever the steepest descent algorithm converges to what it believes to be a sub-optimal Q (a stagnation region), the destabilization process comes into effect by seeking out a new direction of descent in the objective function space in an attempt to find the minimum point (point of lowest Q). The destabilization process is initiated every time the steepest descent algorithm converges (flattening out of the Q-curve) in order to ensure that the final Q realised is the optimal Q. The 59th iteration was selected as our best-case since it delivered the lowest Q with an overall model error reduction value of 78.8%.

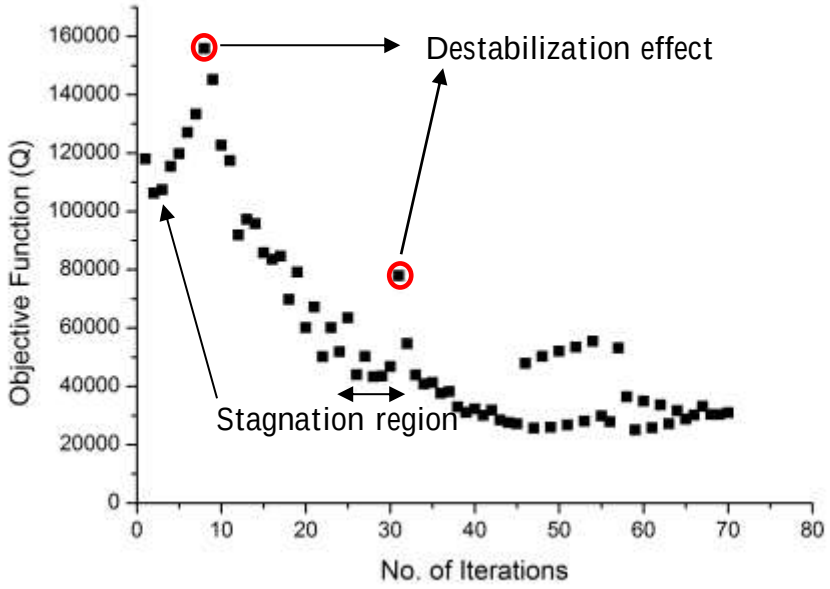

Figure 4-33: Progression of the objective function (Q) vs. number of iterations for case example 4.

The model responses defined for Case Example 4 are similar to those of the previous three case examples. Best-case results for the most offending model responses are presented in Figure 4-34. Also, the R-squared values for all model responses generated for the best-case result obtained from UHM is presented in Table 4-4.

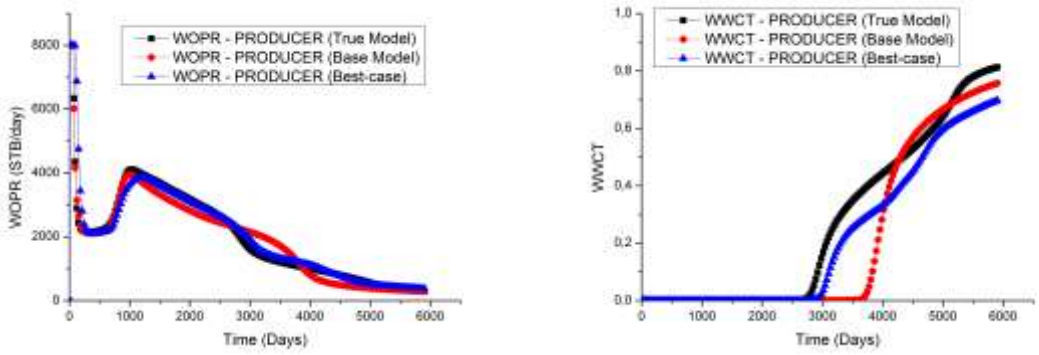

Figure 4-34: Best-case results for the most offending model responses after performing UHM for case example 4.

Table 4-4: R-squared values for the best-case result obtained from UHM for case example 4.

Well Name	WBHP	WWCT	WOPR
PRODUCER	100.0%	97.9%	98.2%
Obs 1	100.0%	98.7%	99.4%
Obs 2	100.0%	99.4%	99.2%

INJECTOR	98.9%	–	–
$R^2 \geq 97\%$; $R^2 < 97\%$			

In order to reveal hidden vertical communication between reservoir layers, Equation (46) is used to generate the permeability ratio map for the best-case result obtained from UHM. As described in Equation (45), the permeability ratio map is calculated by dividing the best-case K_z array by the base-case K_z array.

$$PERM\ Ratio\ Map = \frac{(Kz)_{best\ case}}{(Kz)_{base\ case}} \tag{46}$$

K_x & K_y are excluded from Equation (46) because they play no significant role in revealing hidden vertical communication between reservoir layers. Figure 4-35 and Figure 4-36 shows the permeability ratio map obtained for Case Example 4 for all 3 layers. As seen in Figure 4-35 and 4-36, grid blocks coloured in light blue have a permeability ratio value of 1.0 suggesting that no changes were made to the original K_z values in these grid blocks.

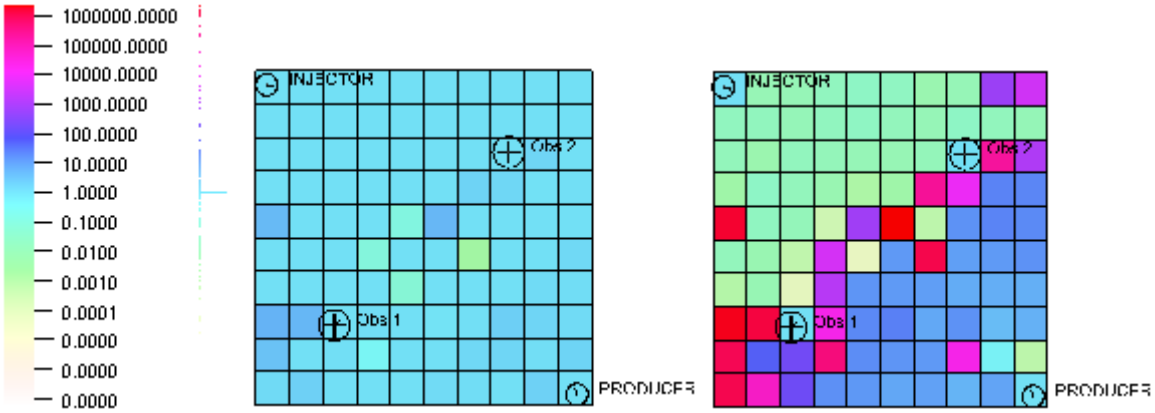

Figure 4-35: Permeability ratio maps generated for case example 4 for the 1st and 2nd layer respectively.

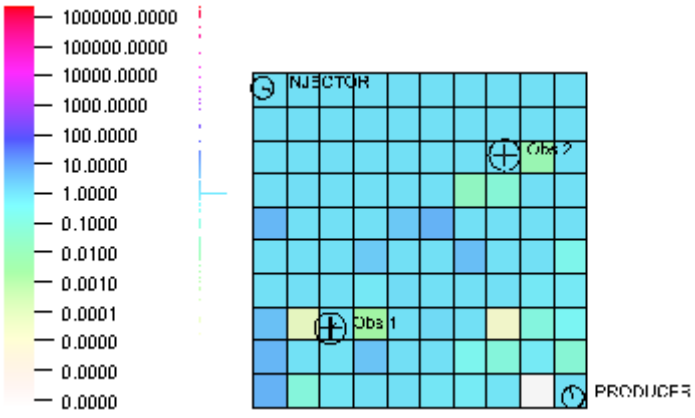

Figure 4-36: Permeability ratio map generated for case example 4 for the 3rd layer.

The expression provided in Equation (47) can be used to generate a vertical communication indicator map from the permeability ratio map. The expression "return (max. of PERM Ratio Map)" in Equation (47) highlights regions in the permeability ratio map that are very likely to exhibit some form of vertical communication between layers while the expression "return (1.0)" in Equation (47) eliminates regions that show no concrete degree of vertical communication.

$$Vert.Comm.Indicator\ Map = if\ (PERM\ Ratio\ Map > \gamma_{vert.comm.});\ return\ (max.of\ PERM\ Ratio\ Map);\ else\ return\ (1.0) \quad (47)$$

Figure 4-37 and Figure 4-38 presents the vertical communication indicator maps capturing layers with high K_z values (red-coloured grid blocks) which is indicative of vertical communication. The vertical communication threshold value, $\gamma_{vert.comm.}$, is a positive value that filters out regions of permeability increase that are highly unlikely to be potential zones with a reasonable degree of vertical communication. In this case example, the threshold value that reveals vertical communication between the 1st and 3rd layer through the 2nd layer is $\gamma_{vert.comm.}$ = 500. Above this threshold value, information about the existence of vertical communication through the 2nd layer may be lost.

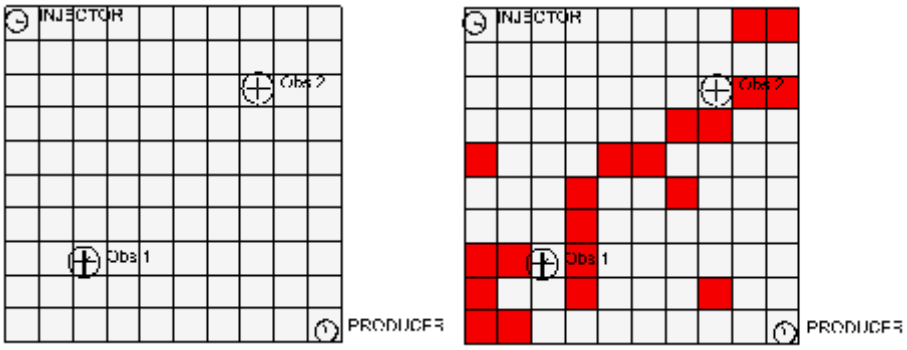

Figure 4-37: Vertical communication indicator maps for case example 4 generated at $\gamma_{vert.comm.}$ = 500 for the 1st & 2nd layer respectively.

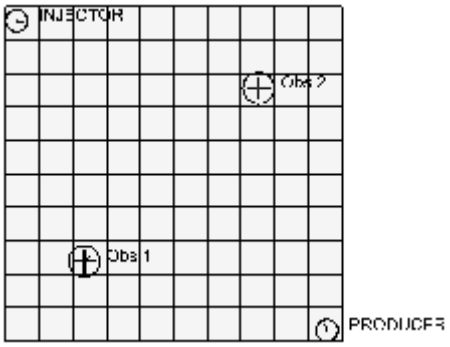

Figure 4-38: Vertical communication indicator map for case example 4 generated at $\gamma_{vert.comm.}$ = 500 for the 3rd layer.

4.3.5 Case Example 5: Revealing a Hidden Fault in an Aquifer-dominated Multi-layered Reservoir

In an attempt to evaluate the effectiveness of the proposed method with reservoir models devoid of water injectors for pressure maintenance, this case example is formulated with 4 vertical producers in a synthetic heterogeneous model containing an edge-drive aquifer.

The test model used here has grid dimensions equal to 20 x 20 x 5 in the X, Y and Z directions and all grid blocks are active. The size of each grid block in the X and Y direction is 500 ft (152 metres). In the Z direction, each grid block size is 20 ft (6 metres). The model contains predominantly oil and water and no free gas evolved during a 10-year production period. The porosity and permeability distribution are generated using the sequential Gaussian simulation method. Porosity ranges from 17% to 23% while the horizontal permeability values ranges from 35 mD to 287 mD. The vertical permeability is 10% of the horizontal permeability. The relative permeability curve for the entire field is shown in Figure 4-5. The oil-water contact is placed beneath the bottom of the last producing layer (the 5th layer).

All 4 vertical producers are controlled by their combined oil and water production rates. Each producer produces a combined oil and water rate of 40000 barrels of liquid per day (approximately 6350 m^3/day). All producers are perforated in all 5 layers. The permeability (K_x) and porosity (ø) distribution are shown in Figure 4-39 and Figure 4-40 respectively. A sealing fault running through all 5 layers is introduced into the test model by deactivating 13 grid blocks between producer P1 and producer P2 (see Figure 4-41). In addition, the edge-based aquifer with aquifer permeability of 275 mD and aquifer porosity of 20% is introduced in one side of the model in every layer as shown in Figure 4-42. This is the true model.

In the base model, information about the sealing fault (deactivated grid blocks) is completely removed. This means that the deactivated grid blocks in the true model are activated in the base model (see Figure 4-43). The solution of the true model is defined as measured data in the base model. No Gaussian noise is added to the measured data.

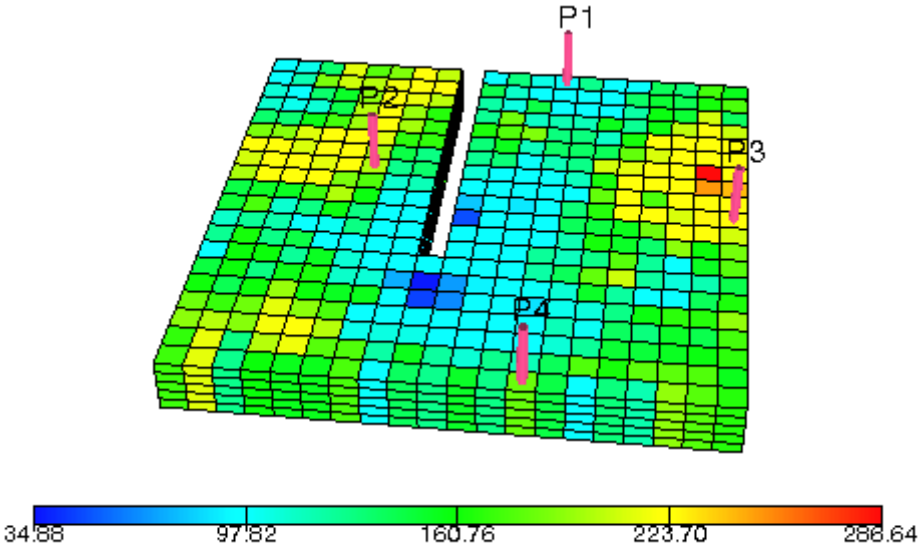

Figure 4-39: K_x distribution of the true model for case example 5.

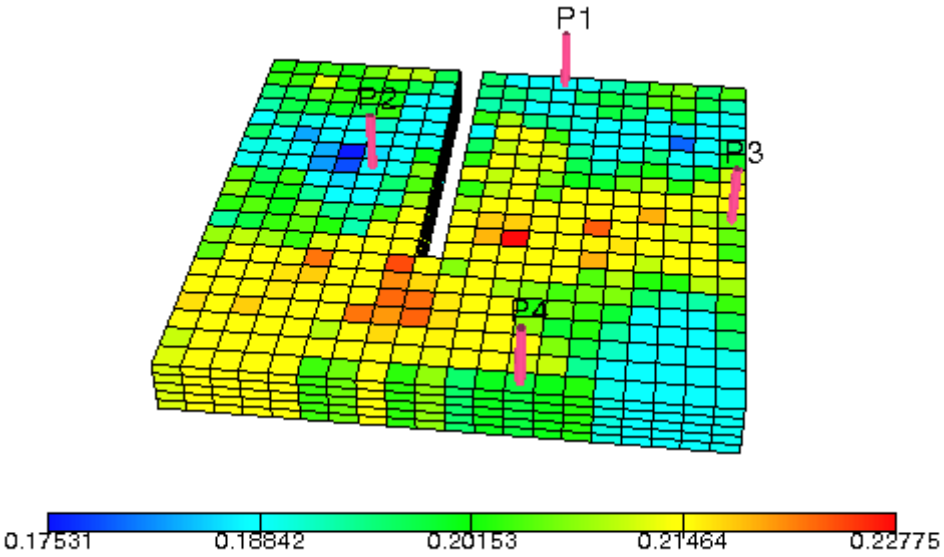

Figure 4-40: Porosity distribution of the true model for case example 5.

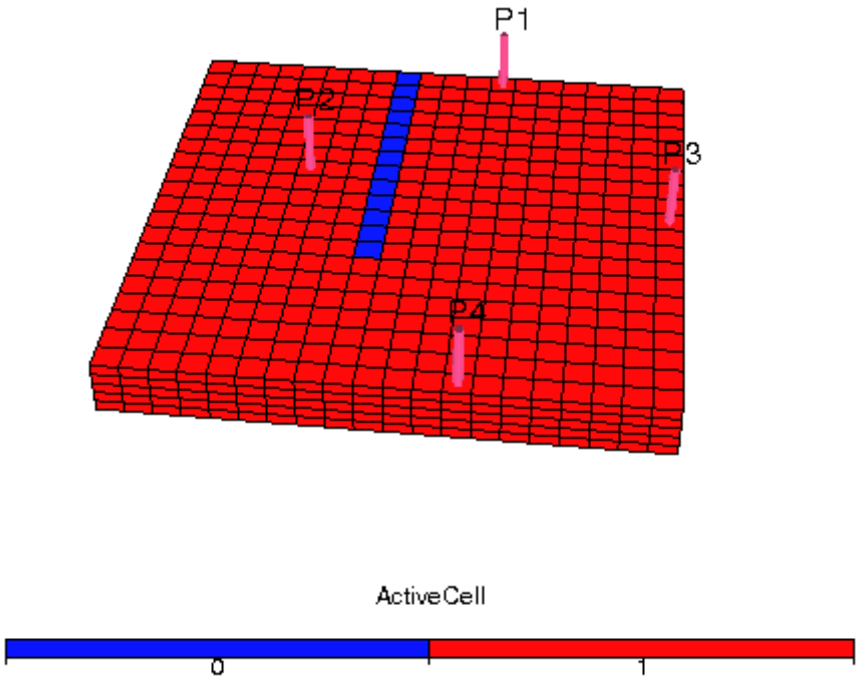

Figure 4-41: Sealing fault modelled as deactivated grid blocks (in blue colour).

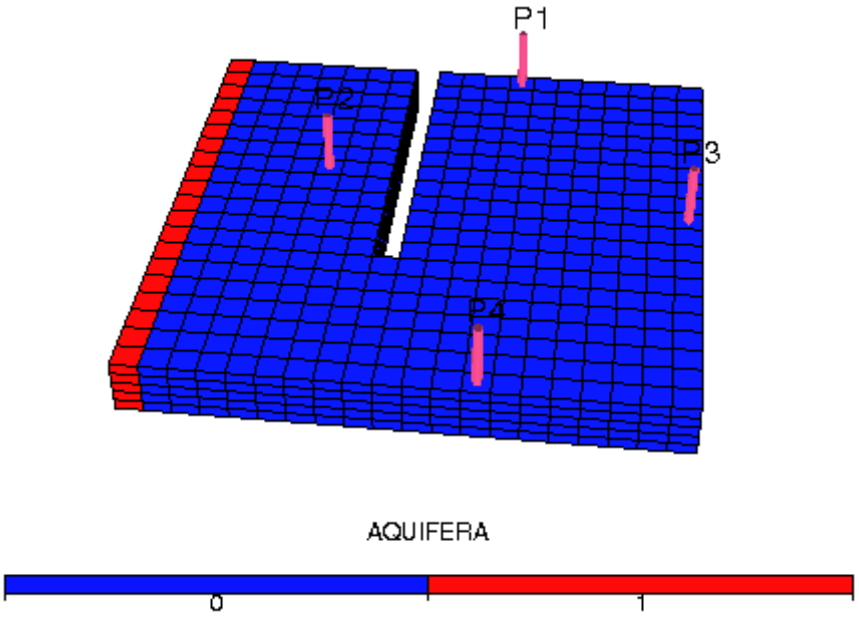

Figure 4-42: Location of edge-drive aquifer coloured in red.

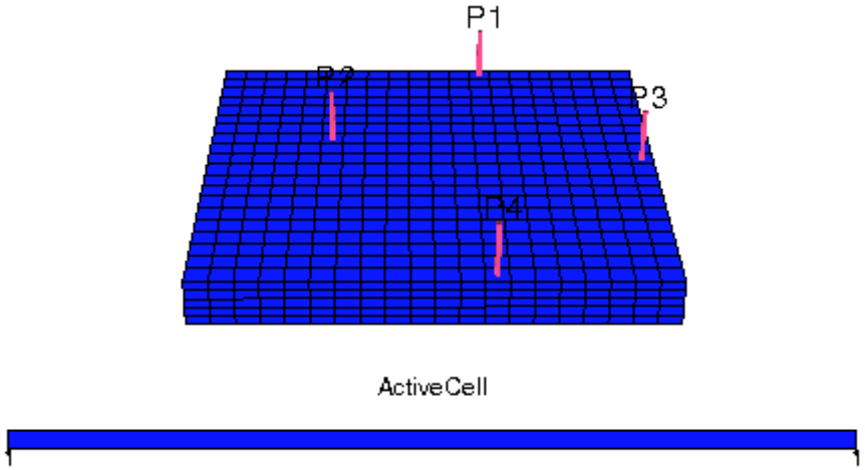

Figure 4-43: Base model showing all 2000 active grid blocks.

Similar to Case Example 1, horizontal permeabilities (K_x & K_y) were defined as model parameters prior to performing UHM using the adjoint method. The uncertainty limits for the horizontal permeabilities are described by Equation (37) where $K_{x_{max}}$ & $K_{y_{max}}$ represents the original or default maximum values for permeability in the X and Y direction which are $K_{x_{max}} = K_{y_{max}} =$ 287 mD. In addition, the initial assumptions employed in Case Example 1 are retained here (see Section 4.3.1).

By employing Equation (37) in the UHM stage, the progression of the objective function (Q) with increasing number of iterations is presented in Figure 4-44. A total of 57 iterations were executed in order to reach an optimal Q. This is so because the step size, μ_{K_x,K_y} = 10.75 mD^2, is utilized. As seen in Figure 4-44, the objective function value (or overall model error) reduced by a factor of 10 over the first 20 iterations. Subsequent iterations experienced a rather slow convergence to an optimal Q. The 32nd iteration was selected as our best-case since it delivered the lowest Q with an overall model error reduction value of 96.1%.

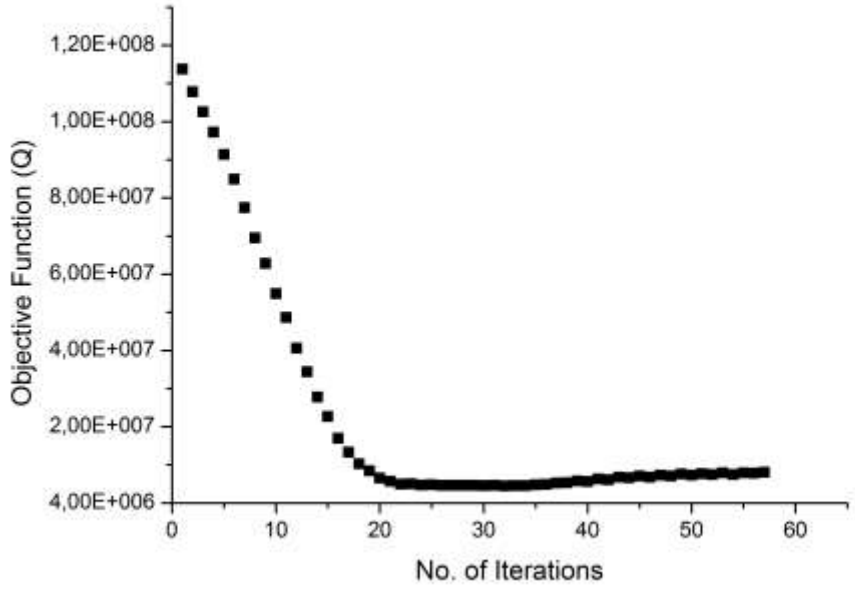

Figure 4-44: Progression of the objective function (Q) vs. number of iterations for case example 5.

The model responses defined for Case Example 5 are similar to previous case examples. Best-case results for the most offending model responses are presented in Figure 4-45. In addition, the R-squared values for all model responses generated for the best-case result obtained from UHM is presented in Table 4-5.

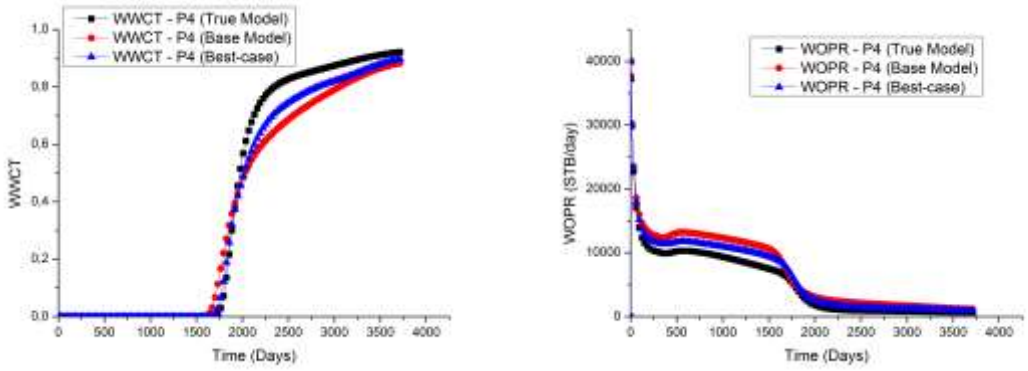

Figure 4-45: Best-case results for the most offending model responses after performing UHM for case example 5.

Table 4-5: R-squared values for the best-case result obtained from UHM for case example 5.

Well Name	WBHP	WWCT	WOPR
P1	99.9%	100.0%	98.8%
P2	99.8%	99.7%	99.9%
P3	99.9%	100.0%	98.7%
P4	99.9%	98.5%	98.3%
$R^2 \geq 97\%$; $R^2 < 97\%$			

In order to reveal the location of the hidden fault, the permeability ratio map for the 1st and 3rd layer (shown in Figure 4-46 and Figure 4-47) are generated using Equation (39). The yellow-coloured region represents grid blocks with little or no change in permeability. These grid blocks have a permeability ratio values of 1.0. Grid blocks coloured in red have permeability ratio values greater than 1.0 due to the existing reservoir heterogeneity in the base model. Grid blocks with colours varying from blue to purple identifies regions with extreme permeability reduction.

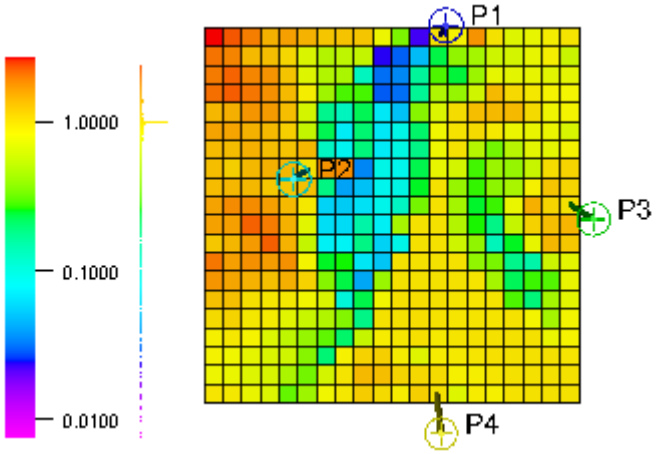

Figure 4-46: Permeability ratio map generated for case example 5 (1st layer).

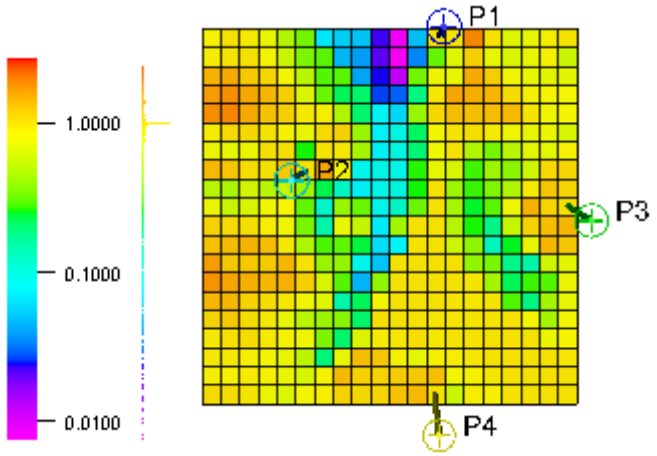

Figure 4-47: Permeability ratio map generated for case example 5 (3rd layer).

The expression provided in Equation (40) can be used to generate the fault indicator map for Case Example 5 from the permeability ratio maps. Figure 4-48 and Figure 4-49 presents the fault indicator maps for the 1st and 3rd layer capturing the location and shape of the revealed fault in purple-coloured grid blocks. The threshold value that reveals the location of the hidden fault is γ_{fault} = 9×10^{-2}. Interestingly, the revealed fault lies in a similar location as the sealing fault in the true model as shown in Figure 4-41.

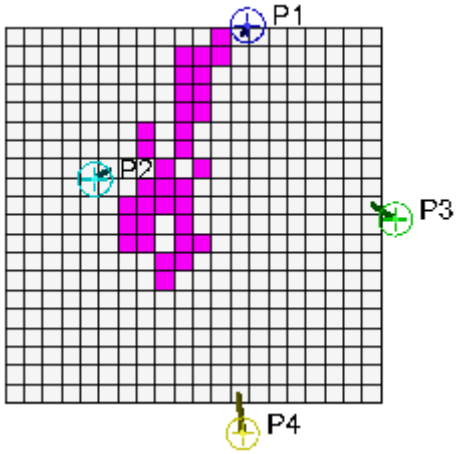

Figure 4-48: Fault indicator map for case example 5 generated at γ_{fault} = 9×10^{-2} (1st layer).

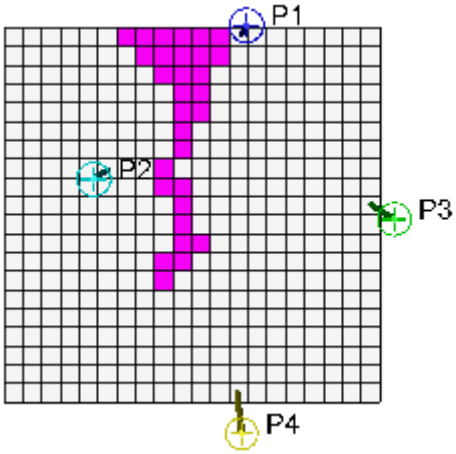

Figure 4-49: Fault indicator map for case example 5 generated at γ_{fault} = 9×10^{-2} (3rd layer).

This case example demonstrates the potency of the proposed method in improving reservoir characterization in reservoir simulation models that are strongly aquifer-dominated. Most state-of-the-art methods like the CRM [58] and INSIM-FT [64] find it challenging to improve reservoir characterization in aquifer-dominated reservoir models.

4.3.6 Case Example 6: Horizontal Well Test

The aim of setting up this case example is to evaluate the efficacy of the proposed method in revealing hidden reservoir features in multi-layered reservoir models with horizontal wells. The test model with dimensions 20 x 20 x 5 contains 5 vertical injectors and 4

horizontal producers (see Figure 4-50). All 2000 grid blocks are active. The size of the each grid block in the X and Y direction is fixed at 500 ft (152 metres). In the Z direction, the grid block size is 20 ft (6 metres).

The model contains mainly oil and water with no free gas evolving over a 10-year production period. The oil-water contact is placed beneath the last producing layer. A constant porosity value of 20% and a constant horizontal permeability value of 275 mD is assigned everywhere in the model. A vertical permeability of 27.5 mD is assigned to every grid block. The water and oil viscosity are retained at 0.3 cp and 1.3 cp respectively. The relative permeability curve described in Figure 4-5 is retained in this model. A sealing fault is introduced in the South-Eastern part of the reservoir which completely isolates injector INJ5, producers P3 and P4 from the rest of the field. This is the true model (see Figure 4-51).

An under-injection waterflooding strategy with a VRR < 1 is implemented. All 5 vertical injectors controlled by their water injection rates each injects 35000 barrels of water per day (approximately 7940 m^3/day) while all 4 horizontal producers controlled by their combined oil and water rates each produces 40000 barrels of liquid per day (approximately 6350 m^3/day). All vertical injectors are perforated in all 5 layers while all horizontal producers are completed and perforated only in the 3rd layer (see green connections in Figure 4-50).

In the base model, the sealing fault is completely removed. Permeabilities in grid blocks housing all injectors are unchanged since core data is assumed to be available for each well. In the case of the horizontal producers, it is assumed that core data only exists for the producers drilled into and perforated in the 3rd layer. The solution of the true model is defined as measured data in the base model. No Gaussian noise is added to the measured data.

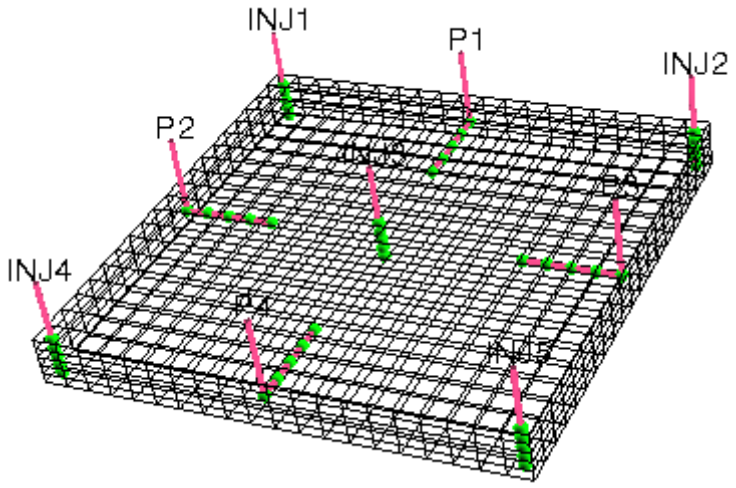

Figure 4-50: True model showing model structure and well arrangement.

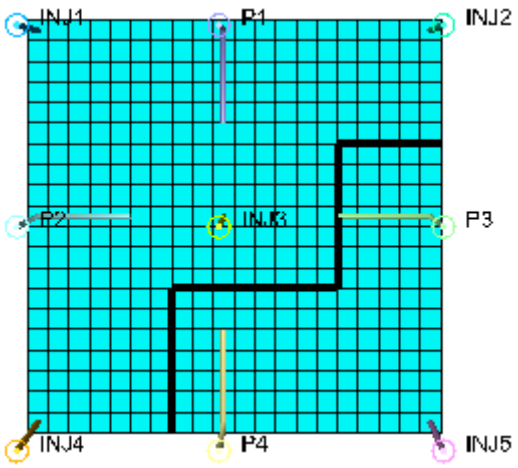

Figure 4-51: Top view of true model capturing sealing fault (in thick black line).

In order to reveal the location of the hidden faults, horizontal permeabilities (K_x & K_y) were defined as model parameters prior to performing UHM using the adjoint method. The uncertainty limits for the horizontal permeabilities are described by Equation (37) where $K_{x_{max}}$ & $K_{y_{max}}$ represents the original or default maximum values for permeability in the X and Y direction which are $K_{x_{max}} = K_{y_{max}} = 275$ mD. In addition, the initial assumptions employed in Case Example 1 are retained here (see Section 4.3.1).

By employing Equation (37) in the UHM stage, the progression of the objective function (Q) with increasing number of iterations is presented in Figure 4-52. A total of 410 iterations were executed in order to reach an optimal Q. This is so because the step size, μ_{K_x,K_y} = 10.75 mD^2, is utilized. As seen in Figure 4-52, the objective function value (or overall model error) reduced by a factor of 1000 over the entire 410 iterations. The 405th iteration was selected as our best-case since it delivered the lowest Q with an overall model error reduction value of 99.6%. Of course, one can argue that a best-case solution can also be selected between the 50th and the 100th iteration. Since the model runtime is approximately 4 seconds, a large number of iterations can be executed to find an optimal solution. In real field problems with hundreds of thousands of grid blocks where simulation time are in hours, 100 iterations or less can be executed.

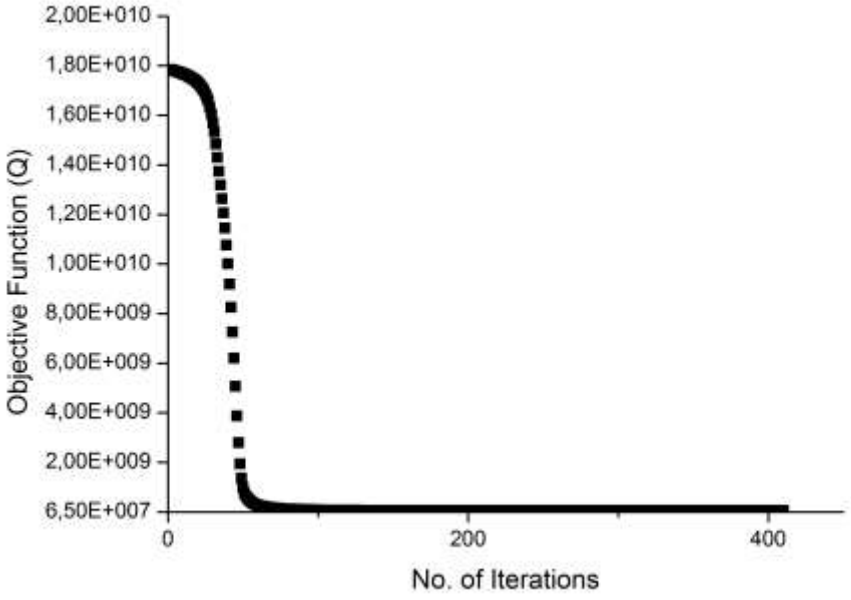

Figure 4-52: Progression of the objective function (Q) vs. number of iterations for case example 6.

The model responses defined for this case example are similar to those of previous case examples. Best-case results for the most offending model responses are presented in Figure 4-53. In addition, the R-squared values for all model responses generated for the best-case result obtained from UHM is presented in Table 4-6.

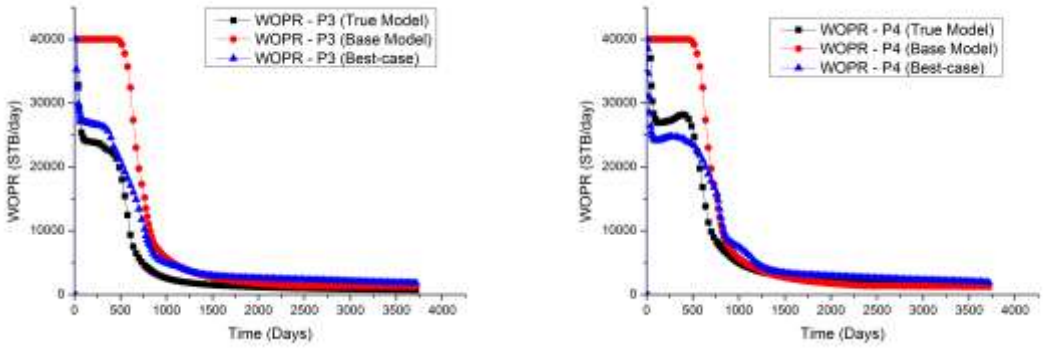

Figure 4-53: Best-case results for the most offending model responses after performing UHM for case example 6.

Table 4-6: R-squared values for the best-case result obtained from UHM for case example 6.

Well Name	WBHP	WWCT	WOPR
P1	99.8%	98.8%	99.1%
P2	99.9%	98.7%	98.9%
P3	100.0%	99.3%	98.4%

P4	100.0%	99.2%	98.3%
INJ1	99.9%	—	—
INJ2	99.9%	—	—
INJ3	99.9%	—	—
INJ4	100.0%	—	—
INJ5	99.6%	—	—
$R^2 \geq 97\%$; $R^2 < 97\%$			

In order to reveal the location of the hidden fault, the permeability ratio maps (see Figure 4-54 and Figure 4-55) are generated using Equation (39). The white-coloured region represents grid blocks with little or no change in permeability. Grid blocks with colours varying from light-yellow to purple identifies regions with extreme permeability reduction.

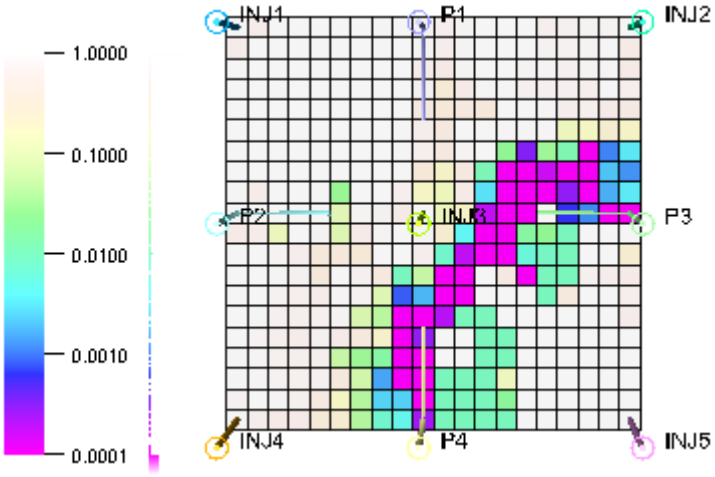

Figure 4-54: Permeability ratio map generated for case example 6 (1st layer).

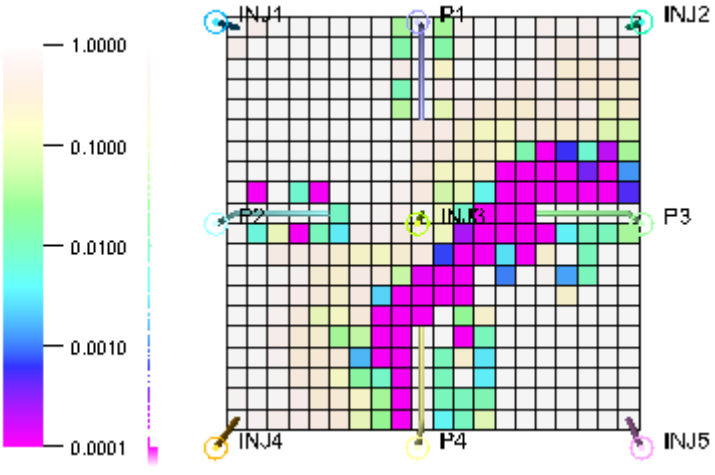

Figure 4-55: Permeability ratio map generated for case example 6 (3rd layer).

As seen in Figure 4-55, the permeability in the grid blocks housing all 4 horizontal producers in the 3rd layer are unchanged since we assumed that core data exists for the horizontal producers. This is indicated by the white-coloured grid blocks with

permeability ratio values of 1.0. The expression provided in Equation (40) can be used to generate the fault indicator maps from the permeability ratio maps. Figure 4-56 and Figure 4-57 presents the fault indicator maps for the 1st and 3rd layer capturing the location and shape of the revealed fault in purple-coloured grid blocks. The threshold value that reveals the location of the hidden fault is γ_{fault} = 8×10-4.

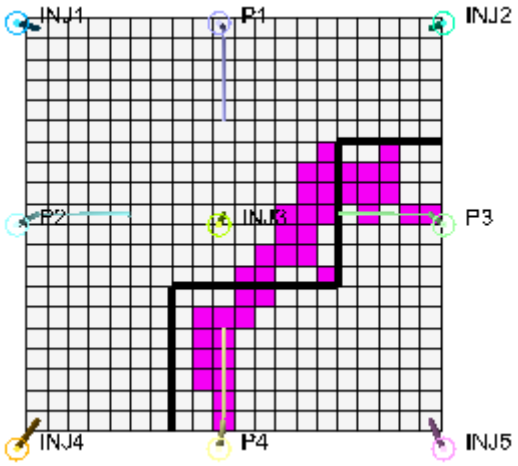

Figure 4-56: Fault indicator map for case example 6 generated at γ_{fault} = 8×10-4 (1st layer).

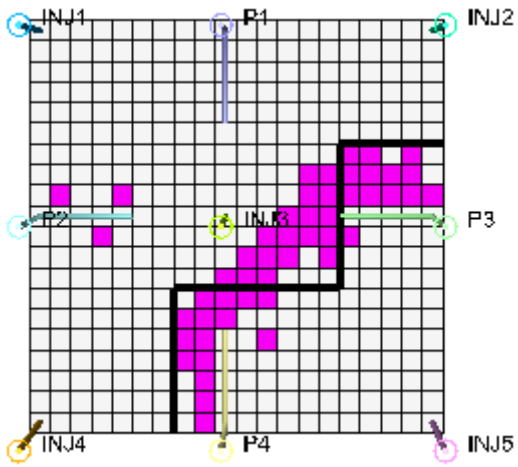

Figure 4-57: Fault indicator map for case example 6 generated at γ_{fault} = 8×10-4 (3rd layer).

For easier comparison, the sealing fault in the true model (in thick black line) and the revealed fault (purple-coloured grid blocks) are both included in Figure 4-56 and Figure 4-57 respectively. Although the revealed fault takes a slightly different shape, its location is very much similar to the true model sealing fault.

4.3.7 Models Experiencing Changes in Flow Patterns over Time

So far, most of the case examples discussed earlier borders around revealing various types of hidden reservoir features in reservoir simulation models with different injection strategies and well architectures. Before the proposed method can be applied to real-field

problems, it is important to evaluate its effectiveness especially in cases where certain actions performed on real-life petroleum reservoirs can induce significant changes in flow pattern over time. Examples of such actions include injector-to-producer conversion and vice versa, shutting-in a well that has been online for some time and the addition of a new well (e.g. infill well). In this section, 3 case studies are discussed. In the first case study, the efficacy of the proposed method in revealing a hidden fault in a reservoir model with injector-to-producer conversion scenario undergoing an under-injection waterflooding strategy (VRR < 1) is presented. The second case study demonstrates the effectiveness of the proposed method in revealing a hidden fault in a test model with two producers which are shut-in for a period of 4 years. The waterflooding strategy adopted in the second case study is the over-injection waterflooding strategy (VRR > 1). In the third case study, the proposed method is evaluated with a test model undergoing a par-injection waterflooding strategy (VRR = 1). At initialization, the test model contains 4 vertical injectors and 4 vertical producers. After approximately 5 years of production, an infill producer is drilled in the middle of the reservoir and completed in all 5 layers. The goal of the third case study is to reveal the location and shape of the sealing fault which is hidden in the base model despite changes in flow pattern induced by the addition of the infill producer.

4.3.7.1 Injector-to-Producer Conversion Test

The effectiveness of the proposed method in revealing hidden reservoir features not captured in reservoir simulation models undergoing actions that significantly induce changes in flow patterns over time is put to the test. The test model used is a 20 x 20 x 5 homogeneous model with 4 vertical injectors, 4 vertical producers and a vertical well whose phase alters repeatedly between being an oil producer and a water injector over the entire production period of 10 years. The size of each grid block in the X and Y direction is fixed at 500 ft (152 metres). In the Z direction, the grid block size is 20 ft (6 metres). All 2000 grid blocks are active. The model contains mainly oil and water with no free gas evolving over the 10-year production period. The oil-water contact is located beneath the last producing layer. A constant porosity value of 20% and a constant horizontal permeability of 275 mD is assigned everywhere in the model. The vertical permeability in every grid block is generated by multiplying the horizontal permeability by a value of 0.1. A sealing fault is introduced around the neighbourhood of injector INJ5, producers P3 and P4 to completely isolate them from the rest of the field. The water and oil viscosity are retained at 0.3 cp and 1.3 cp respectively. The relative permeability curve described in Figure 4-5 is retained in this model. This is the true model (see Figure 4-58).

An under-injection waterflooding strategy with a VRR < 1 is implemented. All injectors controlled by their water injection rates each injects 30000 barrels of water per day (approximately 4760 m^3/day) while all producers controlled by their combined oil and water rates each produces 40000 barrels of liquid per day (approximately 6350 m^3/day). All injectors and producers are perforated in all 5 layers. Well INJ3 located in the middle

of the reservoir is intermittently converted from a water injector to an oil producer and vice versa over the 10-year production period. In order to model the injection-to-producer conversion process, two wells are completed in the same location as well INJ3. Well INJ3_INJ refers to well INJ3 operating as a water injector while well INJ3_PRO refers to well INJ3 operating as an oil producer. Both wells do not operate simultaneously. This means that when well INJ3_INJ is injecting water, well INJ3_PRO is shut and vice versa. The water injection rate profile for well INJ3_INJ is shown in Figure 4-59.

In the base model, all information about the sealing fault are completely removed. The permeability in grid blocks housing all injectors and producers are unchanged since core data is assumed to be available for each well. The solution of the true model is defined as measured data in the base model. No Gaussian noise is added to the measured data.

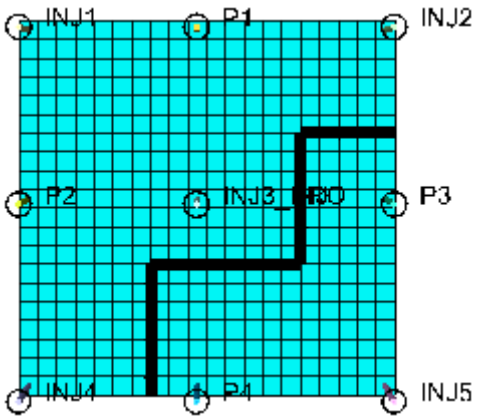

Figure 4-58: True model capturing the location of wells and sealing fault (in thick black line).

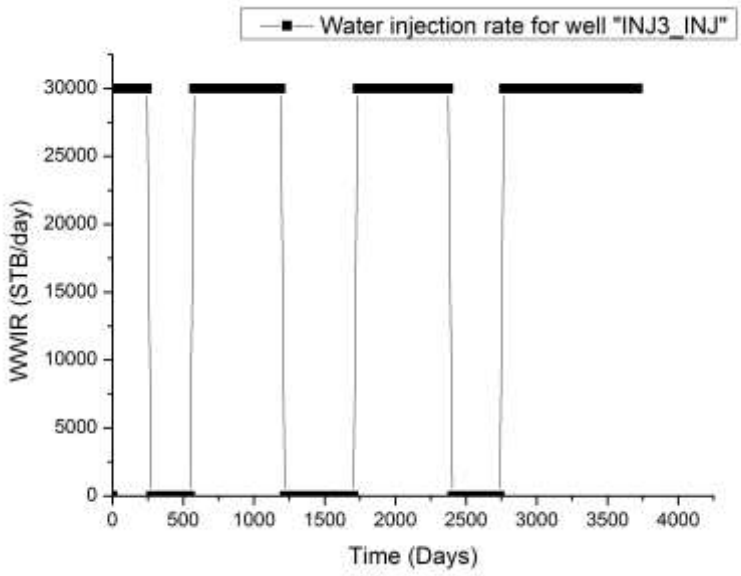

Figure 4-59: Water injection rate profile for well INJ3_INJ.

Like in all previous case examples presented, the first step required for revealing the location of the hidden fault(s) is to define the model parameters prior to performing UHM. The model parameters required are the horizontal permeabilities (K_x & K_y). The uncertainty limits for the horizontal permeabilities is described by Equation (37) where $K_{x_{max}} = K_{y_{max}} = 275$ mD. In addition, the initial assumptions employed in Case Example 1 are retained here (see Section 4.3.1).

By employing Equation (37) in the UHM stage, the progression of the objective function (Q) with increasing number of iterations is presented in Figure 4-60. A total of 420 iterations were executed in order to reach an optimal Q. This is so because the step size, μ_{K_x,K_y} = 10.75 mD^2, is utilized. As seen in Figure 4-60, the objective function value (or overall model error) reduced by a factor of 100 over the entire 420 iterations. The 408th iteration was selected as our best-case since it delivered the lowest Q with an overall model error reduction value of 97.8%.

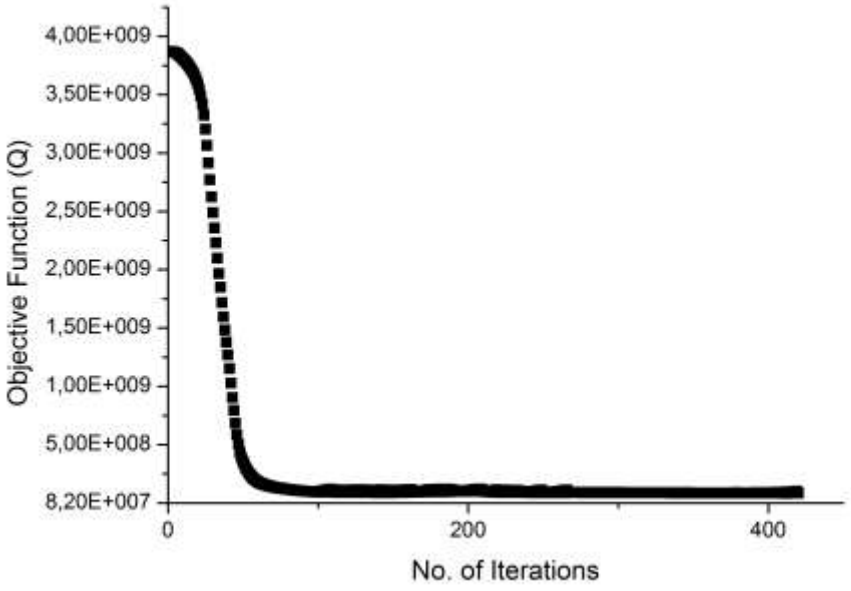

Figure 4-60: Progression of the objective function (Q) vs. number of iterations for the injector-to-producer conversion test.

The model responses defined for the injector-to-producer conversion test are well water-cut (WWCT), well oil production rate (WOPR) and well bottom-hole flowing pressure (WBHP). Best-case results for the most offending model responses are presented in Figure 4-61. In addition, the R-squared values for all model responses generated for the best-case result obtained from UHM is presented in Table 4-7.

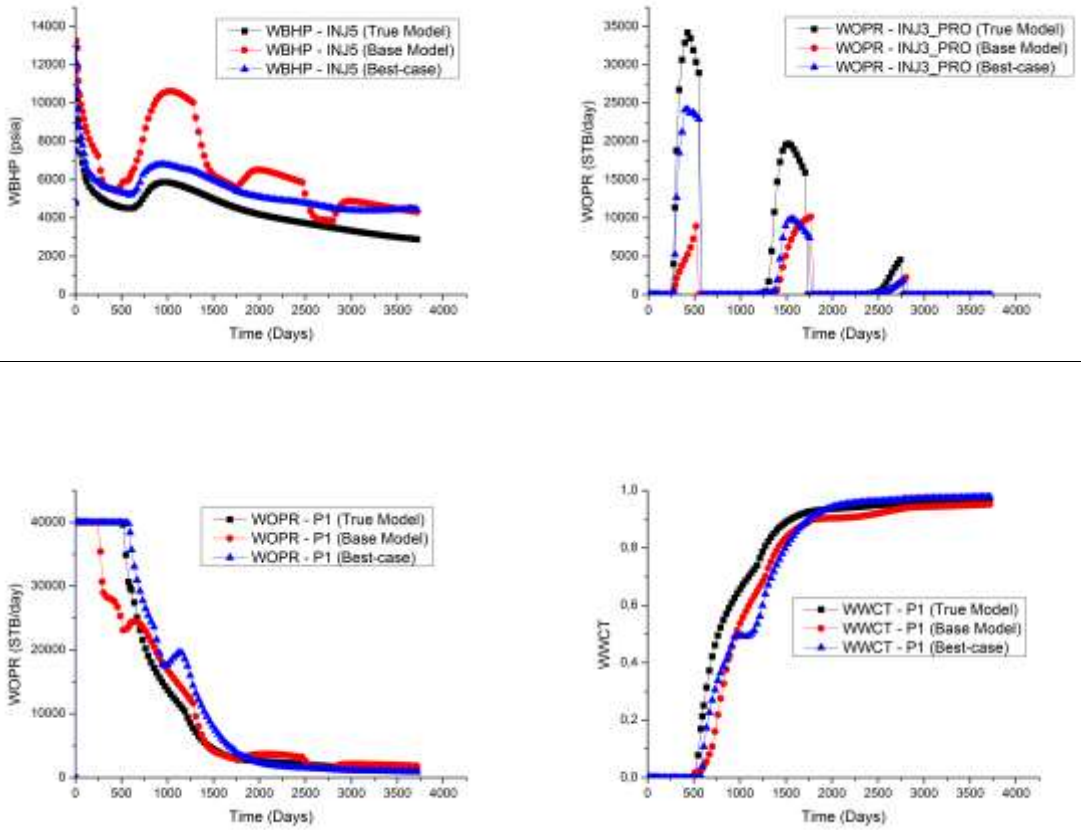

Figure 4-61: Best-case results for the most offending model responses after performing UHM for the injector-to-producer conversion test.

Table 4-7: R-squared values for the best-case result from UHM for the injector-to-producer conversion test.

Well Name	WBHP	WWCT	WOPR
P1	99.5%	97.6%	97.8%
P2	99.6%	97.9%	98.1%
P3	100.0%	98.3%	99.6%
P4	100.0%	98.5%	99.4%
INJ3_PRO	99.7%	97.5%	97.0%
INJ1	99.7%	—	—
INJ2	99.8%	—	—
INJ3_INJ	99.9%	—	—
INJ4	99.8%	—	—
INJ5	93.1%	—	—
$R^2 \geq 97\%$; $R^2 < 97\%$			

In order to reveal the location of the hidden fault, the permeability ratio map for the 1st and 3rd layer (see Figure 4-62 and Figure 4-63) are generated using Equation (39). The

white-coloured region represents grid blocks with little or no change in permeability. Grid blocks with colours varying from light-yellow to purple identifies regions with extreme permeability reduction.

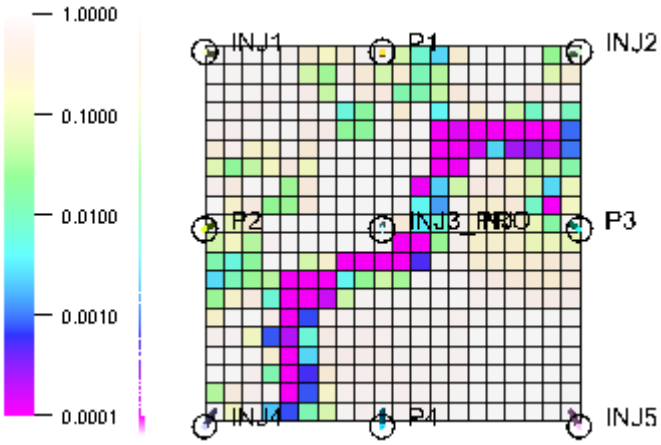

Figure 4-62: Permeability ratio map generated for the injector-to-producer conversion test (1st layer).

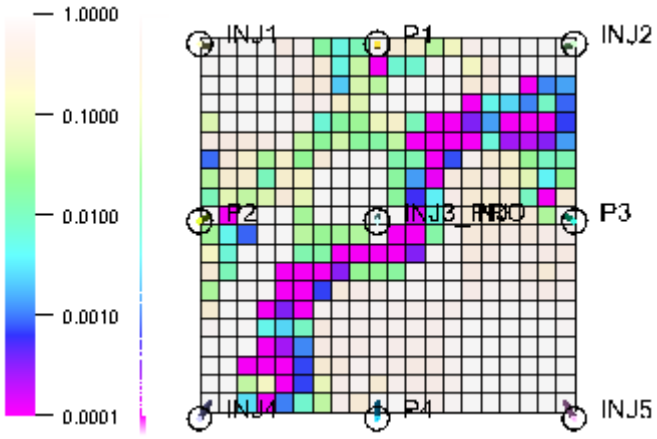

Figure 4-63: Permeability ratio map generated for the injector-to-producer conversion test (3rd layer).

As seen in Figure 4-62 and Figure 4-63, the permeability in the grid blocks housing all wells are unchanged since we assumed that core data exists for all wells. This is indicated by the white-coloured grid blocks with permeability ratio values of 1.0. The expression provided in Equation (40) can be used to generate the fault indicator maps from Figure 4-62 and Figure 4-63. Figure 4-64 and Figure 4-65 presents the fault indicator map for the 1st and 3rd layer capturing the location and shape of the revealed fault in purple-coloured grid blocks. The threshold value that reveals the location of the hidden fault is $\gamma_{fault} = 5\times10^{-3}$.

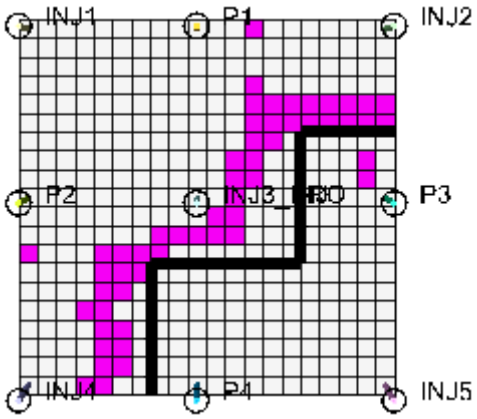

Figure 4-64: Fault indicator map for the injector-to-producer conversion test generated at γ_{fault} = 5×10^{-3} (1st layer).

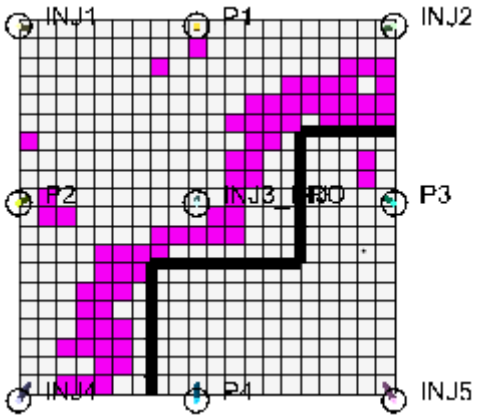

Figure 4-65: Fault indicator map for the injector-to-producer conversion test generated at γ_{fault} = 5×10^{-3} (3rd layer).

The location and shape of the revealed fault (purple-coloured grid blocks) is very much similar to the sealing fault in the true model (in thick black line) as seen in Figure 4-64 and Figure 4-65 respectively.

4.3.7.2 Well Shut-in Test

Shutting-in injectors or producers for a short or relatively long period of time can induce significant changes in flow patterns in a petroleum reservoir. The impact of these changes on the potency of the proposed method in revealing hidden reservoir features is evaluated using a multi-layered homogeneous model with dimension 20 x 20 x 5 which contains 5 vertical injectors and 4 vertical producers. The model grid sizes are similar to the previous case study (injector-to-producer conversion test). All grid blocks are active and the model contains predominantly oil and water with no free gas evolving over a 10-year production period. The oil-water contact exist below the last producing layer. A constant porosity value of 20% and a constant horizontal permeability of 275 mD is assigned everywhere in the model. The vertical permeability in every grid block is generated by multiplying the horizontal permeability by a value of 0.1. A sealing fault is introduced around the vicinity of injector INJ5, producers P3 and P4 to completely isolate them from the rest

of the field. The water and oil viscosity are retained at 0.3 cp and 1.3 cp respectively. The relative permeability curve described in Figure 4-5 is retained in this model. This is the true model (see Figure 4-66).

An over-injection waterflooding strategy with a VRR > 1 is implemented. All injectors controlled by their water injection rates each injects 50000 barrels of water per day (approximately 7950 m^3/day) while all producers controlled by their combined oil and water rates each produces 40000 barrels of liquid per day (approximately 6350 m^3/day). All injectors and producers are perforated in all 5 layers. Producers P1 and P4 are shut for a period of 4 years (between the 2nd and the 6th year of production). The water-cut profile for producers P1 and P4 obtained from the true model is shown in Figure 4-67.

In the base model, all information about the sealing fault are completely removed. The permeability in grid blocks housing all injectors and producers are unchanged since core data is assumed to be available for each well. The solution of the true model is defined as measured data in the base model. No Gaussian noise is added to the measured data. The reservoir characterization problem presented here is formulated in this manner because sealing faults are the most challenging reservoir feature to reveal.

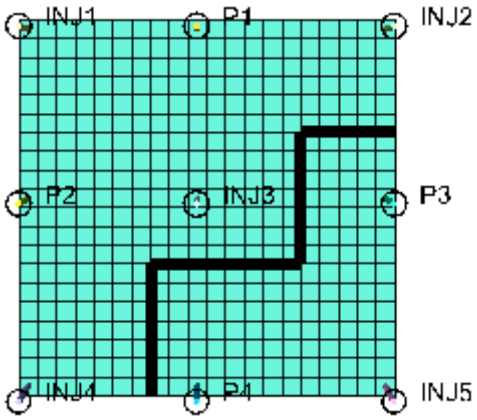

Figure 4-66: True model capturing the location of the sealing fault (in thick black line).

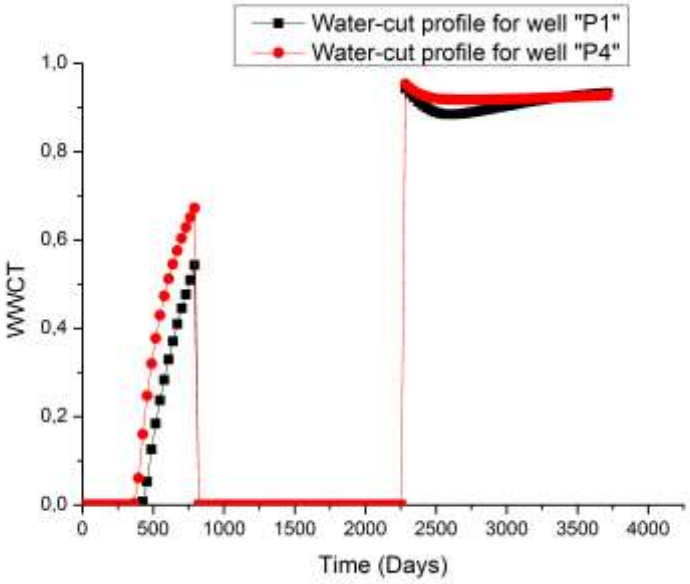

Figure 4-67: Water-cut profile for producers P1 and P4 obtained from true model.

In order to reveal the location and shape of the sealing fault in the base model, horizontal permeabilities (K_x & K_y) are defined as model parameters prior to performing UHM. The uncertainty limits for the horizontal permeabilities is described by Equation (37) where $K_{x_{max}} = K_{y_{max}} = 275$ mD. In addition, the initial assumptions employed in Section 4.3.1 are retained here.

By employing Equation (37) in the UHM stage, the progression of the objective function (Q) with increasing number of iterations is presented in Figure 4-68. A total of 500 iterations were executed in order to reach an optimal Q. This is so because the step size, μ_{K_x,K_y} = 5.0 mD^2, is utilized. As seen in Figure 4-68, the objective function value (or overall model error) reduced by a factor of 100 over the entire 500 iterations. The 461th iteration was selected as our best-case since it delivered the lowest Q with an overall model error reduction value of 98.9%.

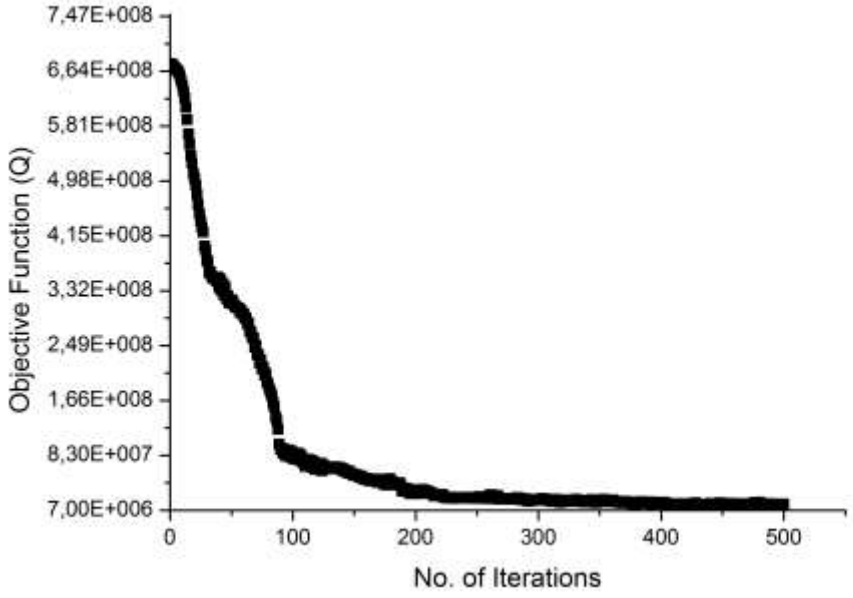

Figure 4-68: Progression of the objective function (Q) vs. number of iterations for the well shut-in test.

The model responses defined for the well shut-in test are well water-cut (WWCT), well oil production rate (WOPR) and well bottom-hole flowing pressure (WBHP). Best-case results for the most offending model responses are presented in Figure 4-69. In addition, the R-squared values for all model responses generated for the best-case result obtained from UHM is presented in Table 4-8.

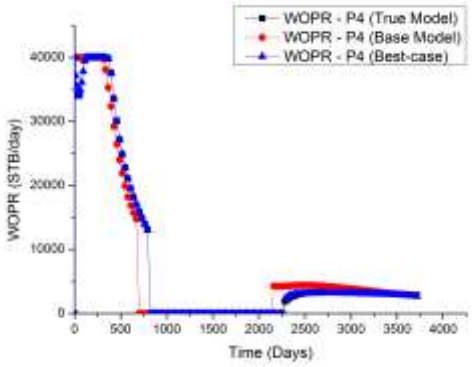

Figure 4-69: Best-case results for the most offending model responses after performing UHM for the well shut-in test.

Table 4-8: R-squared values for the best-case result from UHM for the well shut-in test.

Well Name	WBHP	WWCT	WOPR
P1	99.9%	99.9%	99.9%
P2	99.9%	99.8%	99.8%

P3	99.9%	99.9%	99.9%
P4	99.9%	99.9%	98.1%
INJ1	99.9%	—	—
INJ2	99.9%	—	—
INJ3	100.0%	—	—
INJ4	99.9%	—	—
INJ5	99.9%	—	—
$R^2 \geq 97\%$; $R^2 < 97\%$			

In order to reveal the location of the hidden fault, the permeability ratio map for the 3rd layer (see Figure 4-70) is generated using Equation (39). The white-coloured region represents grid blocks with little or no change in permeability. Grid blocks with colours varying from light-yellow to purple identifies regions with extreme permeability reduction.

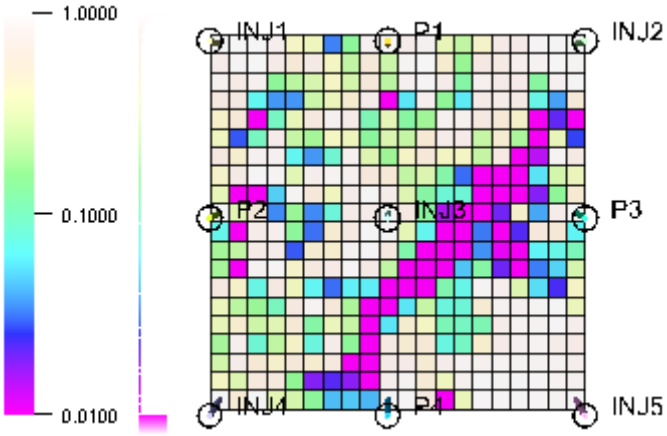

Figure 4-70: Permeability ratio map generated for the well shut-in test (3rd layer).

As seen in Figure 4-70, the permeability in the grid blocks housing all wells are unchanged since we assumed that core data exists for all wells. This is indicated by the white-coloured grid blocks with permeability ratio values of 1.0. The expression provided in Equation (40) can be used to generate the fault indicator map from Figure 4-70. Figure 4-71 presents the fault indicator map for the 3rd layer capturing the location and shape of the revealed fault in purple-coloured grid blocks. The threshold value that reveals the location of the hidden fault is $\gamma_{fault} = 5\times10^{-2}$. The location and shape of the revealed fault (purple-coloured grid blocks) is quite similar to the sealing fault in the true model (in thick black line) as seen in Figure 4-71. A similar shape and location of the revealed fault is observed in the 1st, 2nd, 4th and 5th layer as well. Results obtained from this test proves that the proposed method is not negatively impacted by the action of shutting-in wells either for a short or prolonged time period.

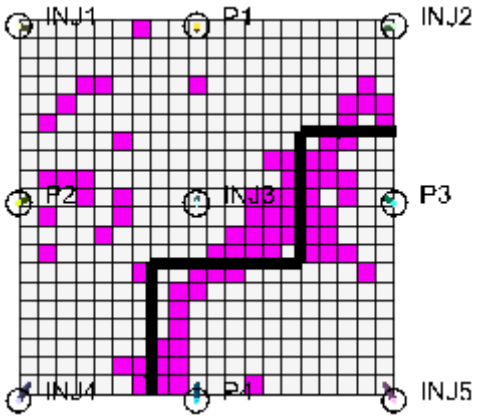

Figure 4-71: Fault indicator map for the well shut-in test generated at γ_{fault} = 5×10^{-2} (3rd layer).

4.3.7.3 Infill Well Test

The goal of adding infill wells in brownfield reservoirs is to increase the field ultimate recovery. Also, the addition of infill wells in petroleum reservoirs alters the flow pattern of hydrocarbons and increases sweep in regions where hydrocarbon saturation is highest. In other cases, infill wells (especially infill producers) can be used to produce large pockets of unswept hydrocarbons after extensive waterflooding. In this case study, we examine the effect of adding an infill producer on the capability of the proposed method in revealing hidden reservoir features. The test model used is a homogeneous model with dimension 20 x 20 x 5 which contains 4 vertical injectors and 4 vertical producers at initialization. The model grid sizes are similar to the previous two case studies (injector-to-producer conversion and well shut-in tests). All grid blocks are active and the model contains predominantly oil and water with no free gas evolving over a 10-year production period. The oil-water contact exist below the last producing layer. A constant porosity value of 20% and a constant horizontal permeability of 275 mD is assigned everywhere in the model. The vertical permeability in every grid block is generated by multiplying the horizontal permeability by a value of 0.1. Similar to the injection-to-producer conversion and well shut-in tests, a sealing fault is introduced around the neighbourhood of injector INJ5, producers P3 and P4 to completely isolate them from the rest of the field. The water and oil viscosity are retained at 0.3 cp and 1.3 cp respectively. The relative permeability curve described in Figure 4-5 is retained in this model. This is the true model.

A par-injection waterflooding strategy with a VRR = 1 is implemented. All injectors controlled by their water injection rates each injects 40000 barrels of water per day (approximately 6350 m^3/day) while all producers controlled by their combined oil and water rates each produces 40000 barrels of liquid per day (approximately 6350 m^3/day). All injectors and producers are perforated in all 5 layers. After approximately 5 years of production, an infill producer "P-NEW1" is drilled and completed in all 5 layers (see Figure 4-72). The infill producer "P-NEW1" is located in the centre of the model. The infill producer "P-NEW1" is also controlled by its combined oil and water rates which is

set at 40000 barrerls of liquid per day (approximately 6350 m^3/day). The water-cut profile for the infill producer "P-NEW1" obtained from the true model is shown in Figure 4-73.

In the base model, all information about the sealing fault are completely removed. The permeability in grid blocks housing all injectors and producers are unchanged since core data is assumed to be available for each well. The solution of the true model is defined as measured data in the base model. No Gaussian noise is added to the measured data.

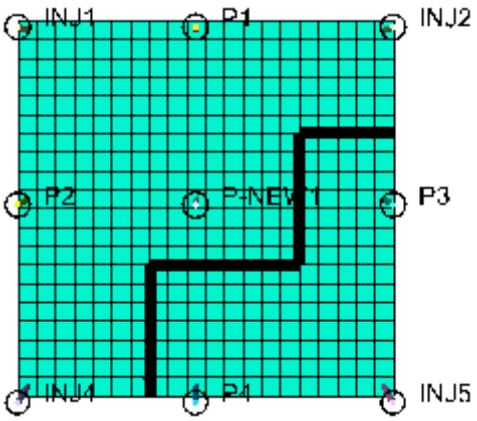

Figure 4-72: True model capturing the location of wells (including the infill producer "P-NEW1") and the sealing fault (in thick black line).

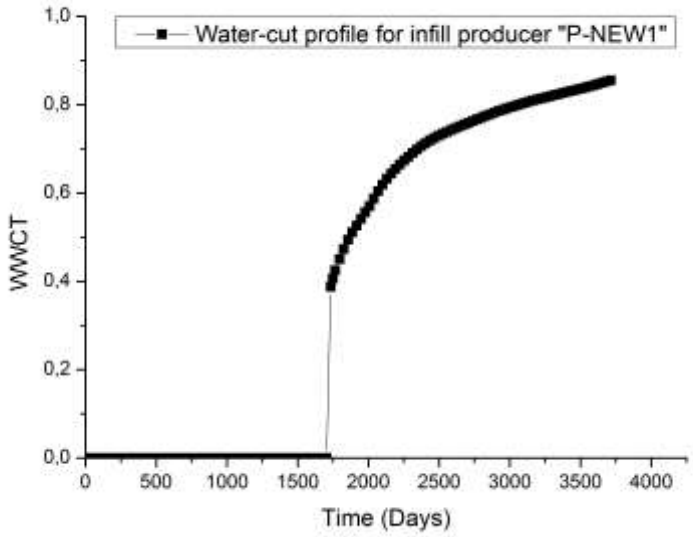

Figure 4-73: Water-cut profile for infill producer "P-NEW1" obtained from true model.

In order to reveal the location and shape of the sealing fault in the base model, horizontal permeabilities (K_x & K_y) are defined as model parameters prior to performing UHM. The uncertainty limits for the horizontal permeabilities is described by Equation (37) where

$K_{x_{max}} = K_{y_{max}}$ = 275 mD. In addition, the initial assumptions employed in Section 4.3.1 are retained here.

By employing Equation (37) in the UHM stage, the progression of the objective function (Q) with increasing number of iterations is presented in Figure 4-74. A total of 500 iterations were executed in order to reach an optimal Q (the lowest possible objective function value attainable over 500 iterations). This is so because the step size, μ_{K_x,K_y} = 5.0 mD^2, is utilized. As seen in Figure 4-74, the objective function value reduced by a factor of 10 over the entire 500 iterations. The 481th iteration was selected as our best-case since it delivered the lowest Q with an overall model error reduction value of 94.9%.

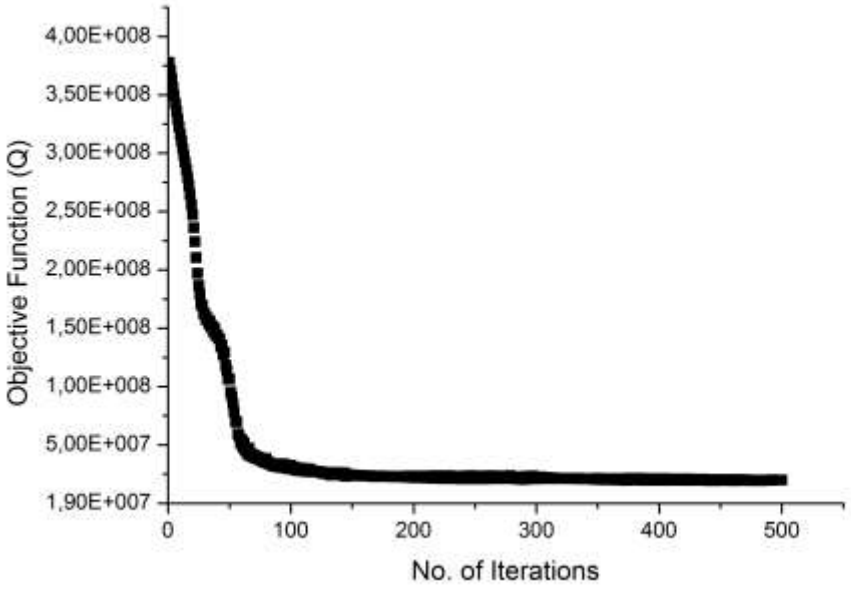

Figure 4-74: Progression of the objective function (Q) vs. number of iterations for the infill well test.

The model responses defined for the infill well test are well water-cut (WWCT), well oil production rate (WOPR) and well bottom-hole flowing pressure (WBHP). Best-case results for the most offending model responses are presented in Figure 4-75. In addition, the R-squared values for all model responses generated for the best-case result obtained from UHM is presented in Table 4-9.

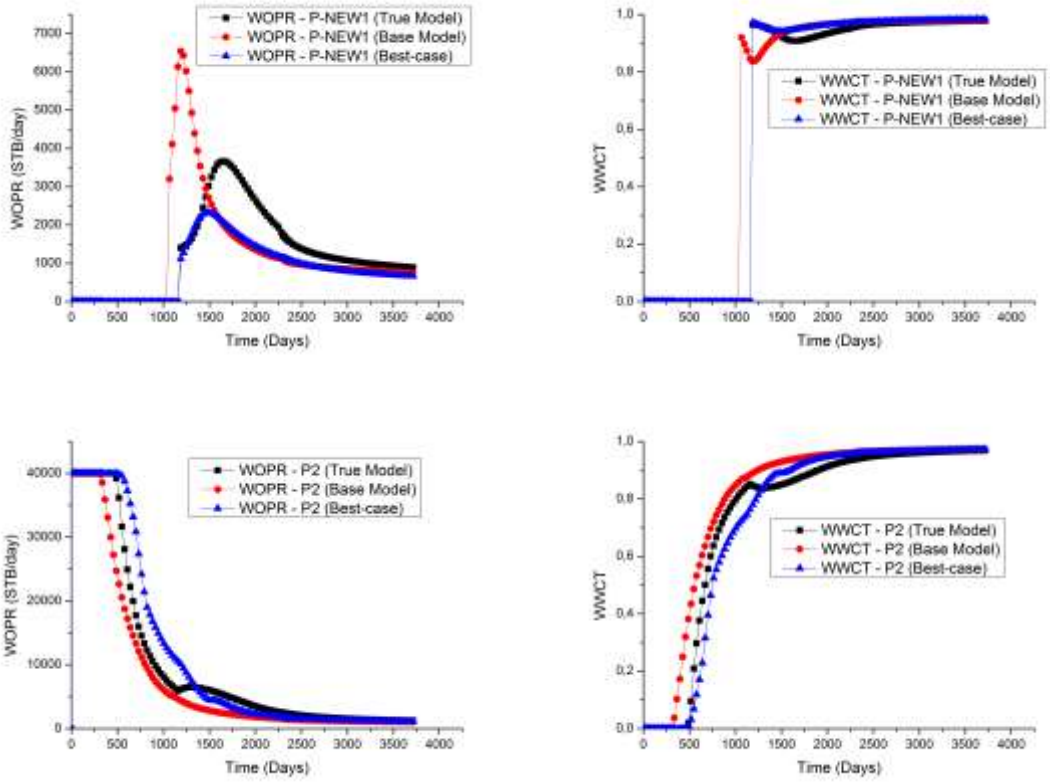

Figure 4-75: Best-case results for the most offending model responses after performing UHM for the infill well test.

Table 4-9: R-squared values for the best-case result obtained from UHM for the infill well test.

Well Name	WBHP	WWCT	WOPR
P1	99.8%	99.3%	99.2%
P2	99.9%	98.8%	98.9%
P3	99.9%	99.9%	99.8%
P4	99.8%	99.2%	99.3%
P-NEW1	99.8%	99.1%	93.8%
INJ1	99.8%	—	—
INJ2	99.8%	—	—
INJ4	99.8%	—	—
INJ5	99.7%	—	—
$R^2 \geq 97\%$; $R^2 < 97\%$			

In order to reveal the location of the hidden fault, the permeability ratio maps for the 1st and 3rd layer (see Figure 4-76 and Figure 4-77) is generated using Equation (39). The white-coloured region represents grid blocks with little or no change in permeability. Grid blocks with colours varying from light-yellow to purple identifies regions with extreme permeability reduction.

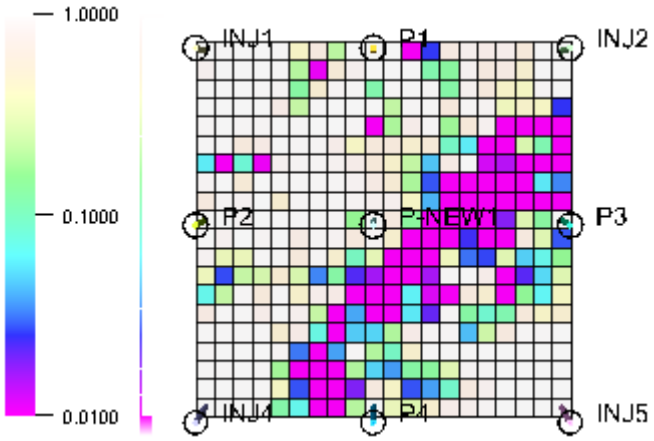

Figure 4-76: Permeability ratio map generated for the infill well test (1st layer).

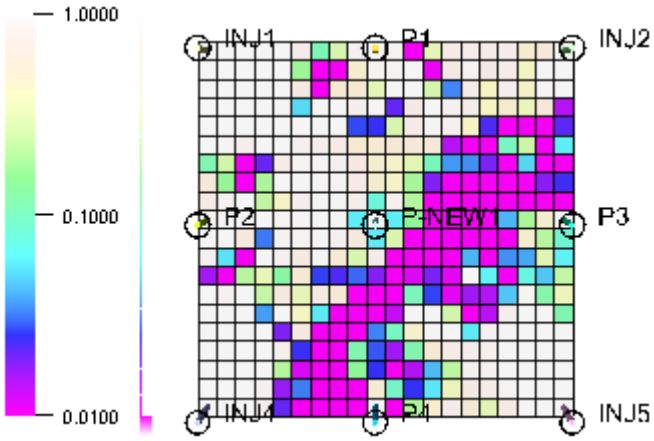

Figure 4-77: Permeability ratio map generated for the infill well test (3rd layer).

As seen in Figure 4-76 and Figure 4-77, the permeability in the grid blocks housing all wells are unchanged since we assumed that core data exists for all wells. This is indicated by the white-coloured grid blocks with permeability ratio values of 1.0. The expression provided in Equation (40) can be used to generate the fault indicator maps from Figure 4-76 and Figure 4-77. Figure 4-78 and Figure 4-79 presents the fault indicator maps for the 1st and 3rd layer capturing the location and shape of the revealed fault in purple-coloured grid blocks. The threshold value that reveals the location of the hidden fault is γ_{fault} = 1×10^{-2}. The location and shape of the revealed fault (purple-coloured grid blocks) is quite similar to the sealing fault in the true model (in thick black line) as seen in Figure 4-78 and Figure 4-79 respectively.

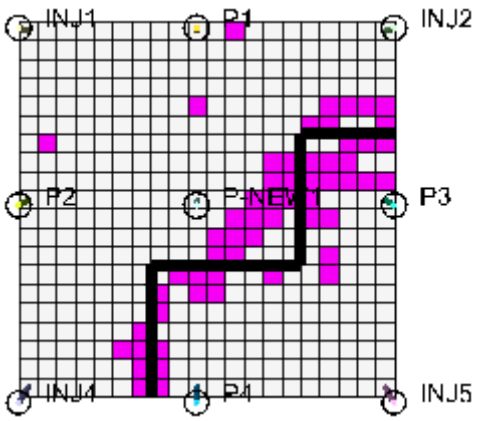

Figure 4-78: Fault indicator map for the infill well test generated at γ_{fault} = 1×10^{-2} (1st layer).

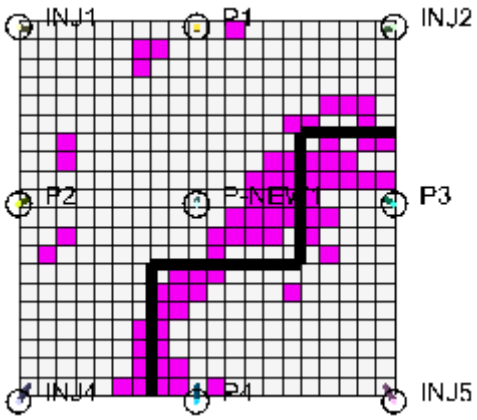

Figure 4-79: Fault indicator map for the infill well test generated at γ_{fault} = 1×10^{-2} (3rd layer).

4.3.8 CRM vs. INSIM-FT vs. Proposed Method (Extracted from EAGE ECMOR XVI Paper [84])

In order to ascertain the superiority of the proposed method to other existing methods available in literature, we compared its performance to the most prominent state-of-the-art approaches reported in literature. These state-of-the-art methods have been used extensively to improve reservoir characterization using only injection and production data like rates and pressures. Of these prominent methods, the two most widely used are the Capacitance Resistance Model (CRM) [85] and the Interwell Numerical Simulation Model with Front Tracking (INSIM-FT) [64].

The test model used to evaluate INSIM-FT [64] and CRM [85] is similar in structure and well arrangements to the test model earlier described in Section 4.3.7.2 (well shut-in test). The test model developed by Wanderley de Holanda [85] for evaluating the CRM approach is a 5-layer, 2-phase homogeneous model with constant porosity and permeability. The model contains oil and water with no free gas evolving during production. On the other hand, the test model developed by Guo and Reynolds [64] for evaluating the INSIM-FT approach is a single layer homogeneous model with constant

porosity and permeability. The model constructed by Guo and Reynolds [64] also contains oil and water with no free gas evolving during production.

4.3.8.1 CRM Approach vs. Proposed Method

The CRM approach utilized by Wanderley de Holanda [85] is a data-driven, model-free approach that characterizes reservoirs by studying the relationship between varying well injection and production rates. Like in an interference well test, CRM quantifies the relationship between any injector-producer pair by oscillating the injection rates at injectors and monitoring the rate response at producers as seen in Figure 4-80. Using only the injection and production data (rates and BHPs), CRM is capable of providing an approximate characterization of most petroleum reservoirs using so-called "connectivity maps". Several variants of the CRM exist in literature [86], [87], [88] and their applicability is dependent on the nature of the reservoir characterization problem one wishes to investigate. Additional information on how the CRM works can be found in [58], [89], [85] and [90].

Figure 4-80: The CRM Approach [90].

In order to compare the performance of our proposed method with the CRM employed by Wanderley de Holanda [85], a test model similar in structure and well arrangement to that described in Wanderley de Holanda [85] is constructed. A summary of both test model properties is provided in Table 4-10.

Table 4-10: Test model properties used for evaluating the CRM and our proposed method.

Properties	Test model used for CRM Approach [85]	Our test model
Number of grid blocks	33 x 33 x 5	20 x 20 x 5
Grid sizes (metres)	24 x 24 x 12	152 x 152 x 6
Injector-producer distance (metres)	260	1372
Porosity (%)	0.2	0.2
Horizontal permeability (mD)	200	275
Vertical permeability (mD)	20	27.5
Rock compressibility (bar^{-1})	1.4×10^{-5}	4.4×10^{-5}

Initial reservoir pressure (bar)	86	331
Initial water saturation	0.3	0.35
Initial oil saturation	0.7	0.65
End-point water relative permeability	0.3	1.0
End-point oil relative permeability	1.0	1.0

A side view of the test model used to evaluate the CRM is presented in Figure 4-81. The blue coloured region in Figure 4-81 is a low permeability region with a horizontal permeability of 1 mD and a vertical permeability of 0.1 mD. This blue coloured region acts as a flow barrier and isolates the injector (INJ2) and two producers (PROD1 and PROD3) from the rest of the field. This is their true model and the solution obtained from using a commercial reservoir simulator is specified as measured data which is what is needed by CRM to characterize a reservoir. It is also noteworthy to mention that a varying-injection waterflooding strategy is implemented with injection rates varying from 48 m^3/day (300 STB/day) to 401 m^3/day (2520 STB/day) on a monthly basis. All injectors are controlled by their injection rates. For the producers which are BHP-controlled, the minimum and maximum BHP alternating on a monthly basis is set between 8.3 bar (120 psi) and 12.5 bar (180 psi) respectively.

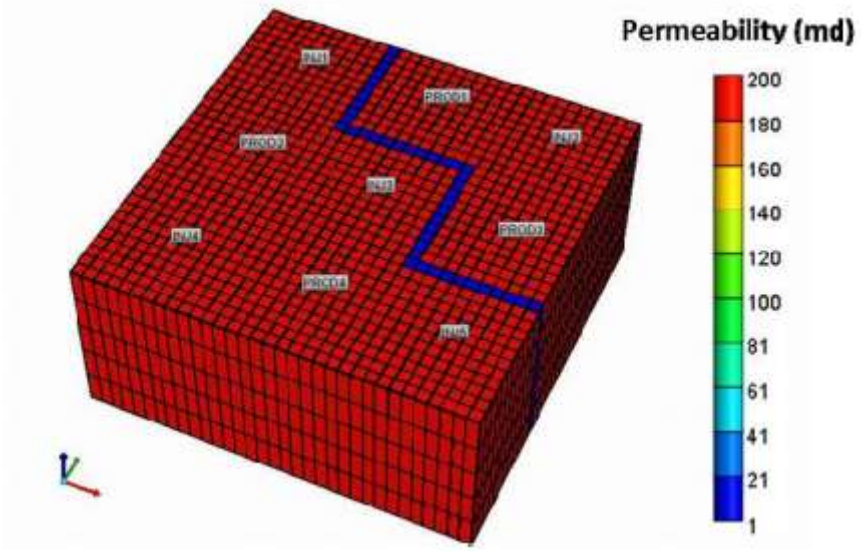

Figure 4-81: Permeability field of the test model used in evaluating the CRM highlighting the location of the flow barrier (in blue colouration) [85].

In an attempt to reproduce the test model and flow barrier described in Wanderley de Holanda [85], we constructed a test model using the properties described in Table 4-10. By dividing the field permeability by the permeability of the flow barrier in Wanderley de Holanda [85], a value of 5×10^{-3} is obtained which was assumed to be the fault transmissibility multiplier (MULTFLT) for the fault that was modelled into our test model. This fault is indicated by a thick black line isolating injector (INJ4) and producers (P2 and P4) from the rest of the field. Please note that different well names are used in

both models but the well arrangements are the same. A top and side view of our test model is shown in Figure 4-82. This is our true model. The solution of the true model is defined as measured data in the base model.

Compared to Wanderley de Holanda [85], we adopted a constant rate over-injection waterflooding strategy (VRR > 1). All injectors controlled by their water injection rates each injects 50000 barrels of water per day (approximately 7950 m^3/day) while all producers controlled by their combined oil and water rates each produces 40000 barrels of liquid per day (approximately 6350 m^3/day). The base model which is required as an input for UHM using the adjoint method does not contain fault information. Also, we assume that core data exists for all wells therefore the permeability and porosity values in grid blocks housing wells are not changed during UHM.

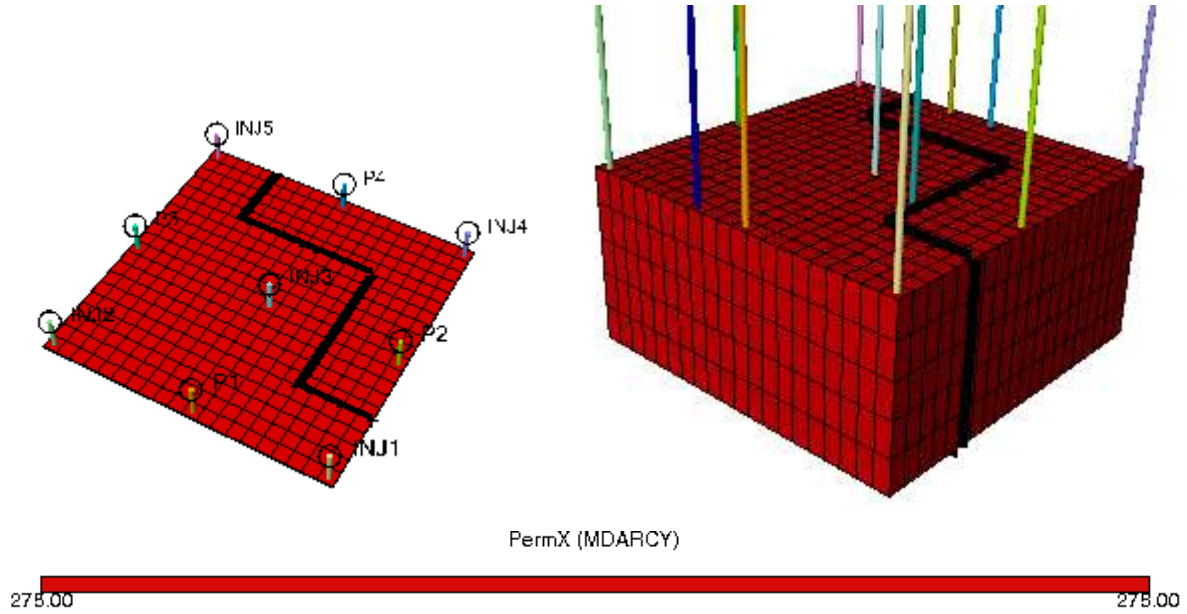

Figure 4-82: Top and side view of the permeability field of our true model with fault/flow barrier indicated by a thick black line.

According to Wanderley de Holanda [85], the connectivities ($f_{i,j}$) estimated for each injector-producer pair, the time constants (τ_j) and the productivity indices (J_j) for each producer are the main outputs for characterizing reservoirs using the CRM. The connectivities, time constants and productivity indices are defined as input parameters (or model parameters) for the history matching problem in order to obtain very good matches for well rates and BHPs. Time constants captures the time lag and attenuation of the system response (production rates) to the stimuli (fluctuating injection rates and BHPs). Connectivities are volume fractions of injected water that flows towards producers. With the connectivities, time constants and productivity indices determined via history matching, the presence of hidden reservoir features like faults and channels can be inferred. The connectivity, time constant and productivity index estimates according to Wanderley de Holanda [85] are shown in Table 4-11 and Table 4-12 respectively. Wanderley de Holanda [85] did not mention the optimization algorithm

used during history matching to determine the combination of connectivities, time constants and productivity indices values that minimizes the objective function. However, they made reference to the speed of the optimization process and this hints at the possible use of a non-gradient-based optimization algorithm.

Table 4-11: Connectivity estimates obtained using the CRM approach [85].

j \ i	INJ1	INJ2	INJ3	INJ4	INJ5
PROD1	0.021	0.518	0.000	0.068	0.092
PROD2	0.660	0.000	0.490	0.412	0.244
PROD3	0.000	0.482	0.000	0.117	0.101
PROD4	0.319	0.000	0.510	0.403	0.563
Sum	1.000	1.000	1.000	1.000	1.000

Table 4-12: Time constant and productivity index estimates obtained using the CRM approach [85].

Producers	τ_j	J_j
PROD1	29.63	12.71
PROD2	20.63	0.00
PROD3	35.96	16.29
PROD4	17.01	9.55

Figure 4-83 presents the connectivity map generated from Table 4-11 by Wanderley de Holanda [85]. As seen in Figure 4-83, connectivity between any injector-producer pair is indicated by a directional arrow. The larger the magnitude of these directional arrows, the more the connectivity existing between any injector-producer pair. From 4-83, one can clearly observe that injector INJ2 communicates with producers PROD1 and PROD3. Also, injectors INJ1 and INJ3 does not communicate with producers PROD1 and PROD3 since the fault of almost sealing nature isolates these producers from the rest of the field.

Injector INJ5 seems to contradict the true model by allowing slight communication with producer PROD3. This should not be the case as the fault is almost practically sealing. In other cases, some degree of communication can be visibly observed between injector INJ1 and producer PROD4 and between injector INJ5 and producer PROD2 despite the distance between them. One will expect the waterfront emanating from injectors INJ3 and INJ5 to cancel out, therefore preventing any form of communication between injector INJ5 and PROD2. In addition, only one connectivity map (Figure 4-83) is generated by Wanderley de Holanda [85] in order to infer the presence of the hidden flow barrier/fault. This connectivity map is generated by averaging the results across all 5 layers. In a model that is strongly heterogeneous, averaging the results obtained across all layers in order

to generate a connectivity map will introduce some bias when inferring hidden reservoir features. Finally, an approximate location and shape of the flow barrier (or fault) is not revealed by the connectivity map generated using CRM. The presence of the flow barrier is only inferred based on connectivities. The thick blue line in Figure 4-83 was inserted by Wanderley de Holanda [85] since they already knew what the flow barrier looked like in the true model.

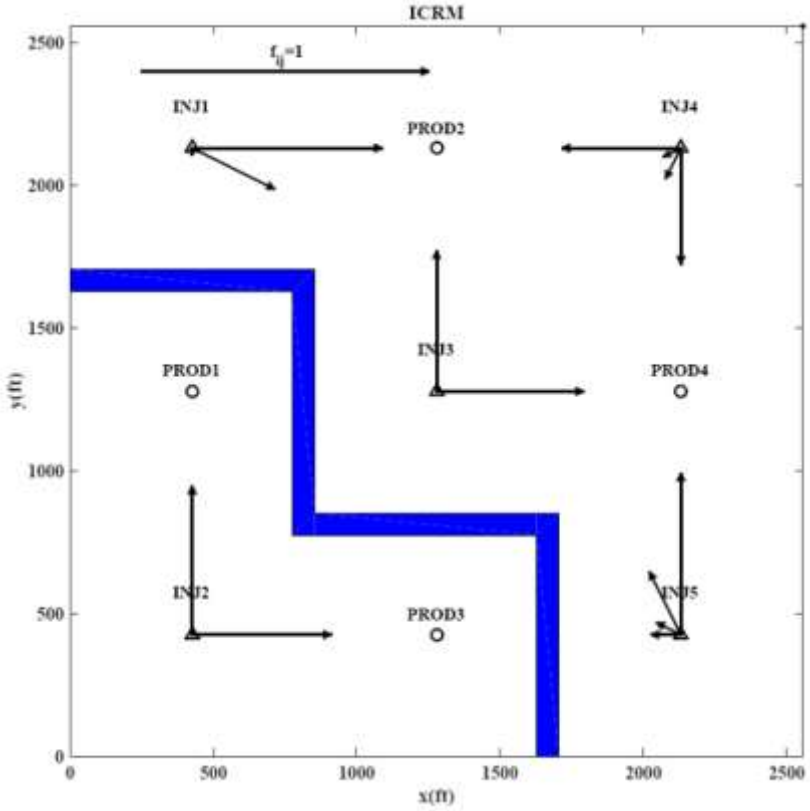

Figure 4-83: Connectivity map inferring fault location in thick blue line [85].

Using our proposed method, we begin by defining horizontal permeabilities (K_x & K_y) as model parameters prior to performing UHM. The uncertainty limits for the horizontal permeabilities is described by Equation (37) where $K_{x_{max}} = K_{y_{max}} = 275$ mD. In addition, we assumed that core data exists for all wells therefore the permeability values in grid blocks housing wells are unchanged.

By employing Equation (37) in the UHM stage, the progression of the objective function (Q) with increasing number of iterations is presented in Figure 4-84. A total of 450 iterations were executed in order to reach an optimal Q. This is so because the step size, μ_{K_x,K_y} = 10.75 mD^2, is utilized. As seen in Figure 4-84, the objective function value reduced by a factor of 1000 over the entire 450 iterations. In addition, a relatively long stagnation period (from the 31st to the 215th iteration) is observed in Figure 4-84. It appears that it took a couple of destabilizations to veer the optimization direction away from the local minima in which it got trapped. The small image in Figure 4-84 captures the objective function plot as a 3-D surface showing what the stagnation region can look

like. The 441th iteration was selected as our best-case since it delivered the lowest Q with an overall model error reduction value of 99.5%. If fewer than 215 iterations were executed using the same step size, then the objective function value would have been reduced by only a factor of 10 yielding an overall model error reduction value of 65.2% if 104th iteration was chosen as the best-case.

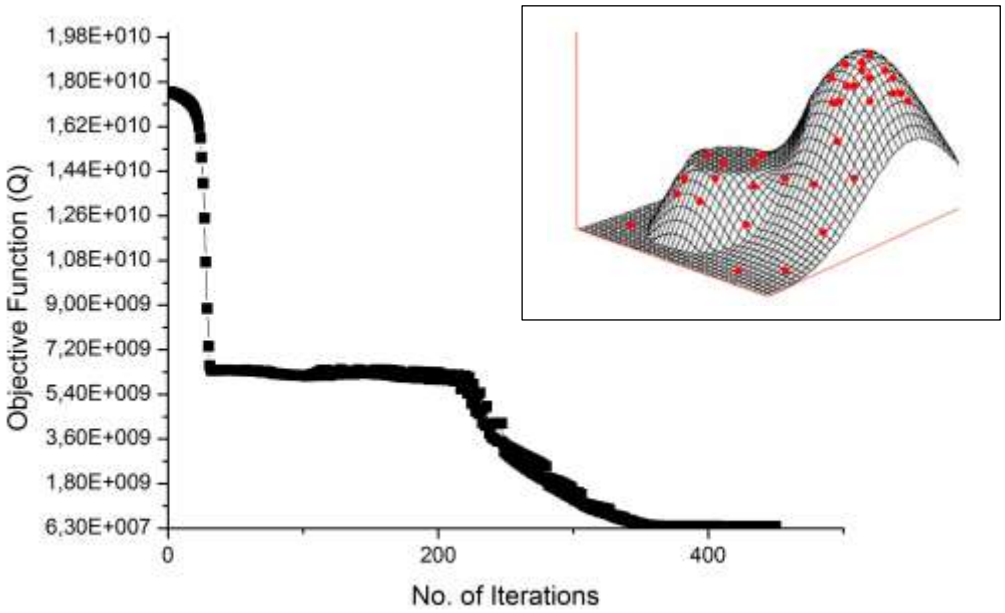

Figure 4-84: Objective function (Q) vs. number of iterations.

The model responses defined for this test are well water-cut (WWCT), well oil production rate (WOPR) and well bottom-hole flowing pressure (WBHP). Best-case results for the most offending model responses are presented in Figure 4-85. In addition, the R-squared values for all model responses generated for the best-case result obtained from UHM is presented in Table 4-13.

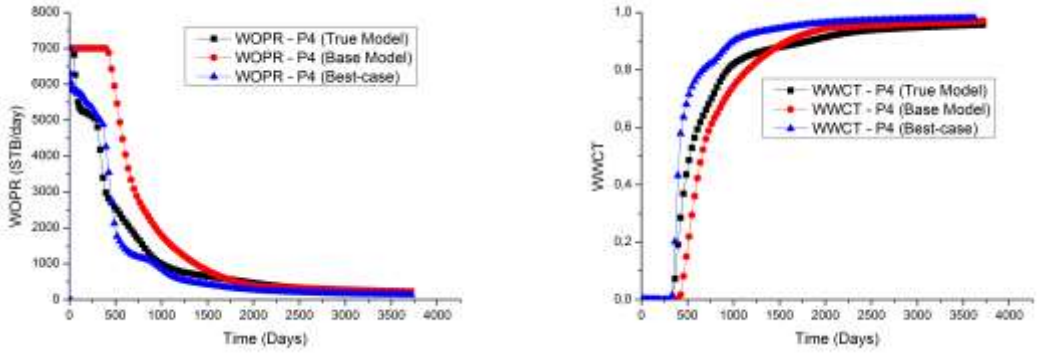

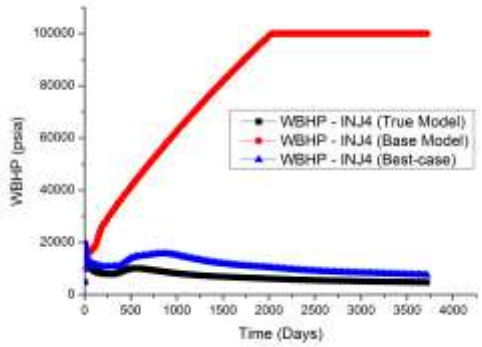

Figure 4-85: Best-case results for the most offending model responses after performing UHM.

Table 4-13: R-squared values for the best-case result obtained from UHM.

Well Name	WBHP	WWCT	WOPR
P1	99.7%	99.0%	99.4%
P2	99.9%	99.1%	99.3%
P3	99.7%	99.2%	99.7%
P4	99.9%	97.9%	97.5%
INJ1	99.8%	—	—
INJ2	99.8%	—	—
INJ3	99.8%	—	—
INJ4	98.5%	—	—
INJ5	99.8%	—	—
$R^2 \geq 97\%$; $R^2 < 97\%$			

In order to reveal the location of the hidden fault using our proposed method, the permeability ratio maps for the 1st and 3rd layer (see Figure 4-86 and Figure 4-87) is generated using Equation (39). The white-coloured region represents grid blocks with little or no change in permeability. Grid blocks with colours varying from light-yellow to purple identifies regions with extreme permeability reduction.

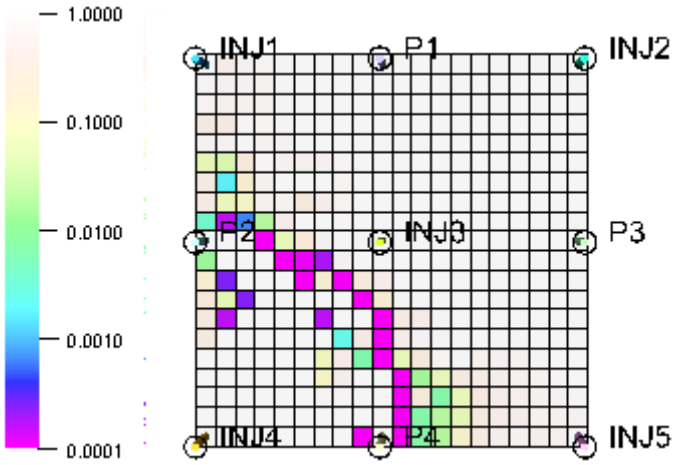

Figure 4-86: Permeability ratio map generated for the 1st layer.

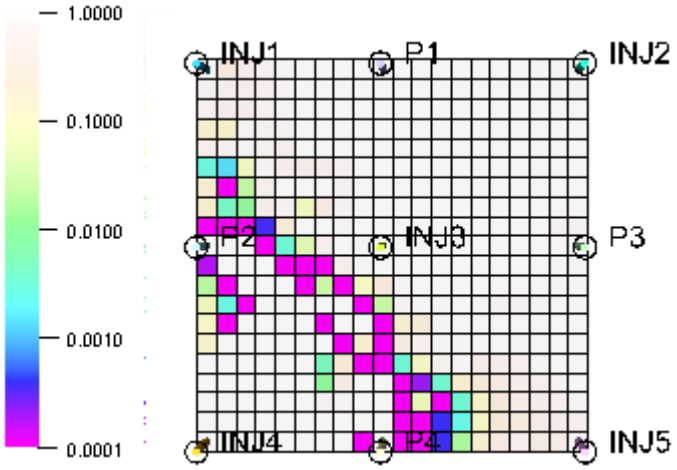

Figure 4-87: Permeability ratio map generated for the 3rd layer.

As seen in Figure 4-86 and Figure 4-87, the permeability in the grid blocks housing all wells are unchanged since we assumed that core data exists for all wells. This is indicated by the white-coloured grid blocks with permeability ratio values of 1.0. The expression provided in Equation (40) can be used to generate the fault indicator maps from Figure 4-86 and Figure 4-87.

Figure 4-88 and Figure 4-89 presents the fault indicator maps for the 1st and 3rd layer capturing the location and shape of the revealed fault in purple-coloured grid blocks. The threshold value that reveals the location of the hidden fault is γ_{fault} = 5×10^{-3} (which is actually the fault transmissibility multiplier of the fault in the true model). The location of the revealed fault (the set of connecting purple-coloured grid blocks) is in agreement with the fault in the true model (in thick black line) as seen in Figure 4-88 and Figure 4-89 respectively. However, the shape of the revealed fault is slightly different from the fault in the true model.

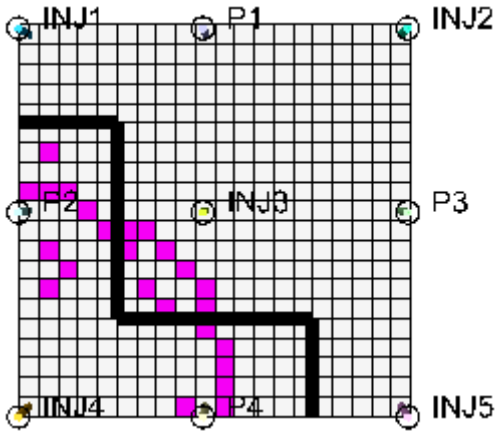

Figure 4-88: Fault indicator map for the 1st layer generated at γ_{fault} = 5×10-3.

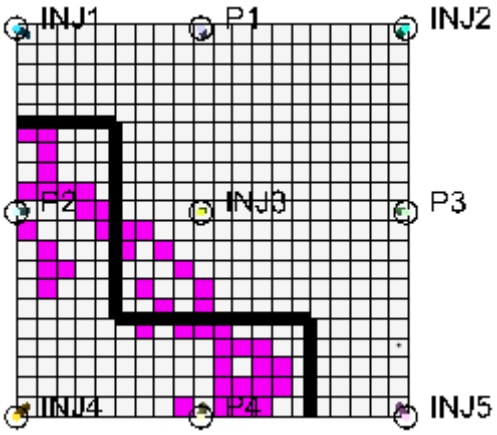

Figure 4-89: Fault indicator map for the 3rd layer generated at γ_{fault} = 5×10-3.

It is important to mention that despite implementing a constant rate over-injection waterflooding strategy which is not supported by CRM, the proposed method proved its effectiveness in providing an approximate location and shape of the fault/flow barrier which was originally hidden in the base model. In addition, rather than averaging the results across all layers in order to generate a connectivity map as required by CRM, a fault indicator map can be generated for each layer present in the model using our proposed method.

4.3.8.2 INSIM-FT Approach vs. Proposed Method

The INSIM-FT approach developed by Guo and Reynolds [64] characterizes petroleum reservoirs as a set of connective flow volumes as shown in Figure 4-90. In addition, INSIM-FT is a reservoir simulator of its own that solves pressure equations using the IMPES approach (IMplicit Pressure Explicit Saturation) to compute pressures and saturations at well nodes. The Buckley-Leverett equation combined with a front-tracking method [67] is used to determine saturation profiles (pseudo-streamlines) along connections between well pairs. This process allows the IMSIM-FT to handle actions that can induce significant changes in flow pattern over time (e.g. injector-to-producer conversion etc.).

The inclusion of the front-tracking method [67] also ensures improved inter-well connectivity estimation and support for reservoir without injectors (aquifer-dominated reservoirs). Similar to the CRM, injection and production data are required to estimate model parameters such as transmissibilities ($T_{i,1}, T_{i,2}, T_{i,3}$) between well pairs, pore volume ($V_{p_{i,1}}, V_{p_{i,2}}, V_{p_{i,3}}$) between well pairs and the field or regional relative permeability curve(s). The transmissibility and pore volume between well pairs is analogous to inter-well permeability and porosity. The INSIM-FT approach requires no prior knowledge of the field geology and petrophysical properties in order to characterize a reservoir.

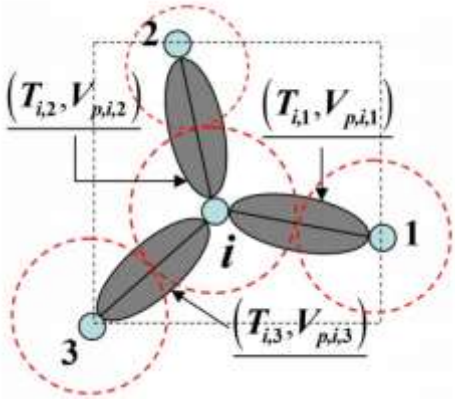

Figure 4-90: Connective flow units between well pairs [64].

In Figure 4-91, two true models are presented: the model formulated by Guo and Reynolds [64] and our adaptation of their model. As seen in Figure 4-91, Guo and Reynolds [64] introduced a sealing fault in their true model by deactivating certain number of grid blocks. We chose to introduce a real sealing fault (in thick black line) in order to retain the same oil in place in both our true model and base model.

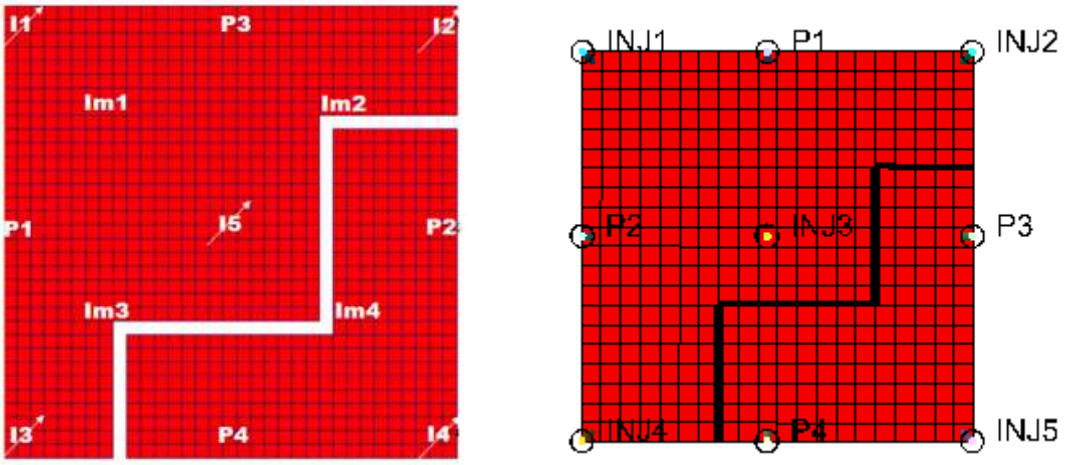

True Model (Guo and Reynolds [64]) **Our True Model**

Figure 4-91: Comparison between true models.

Both test models are similar in structure and well arrangement. A summary of both test model properties is provided in Table 4-14. The solution of their true model obtained from using a commercial reservoir simulator is specified as measured data which is all that is required by INSIM-FT in order to characterize petroleum reservoirs. Although, a varying-injection waterflooding strategy is implemented in their test model, Guo and Reynolds [64] stated that the INSIM-FT could also be used with models undergoing a constant rate water injection strategy. No recent publication has been made to that effect. All injectors are controlled by their water injection rates although the injection rate data were not specified. For the producers which are BHP-controlled, a constant BHP value of 17 bar is assigned.

Compared to Guo and Reynolds [64], we adopted a constant rate over-injection strategy (VRR > 1). All injectors controlled by their water injection rates each injects 10000 barrels of water per day (approximately 1590 m^3/day) while all producers controlled by their combined oil and water rates each produces 7000 barrels of liquid per day (approximately 1110 m^3/day). The base model which is required as an input for UHM using the adjoint method does not contain fault information. Also, we assume that core data exists for all wells therefore the permeability and porosity values in grid blocks housing wells are not changed during UHM.

Table 4-14: Test model properties used for evaluating the INSIM-FT and our proposed method

Properties	Test model used for INSIM-FT Approach [64]	Our test model
Number of grid blocks	33 x 33 x 1	20 x 20 x 1
Grid sizes (metres)	24 x 24 x 59	152 x 152 x 6
Injector-producer distance (metres)	260	1372
Porosity (%)	0.2	0.2
Horizontal permeability (mD)	200	275
Vertical permeability (mD)	20	27.5
Rock compressibility (bar^{-1})	1.4×10^{-5}	4.4×10^{-5}
Initial reservoir pressure (bar)	86	331
Oil viscosity (cp)	1.0	1.3
Water viscosity (cp)	1.0	0.3
Production period (years)	6	10

According to Guo and Reynolds [64], imaginary wells denoted by "Im1, Im2, Im3 & Im4" (see Figure 4-91) placed between well pairs increases the number of possible flow paths travelled by the injected water and prevents direct injector-injector and producer-producer connections. These imaginary wells are neither injectors nor producers and thus their total flow rate at any given time is always zero. Similar to the CRM approach,

connectivity maps are also required by INSIM-FT to infer the presence of hidden reservoir features like faults and channels. These connectivity maps are designed a priori describing how wells are connected to one another prior to the commencement of history matching. Wells not defined and connected in the connectivity map are not considered in the history matching phase. Only producers are history-matched since the true water injection rates and pressures are specified in INSIM-FT for all injectors. Furthermore, Guo and Reynolds [64] reported that history matching is performed using the INSIM-FT coupled with an ensemble smoother with multiple data assimilation (ES-MDA) [68] starting with 250 initial realizations of prior model parameters (i.e. transmissibility, pore volume and relative permeability parameters). All 250 initial realizations of relative permeability curves prior to history matching is presented in Figure 4-92. The red line represents the true model relative permeability curves and the blue lines represents all 250 initial realizations of relative permeability curves.

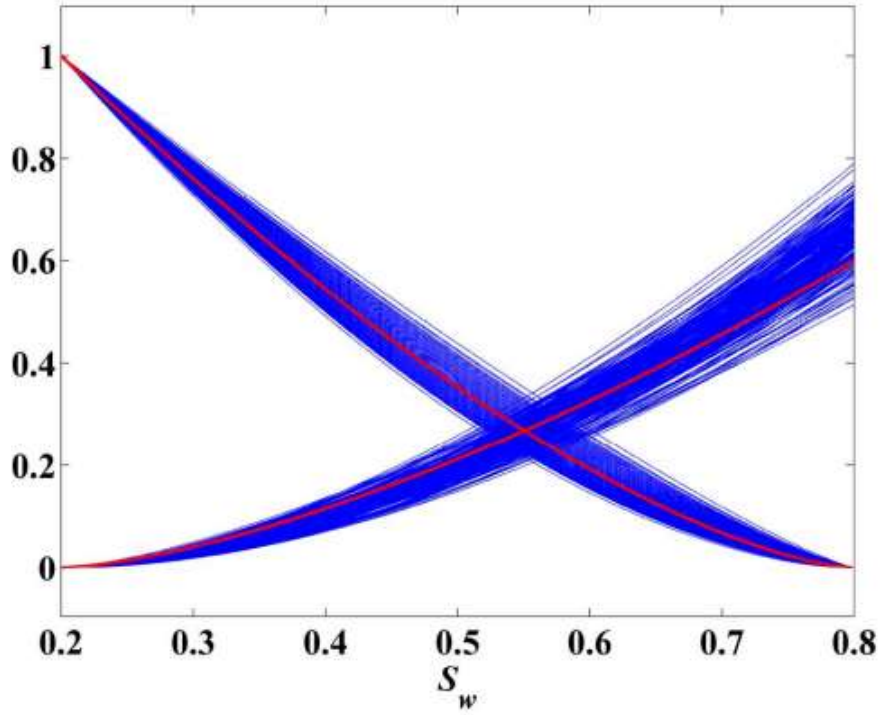

Figure 4-92: All 250 initial realizations of relative permeability curves [64].

History-match results for WOPR for producers isolated by the sealing fault are presented in Figure 4-93. The estimated WOPR obtained from all 250 prior INSIM-FT models of different model parameters are displayed in grey lines. The red circles with a red line running through it are the true values of WOPR obtained from their true model. The red line without the red circles (beginning after 2000 days) represents the prediction phase which is not our focus here.

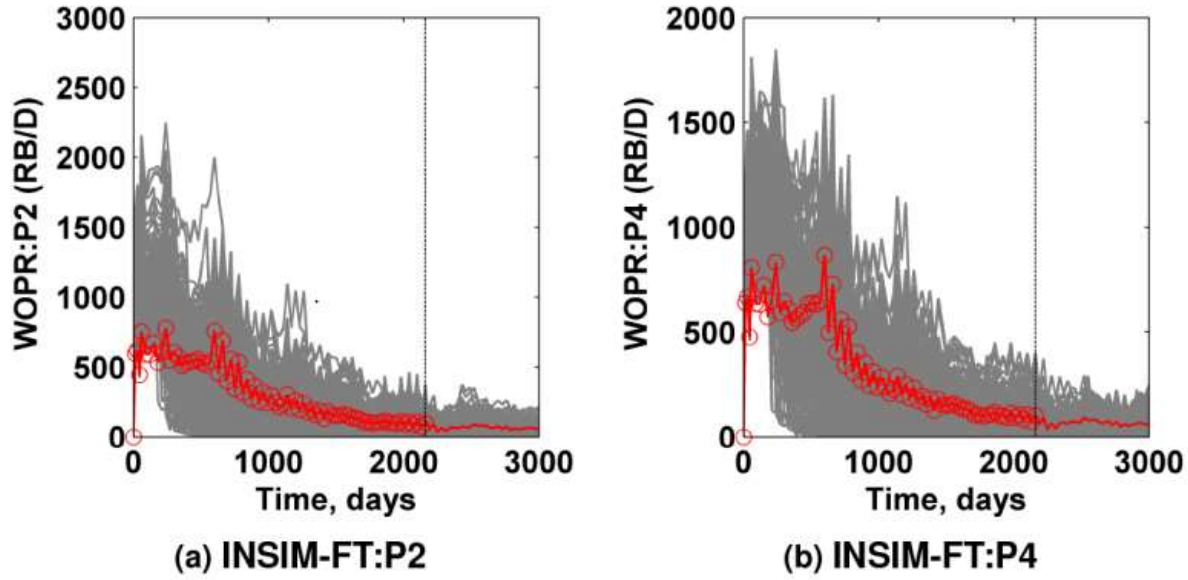

Figure 4-93: Estimated WOPR obtained for all 250 prior INSIM-FT models [64].

The multiple best-case INSIM-FT models that delivered good history-match for WOPR for the producers isolated by the sealing fault are shown in Figure 4-94. Also, the multiple best-case relative permeability curves (in blue) that delivered the best-case history-match results is shown in Figure 4-95. The red line represents the true model relative permeability curves.

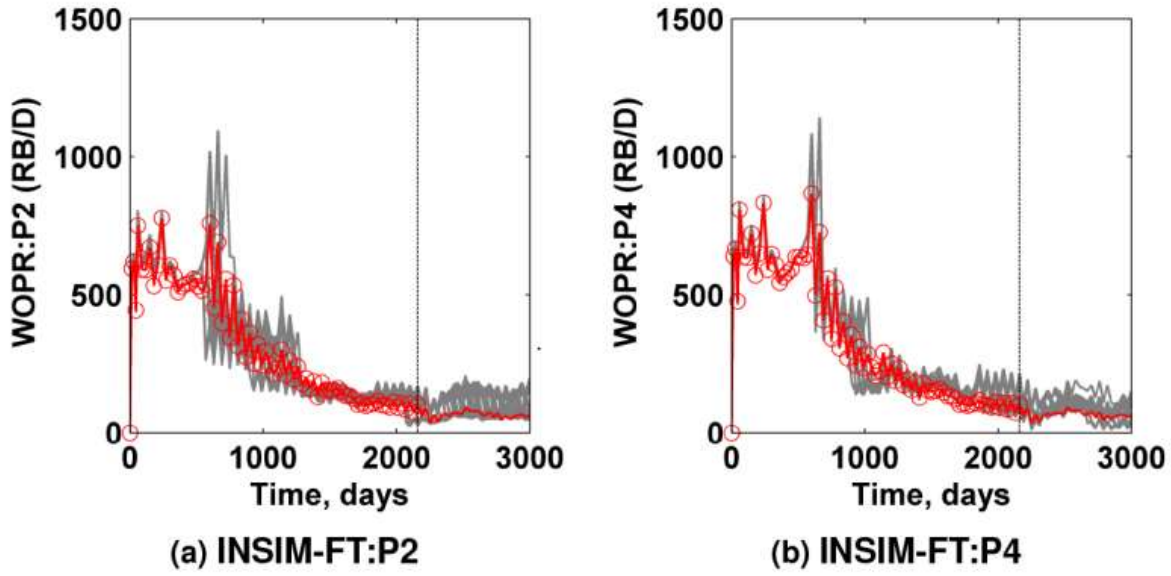

Figure 4-94: Multiple best-case INSIM-FT models capturing WOPR matching [64].

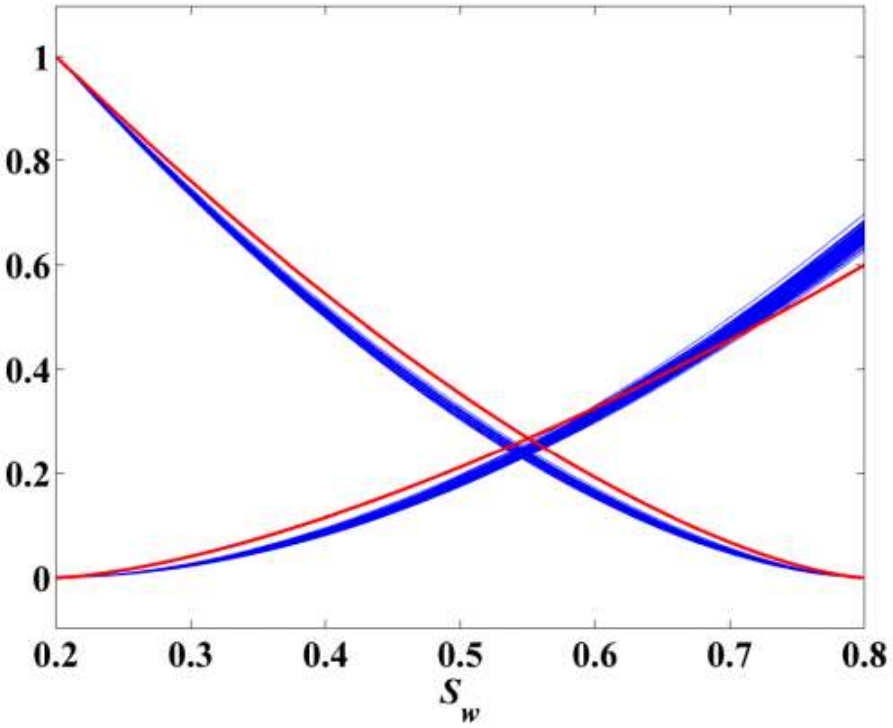

Figure 4-95: Multiple best-case relative permeability curves [64].

Only model responses related to WOPR are history-matched. The WWIR for each injector is not history-matched nor defined as part of the history matching objective function since the true water injection rates are specified in INSIM-FT for all injectors. Also, it is unknown if the WWCT for all producers is considered as model responses to be included in the objective function. No history match plots were presented for WWCT.

Figure 4-96 presents the inter-well connectivity map generated using their history-match results. The length of the red bar connotes the magnitude of connectivity between well pairs. The direction of the red bar is indicative of communication between well pairs. In Figure 4-96, one can observe that injectors INJ2, INJ3 and INJ5 does not communicate with producers P2 and P4. Similar to the CRM approach, their approach inferred the possible location of the sealing fault but failed to provide an approximate shape of the fault.

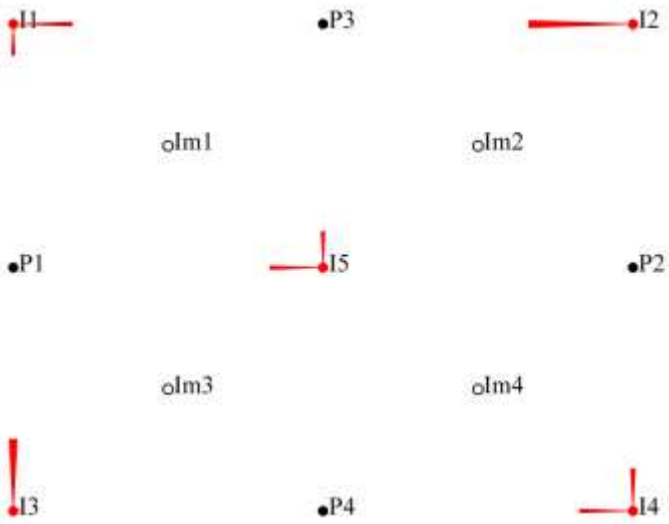

Figure 4-96: Connectivity map generated with the INSIM-FT approach [64].

Again, we evaluated the effectiveness of the proposed method using a test model (see Figure 4-91) that is quite similar to that used by Guo and Reynolds [64]. The model parameters defined for the problem of revealing the hidden fault prior to performing UHM are the horizontal permeabilities (K_x & K_y). The uncertainty limits for the horizontal permeabilities is described by Equation (37) where $K_{x_{max}} = K_{y_{max}} = 275$ mD. In addition, we assumed that core data exists for all wells therefore the permeability values in grid blocks housing wells are unchanged.

By employing Equation (37) in the UHM stage, the progression of the objective function (Q) with increasing number of iterations is presented in Figure 4-97. A total of 400 iterations were executed in order to reach an optimal Q. This is so because the step size, μ_{K_x,K_y} = 10.75 mD^2, is utilized. As seen in Figure 4-97, the objective function value reduced by a factor of 1000 over the entire 400 iterations. The 357th iteration was selected as our best-case since it delivered the lowest Q with an overall model error reduction value of 99.6%.

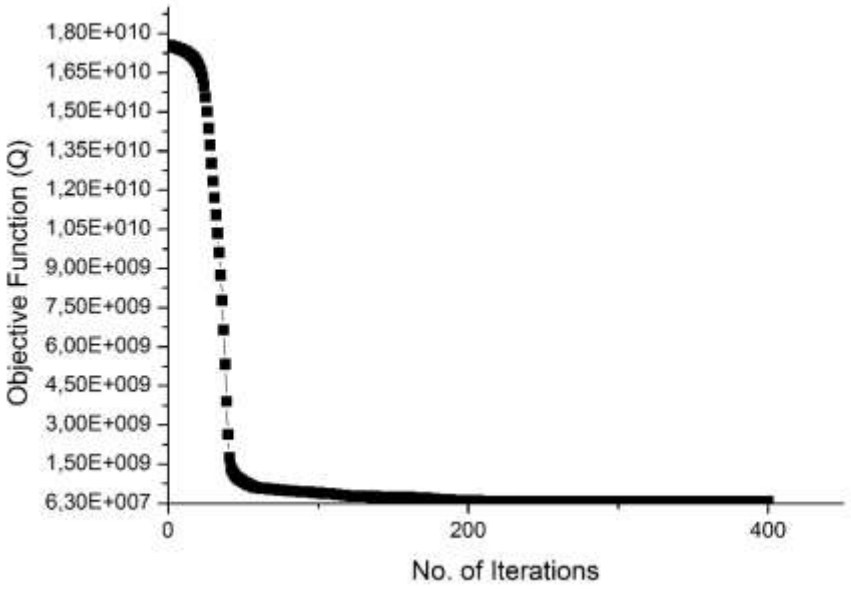

Figure 4-97: Objective function (Q) vs. number of iterations.

The model responses defined for this test are well water-cut (WWCT), well oil production rate (WOPR) and well bottom-hole flowing pressure (WBHP). Best-case result for the most offending model responses are presented in Figure 4-98. In addition, the R-squared values for all model responses generated for the best-case result obtained from UHM is presented in Table 4-15.

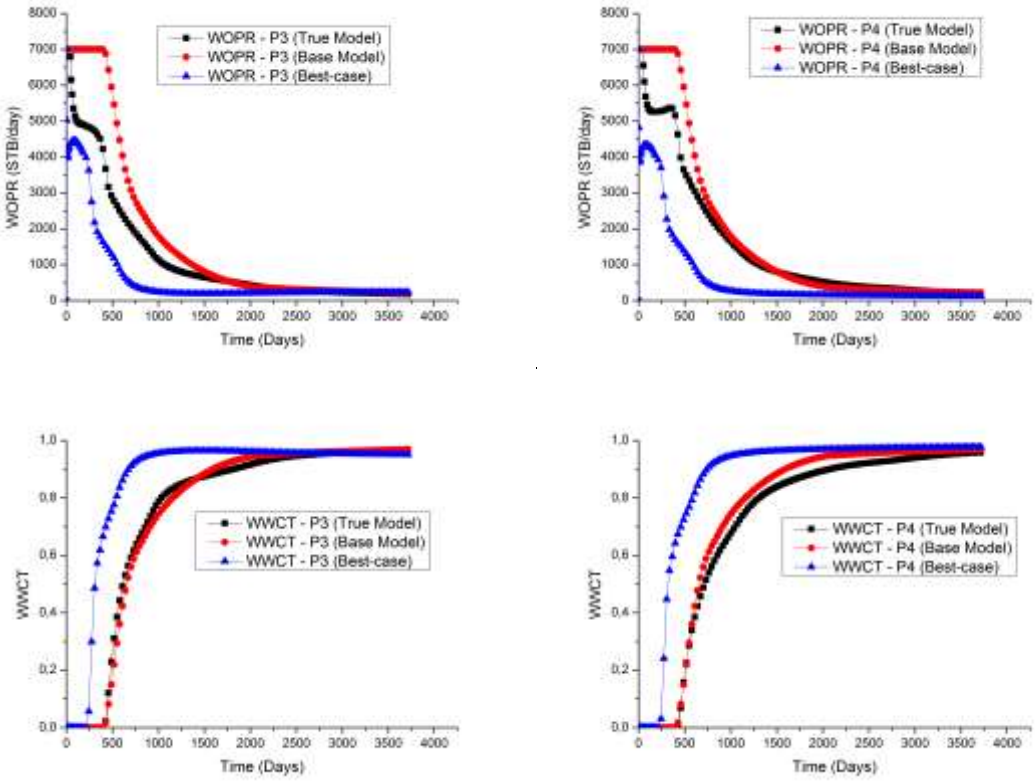

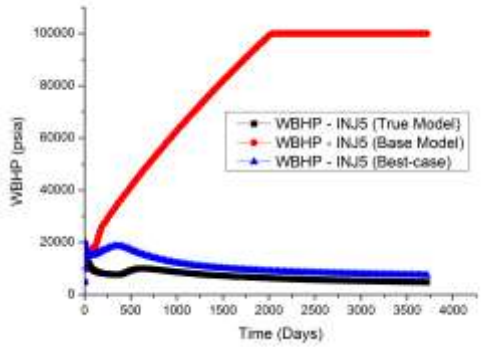

Figure 4-98: Best-case results for the most offending model responses after performing UHM.

Table 4-15: R-squared values for the best-case result obtained from UHM.

Well Name	WBHP	WWCT	WOPR
P1	99.7%	99.0%	99.4%
P2	99.7%	99.1%	99.3%
P3	99.9%	99.2%	96.2%
P4	99.9%	98.3%	97.2%
INJ1	99.8%	—	—
INJ2	99.8%	—	—
INJ3	99.7%	—	—
INJ4	98.8%	—	—
INJ5	90.6%	—	—
$R^2 \geq 97\%$; $R^2 < 97\%$			

In order to reveal the location of the hidden fault using our proposed method, the permeability ratio map (see Figure 4-99) for the single producing layer is generated using Equation (39). The white-coloured region represents grid blocks with little or no change in permeability. Grid blocks with colours varying from light-green to dark blue and purple identifies regions with extreme permeability reduction.

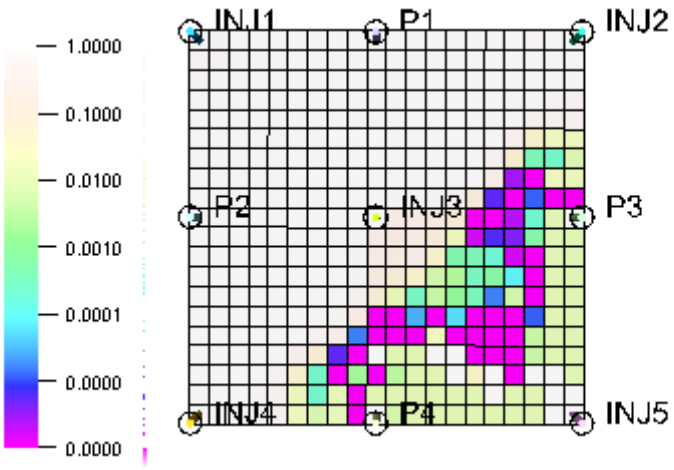

Figure 4-99: Permeability ratio map generated.

As seen in Figure 4-99, the permeability in the grid blocks housing all wells are unchanged since we assumed that core data exists for all wells. This is indicated by the white-coloured grid blocks with permeability ratio values of 1.0. The expression provided in Equation (40) can be used to generate the fault indicator map from Figure 4-99. Figure 4-100 presents the fault indicator map for the single producing layer capturing the location and shape of the revealed fault in purple-coloured grid blocks. The threshold value that reveals the location of the hidden fault is γ_{fault} = 5×10^{-6}. The location of the revealed fault (the set of connecting purple-coloured grid blocks) is in agreement with the fault in the true model (in thick black line) as seen in Figure 4-100. In addition, the shape of the revealed fault is very much similar to the fault in the true model.

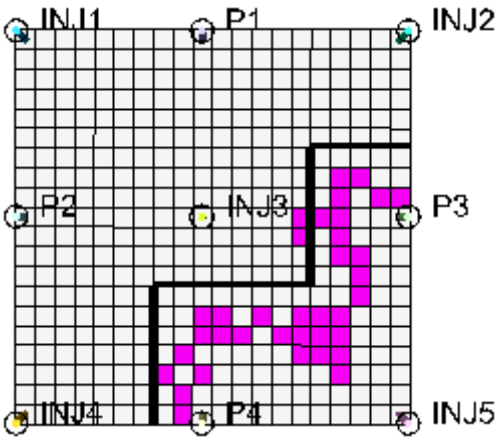

Figure 4-100: Fault indicator map generated at γ_{fault} = 5×10^{-6}.

In summary, the proposed method proved its superiority over the CRM and INSIM-FT approaches by providing an approximate location and shape of the fault which were originally hidden in the base model. Based on the performance comparison assessment between the CRM, INSIM-FT and our proposed method and with additional information provided in literature, Table 4-16 presents a detailed summary of key strong and weak points of each method for improving reservoir characterization.

Table 4-16: Comparing state-of-the-art methods with the proposed method for improving reservoir characterization

CRM Approach	INSIM-FT Approach	Proposed Approach
Suitable for Water & Gas flooding	Waterflooding; no reported Gas flooding test	Waterflooding; yet to be tested with Gas flooding
—	—	Not efficient for measurement errors > ±15%
Handles varying injection rates only	Handles constant and varying injection rates	Handles constant and varying injection rates
Injector must exist in the model (Aquifer not supported)	Aquifer treated as a virtual well node (e.g. a virtual injector)	Can be applied in aquifer-dominated reservoirs without injectors
Cannot handle models experiencing changes in flow patterns over time (e.g. injector-to-producer conversion or vice versa etc.)	Handles injector-to-producer conversion or vice versa and wells shut-in for a short or long time	Handles injector-to-producer conversion or vice versa, wells shut-in for a short or long time and the addition of new wells over time
Far less computational effort required	Far less computational effort required	Computationally intensive for large field problems
Reservoir simulator not required	Reservoir simulator not required	Reservoir simulator required
Prior knowledge of reservoir geology not required. Only injection and production data are required	Prior knowledge of reservoir geology not required. Only injection and production data are required	A starting reservoir model together with available injection and production data are required
Only suited for varying-injection waterflooding strategy	Suited for under-injection, par-injection, over-injection and varying-injection waterflooding strategy	Suited for under-injection, par-injection, over-injection and varying-injection waterflooding strategy
Location of hidden reservoir features are approximately inferred using so-called "connectivity maps"	Location of hidden reservoir features are approximately inferred using so-called "connectivity maps"	Location of hidden reservoir features are revealed using reservoir feature indicator maps
Only one connectivity map is generated for the entire model	Only one connectivity map is generated for the entire model	Reservoir feature indicator maps are generated for

		each reservoir layer in the model
No information on shape of hidden reservoir feature(s)	No information on shape of hidden reservoir feature(s)	An approximate location and shape of hidden reservoir feature is revealed
No imaginary well(s) needed	Requires imaginary wells for front-tracking purposes	No imaginary well(s) needed
Limited to vertical wells only	Supports vertical and horizontal wells. An horizontal well is defined as multiple vertical wells	Support various types of well architectures (vertical, horizontal, slanted wells etc.)
They are mostly applied to history matching problems with inter-well connectivity issues. In other words, they are only used to infer the presence of faults and channels in reservoir models	Also applied in history matching problems with inter-well connectivity issues	Can be applied to history matching problems to reveal the approximate location and/or shape of faults, channels, fractures and vertical or non-vertical communication

4.4 Development of Reservoir Feature Detection Algorithms

Based on the numerous case examples and case studies provided in Section 4.3, a proposed catalogue for improving reservoir characterization in reservoir simulation models is created that takes into account model parameters like horizontal permeability, vertical permeability and porosity which are the main drivers for revealing certain types of reservoir features. The key model parameter(s) which are required to reveal certain reservoir features were deduced as a result of extensive and rigorous evaluations using a handful of reservoir models containing various types of reservoir features. Some of these evaluations are presented in Section 4.3.

Table 4-17: Proposed catalogue for improving reservoir characterization in reservoir simulation models using our proposed method.

Main Drivers →	Kx	Ky	Kz	Phi
Hidden Reservoir Feature to be Revealed ↓				
Fault	x	x		
Channel	x	x	x	
Oil Initially in Place (OIIP)				x
Bottom-drive Aquifer			x	x
Vertical Communication between Zones			x	

Structure/Geometry Issues				x
Fractures	x	x	x	
Wrong Permeability Distribution	x	x	x	
Wrong Porosity Distribution				x
Hard-to-match wells close to reservoir boundary				x

Using the proposed catalogue presented in Table 4-17 and an in-depth assessment of numerous case examples tested, a collection of reservoir feature detection algorithms are developed for some of these reservoir features. The development of these algorithms facilitates easier identification of hidden reservoir features in any reservoir model. The premise behind the development of these algorithms stemmed from the differences in threshold values (γ) required to reveal hidden reservoir features as observed from aforementioned case examples reported in Section 4.3. By utilizing the range of threshold values (γ) required to reveal a particular reservoir feature, these simple and effective algorithms combined with some heuristic approach were formulated.

4.4.1 Fault Detection Algorithm

The fault detection algorithm is formulated based on numerous tests performed with the goal of revealing sealing faults. The fault detection algorithm consists of three parts. The first part requires the generation of the permeability ratio map (PERM Ratio Map). K_z is exempted from the fault detection algorithm since its influence in revealing hidden fault is practically negligible even in multi-layered reservoir models. This assertion was validated over the course of numerous tests performed. The second part enables the generation of a fault indicator map for each reservoir layer using a simple and effective algorithm to reveal hidden fault location and shape from the permeability ratio map. The third part of the fault detection algorithm utilizes a heuristic approach to determine if a revealed fault is sealing or non-sealing. Typical ranges for γ_{fault} is 0.3 or lower.

$$PERM\ Ratio\ Map = \frac{(Kx * Ky)_{best\ case}}{(Kx * Ky)_{base\ case}}$$

$$Fault\ Indicator\ Map = if\ (PERM\ Ratio\ Map > \gamma_{fault});\ return\ (1.0);\ else\ return\ (\gamma_{fault})$$

$$Estimating\ degree\ of\ sealingness\ (MULTFLT) = if\ (\gamma_{fault} < 10^{-2});\ set\ MULTFLT = 0.0;\ else\ set\ MULTFLT = \gamma_{fault}$$

4.4.2 Channel/Fracture Detection Algorithm

The detection of channel and fracture location in reservoir simulation models is possible using the channel/fracture detection algorithm. The channel/fracture detection algorithm also consists of three parts. The first part requires the generation of the permeability ratio map. Unlike the fault detection algorithm, K_z plays a significant role

in revealing hidden channels/fractures especially in multi-layered reservoir models. The second part enables the generation of a channel/fracture indicator map per reservoir layer for revealing the location of channels/fractures. The third part utilizes a heuristic approach to estimate the permeability multiplier value that must be multiplied by the base-case K_x, K_y & K_z arrays in the region where the channel/fracture is revealed in order to estimate channel and fracture permeability in that region. Typical ranges for $\gamma_{ch./fr.}$ is 1.6 or higher.

$$PERM\ Ratio\ Map = \frac{(Kx * Ky * Kz)_{best\ case}}{(Kx * Ky * Kz)_{base\ case}}$$

$$Channel/Fracture\ Indicator\ Map = if\ (PERM\ Ratio\ Map > \gamma_{ch./fr.});\ return\ (max.of\ PERM\ Ratio\ Map); else\ return\ (1.0)$$

$$Estimating\ permeability\ multiplier\ (KMULT) = if\ \left(\gamma_{ch./fr.} < 10^{0.2}\right); set\ KMULT = 1.0; else\ set\ KMULT = \gamma_{ch./fr.}$$

4.4.3 Aquifer Detection Algorithm

The detection of aquifer presence (especially bottom-drive aquifers) is possible using the aquifer detection algorithm. The aquifer detection algorithm consists of three parts. The first part requires the generation of the vertical permeability (K_z) and porosity (ø) ratio map as one entity. The second part enables the generation of an aquifer indicator map for identifying signature patterns that should exist if an aquifer or water body is hidden in the reservoir simulation model. When identifying the location of a hidden aquifer or water body, it is important to observe constant or increasing $Kz * \emptyset$ product from the layer of first well sighting from the top of the formation to the layer where the oil-water contact lies in the reservoir simulation model. If such signature pattern is observed, then there is a very strong possibility that a bottom-drive aquifer or a water body is hidden in the reservoir simulation model. The third part utilizes a heuristic approach to confirm the existence of a hidden aquifer or hidden water body in the reservoir simulation model. "Aqu.Ind. = 0" means that no hidden aquifer or water body exist in the model and "Aqu.Ind. = 1" means that a hidden aquifer or water body exist in the model. Typical ranges for $\gamma_{aquifer}$ is 1.3 or higher. *Please note that the aquifer indicator map is only used to infer the existence of an aquifer or water body. It cannot reveal the precise location of hidden aquifers or water bodies in reservoir simulation model.*

$$PERMZ\_PORO\ Ratio\ Map = \frac{(Kz * \emptyset)_{best\ case}}{(Kz * \emptyset)_{base\ case}}$$

$$Aquifer\ Indicator\ Map = if\ (PERMZ\_PORO\ Ratio\ Map > \gamma_{aquifer});\ return\ (max.of\ PERMZ\_PORO\ Ratio\ Map);\ else\ return\ (1.0)$$

$$Confirming\ existence\ of\ aquifer\ or\ water\ body = if\ \left(\gamma_{aquifer} < 10^{0.1}\right);\ set\ Aqu.Ind. = 0;\ else\ set\ Aqu.Ind. = 1$$

4.4.4 Vertical Communication Detection Algorithm

The detection of vertical communication between layers (e.g. accidental fracturing in vertical direction into a shale zone) is possible using the vertical communication detection algorithm. The vertical communication detection algorithm consists of three parts. The first part requires the generation of the permeability ratio map (PERM Ratio Map). The second part enables the generation of a vertical communication indicator map for each reservoir layer in order to reveal layers that communicate with one another. The third part utilizes a heuristic approach to estimate the K_z multiplier value that must be multiplied by the base-case K_z array in the region where vertical communication is revealed in order to estimate K_z permeability in that region. Typical ranges for $\gamma_{vert.comm.}$ is 1.6 or higher.

$$PERM\ Ratio\ Map = \frac{(Kz)_{best\ case}}{(Kz)_{base\ case}}$$

$$Vert.Comm.Indicator\ Map = if\ (PERM\ Ratio\ Map > \gamma_{vert.comm.});\ return\ (max.of\ PERM\ Ratio\ Map);\ else\ return\ (1.0)$$

$$Estimating\ Kz\ multiplier\ (KzMULT) = if\ (\gamma_{vert.comm.} < 10^{0.2});\ set\ KzMULT = 1.0;\ else\ set\ KzMULT = \gamma_{vert.comm.}$$

4.4.5 Non-Vertical Communication Detection Algorithm

The detection of non-vertical communication between reservoir layers (e.g. identifying a shale or non-permeable zone) is possible using the non-vertical communication detection algorithm. The non-vertical communication detection algorithm consists of three parts. The first part requires the generation of the permeability ratio map (PERM Ratio Map). The second part enables the generation of the non-vertical communication indicator map per reservoir layer in order to reveal non-communicating layers. The third part utilizes a heuristic approach to estimate the K_z multiplier value that must be multiplied by the base-case K_z array in the region where non-vertical communication is revealed in order to estimate K_z permeability in that region. Typical ranges for $\gamma_{non-vert.comm.}$ is 0.01 or lower.

$$PERM\ Ratio\ Map = \frac{(Kz)_{best\ case}}{(Kz)_{base\ case}}$$

$$Non-Vert.Comm.Indicator\ Map = if\ (PERM\ Ratio\ Map > \gamma_{non-vert.comm.});\ return\ (1.0);\ else\ return\ (\gamma_{non-vert.comm.})$$

$$Estimating\ Kz\ multiplier\ (KzMULT) = if\ (\gamma_{vert.comm.} < 10^{-2});\ set\ KzMULT = 0.0;\ else\ set\ KzMULT = \gamma_{vert.comm.}$$

4.5 Validation of Hidden Reservoir Feature Location and Shape using Adjoint-derived Sensitivities

Adjoint-derived sensitivities obtained alongside with the best-case permeability and/or porosity arrays from UHM can be used to validate results obtained using the formulated reservoir feature detection algorithm. To demonstrate the potency of revealing hidden reservoir features using adjoint-derived sensitivities for permeability and/or porosity, two examples are presented. The first example can be considered as a continuation of Case Example 2 reported in Section 4.3.2. In the first example, an attempt is made to validate the location and shape of the revealed X-like channels with the adjoint-derived sensitivity for model parameter K_x. In the second example, the location of a hidden fault revealed using the fault indicator map and the adjoint-derived sensitivity for K_x and K_y are compared. The lines of MATLAB code written for interpreting adjoint-derived sensitivities is available in Appendix B.

4.5.1 Case Example 2: Revealing Channels using K_x Adjoint Sensitivity

The best-case adjoint-derived sensitivity for model parameter K_x obtained for Case Example 2 is presented in Figure 4-101. K_x and K_y adjoint sensitivities are very much similar and this is the reason why the K_x adjoint sensitivity alone is shown. Though the adjoint-derived sensitivity for K_x shares similar resemblance with the channel indicator map presented in Figure 4-16, information about the actual permeability values for the revealed channel can only be obtained using the channel detection algorithm.

Typically, adjoint-derived sensitivities for any optimization problem can be positive, negative or zero. In Figure 4-101, grid blocks with zero sensitivity value suggests that the (present) grid block property value has no influence on the objective function. In other words, retaining the K_x values for these grids will not influence the objective function. A grid block with a positive sensitivity value suggests a decrease in the grid block property value (e.g. decreasing K_x for that grid block) in order to reduce the objective function. The white X marker in Figure 4-101 and Figure 4-102 identifies the location of all 4 vertical injectors (INJ1, INJ2, INJ3 & INJ4) while the white circle marker identifies the location for the vertical producer (P5). The best-case K_z adjoint sensitivity

is also not shown here because all grid blocks had zero values. This is simply because Case Example 2 is a single layer model.

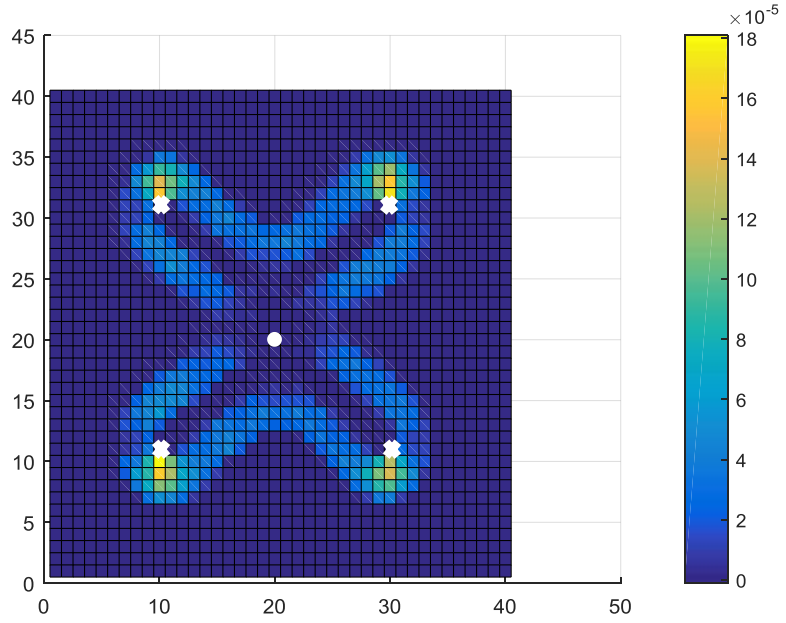

Figure 4-101: 2-D adjoint sensitivity plot of Q to K_x for Case Example 2.

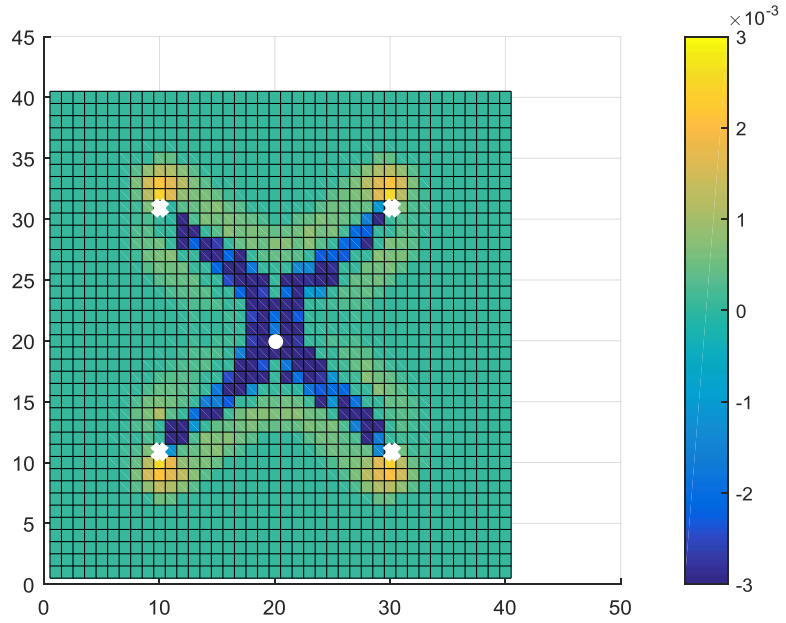

Figure 4-102: 2-D adjoint sensitivity plot of Q to K_x for Case Example 2 prior to convergence to the global minima.

In Figure 4-102, a 2-D adjoint sensitivity plot of the objective function (Q) to model parameter K_x at some iteration (49th iteration) prior to convergence to the global minima (best-case result) is presented. Compared to Figure 4-101, one can notice some grid blocks with negative sensitivity values exist. This suggests an increase in the grid block property

value (e.g. increasing K_x for that grid block) in order to reduce the objective function. In addition, in both Figure 4-101 and Figure 4-102, zero sensitivity values can be observed in all grid blocks housing wells since we assumed that core data exists for these wells.

4.5.2 Revealing Faults using K_x & K_y Adjoint Sensitivity

Faults revealed through the use of the fault detection algorithm can also be validated using K_x and K_y adjoint-derived sensitivities. To demonstrate this, we present a fault indicator map and adjoint-derived sensitivities for a multi-layered semi-heterogeneous reservoir model evaluated with our proposed method. Using the fault detection algorithm, the best-case K_x and K_y arrays are used to generate the fault indicator map (see Figure 4-103). The best-case K_x and K_y adjoint-derived sensitivities are also presented individually (see Figure 4-104 and Figure 4-105).

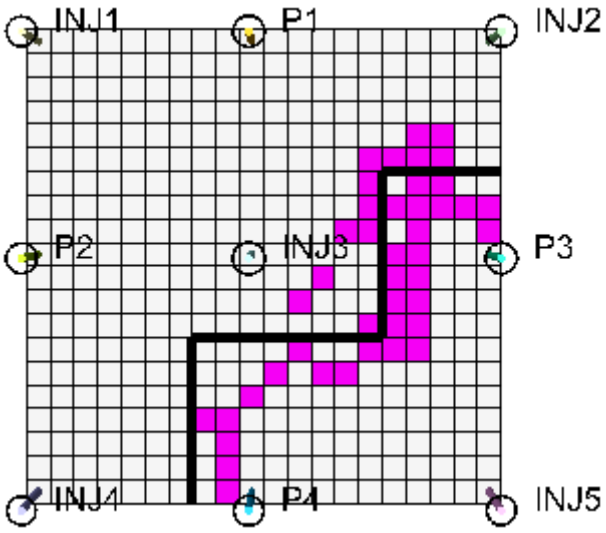

Figure 4-103: Fault indicator map showing revealed fault (in purple-coloured grid blocks) and the true model fault (in thick black line).

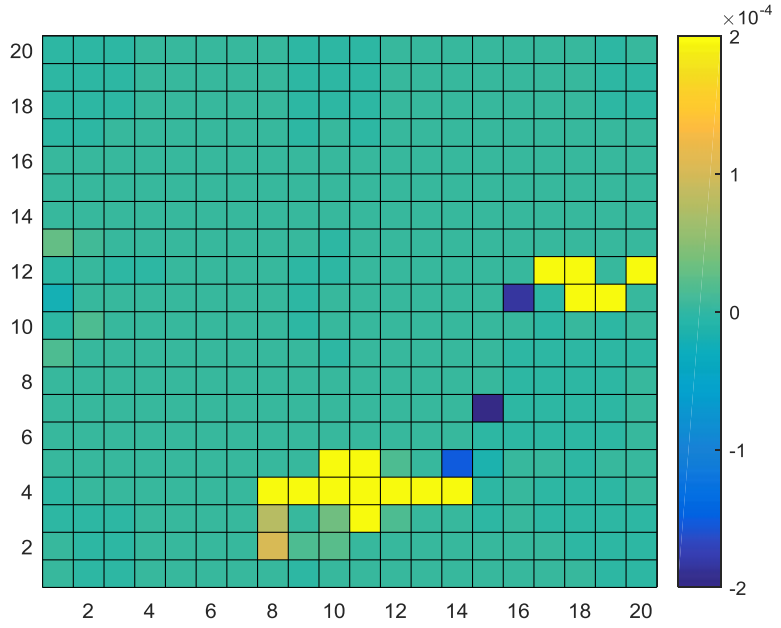

Figure 4-104: 2-D adjoint sensitivity plot of Q to K_x obtained at the iteration that yielded the best-case result.

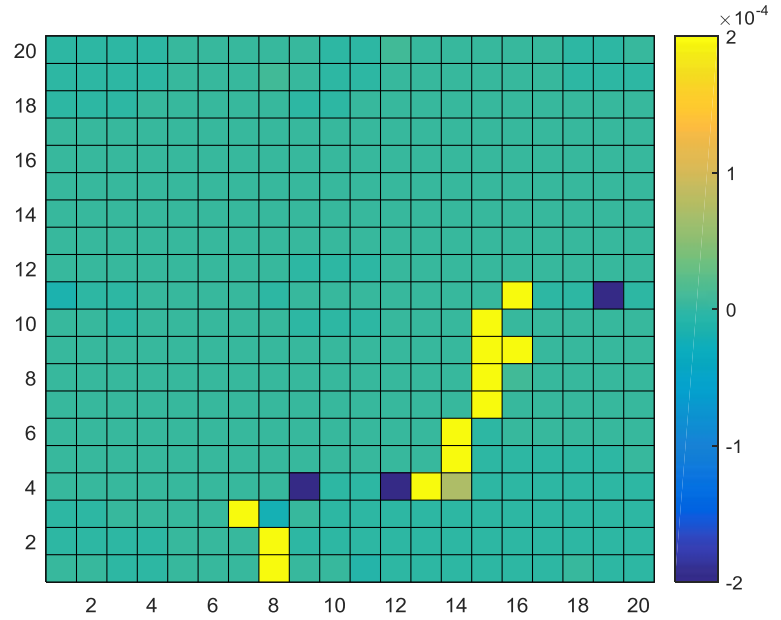

Figure 4-105: 2-D adjoint sensitivity plot of Q to K_y obtained at the iteration that yielded the best-case result.

In Figure 4-104 and Figure 4-105, negative sensitivity values can be found but they are of no interest to us since they suggest permeability values in certain grid blocks that should be increased by some magnitude. Only positive sensitivity values are of immense interest in revealing fault locations using adjoint-derived sensitivities. Consequently, the negative sensitivity values in Figure 4-104 and Figure 4-105 are ignored by replacing all negative sensitivity values with zero values as shown in Figure 4-106 and Figure 4-107.

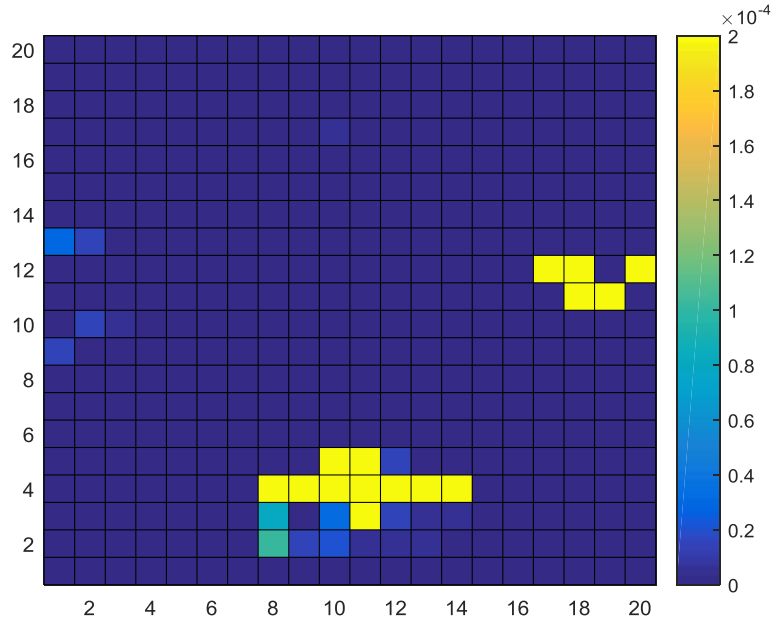

Figure 4-106: Modified 2-D adjoint sensitivity plot of Q to K_x obtained at the iteration that yielded the best-case result.

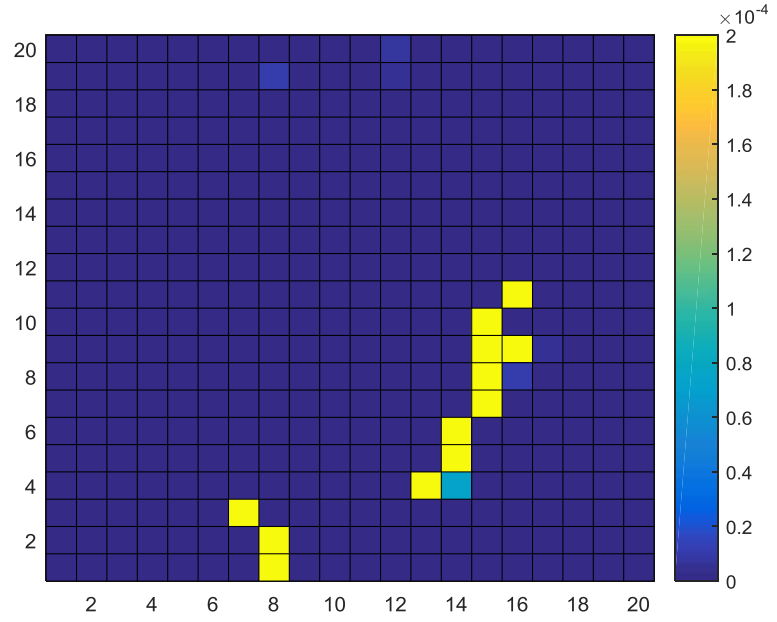

Figure 4-107: Modified 2-D adjoint sensitivity plot of Q to K_y obtained at the iteration that yielded the best-case result.

Following this action, the next step is to define 4 categories for identifying the fault location using the modified adjoint-derived sensitivities for K_x and K_y. The implementation of these categories aids in revealing the fault and providing information about the fault faces of the revealed fault (i.e. X-face or Y-face). The fault indicator map does not provide information on revealed fault faces. The 4 categories adopted are displayed in Figure 4-108.

In category number 1, a grid block is assigned a value of 1 if both the adjoint-derived sensitivity for K_x and K_y are zero for that grid block. This means that the grid block cannot be a fault block. In category number 2, a grid block is assigned a value of 2 if the adjoint-derived sensitivity for K_x is greater than zero and the adjoint-derived sensitivity for K_y is zero. This means that the grid block is very likely a fault block and the fault exist in the X-face. In category number 3, a grid block is assigned a value of 3 if the adjoint-derived sensitivity for K_x is zero and the adjoint-derived sensitivity for K_y is greater than zero. This means that the grid block has a very good chance of being a fault block and the fault exist in the Y-face. In category number 4, a grid block is assigned a value of 4 if both the adjoint-derived sensitivity for K_x and K_y are greater than zero for that grid block. This means that the grid block is very likely a fault block and the fault can exist in either the X-face or the Y-face.

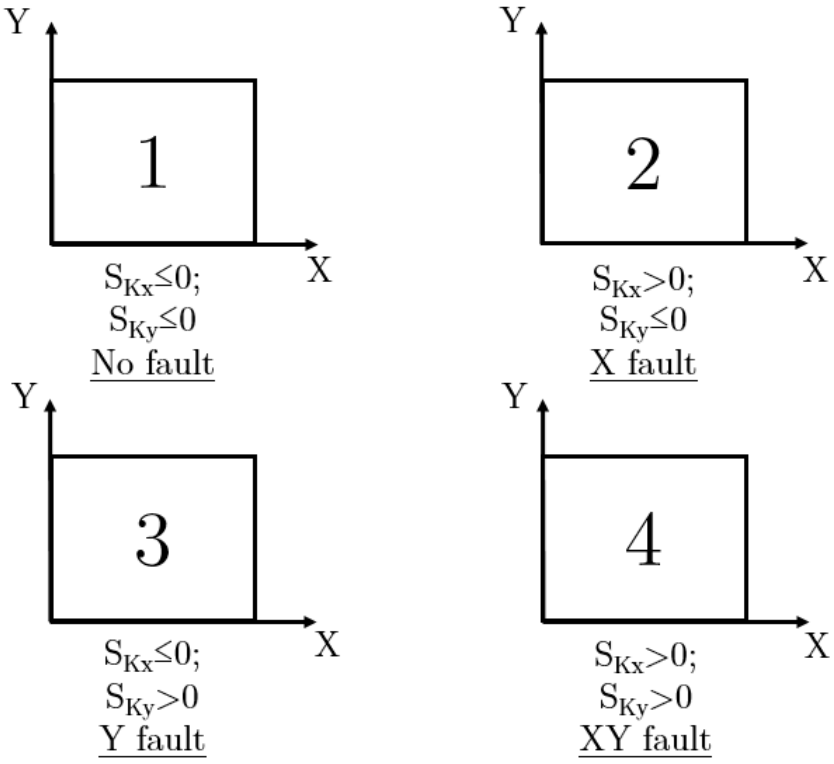

Figure 4-108: All 4 categories defined for identifying fault location and fault faces.

By applying the defined categories for identifying fault location to Figure 4-106 and Figure 4-107, a colour mapping of the modified K_x and K_y adjoint-derived sensitivity is presented in Figure 4-109. The location of the true model fault is indicated by the thick black line. Although not shown in Figure 4-109, in grid blocks housing wells like P3, P4 and INJ5, a grid block value of 1 is assigned since we assume core data exists for these wells. Grid blocks with values greater than 1 lying outside the region where the true model fault exist are not considered as fault blocks since they do not form a set of connecting grid blocks.

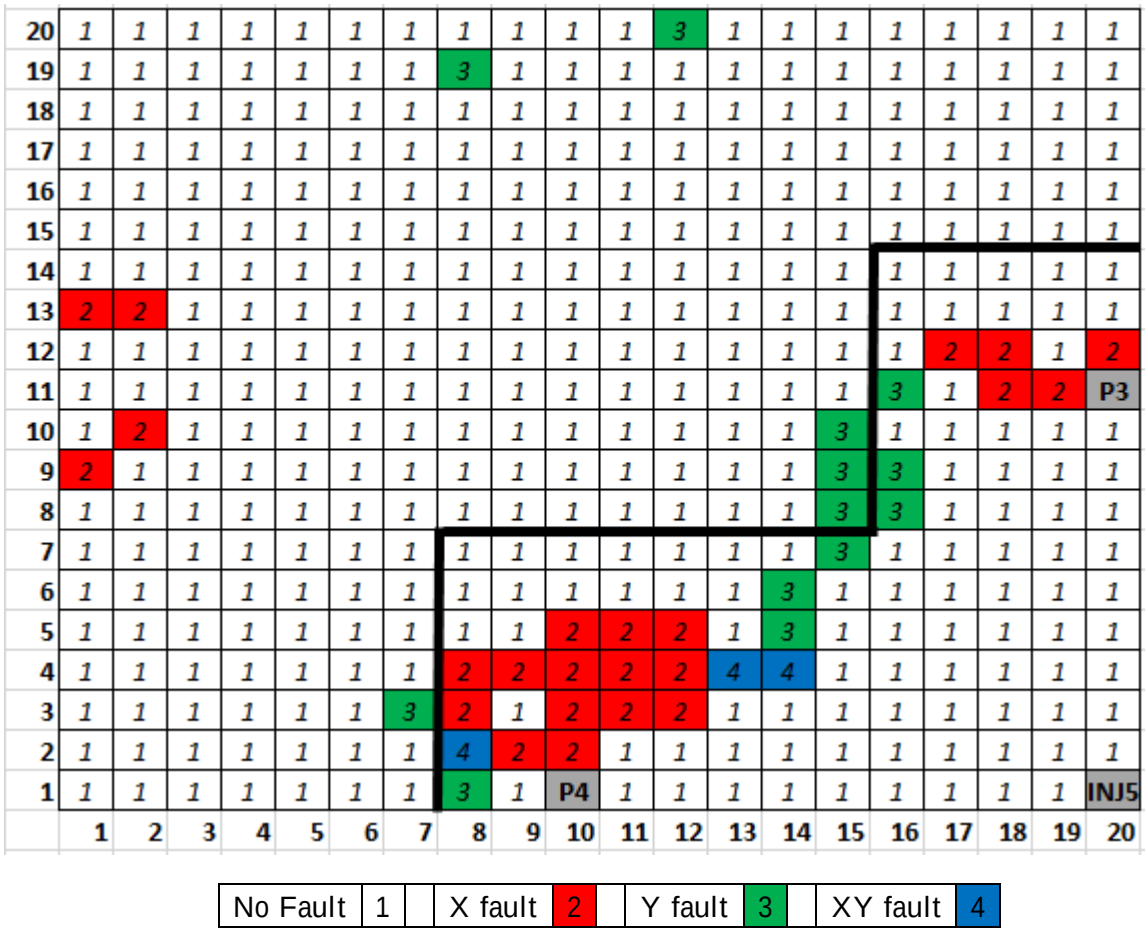

Figure 4-109: Colour mapping of modified K_x and K_y adjoint-derived sensitivity based on all 4 categories.

4.6 Revealing Hidden Reservoir Features using Pattern Detection Algorithms

In an attempt to improve on the reservoir feature indicator maps obtained using the formulated reservoir feature detection algorithms, two pattern detection algorithms are developed and evaluated. The first algorithm which is the modified Canny edge-detection method can be used to identify area-based reservoir features like channels, fractures etc. using for instance the channel indicator map as an input. In addition, the modified Canny edge-detection algorithm eliminates artefacts or outliers that are present in reservoir feature indicator maps. The second algorithm developed which is called the "fault shape detection algorithm" can be used to delineate faults in form of fault lines from fault indicator maps. The fault shape detection algorithm objectively determines revealed fault shape in form of fault lines for any fault indicator map defined as input. In the following sub-sections, examples are provided with results obtained from using both pattern detection algorithms.

4.6.1 Detecting Channels with the Modified Canny Edge-detection Method

The modified Canny edge-detection method which is based on the Canny edge-detection method [82] also includes a built-in function for removing artefacts or outliers in channel/fracture indicator maps resulting from not implementing tight simulator solver settings (see Section 4.8 for more details on the issue). The addition of this function improves the quality of the final channel/fracture indicator map generated. An example capturing how the modified Canny-edge detection method works is provided in the following paragraph.

A channel indicator map similar to that in Case Example 2 is used as an input image for the modified Canny edge-detection method. This channel indicator map contains some artefacts/outliers which can be easily seen in Figure 4-110. The orange-coloured region identifies the location of the revealed channels while the light-green-coloured regions existing between any two channels are added artefacts. The sky-blue-coloured regions located outside the area containing the revealed channels are regions where no changes are made to the existing reservoir permeability.

Figure 4-110: Input image containing channels with added artefacts.

Conversion of Figure 4-110 to a black and white image (BW image) results in the generation of Figure 4-111. This process is crucial before the modified Canny edge-detection method can be applied. By executing the modified Canny edge-detection method on the input image, the resulting channel indicator map ridded of the existing artefacts is generated as shown in Figure 4-112. The lines of MATLAB code that make up the modified Canny edge-detection method are available in Appendix C.

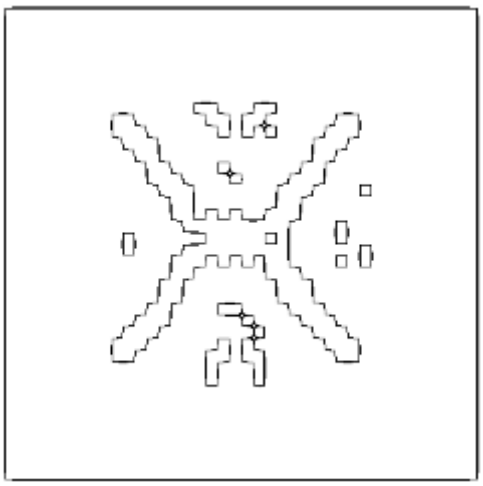

Figure 4-111: BW image of the input image (channel indicator map).

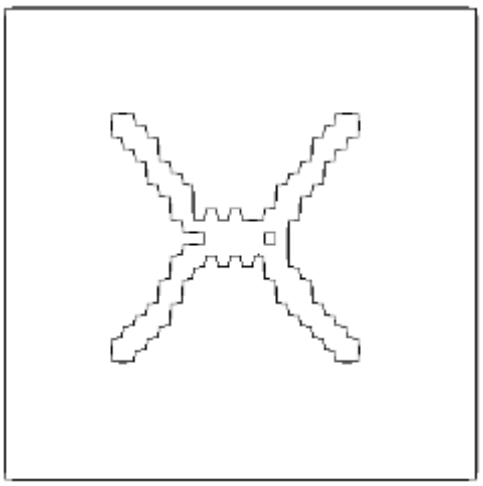

Figure 4-112: Modified input image after removing artefacts.

4.6.2 Estimating Fault Shape using the Fault Shape Detection Algorithm

Information obtained from fault indicator maps with clearly revealed fault shapes can be easily interpreted by reservoir engineers with very little room for subjective bias. On the other hand, when more than one fault shape can be extracted from a fault indicator map, the option of whether to choose one fault pattern over another can be challenging especially when human intervention is necessary. For this reason, the fault shape detection algorithm is developed to objectively determine fault shapes from fault indicator maps in form of fault lines without any form of human involvement. Two examples capturing how the fault shape detection algorithm works is provided in the following paragraphs. The lines of MATLAB code that make up the fault shape detection algorithm are available in Appendix C.

The first example is a relatively simple case. The fault indicator map generated using the fault detection algorithm clearly provides a distinct shape of the revealed faults. The input image for the fault shape detection algorithm is the fault indicator map. Upon its conversion to a BW image, the input image takes a new form as shown in Figure 4-113. The combination of the black grid blocks that takes the shape of a fault is the revealed faults obtained using a fault indicator map. Without the use of the fault shape detection algorithm, it is relatively easy to delineate the revealed faults in form of fault lines.

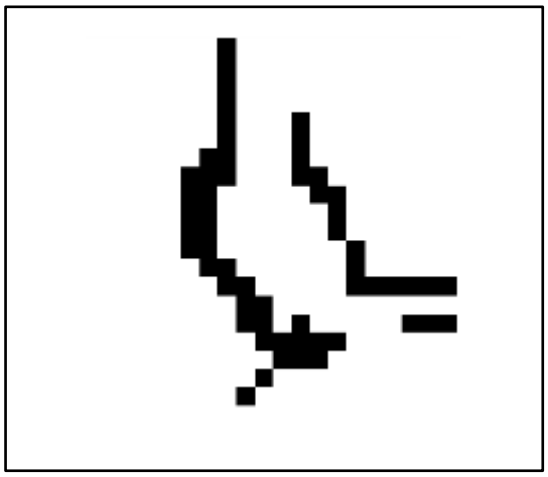

Figure 4-113: BW image of fault indicator map for the first example.

After applying the fault shape detection algorithm to Figure 4-113, the resulting fault map containing only fault lines is shown in Figure 4-114. Please note that the estimated fault lines in Figure 4-114 are continuous lines.

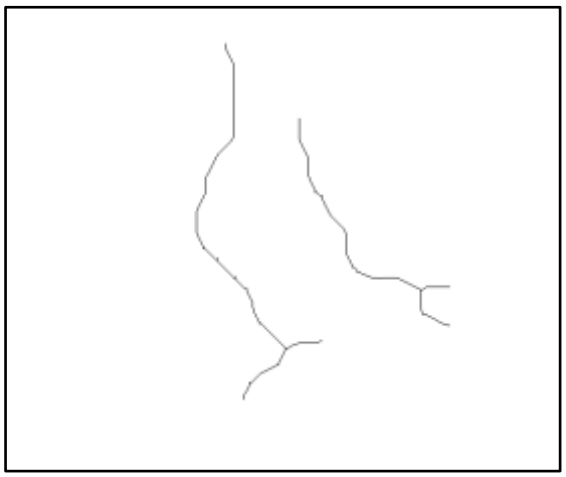

Figure 4-114: Estimated fault shapes in form of fault lines for the first example.

The second example is rather more challenging. Figure 4-115 is the converted input image (fault indicator map) to a BW image. Looking at Figure 4-115, there are many possible fault lines that can be delineated from the same fault indicator map. Without the use of the fault shape detection algorithm, reservoir engineers will be forced to make some guesses in order to arrive at one fault line.

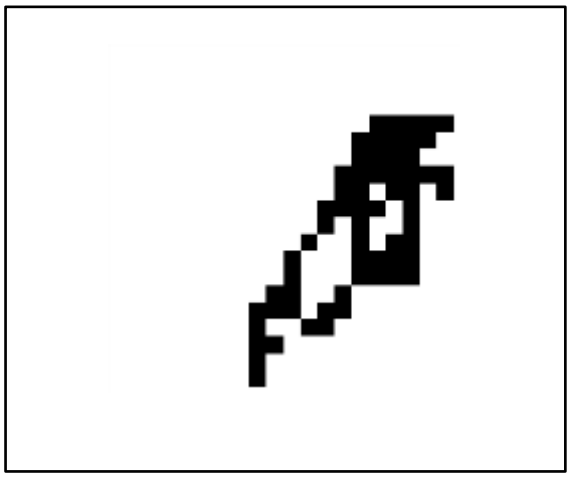

Figure 4-115: BW image of fault indicator map for the second example.

Using the fault shape detection algorithm, the resulting fault map containing the estimated fault line from Figure 4-115 is shown in Figure 4-116. Please note that the estimated fault line in Figure 4-116 is a continuous line.

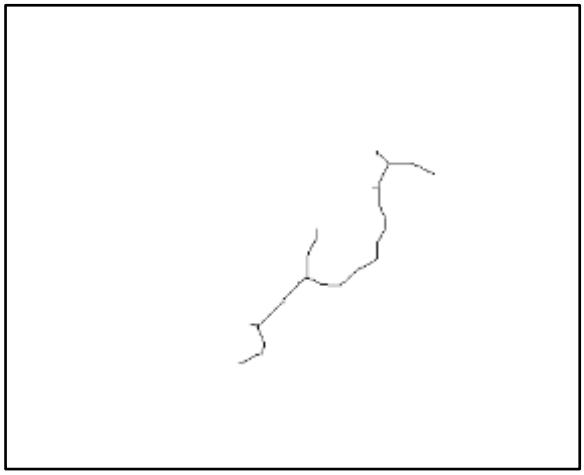

Figure 4-116: Estimated fault shape in form of a fault line for the second example.

4.7 Influence of Noisy Production Data on the Proposed Method (Extracted from SPE-184951-MS Paper [91])

Production data containing noise (errors or outliers in measured data) can have a detrimental impact on history matching and methods for improving reservoir characterization [92]. This is simply because production data are the only truly known data that can be readily measured from brownfields. In order to understand the impact of noisy production data on our proposed method, an illustration is provided using a semi-synthetic heterogeneous model, PUNQ-S3, which has been extensively used to evaluate history matching and uncertainty quantification workflows.

The PUNQ-S3 model is built using data obtained from a West African oil field. The model has dimension 19 x 28 x 5 with $\Delta X = \Delta Y = 180$ metres and ΔZ varying from 1.3

metres to 9 metres per layer. Only 1761 grid blocks out of a total of 2660 grid blocks are active. Porosity ranges from 1% to 30%. The horizontal permeability ranges from 0.51 mD to 1000 mD while the vertical permeability ranges from 0.23 mD to 500 mD. A total of 6 vertical producers which are oil-rate (ORAT) controlled exist in the field. A BHP target of 120 bars is also set for all 6 vertical producers. Each vertical producer is completed in at most two layers which is either the 3rd, 4th or 5th layer. The model contains oil with dissolved gas, water and a gas gap at initialization (see blue colouration in Figure 4-117) existing in the middle of all 6 vertical producers. Edge-drive aquifers are responsible for maintaining pressure support across all 5 layers. These edge-drive aquifers exist in the North-West and South-West part of the field. No injector well is present in the field. Figure 4-117 presents the top structure of the PUNQ-S3 model. For more information about the PUNQ-S3 reservoir model, please read up the article written by Floris [93].

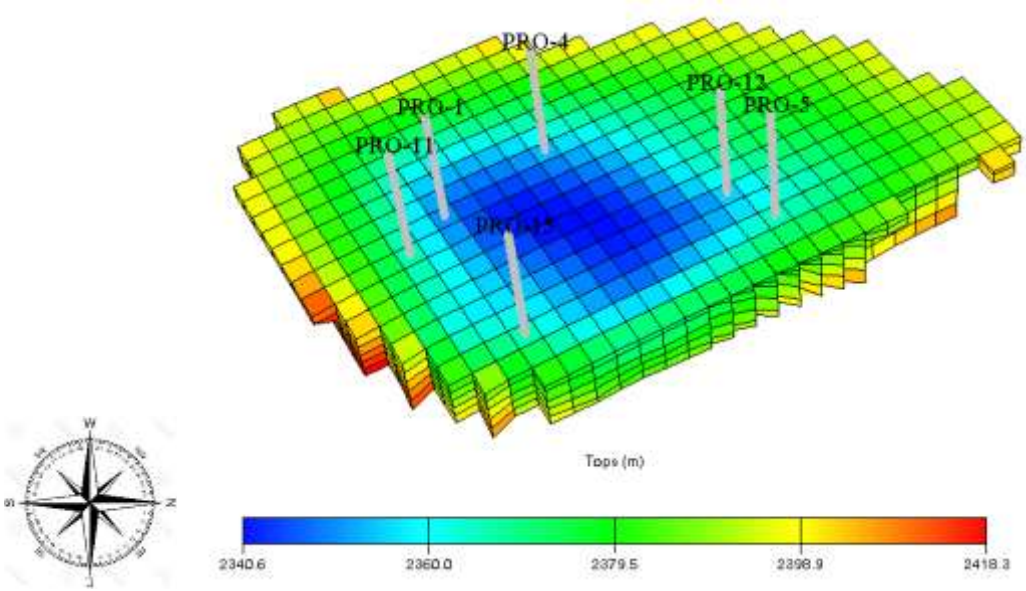

Figure 4-117: Top structure of the PUNQ-S3 model.

A reservoir characterization problem is formulated with the PUNQ-S3 model which entails revealing a hidden fault in a base model that is present in the true model. The fault, which is modelled by deactivating some grid blocks, cut across all 5 layers and consequently impedes water flow from the edge-drive aquifers to neighbouring producers (see Figure 4-118). Deactivated grid blocks are represented in blue while activated grid blocks are represented in red. Also, a new vertical producer "PRO-X" is completed at initialization in the 4th producing layer between the aquifer and the introduced fault. The solution of the true model (model containing fault information) is defined as measured data for the base model. No Gaussian noise is added to the measured data.

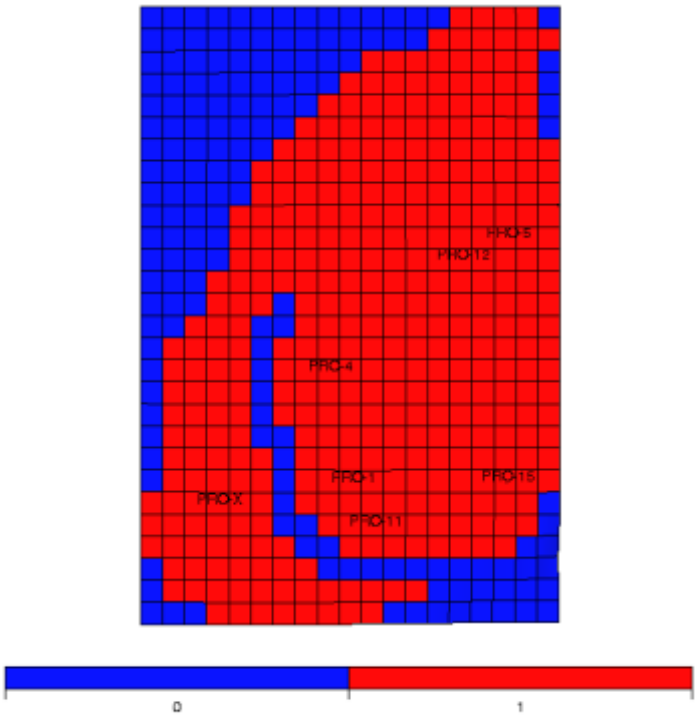

Figure 4-118: PUNQ-S3 model capturing deactivated grid blocks used for modelling a fault and the introduced vertical producer "PRO-X".

In order to reveal the hidden fault, horizontal permeabilities (K_x & K_y) are defined as model parameters prior to performing UHM. This is the case because K_x & K_y are key model parameters for revealing hidden faults as provided in the proposed catalogue for improving reservoir characterization in Table 4-17. The uncertainty limits for the horizontal permeabilities is described by Equation (37) where $K_{x_{max}} = K_{y_{max}} = 1000$ mD. In addition, we assumed that core data exist for all wells therefore the permeability values in grid blocks housing wells are unchanged.

During the UHM stage, a total of 440 iterations were executed in order to reach an optimal Q. This is so because the step size, μ_{K_x,K_y} = 30 mD^2, is utilized. The objective function value reduced by a factor of 100 over the entire 440 iterations yielding an overall model error reduction value of 94.0%. The better the UHM results, the more likely that our proposed method can reveal hidden reservoir features.

The model responses defined for this test are well oil production rate (WOPR), well water production rate (WWPR) and the well gas production rate (WGPR). Best-case results for the most offending model responses (model responses with the worst match results) are presented in Figure 4-119. In addition, the R-squared values for all model responses generated for the best-case result obtained from UHM is presented in Table 4-18.

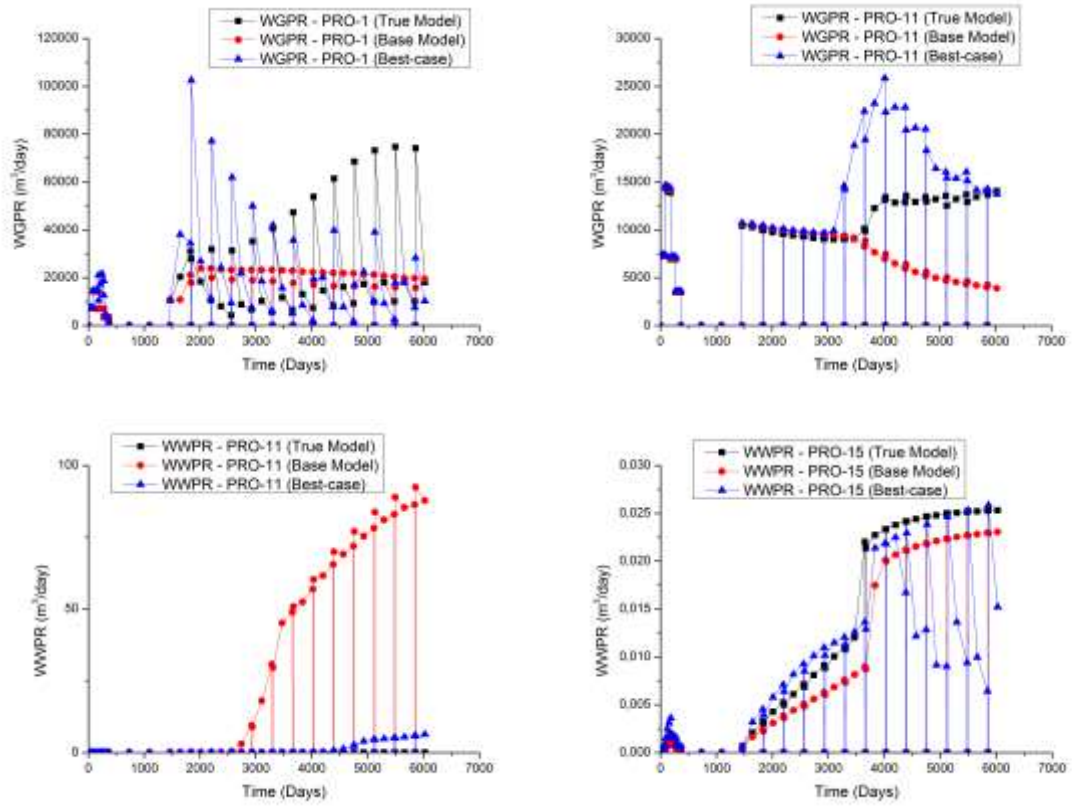

Figure 4-119: Best-case results for the most offending model responses after performing UHM on the PUNQ-S3 base model.

Table 4-18: R-squared values for the best-case result from UHM on the PUNQ-S3 base model.

Well Name	WGPR	WWPR	WOPR
PRO-1	41.7%	93.0%	94.4%
PRO-4	97.2%	97.0%	99.9%
PRO-5	99.9%	99.1%	100.0%
PRO-11	90.3%	71.9%	98.6%
PRO-12	99.8%	99.9%	99.9%
PRO-15	94.7%	80.2%	96.7%
PRO-X	98.8%	94.2%	99.0%
$R^2 \geq 97\%$; $R^2 < 97\%$			

In order to reveal the location of the hidden fault using our proposed method, the permeability ratio maps for the 1st and 4th layer (see Figure 4-120 and Figure 4-121) are generated using the first part of the fault detection algorithm. The green-coloured region represents grid blocks with little or no change in permeability. These grid blocks have a permeability ratio value of 1.0. Grid blocks coloured in yellow and red have permeability ratio values greater than 1.0 due to the existing reservoir heterogeneity in the PUNQ-S3

base model. Grid blocks with colours such as blue and purple identifies regions with extreme permeability reduction.

A closer look at Figure 4-120 and Figure 4-121 (the 1st and 4th layer) already indicates the hidden fault coloured in purple which is located in the South-Western part of the field. The hidden fault completely isolates producer "PRO-X" from the rest of the field in the 1st layer. In the 4th layer, the hidden fault slightly isolates producer "PRO-X" from other wells. The combination of fault patterns observed in the 1st and 4th layer is also observed in other layers as well.

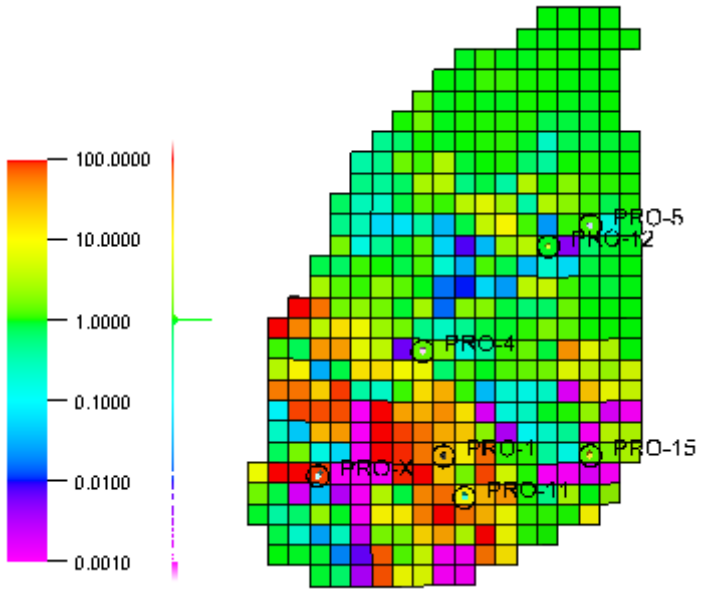

Figure 4-120: Permeability ratio map generated for the 1st layer (PUNQ-S3).

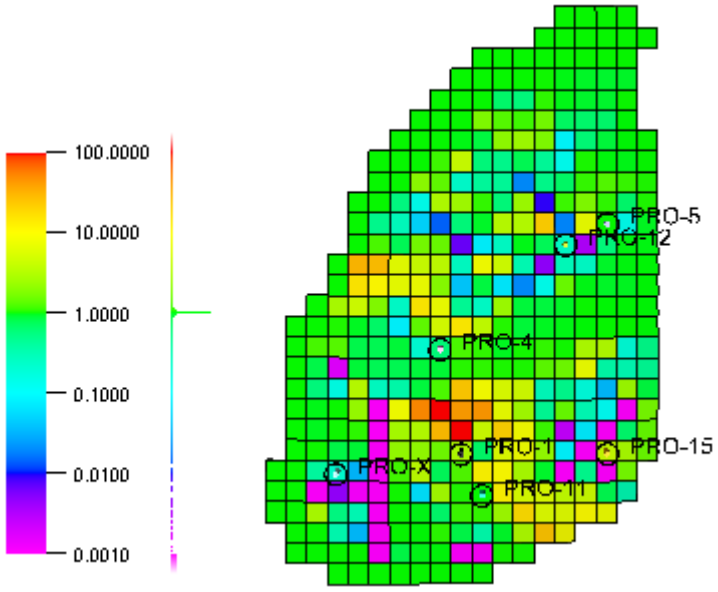

Figure 4-121: Permeability ratio map generated for the 4th layer (PUNQ-S3).

The second part of the fault detection algorithm can be used to generate the fault indicator map from Figure 4-120 and Figure 4-121. Figure 4-122 and Figure 4-123 presents the fault indicator map generated for the 1st and 4th layer capturing the location and shape of the revealed fault in purple-coloured grid blocks. The threshold value that reveals the location of the hidden fault is γ_{fault} = 5×10^{-3}. The location of the revealed fault (the set of connecting purple-coloured grid blocks) differs slightly from the fault in the true model as shown in Figure 4-118. Despite that, the revealed fault acts to prevent the flow of water from the aquifer to other producers.

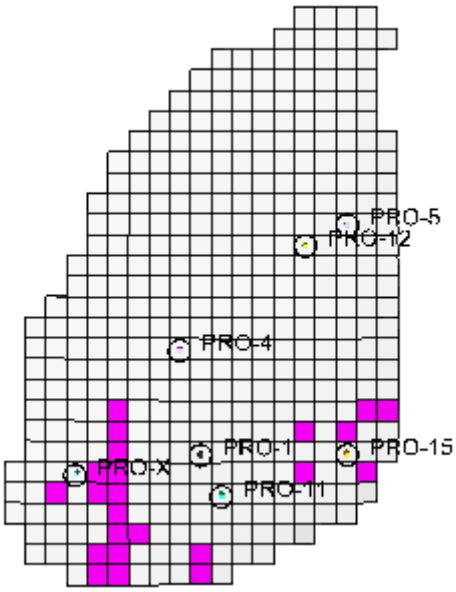

Figure 4-122: Fault indicator map generated at γ_{fault} = 5×10^{-3} for the 1st layer (PUNQ-S3).

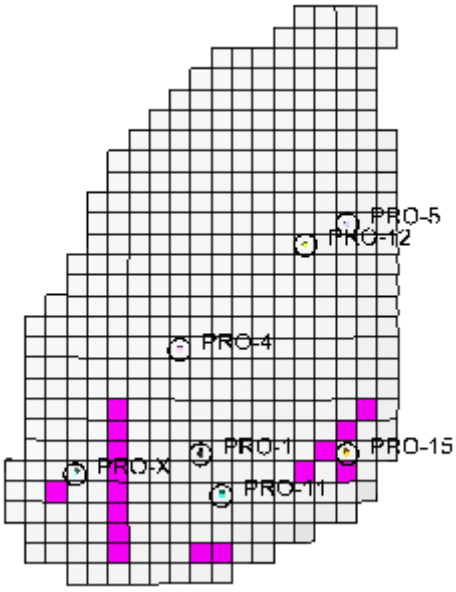

Figure 4-123: Fault indicator map generated at γ_{fault} = 5×10^{-3} for the 4th layer (PUNQ-S3).

In order to demonstrate the influence of production noise on the proposed method, the entire process is repeated with Gaussian noise of +15% and +30% added to the measured data. The fault indicator maps generated for the 1st and 4th layer for the +15% and +30% Gaussian noise cases are presented in Figure 4-124 and Figure 4-125 respectively.

As seen in Figure 4-124, the proposed method is not negatively impacted by the +15% Gaussian noise case. Although a noticeable drop in overall model error reduction value from 94.0% (recorded for the 0.0% Gaussian noise case) to 88.4% is observed, the proposed method remained effective in revealing the approximate location and shape of the hidden fault. In fact, very little discrepancies exists between the fault indicator maps generated for the 0.0% Gaussian noise case and the +15% Gaussian noise case.

In Figure 4-125, no information about the hidden fault is visible as a result of the introduction for +30% Gaussian noise. This suggests that the effectiveness of the proposed method in revealing hidden reservoir features deteriorates significantly with Gaussian noise beyond ±15%.

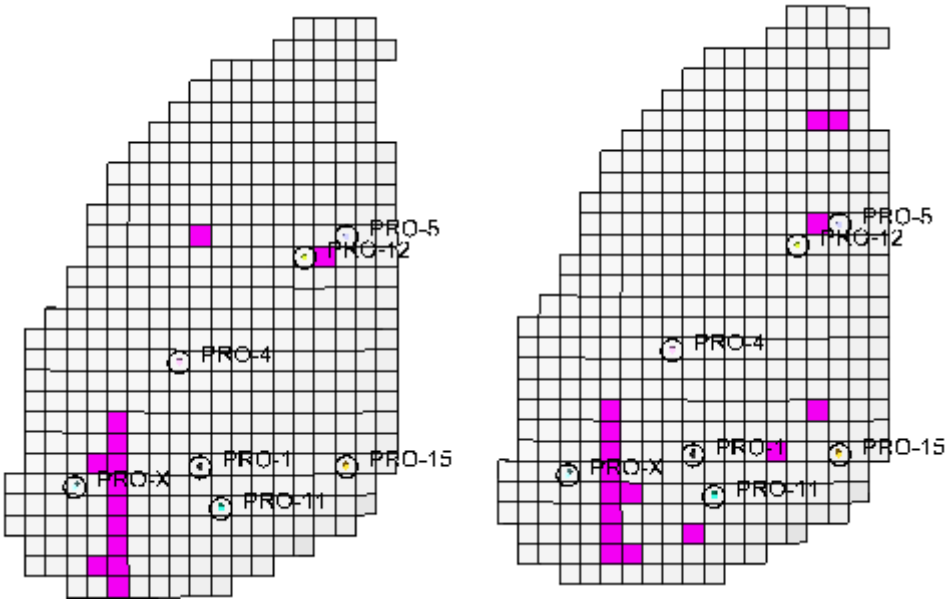

Figure 4-124: Fault indicator map generated at γ_{fault} = 5×10^{-3} for the +15% Gaussian noise case (left image = 1st layer; right image = 4th layer).

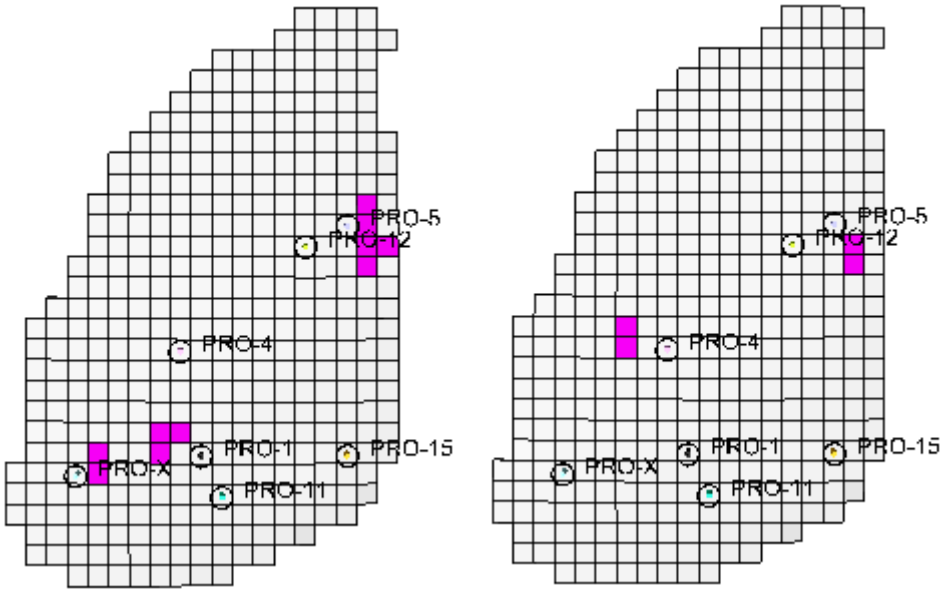

Figure 4-125: Fault indicator map generated at γ_{fault} = 5×10^{-3} for the +30% Gaussian noise case (left image = 1st layer; right image = 4th layer).

4.8 Influence of Numerical Noise on the Proposed Method

Gradient-based optimization methods like the steepest descent algorithm applied to history matching and other minimization problems require the analytical gradient of the objective function with respect to model parameters. One way of computing the analytical gradient is by using the adjoint method [45], [94]. In order for the adjoint method to compute the analytical gradient, numerical gradients obtained from the numerical reservoir simulator are necessary which are rarely accurately calculated as a result of numerical noise in simulation results. In reservoir simulation, it is almost impossible to completely eliminate numerical noise. Rather, they can be dampened by implementing tight solver settings (or tight convergence criteria). Although the calculated numerical gradients become more accurate with tighter solver settings defined, the total simulation time increases exponentially which is not desirable as this harms optimization efficiency [95]. In this thesis, the term "numerical noise" means numerical simulation (or forward simulation) errors resulting from poor convergence of linear and non-linear equations solved by the numerical reservoir simulator. This action usually results in the non-smoothness of the objective function [96].

The impact of numerical noise on the proposed method is analysed using a semi-heterogeneous model with structure and well arrangements similar to that of Section 4.3.7.2 (well shut-in test). The model contains 5 vertical injectors and 4 vertical producers with dimensions 20 x 20 x 5 in the X, Y and Z directions. All 2000 grid blocks are active. The size of each grid block in the X and Y direction is fixed at 500 ft (152 metres). In the Z direction, the grid block size is 20 ft (6 metres). The model contains mainly oil and water with no free gas evolving over a 10-year production period. The horizontal (K_x, K_y)

and vertical (K_z) permeability distribution are obtained using the sequential Gaussian simulation method while a constant porosity value of 20% is assigned everywhere in the model. Horizontal permeability varies from 35 mD to 287 mD while the vertical permeability is obtained by multiplying the horizontal permeability by a value of 0.1. A sealing fault is introduced in the model as shown in Figure 4-126 which isolates injector INJ5 and producers P3 and P4 from the rest of the field. Water and oil viscosity are retained at 0.3 cp and 1.3 cp respectively. Figure 4-5 describes the relative permeability curve used in the model. This is the true model.

An over-injection waterflooding strategy with a VRR > 1 is implemented. All 5 vertical injectors controlled by their water injection rates each injects 50000 barrels of water per day (approximately 7950 m^3/day) while all 4 vertical producers controlled by their combined oil and water rates each produces 40000 barrels of liquid per day (approximately 6350 m^3/day). All injectors and producers are perforated in all 5 layers. Information about the sealing fault is completely removed from the base model. Permeabilities in grid blocks housing all injectors and producers are unchanged since core data is assumed to be available for each well. The solution of the true model is defined as measured data in the base model. No Gaussian noise is added to the measured data.

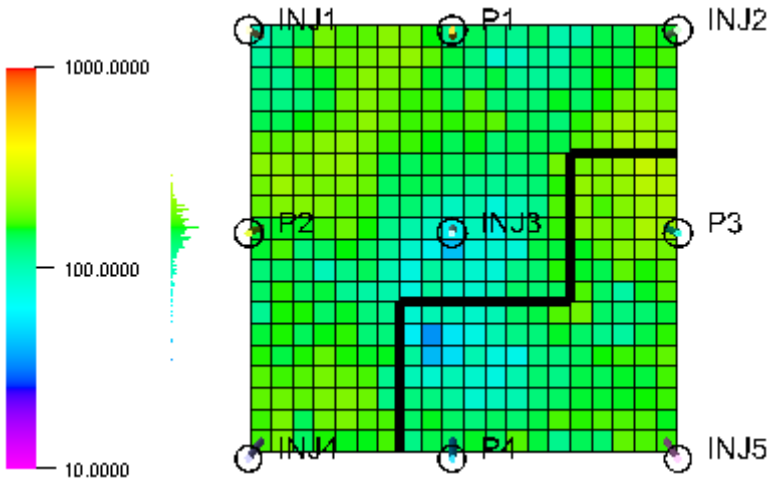

Figure 4-126: True model capturing permeability distribution and sealing fault location (in thick black line).

The effect of numerical noise on the proposed method is explored using the semi-heterogeneous multi-layered reservoir model described above. In an attempt to reveal the location and approximate shape of the hidden fault in the base model, two classes of simulator solver settings are defined. These classes are the "default" and "tight" simulator solver settings. A summary of the default and tight simulator solver settings defined are provided in Table 4-19. The solution of the true model which is defined as measured data in the base model is generated using the tight simulator solver settings. The fully implicit option (implicit pressure and implicit saturation) is defined for this example and also for all case examples previously described in this thesis.

Table 4-19: Summary of the default and tight solver settings used in this example.

Simulator Solver Settings	Convergence Error		Max. Material Balance Error	Max. Well Flow Rate Convergence Error
	Linear	Non-Linear		
Default	10^{-3}	10^{-2}	10^{-6}	10^{-3}
Tight	10^{-9}	10^{-9}	10^{-9}	10^{-9}

4.8.1 Revealing the Hidden Fault with the Default vs. Tight Simulator Solver Settings

In order to reveal the approximate location and shape of the hidden fault in the base model, horizontal permeabilities (K_x & K_y) are defined as model parameters prior to performing UHM. This is simply because K_x & K_y are key model parameters for revealing hidden faults as provided in the proposed catalogue for improving reservoir characterization in Table 4-17. The uncertainty limits for the horizontal permeabilities is described by Equation (37) where $K_{x_{max}} = K_{y_{max}} = 287$ mD. In addition, we assumed that core data exists for all wells therefore the permeability values in grid blocks housing wells are unchanged.

In the UHM stage, the step size μ_{K_x,K_y} = 10.75 mD^2 is utilized for both the default and tight solver settings. Using the default solver settings, an overall model error reduction value of 99.1% is realized while an overall model error reduction value of 99.5% is recorded using tight solver settings. The objective function (Q) vs. number of iterations plot for the default and tight solver settings cases are jointly shown in Figure 4-127.

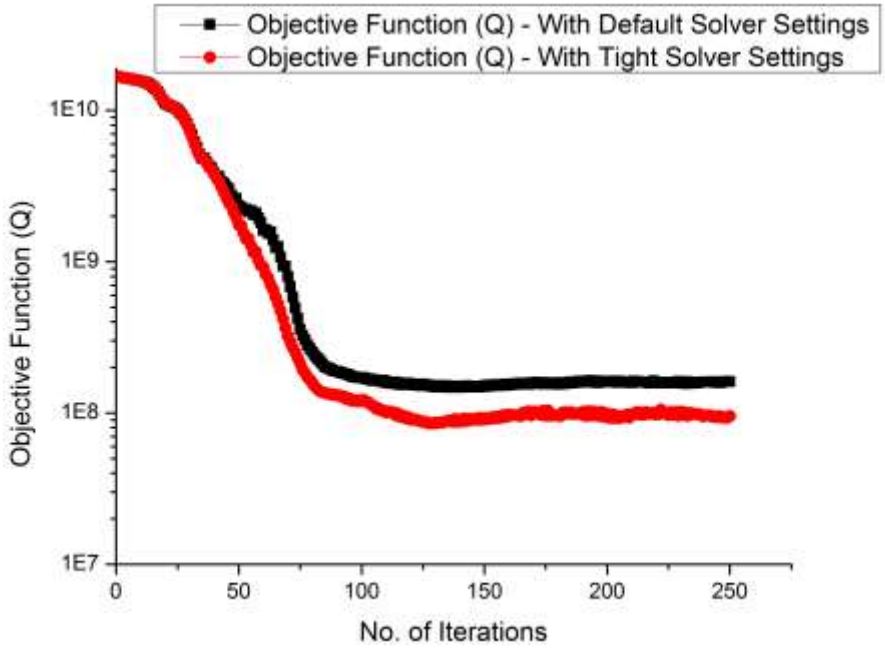

Figure 4-127: Semi-log plot of objective function (Q) vs. number of iterations.

The objective function vs. number of iterations plots presented in Figure 4-127 is a semi-log plot. The objective function values are presented in log scale in order to show the difference in objective function progression with increasing number of iterations as a result of the simulator solver settings used. Using the default solver settings, Q reduced by a factor of 100 while a reduction in Q by a factor of approximately 1000 is recorded when tight solver settings are used.

The model responses defined for this test are well water-cut (WWCT), well oil production rate (WOPR) and well bottom-hole flowing pressure (WBHP). The R-squared values generated for the best-case result obtained from UHM using both the default and tight simulator solver settings are provided in Table 4-20. R-squared values for the tight solver settings case is provided in brackets in Table 4-20.

Table 4-20: R-squared values for the best-case result from UHM using both the default and tight solver settings.

Well Name	WBHP	WWCT	WOPR
P1	99.8% (99.8%)	93.5% (94.1%)	92.9% (93.6%)
P2	99.8% (99.9%)	92.7% (93.8%)	93.3% (95.1%)
P3	99.9% (99.9%)	90.2% (91.1%)	89.7% (94.3%)
P4	99.9% (99.9%)	94.5% (97.4%)	94.1% (97.1%)
INJ1	99.7% (99.8%)	—	—
INJ2	99.8% (99.9%)	—	—
INJ3	99.7% (99.9%)	—	—
INJ4	99.7% (99.9%)	—	—
INJ5	91.6% (97.3%)	—	—
$R^2 \geq 97\%$; $R^2 < 97\%$			

As observed in Table 4-20, in all model responses, the R-squared values improved significantly for the tight solver settings case. In addition, for 3 model responses (WBHP@INJ5, WWCT@P4 and WOPR@P4), the target R-squared value (97%) indicative of an excellent history-match is exceeded. These results confirm that numerical noise has a significant impact on the performance of the adjoint method. In other words, inaccurate numerical gradients generated by the numerical reservoir simulator due to numerical noise can negatively impact the sensitivities computed by the adjoint method. Certainly, this will inevitably lead to the degradation of convergence performance during the model parameter update stage using any gradient-based optimization algorithms (e.g. steepest descent algorithm). At worst, convergence to an optimal solution (a global minima) may not be achieved.

Furthermore, comparison between the simulation run time, time steps, Newton steps and the linear solver steps are made for the best-case result obtained from UHM for the default and tight solver settings cases. A summary of the simulation performance using

the default and tight solver settings is listed in Table 4-21. As expected, it took a shorter CPU time to execute a complete simulation run with the default solver settings than using the tight solver settings.

Table 4-21: Summary of the simulation performance of the best-case result from UHM for the default and tight solver settings.

Simulator Solver Settings	Simulation Time (Seconds)	Time Steps	Newton Steps	Linear Solver Steps
Default	2.32	155	381	1957
Tight	4.20	155	595	6946

In order to reveal the location of the hidden fault using our proposed method, the permeability ratio maps for the default and tight solver settings for the 4th layer are generated using the first part of the fault detection algorithm as shown in Figure 4-128. The yellow-coloured region represents grid blocks with little or no change in permeability. These grid blocks have a permeability ratio value of 1.0. Grid blocks coloured in dark-yellow and red have permeability ratio values greater than 1.0 due to the existing reservoir heterogeneity in the model. Grid blocks with colours such as blue and purple identifies regions with extreme permeability reduction.

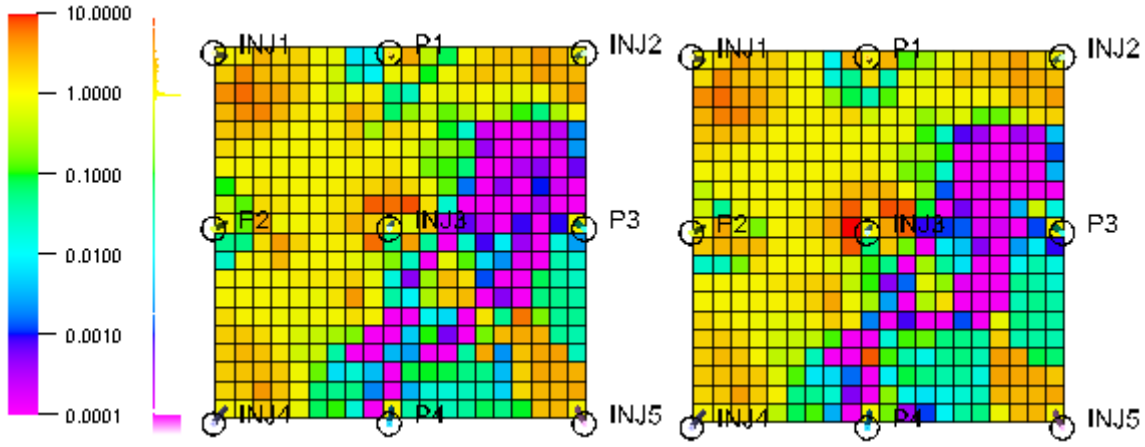

Figure 4-128: Permeability ratio map generated for the default (left) and tight (right) solver settings for the 4th layer.

The second part of the fault detection algorithm is used to generate the fault indicator map for the default and tight solver settings for the 4th layer as shown in Figure 4-129. In Figure 4-129, the threshold value used to reveal the location of the hidden fault is γ_{fault} = 1×10^{-2}. At a smaller threshold value (γ_{fault} = 5×10^{-3}) as in Figure 4-130, the shape of the revealed fault becomes more pronounced for the default and tight solver settings cases. At an even smaller threshold value (γ_{fault} = 1×10^{-3}) as in Figure 4-131, a much more distinct shape of the revealed fault is observed for the case with tight solver settings. The case with default solver settings starts to lose information about the fault.

Finally, at an extremely small threshold value (γ_{fault} = 1×10^{-4}) as in Figure 4-132, a clear and distinct shape of the revealed fault is observed for the case with tight solver settings.

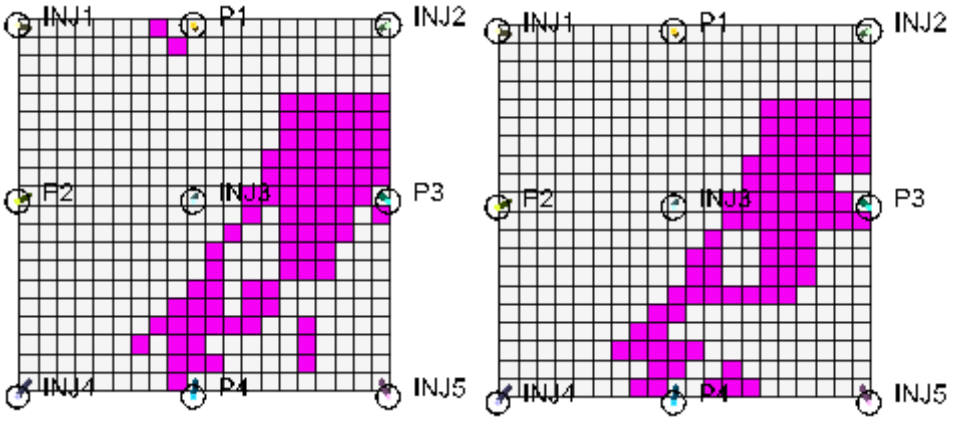

Figure 4-129: Fault indicator map generated for the default (left) and tight (right) solver settings at γ_{fault} = 1×10^{-2} for the 4th layer.

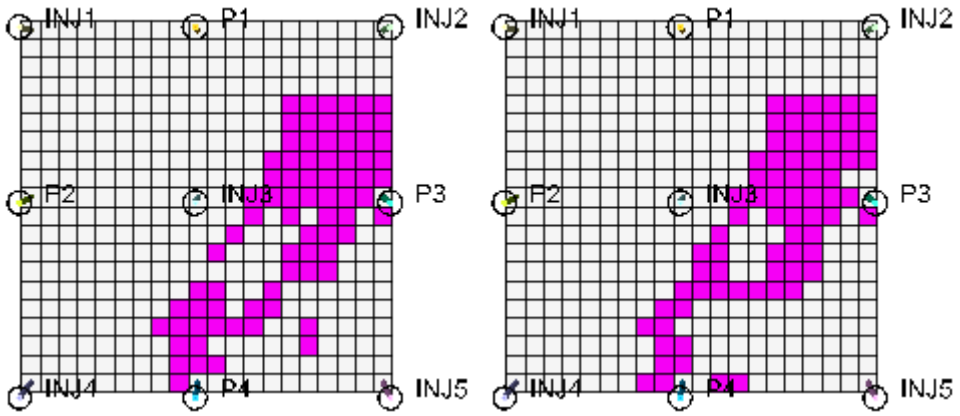

Figure 4-130: Fault indicator map generated for the default (left) and tight (right) solver settings at γ_{fault} = 5×10^{-3} for the 4th layer.

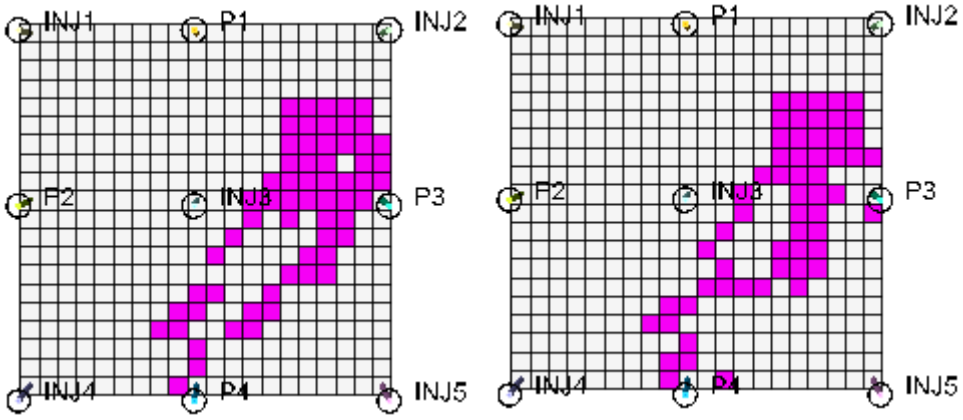

Figure 4-131: Fault indicator map generated for the default (left) and tight (right) solver settings at γ_{fault} = 1×10^{-3} for the 4th layer.

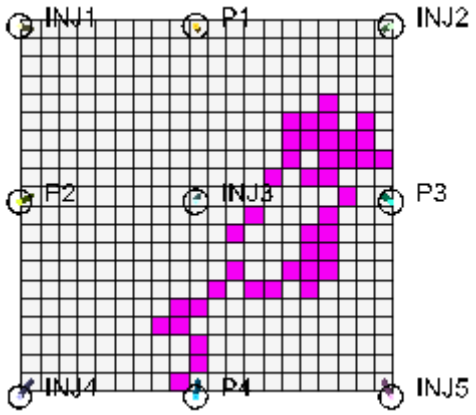

Figure 4-132: Fault indicator map generated for the tight solver settings at γ_{fault} = 1×10^{-4} for the 4th layer.

The true model fault (in thick black line) is compared to Figure 4-130 for the default solver settings with γ_{fault} = 5×10^{-3} and Figure 4-132 for the tight solver settings with γ_{fault} = 1×10^{-4} as shown in Figure 4-132. Remember that the set of connecting purple-coloured grid blocks in each fault indicator map hints at the shape of the revealed fault.

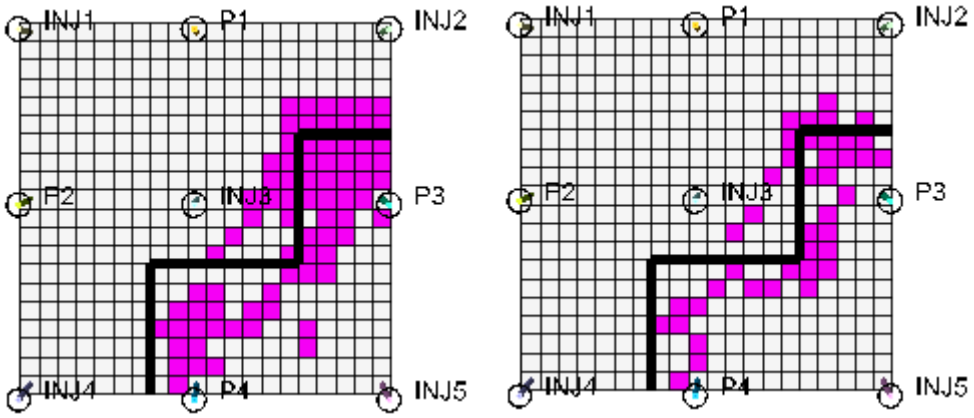

Figure 4-133: Fault indicator maps with true model fault (in thick black line) for the default (left) and tight (right) solver settings for the 4th layer.

From Figure 4-133, the fault indicator map generated for the 4th layer using tight solver settings gives a more detailed shape of the fault than that obtained using default solver settings.

4.9 Benefits from Constrained and Unconstrained History Matching

Constrained history matching (also known as classical history matching or CHM) is a conventional and acceptable history matching practice that respects model parameter uncertainty limits. On the other hand, unconstrained history matching (UHM) is only a means to reveal hidden reservoir features in reservoir simulation models by exploiting the effectiveness of the adjoint method in making modifications to model parameters particularly at grid block level. The benefits of performing CHM and UHM on reservoir

simulation models with hidden reservoir features is examined using the same multi-layered reservoir model described earlier in Section 4.8.

4.9.1 Constrained History Matching (CHM) on Base Model

In this illustration, a base model with hidden fault information is constructed as described in Section 4.8. Measured data (without Gaussian noise) is obtained from the solution of the true model (see Figure 4-126). CHM is then performed on the base model under the assumption that we have no idea that a sealing fault is hidden in the base model. Model parameters defined for the CHM problem are horizontal (K_x & K_y) and vertical (K_z) permeabilities. The permeability distribution is respected during CHM as described by Equation (48) where $K_{x_{min}}, K_{y_{min}}$ & $K_{z_{min}}$ are 35 mD, 35 mD & 3.5 mD respectively. Also, $K_{x_{max}}, K_{y_{max}}$ & $K_{z_{max}}$ are 287 mD, 287 mD & 28.7 mD respectively.

$$K_{x_{min}}, K_{y_{min}}, K_{z_{min}} \leq K_x, K_y, K_z \leq K_{x_{max}}, K_{y_{max}}, K_{z_{max}} \quad (48)$$

The permeabilities in grid block housing wells are unchanged since core data is assumed to be available for all wells. For the CHM problem, the step sizes, μ_{K_x,K_y} = 10.75 mD^2 and μ_{K_z} = 1.075 mD^2, are utilized in order to avoid divergence away from an optimal solution. A total of 110 iterations were executed in an attempt to find an optimal solution (a solution with the lowest Q). The 96th iteration is selected as the best-case since it delivered an overall model error reduction value of 16.8%. The objective function (Q) vs. number of iterations plot for the CHM problem is provided in Figure 4-134.

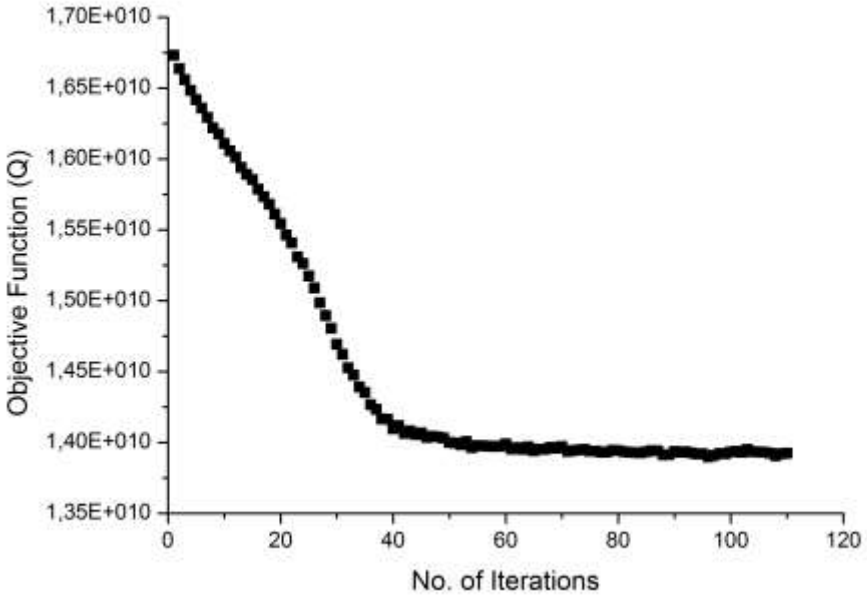

Figure 4-134: Objective function (Q) vs. number of iterations for the CHM problem.

The model responses defined for the CHM problem are well water-cut (WWCT), well oil production rate (WOPR) and well bottom-hole flowing pressure (WBHP). In Table 4-

22, the R-squared values for all model responses before and after CHM are presented. R-squared values for the base model prior to performing CHM are provided in brackets in Table 4-22. As seen in Table 4-22, by limiting the uncertainty range for permeability for the CHM problem, most model responses could not be history-matched. Reservoir simulation models with history-match results of this nature after performing CHM are perfect examples of reservoir models with hidden reservoir features. Best-case results for the most offending model responses obtained from CHM are presented in Figure 4-135.

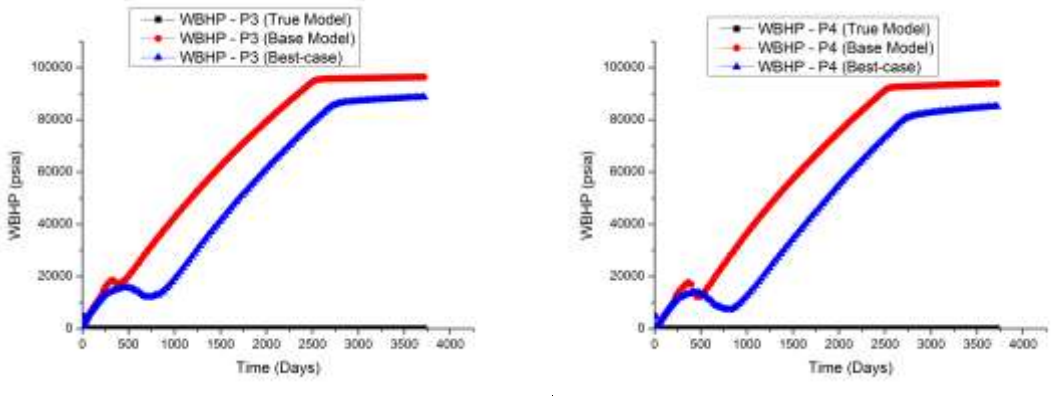

Figure 4-135: Best-case results for the most offending model responses after performing CHM on the base model.

Table 4-22: R-squared values generated for all model responses before and after CHM on the base model.

Well Name	WBHP	WWCT	WOPR
P1	87.3% (85.1%)	97.6% (98.1%)	97.2% (98.1%)
P2	86.8% (85.5%)	97.0% (97.5%)	96.6% (97.4%)
P3	8.9% (4.6%)	98.2% (99.7%)	94.7% (96.2%)
P4	8.3% (4.2%)	99.3% (97.9%)	90.1% (93.6%)
INJ1	82.0% (81.6%)	–	–
INJ2	82.1% (81.7%)	–	–
INJ3	81.7% (81.5%)	–	–
INJ4	82.8% (82.0%)	–	–
INJ5	6.6% (5.3%)	–	–
$R^2 \geq 97\%$; $R^2 < 97\%$			

4.9.2 Unconstrained History Matching (UHM) on Base Model

In an attempt to reveal the hidden reservoir feature(s) in the base model, UHM is performed. The measured data used here is the same as that of the CHM problem. Since we assumed that we have no idea that a sealing fault is hidden in the base model, the model parameters defined for the UHM problem are also horizontal (K_x & K_y) and vertical (K_z) permeabilities. The permeability distribution is not respected during UHM as described by Equation (41) where $K_{x_{max}}, K_{y_{max}}$ & $K_{z_{max}}$ represents the original or

default maximum values for permeability in the X, Y and Z direction which are 287 mD, 287 mD & 28.7 mD respectively. The permeabilities in grid block housing wells are also unchanged since core data is assumed to be available for all wells.

For the UHM problem, the step sizes, μ_{K_x,K_y} = 10.75 mD^2 and μ_{K_z} = 1.075 mD^2, is also retained. A total of 250 iterations were executed in an attempt to find an optimal solution. The 129th iteration is selected as the best-case since it delivered an overall model error reduction value of 99.5%. This suggests an improvement in history-match results by 83.1% when compared to the overall model error reduction value attained for the CHM problem (16.8%). The objective function (Q) vs. number of iterations plot for the UHM and CHM problems are jointly shown in Figure 4-136. In order to clearly show the difference in objective function progression for the UHM and CHM problems, the objective function values in Figure 4-136 are presented in logarithmic scale.

The model responses defined for the UHM problem are also well water-cut (WWCT), well oil production rate (WOPR) and well bottom-hole flowing pressure (WBHP). In Table 4-23, the R-squared values for all model responses before and after UHM are presented. R-squared values for the base model prior to performing UHM are provided in brackets in Table 4-23. In addition, best-case results for the most offending model responses obtained from UHM are presented in Figure 4-137.

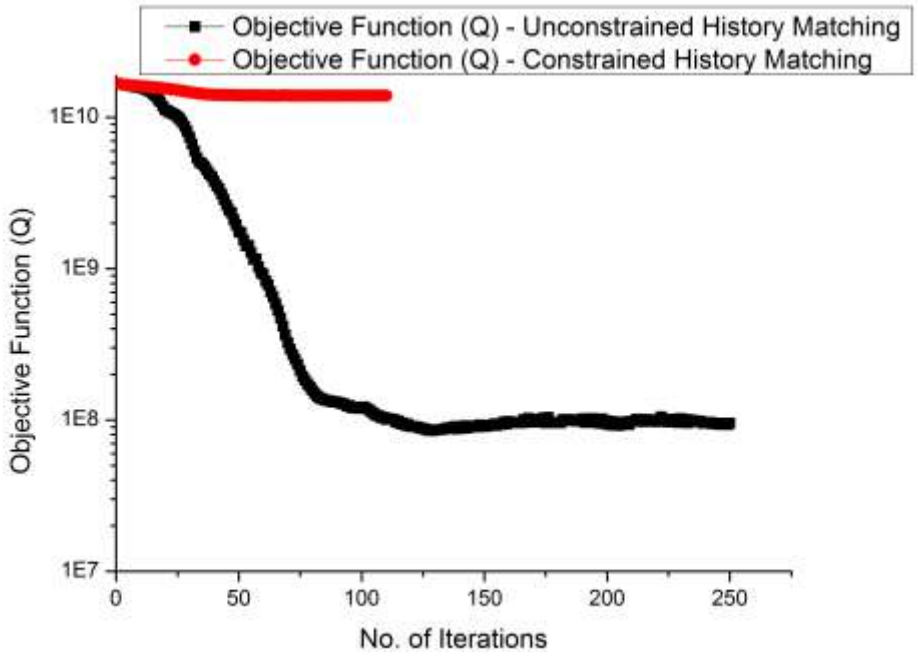

Figure 4-136: Semi-log plot of the objective function (Q) vs. number of iterations for the UHM and CHM problem.

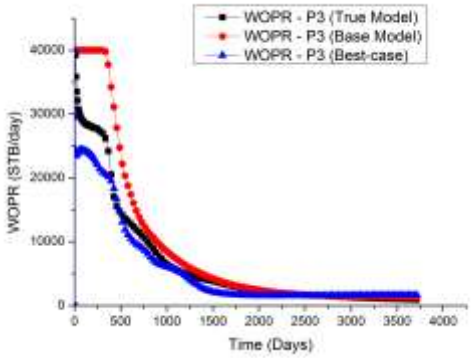

Figure 4-137: Best-case results for the most offending model responses after performing UHM performed on the base model.

Table 4-23: R-squared values generated for all model responses before and after performing UHM on the base model.

Well Name	WBHP	WWCT	WOPR
P1	99.8% (85.1%)	97.5% (98.1%)	97.2% (98.1%)
P2	99.8% (85.5%)	97.1% (97.5%)	97.1% (97.4%)
P3	99.9% (4.6%)	97.3% (99.7%)	96.4% (96.2%)
P4	99.9% (4.2%)	98.2% (97.9%)	97.6% (93.6%)
INJ1	99.8% (81.6%)	—	—
INJ2	99.9% (81.7%)	—	—
INJ3	99.8% (81.5%)	—	—
INJ4	99.8% (82.0%)	—	—
INJ5	98.3% (5.3%)	—	—
$R^2 \geq 97\%$; $R^2 < 97\%$			

As seen in Table 4-23, the effect of specifying the uncertainty limits of permeability in an unconstrained manner tremendously improved the R-squared values for the UHM problem. The next step is to apply the developed fault detection algorithm in order to reveal the approximate location and shape of the hidden fault.

The permeability ratio maps for all 5 layers present in the base model can be generated using the first part of the fault detection algorithm. In Figure 4-138, the permeability ratio map for the 3rd layer is presented which is similar to that of other layers. The yellow-coloured region represents grid blocks with little or no change in permeability. These grid blocks have a permeability ratio value of 1.0. Grid blocks coloured in dark-yellow and red have permeability ratio values greater than 1.0 due to the existing reservoir heterogeneity in the model. Grid blocks with colours such as blue and purple identifies regions with extreme permeability reduction.

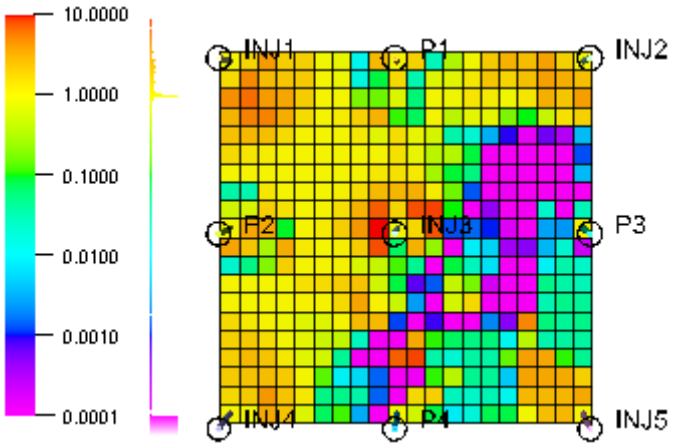

Figure 4-138: Permeability ratio map generated for the 3rd layer.

The second part of the fault detection algorithm is used to generate the fault indicator map from Figure 4-138 as shown in Figure 4-139. In Figure 4-139, the threshold value that reveals the location of the hidden fault is γ_{fault} = 5×10^{-4}. Below this threshold value, we start to lose information about the fault.

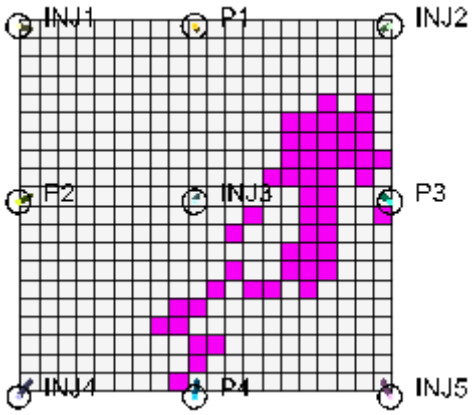

Figure 4-139: Fault indicator map generated from the permeability ratio map at γ_{fault} = 5×10^{-4} for the 3rd layer.

The true model fault (in thick black line) is compared to the revealed fault using the fault indicator map as shown in Figure 4-140. Remember that the set of connecting purple-coloured grid blocks in the fault indicator map hints at the shape of the revealed fault.

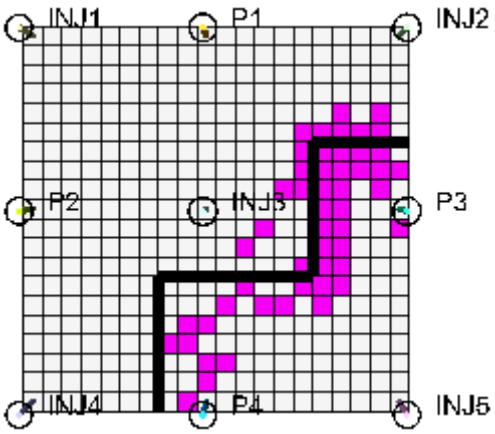

Figure 4-140: Fault indicator map with true model fault (in thick black line) generated for the 3rd layer.

Using the developed fault shape detection algorithm described in Section 4.6, the shape of the revealed fault can be objectively estimated using Figure 4-139 as an input image. The estimated fault shape in form of a fault line is presented in Figure 4-141.

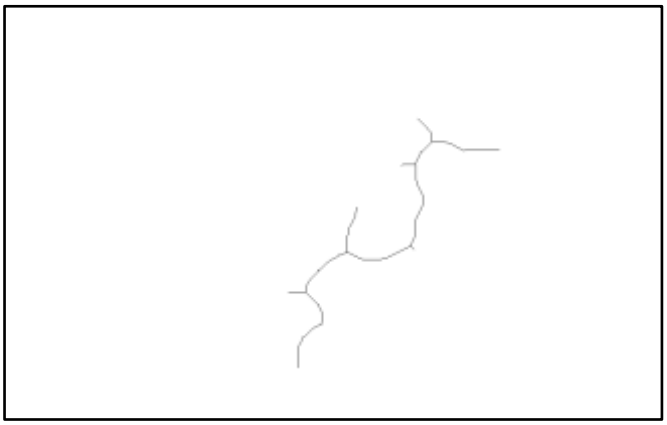

Figure 4-141: Estimated shape of revealed fault in form of a fault line.

Based on Figure 4-141, the fault introduced into the base model (in thick blue line) is shown in Figure 4-142. The true model fault is captured in thick black line in Figure 4-142. The base model with the newly introduced fault is called an "improved model".

The third part of the fault detection algorithm employs the use of a heuristic approach to determine the transmissibility multiplier across the revealed fault (or degree of sealingness or MULTFLT). Since the threshold value that reveals the fault (γ_{fault} = 5×10^{-4}) is less than 0.01, then the transmissibility multiplier across the revealed fault is set to 0.0 in the improved model (i.e. MULTFLT = 0.0 in improved model prior to performing CHM).

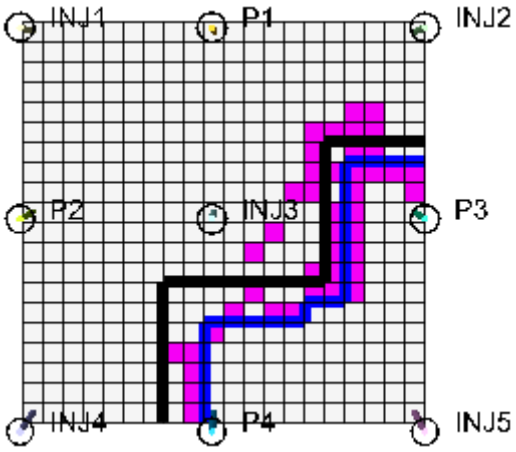

Figure 4-142: Shape of revealed fault in improved model.

4.9.3 Constrained History Matching (CHM) on Improved Model

The improved model containing the revealed fault ("REVFLT") is presented in Figure 4-143. Measured data (without Gaussian noise) is obtained from the solution of the true model (see Figure 4-126). CHM is performed on the improved model with K_x, K_y, K_z & the transmissibility multiplier across the revealed fault (MULTFLT) defined as model parameters for the CHM problem. The original permeability distribution is respected during CHM as described by Equation (48). In addition, the transmissibility multiplier across the revealed fault (MULTFLT) is allowed to vary between 0.0 and 1.0 during CHM. The permeabilities in grid block housing wells in the improved model are unchanged as well since core data is assumed to be available for all wells.

For the CHM problem, the step sizes, μ_{K_x,K_y} = 10.75 mD^2 and μ_{K_z} = 1.075 mD^2, are also retained. A total of 10 iterations were needed to find an optimal solution. The 9th iteration is selected as the best-case since it delivered an overall model error reduction value of 76.9%. The objective function (Q) vs. number of iterations plot capturing the CHM and UHM problems are shown in Figure 4-144.

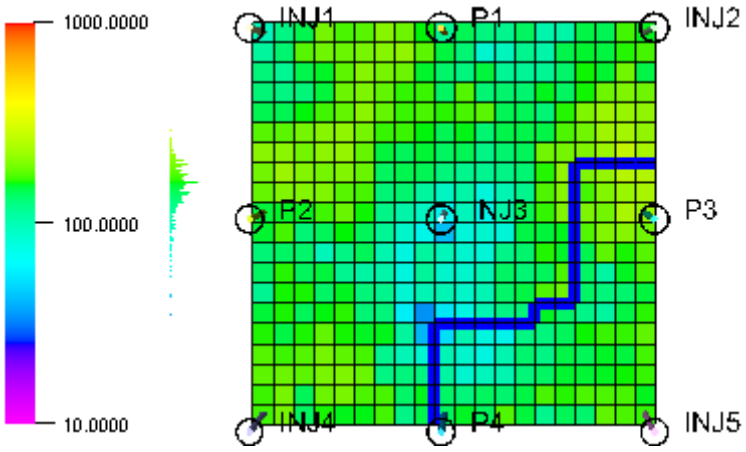

Figure 4-143: Improved model capturing permeability distribution and revealed fault (in thick blue line).

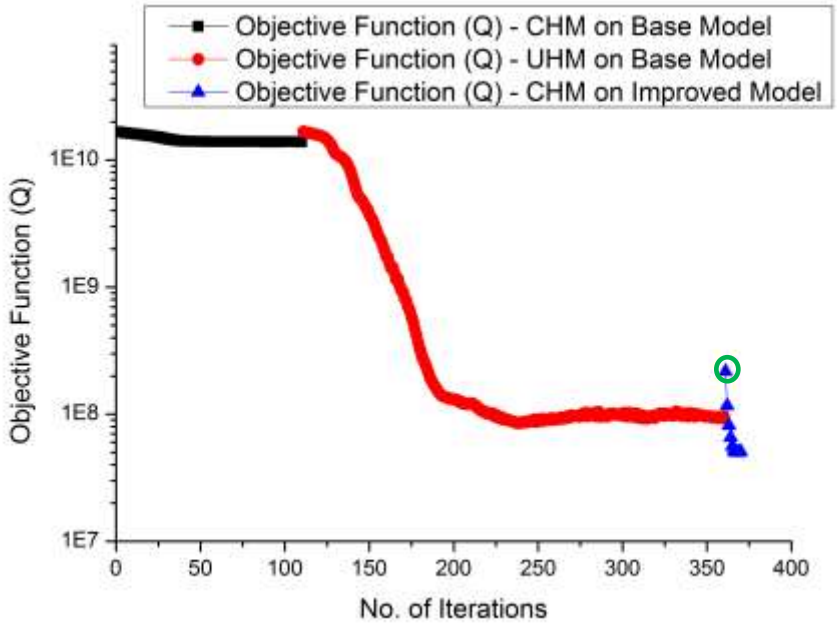

Figure 4-144: Semi-log plot of the objective function (Q) vs. number of iterations for all CHM and UHM performed.

In Figure 4-144, the objective function (Q) is in logarithmic scale while the number of iterations are in Cartesian scale. The objective function vs. number of iterations plot represented in black is that of CHM on the base model which required 110 iterations. The plot in red describes the progression of the objective function with increasing number of iterations for UHM performed on the base model. As seen in Figure 4-144, a total of 250 iterations were executed for UHM performed on the base model. The objective function vs. number of iterations plot for CHM on the improved model is represented in blue in Figure 4-144. The first objective function value encircled in green is a measure of error inherent in the improved model prior to the commencement of CHM. The jump in error after introducing the revealed fault into the base model is as a result of the differences in permeability distribution between the best-case model resulting from UHM and the base model. Only the revealed fault is introduced in the base model.

The model responses defined for the CHM problem are also well water-cut (WWCT), well oil production rate (WOPR) and well bottom-hole flowing pressure (WBHP). In Table 4-24, the R-squared values for all model responses before and after CHM on the improved model are presented. R-squared values for the improved model prior to performing CHM are provided in brackets in Table 4-24. In addition, best-case results for the most offending model responses obtained from CHM are presented in Figure 4-145.

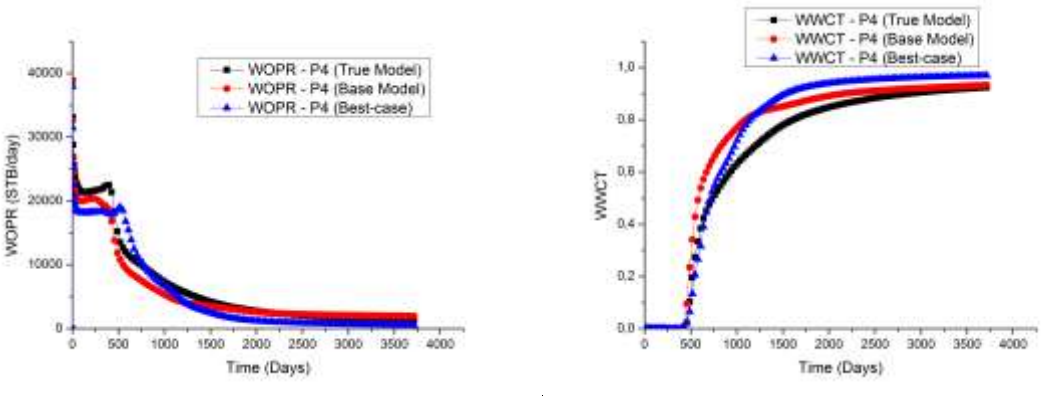

Figure 4-145: Best-case results for the most offending model responses after CHM performed on the improved model.

Table 4-24: R-squared values generated for all model responses before and after CHM on the improved model.

Well Name	WBHP	WWCT	WOPR
P1	99.9% (99.4%)	99.9% (99.9%)	99.9% (99.9%)
P2	99.9% (99.5%)	99.9% (99.8%)	99.9% (99.9%)
P3	99.9% (82.1%)	99.9% (99.6%)	99.2% (98.3%)
P4	99.9% (99.9%)	97.3% (98.0%)	97.5% (98.6%)
INJ1	99.9% (99.4%)	—	—
INJ2	99.9% (99.4%)	—	—
INJ3	99.9% (99.5%)	—	—
INJ4	99.9% (99.4%)	—	—
INJ5	99.6% (93.7%)	—	—
$R^2 \geq 97\%$; $R^2 < 97\%$			

As seen in Table 4-24, all model responses specified for each well are very well calibrated to measured data. This is indicated by the improvement in R-squared values recorded across all model responses. The history-matched improved model is in agreement with measured data when compared to the base model. In addition, as shown in Table 4-25, the assumed transmissibility multiplier across the revealed fault (MULTFLT = 0.0) based on the fault detection algorithm is approximately the same as the MULTFLT estimated from CHM. This proves that our proposed method can be used to improve reservoir characterization in reservoir simulation models with hidden reservoir features.

Table 4-25: Comparison between the MULTFLT of the revealed fault based on the fault detection algorithm and that estimated from CHM.

Revealed Fault	Initial MULTFLT based on Fault Detection Algorithm	Estimated MULTFLT from CHM
"REVFLT"	0.0	1.1×10^{-7}

Figure 4-146 presents a histogram plot that compares the initial/true permeability distribution to the best-case permeability distribution after performing CHM on the improved model. The lines between histogram columns are shown for each permeability distribution. Also, the initial/true K_x distribution is exactly the same as that of K_y. As seen in Figure 4-146, modifications made to permeability during CHM on the improved model are not extreme. These modifications are limited to the vicinity of wells in order to improve history-match results. Figure 4-146 also demonstrates the capability of the proposed method in maintaining geological consistency in the improved model.

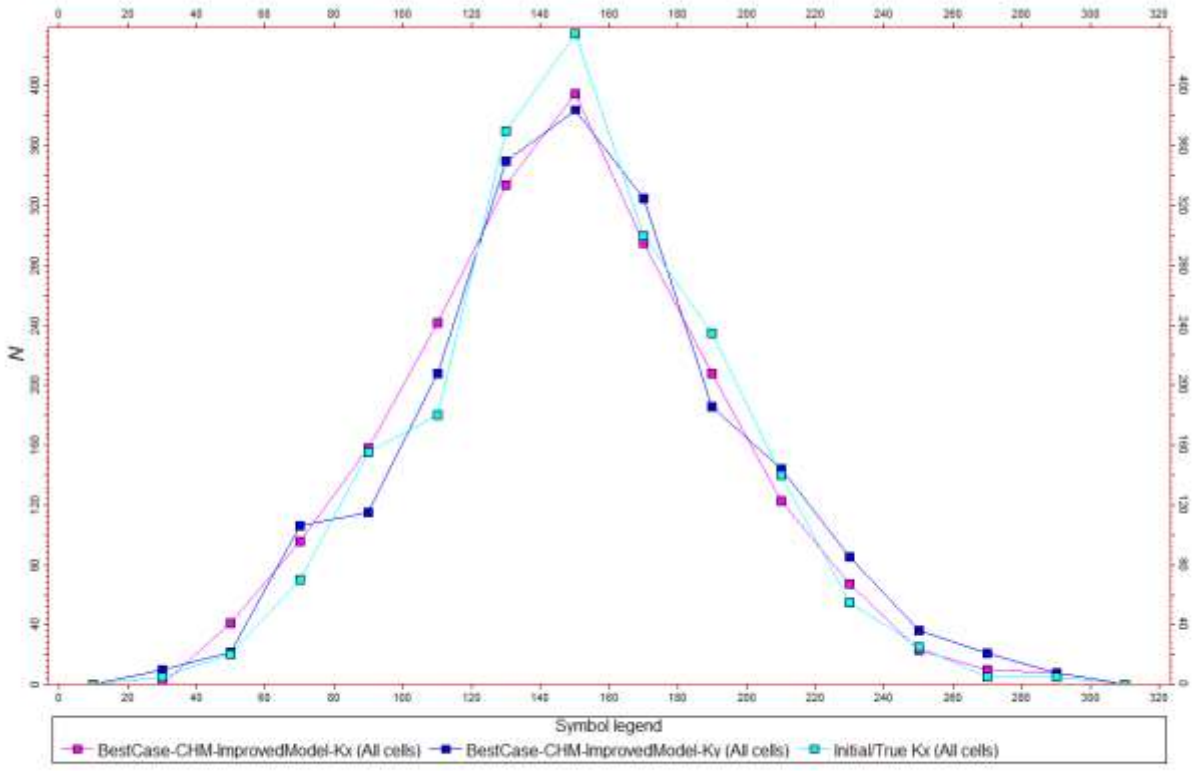

Figure 4-146: Comparison between initial/true permeability distribution and the best-case permeability distribution after CHM on improved model.

4.10 Limitations of the Proposed Method

Despite the level of success recorded so far by the proposed method when compared to the most prominent state-of-the-art methods available in literature, the proposed method suffers from a few limitations namely:

1. Hidden reservoir features located outside well-dominated regions may not be revealed.
2. Sealing faults lying in extremely low permeability regions may not be revealed.
3. Hidden reservoir features existing between two injectors may not be revealed since injector-injector interactions are not taken into consideration. This is as a result of the water front from both injectors cancelling out.
4. The proposed method may not be robust against increasing numerical noise from the numerical reservoir simulator.
5. Observed data with noise/error greater than ±15% can negatively impact the proposed method.
6. Depending on the complexity of the reservoir simulation model to be checked for reservoir characterization issues, it may be necessary to execute all reservoir feature detection algorithms in order to obtain information on the type of reservoir feature that is hidden.

Chapter 5

> "You have to continually press yourself to convert information into action"
>
> John Masters (1914-1983)

5. Application to Real Field Cases

In this chapter, the proposed method is tested with one of the reservoir simulation models received from project sponsors. Other application cases are documented in DGMK project reports which are available only to project sponsors. The reservoir simulation model reported here is developed from real field data. This model is constructed from a field that is still in production till today. Consequently, not much information about the field, well names or other detailed reservoir information are made available in this chapter. Also, an attempt is made to evaluate the effectiveness of the proposed method in cases where an ensemble of reservoir simulation models are required for quantifying uncertainty in the prediction phase. These models are named OLMYPUS reservoir models and they are based on real field data obtained from a virgin oil field in the North Sea. However, the production data for the OLYMPUS models are synthetic.

5.1 DGMK Sponsor Model I

DGMK sponsor model I is a 3-D heterogeneous, faulted oil reservoir with dissolved gas, water and free gas present in the model at initialization. The model structure, petrophysical and fluid properties as well as production data are all based on real field data.

5.1.1 Reservoir Description

The model dimensions are 51 x 30 x 223. The entire model contains a total of 341190 grid blocks and only 27239 grid blocks are active. A total of 9 faults are present in the

model. 8 wells exists in the model - 1 vertical water injector, 5 vertical producers and 2 horizontal producers. Reservoir permeability in the X, Y and Z direction are not isotropic and they vary hugely from 0.02 mD to 13 Darcy. Reservoir porosity varies from 0.1 % to 19%. A total of 3 equilibration regions and 6 fluid-in-place regions exists in the model. One relative permeability curve is representative of the saturation region in the entire model. Also, one PVT table (each for oil, water & gas) exists for the entire model. The total production period is approximately 13 years and all producers are reservoir fluid volume rate controlled (RESV-controlled). This means that production rate from each producer is determined from the average reservoir pressure in the field. The injector is water rate-controlled.

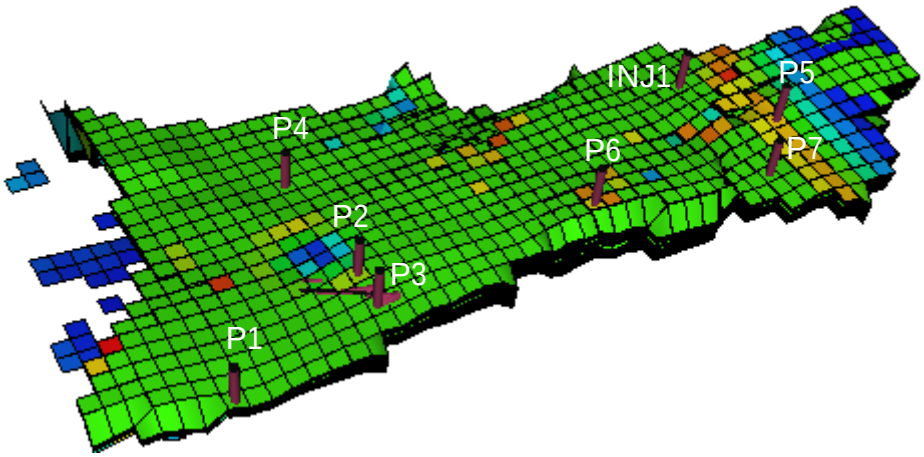

Figure 5-1: Structure of the DGMK sponsor model I.

5.1.2 Constrained History Matching (CHM) on DGMK Sponsor Model I

The model parameters defined for CHM performed on the DGMK sponsor model I are K_x, K_y, K_z, $\emptyset$, transmissibility multiplier across all 9 existing faults (MULTFLTs) and the oil-water and gas-oil relative permeability parameters (i.e. Swi, Sor, N_o, $N_w, N_g, Kro_{max}, Krw_{max}, Krg_{max}$ etc.). Swi & Sor are the initial water saturation and residual oil saturation. N_o, N_w & N_g are the Corey oil, water and gas exponents. Kro_{max}, Krw_{max} & Krg_{max} are the maximum oil, water and gas relative permeability values respectively. These model parameters identified by the sponsor are said to be highly uncertain. Weighting is also implemented for each defined model responses according to their degree of mismatch.

The permeability and porosity distribution are respected during CHM as described by Equation (49) where $K_{x_{min}}, K_{y_{min}}, K_{z_{min}}$ & $\emptyset_{min}$ are the minimum permeability and porosity values. $K_{x_{max}}, K_{y_{max}}, K_{z_{max}}$ & $\emptyset_{max}$ are the maximum permeability and porosity values.

$$K_{x_{min}}, K_{y_{min}}, K_{z_{min}}, \emptyset_{min} \leq K_x, K_y, K_z, \emptyset \leq K_{x_{max}}, K_{y_{max}}, K_{z_{max}}, \emptyset_{max} \quad (49)$$

The permeabilities and porosities in grid block housing all 8 wells are unchanged since core data is available for these wells. For the CHM problem, the step sizes μ_{K_x} = 50 mD^2, μ_{K_y} = 26 mD^2, μ_{K_z} = 10 mD^2 and $\mu_{\emptyset}$ = 0.01 are utilized in order to avoid divergence away from an optimal solution. A total of 50 iterations were executed in an attempt to find an optimal solution. The 28th iteration is selected as the best-case since it delivered an overall model error reduction value of 89.7%. The objective function (Q) vs. number of iterations plot for the CHM problem is shown in Figure 5-2.

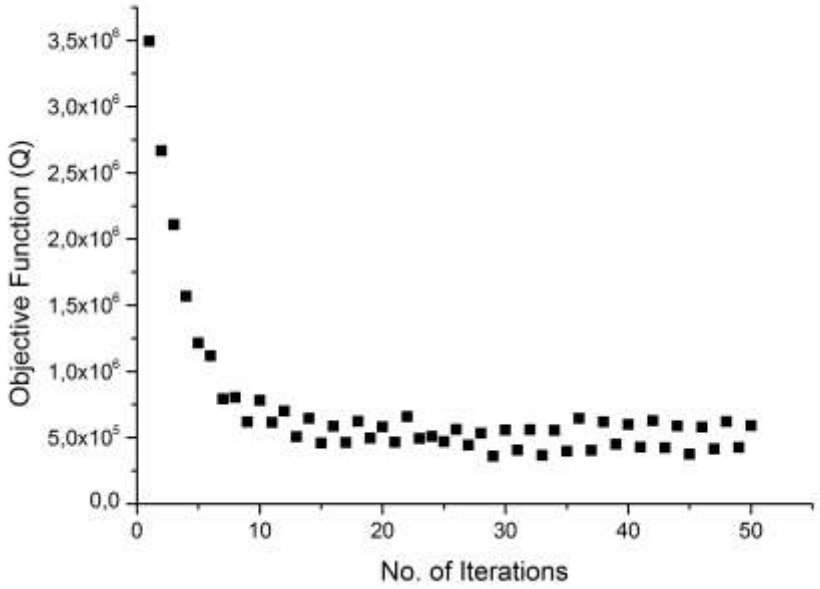

Figure 5-2: Objective function (Q) vs. number of iterations for CHM performed on DGMK sponsor model I.

The model responses defined for the CHM problem are well water-cut (WWCT), well oil production rate (WOPR), well gas production rate (WGPR), well water injection rate (WWIR) and well bottom-hole flowing pressure (WBHP). In Table 5-1, the R-squared values for all model responses before and after CHM are presented. R-squared values for the DGMK sponsor model I prior to performing CHM are enclosed in brackets in Table 5-1. As mentioned earlier, R-squared values are used to describe the history-match quality of model responses. In this evaluation, an R-squared value greater than or equal to 90% means that a very good history-match is achieved while an R-squared value less than 90% means that a satisfactory or poor history-match is achieved. R-squared values for WBHP are not provided in Table 5-1 because very few measured BHP data points are available for each well. This introduced some bias in the calculation of their R-squared values. Best-case results for the most offending model responses obtained from CHM are presented in Figure 5-3.

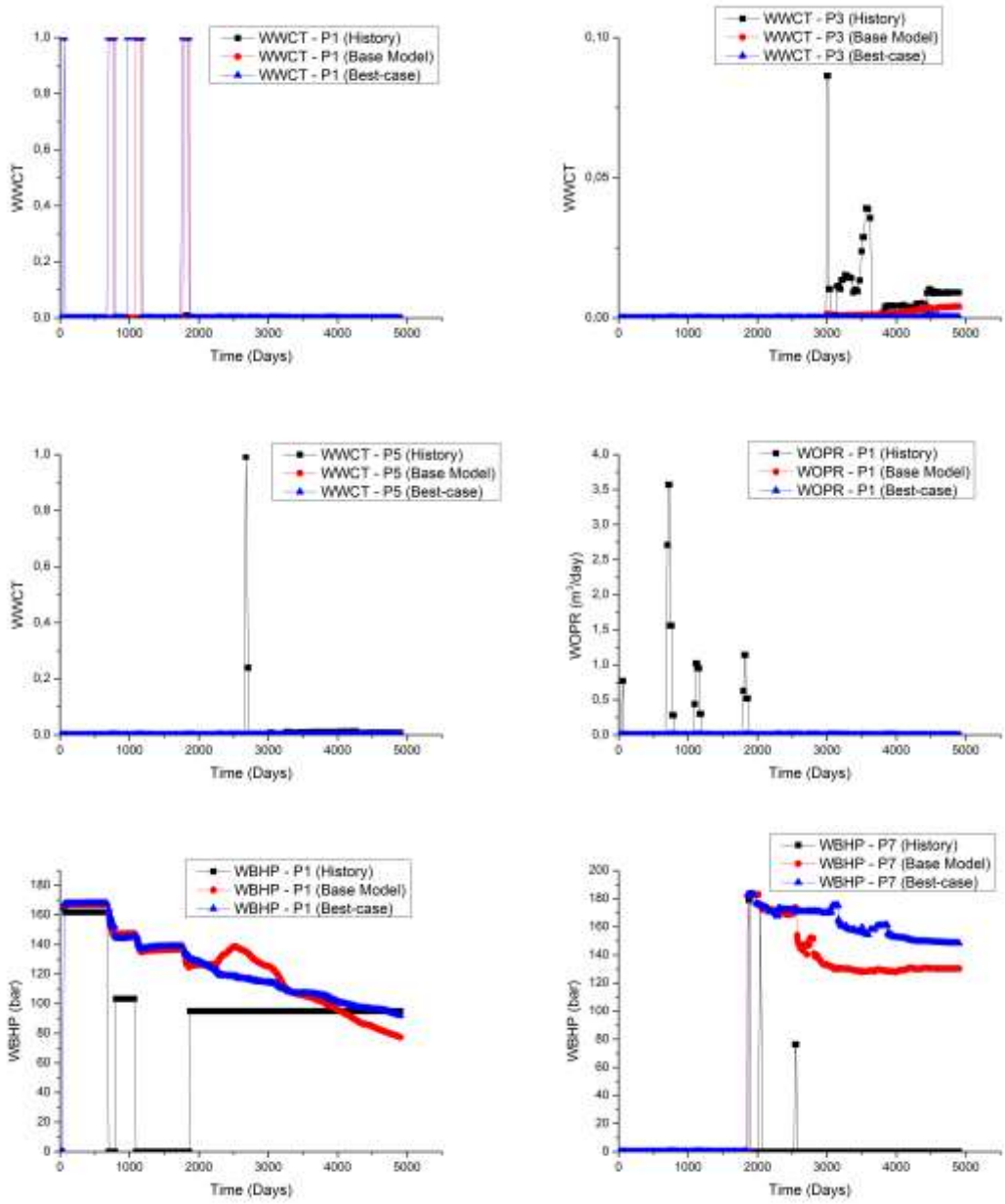

Figure 5-3: Best-case results for the most offending model responses after CHM performed on the DGMK sponsor model I.

Table 5-1: R-squared values generated for all model responses before and after CHM performed on the DGMK sponsor model I.

Well Name	WWCT	WOPR	WGPR	WWIR
P1	11.3% (10.4%)	20.4% (13.6%)	100.0% (100.0%)	–
P2	92.9% (73.1%)	94.1% (75.8%)	97.2% (93.5%)	–
P3	12.3% (12.0%)	97.9% (88.8%)	99.8% (98.6%)	–
P4	100.0% (100.0%)	100.0% (100.0%)	100.0% (100.0%)	–
P5	0.0% (0.0%)	97.9% (97.2%)	99.0% (99.0%)	–
P6	87.4% (85.5%)	98.3% (70.8%)	83.0% (85.5%)	–
P7	93.6% (58.0%)	97.0% (16.6%)	99.9% (99.8%)	–

INJ1	–	–	–	99.6% (99.9%)
$R^2 \geq 90\%$; $R^2 < 90\%$				

From Table 5-1, most of the oil and gas production rates for most producers are history-matched very well. However, the water-cut history-match results for most of the producers are relatively poor. The term "relatively" is used here because visual comparison of the measured data and simulated results in Figure 5-3 for these wells may suggest otherwise. This is just how harsh the R-squared method is for analysing the fitness of measured data to their respective simulated results. Although not shown in Table 5-1, most of the WBHP history-match results for most wells are very good with the exception of P1 and P7 which are shown in Figure 5-3.

A comparison of the base model and the best-case fault transmissibility multiplier after performing CHM is presented in Table 5-2. As seen in Figure 5-4, no significant changes in oil-water and gas-oil relative permeability curves is observed after performing CHM on the DGMK sponsor model I. Table 5-3 presents the stock tank oil initially in place (STOIIP), stock tank water initially in place (STWIIP) and gas initially in place (GIIP) before and after CHM.

Table 5-2: Comparison between the base model and the best-case MULTFLTs after CHM on the DGMK sponsor model I.

Fault Name	Base Model MULTFLT	Best-case MULTFLT
"Fault1"	0.5	0.2
"Fault2"	0.5	0.5
"Fault3"	0.0	0.0
"Fault4"	0.0	0.05
"Fault5"	0.5	0.02
"Fault6"	0.5	0.3
"Fault7"	0.5	0.1
"Fault8"	0.0	0.09
"Fault9"	0.5	0.65

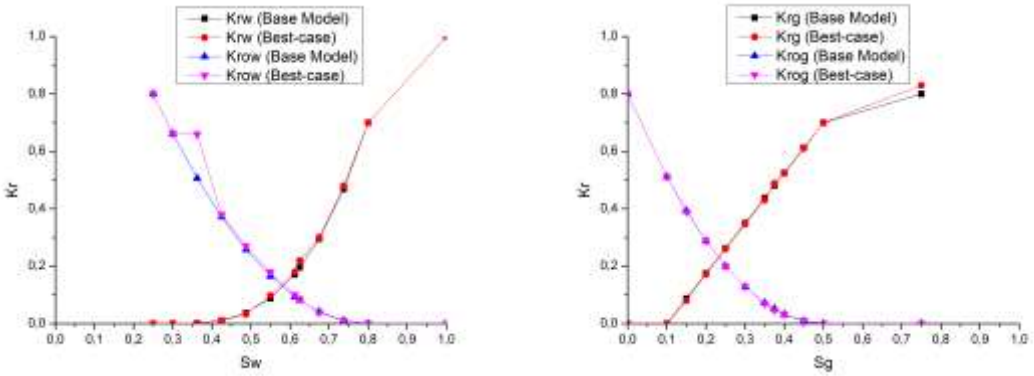

Figure 5-4: Base model vs. best-case oil-water (left) and gas-oil (right) relative permeability curves after CHM on the DGMK sponsor model I.

Table 5-3: STOIIP, STWIIP and GIIP before and after CHM on the DGMK sponsor model I.

Phase	Base Model	Best-case	% Increase (+) or % Decrease (-)
STOIIP (m^3)	0.98×10^6	1.01×10^6	+3.1
STWIIP (m^3)	6.36×10^6	6.59×10^6	+3.6
GIIP (m^3)	1.58×10^8	1.73×10^8	+9.5

5.1.3 Unconstrained History Matching (UHM) on DGMK Sponsor Model I

The UHM process is executed in an attempt to improve the history-match results obtained with CHM. The model parameters defined for the UHM problem are permeabilities (K_x, K_y & K_z) and porosity only. The best-case MULTFLTs for all 9 existing faults and best-case oil-water and gas-oil relative permeability curves from CHM are retained in DGMK sponsor model I. Only permeabilities and porosity are defined as model parameters in the UHM stage. In addition, the permeability and porosity distributions are not respected during UHM as described by Equation (48) where $K_{x_{min}}, K_{y_{min}}, K_{z_{min}}$ & $\emptyset_{min}$ are the minimum permeability and porosity values and are set to 0.0. $K_{x_{max}}, K_{y_{max}}, K_{z_{max}}$ are equally set to 13 Darcy while $\emptyset_{max}$ is set to 19%. The permeabilities and porosities in grid block housing wells are also unchanged since core data is assumed to be available for all wells. Weighting is also implemented for each defined model responses according to their degree of mismatch.

For the UHM problem, the step sizes μ_{K_x} = 100 mD^2, μ_{K_y} = 100 mD^2, μ_{K_z} = 100 mD^2 and $\mu_{\emptyset}$ = 0.02 are utilized. A total of 50 iterations were executed in an attempt to find an optimal solution. The best-case result obtained from UHM showed no significant improvement for all model responses. In other words, the UHM and CHM results were very much similar for all model responses. Table 5-1 is also a representative result for UHM on the DGMK sponsor model I. This is so because the initial permeability and porosity distribution appears unconstrained already (i.e. permeability = 0.5 mD - 13 Darcy and porosity = 0.1% - 19%). The next step is to apply the formulated reservoir

feature detection algorithms to the best-case result obtained from UHM in order to reveal one or more hidden reservoir features.

5.1.3.1 Fault Detection Algorithm applied to DGMK Sponsor Model I

The fault detection algorithm (see Section 4.4.1) is applied in order to reveal hidden faults. The permeability ratio map generated for the 197th layer using the first part of the fault detection algorithm is shown in Figure 5-5. The light-green-coloured regions represents grid blocks with little or no change in permeability. These grid blocks have a permeability ratio value of 1.0. Grid blocks coloured in green have permeability ratio values greater than 1.0 because of existing reservoir heterogeneity in the model. Grid blocks coloured in blue and purple identifies regions with extreme permeability reduction.

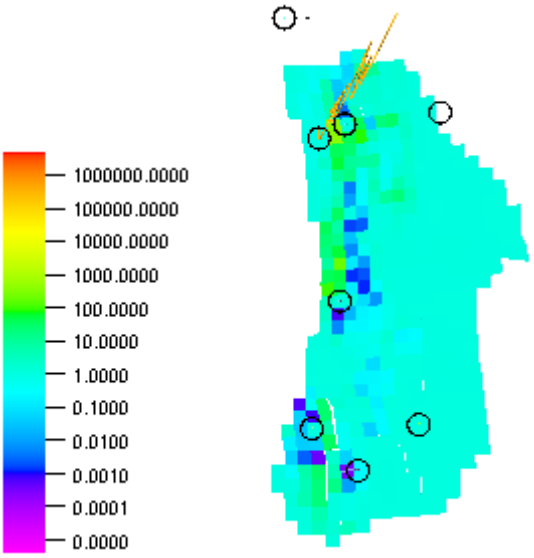

Figure 5-5: Permeability ratio map generated for the 197th layer of the DGMK sponsor model I.

The second part of the fault detection algorithm is used to generate the fault indicator map from Figure 5-5 as shown in Figure 5-6. In Figure 5-6, the threshold value that reveals the location of the hidden fault is $\gamma_{fault} = 5\times10^{-2}$. Below this threshold value, we start to lose information about the fault. Remember that the set of connecting purple-coloured grid blocks in Figure 5-6 hints at the shape of the revealed fault.

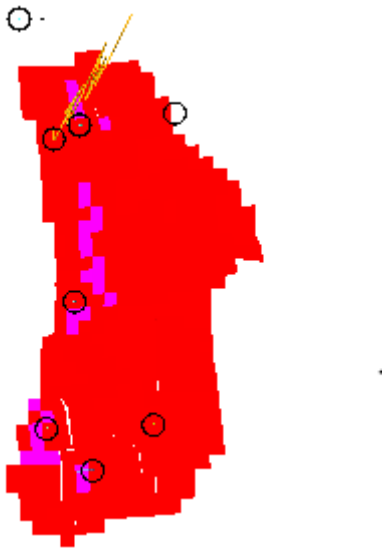

Figure 5-6: Fault indicator map generated from the permeability ratio map at γ_{fault} = 5×10^{-2} for the 197th layer of the DGMK sponsor model I.

Using the developed fault shape detection algorithm described in Section 4.6, the shape of the revealed fault can be objectively estimated using Figure 5-6 as an input image. The estimated fault shape in form of fault lines is presented in Figure 5-7.

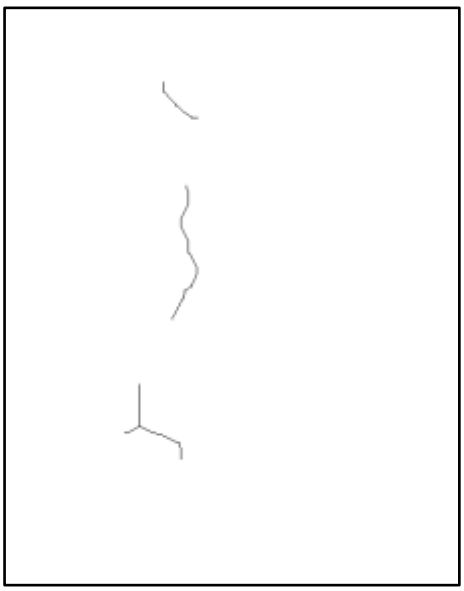

Figure 5-7: Estimated shape of revealed faults in the 197th layer.

In some of the other producing layers, faults are revealed as well. Each of the revealed fault exist at different layers. In some cases, a revealed fault extends beyond one layer. A total of 16 faults were revealed using the fault detection algorithm. Figure 5-8 presents the fault network of the DGMK sponsor model I before and after UHM. The black circles represents well locations. The shape of the 16 faults revealed are based on estimated fault shapes suggested by the fault shape detection algorithm.

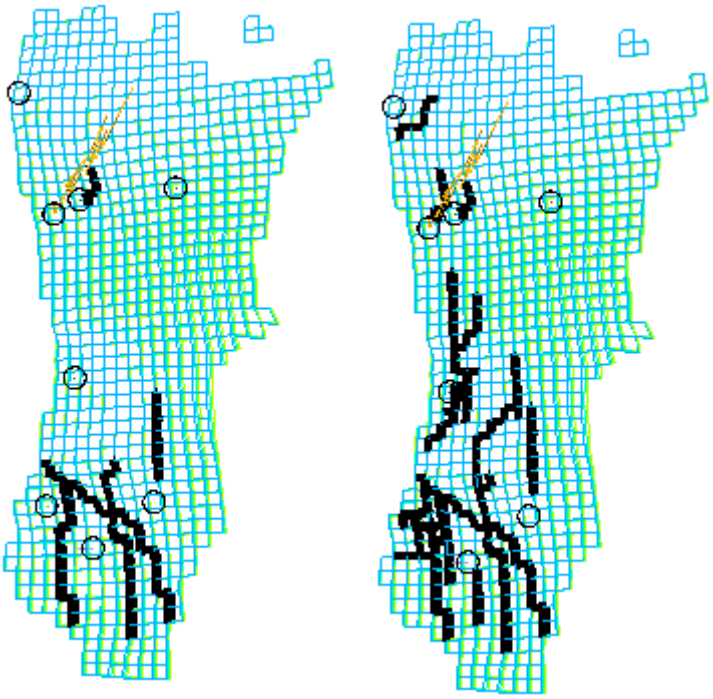

Base Model Best-case from UHM

Figure 5-8: Fault network of the DGMK sponsor model I before and after UHM.

The third part of the fault detection algorithm employs the use of a heuristic approach to determine the transmissibility multiplier across all 16 revealed faults (or degree of sealingness or MULTFLTs). Since the threshold value that revealed all 16 faults is greater than 0.01, then the transmissibility multiplier across the revealed fault is set to 0.05 in the improved model (i.e. MULTFLTs for all 16 revealed faults = 0.05 in improved model prior to CHM).

Other formulated reservoir feature detection algorithms like the channel/fracture and aquifer detection algorithms were applied as well however, results obtained showed no channel(s) connecting the injector INJ1 to any producers. In addition, no hidden aquifer/water body is detected. Channels were revealed that connected only producers (P2, P3 & P6) however this was not taken into consideration in the improved model as this could be indicative of a wrong permeability distribution. Besides, by performing CHM on the improved DGMK sponsor model I with permeability defined as part of the model parameters, the permeability values can be corrected.

5.1.4 Constrained History Matching (CHM) on the Improved DGMK Sponsor Model I

CHM is performed on the improved DGMK sponsor model I. The improved DGMK sponsor model I is the new base model containing all revealed 16 faults from UHM. Each revealed fault is assigned a MULTFLT of 0.05 as estimated from the fault detection algorithm. In all, a total of 25 faults exists in the improved DGMK sponsor model I. The model parameters defined for the CHM problem are porosity, permeabilities (K_x, K_y, K_z)

and the transmissibility multiplier across only the 16 revealed faults. The best-case oil-water and gas-oil relative permeability curves from CHM on the original DGMK sponsor model I are retained since they did not differ strongly from the base model relative permeability curves. Weighting is implemented for all defined model responses according to their degree of mismatch. The original permeability and porosity distribution are respected during CHM as described by Equation (49). In addition, the transmissibility multiplier across all 16 revealed faults are allowed to vary between 0.0 and 1.0 during CHM. The permeabilities and porosities in grid block housing wells in the improved model are unchanged as well since core data is assumed to be available for all wells.

For CHM on the improved DGMK sponsor model I, the step sizes μ_{K_x} = 50 mD^2, μ_{K_y} = 26 mD^2, μ_{K_z} = 10 mD^2 and $\mu_{\emptyset}$ = 0.01 are utilized. A total of 20 iterations were needed to find an optimal solution. The 8th iteration is selected as the best-case since it delivered an overall model error reduction value of 3.2%. A semi-log plot of the objective function (Q) vs. number of iterations capturing CHM on the original and improved DGMK sponsor model I is shown in Figure 5-9. It is important to mention that the objective function vs. number of iteration plot for CHM on the original DGMK sponsor model I is very much similar to the objective function progression realized during UHM.

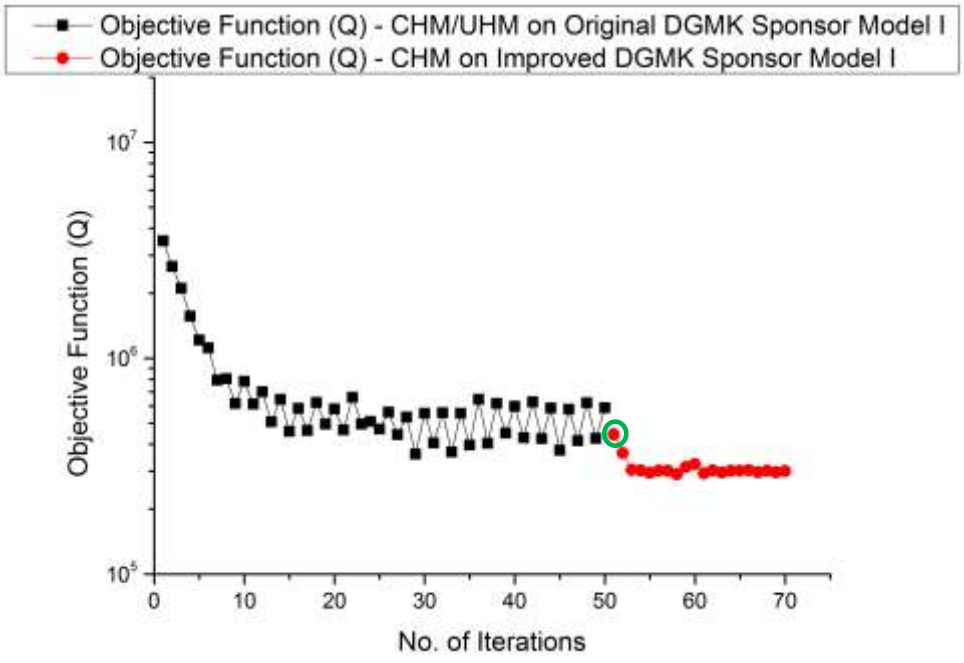

Figure 5-9: Semi-log plot of objective function (Q) vs. number of iterations for all CHM and UHM performed on the DGMK sponsor model I.

In Figure 5-9, the objective function (Q) is in logarithmic scale while the number of iterations is in Cartesian scale. The objective function vs. number of iterations plot represented in black is that of the CHM on the original DGMK sponsor model I which required 50 iterations. The same plot is representative of the UHM performed on the original DGMK sponsor model I. The plot in red describes the progression of the objective

function with increasing number of iterations for CHM performed on the improved DGMK sponsor model I. The first objective function value encircled in green is a measure of error inherent in the improved DGMK sponsor model I prior to the commencement of CHM. The jump in error after introducing all 16 revealed faults is as a result of the differences in permeability and porosity distribution between the best-case result from CHM/UHM and the original model.

All model responses defined earlier (i.e. WWCT, WOPR, WGPR, WBHP & WWIR) are retained. There were significant improvements observed in some model responses (WOPR@P6, WOPR@P7 and WWIR@INJ1). However, the most offending model responses (WWCT@P1, WWCT@P3, WWCT@P5, WOPR@P1, WBHP@P1 and WBHP@P7) showed no significant improvements. In Table 5-4, the R-squared values for all model responses before and after CHM on the improved DGMK sponsor model I are presented. R-squared values for the improved DGMK sponsor model I prior to performing CHM are provided in brackets in Table 5-4.

Table 5-4: R-squared values generated for all model responses before and after CHM on the improved DGMK sponsor model I.

Well Name	WWCT	WOPR	WGPR	WWIR
P1	12.7% (11.1%)	24.5% (18.4%)	100.0% (100.0%)	–
P2	93.4% (75.7%)	95.5% (87.3%)	98.1% (95.0%)	–
P3	20.2% (15.1%)	98.2% (89.6%)	99.2% (98.0%)	–
P4	100.0% (100.0%)	100.0% (100.0%)	100.0% (100.0%)	–
P5	2.2% (0.5%)	98.8% (97.8%)	98.9% (98.2%)	–
P6	90.1% (87.1%)	98.9% (85.7%)	86.0% (81.5%)	–
P7	96.2% (83.4%)	98.6% (80.6%)	99.8% (99.7%)	–
INJ1	–	–	–	100.0% (99.9%)
$R^2 \geq 90\%$; $R^2 < 90\%$				

Furthermore, a comparison is made between the estimated MULTFLT = 0.05 for all 16 revealed faults based on the fault detection algorithm and that obtained after CHM performed on the improved DGMK sponsor model I. Results are presented in Table 5-5. Except in very few cases, the MULTFLTs estimated from CHM are mostly in agreement with the MULTFLTs estimated using the fault detection algorithm.

Table 5-5: Comparison between the MULTFLTs for all 16 revealed faults estimated using the fault detection algorithm and that estimated from CHM performed on the improved DGMK sponsor model I.

Revealed Fault	Initial MULTFLT based on Fault Detection Algorithm	Estimated MULTFLT from CHM
"REVFLT1"	0.05	0.05
"REVFLT2"	0.05	0.05
"REVFLT3"	0.05	0.05
"REVFLT4"	0.05	0.11
"REVFLT5"	0.05	0.004
"REVFLT6"	0.05	0.002
"REVFLT7"	0.05	0.11
"REVFLT8"	0.05	0.001
"REVFLT9"	0.05	0.001
"REVFLT10"	0.05	0.004
"REVFLT11"	0.05	0.05
"REVFLT12"	0.05	0.05
"REVFLT13"	0.05	0.005
"REVFLT14"	0.05	0.07
"REVFLT15"	0.05	0.004
"REVFLT16"	0.05	0.002

Figure 5-10 presents a histogram plot that compares the initial porosity distribution to the best-case porosity distribution after CHM on the improved DGMK sponsor model I. The lines between histogram columns are shown for each porosity distribution. As seen in Figure 5-10, small modifications are made to grid block porosities around the vicinity of wells in order to achieve good history-match results. The initial and final porosity distribution are not so different. Figure 5-10 also shows the capability of the proposed method in maintaining geological consistency in the improved model.

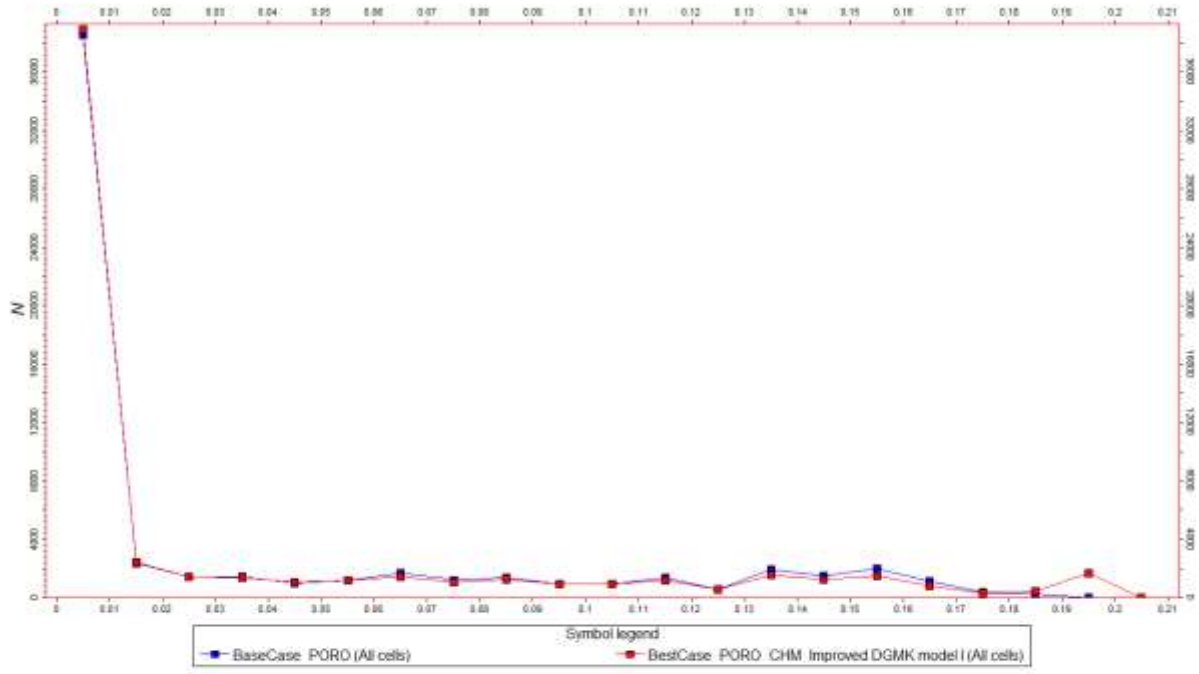

Figure 5-10: Comparison between initial porosity distribution and the best-case porosity distribution after CHM on improved DGMK sponsor model I.

STOIIP, STWIIP and GIIP values for the original DGMK sponsor model I, improved DGMK sponsor model I and best-case result from CHM performed on improved DGMK sponsor model I are presented in Table 5-6. No significant changes in STOIIP is observed. The increase in STWIIP and GIIP is driven by the need to history-match producers producing less water and gas.

Table 5-6: STOIIP, STWIIP and GIIP for the original DGMK sponsor model I, improved DGMK sponsor model I and the best-case result from CHM on improved DGMK sponsor model I.

Phase	Original DGMK Sponsor Model I	Improved DGMK Sponsor Model I	Best-case result from CHM on Improved DGMK Sponsor Model I
STOIIP (m^3)	0.98×10^6	1.01×10^6	1.02×10^6
STWIIP (m^3)	6.36×10^6	6.59×10^6	6.66×10^6
GIIP (m^3)	1.58×10^8	1.73×10^8	1.74×10^8

5.2 OLYMPUS models (Extracted from OIL GAS European Magazine Paper [97])

So far, all the evaluations carried out with synthetic and real field cases have been with the use of single base models. It is common knowledge that oil and gas reservoir development is a high-risk business. Uncertainties abound in every stage of an integrated reservoir management workflow. Uncertainties in the geological models (e.g. structure etc.) combined with uncertainties in petrophysical modelling (e.g. permeability and porosity distribution in the reservoir) can result in the creation of an ensemble of base models. The generation of an ensemble of base models is crucial for quantifying the uncertainty of model parameters and production forecast after history matching [98], [99]. A single base model is not sufficient enough to quantify the effect of uncertainty on production forecast.

In this section, investigations are made on the performance of the proposed method in revealing hidden faults in an ensemble of 3-D field-scale heterogeneous reservoir models under waterflooding through a constant rate under-injection strategy and with favourable mobility ratios. These heterogeneous models called the "OLYMPUS" models are inspired by a virgin oil field in the North Sea [100]. A total of 3 base models make up the ensemble of base models. These base model ensembles represents the extent of uncertainty in permeability distribution (e.g. P10, P50 and P90 case). Porosity and net-to-gross (NTG) ratio distribution in all 3 base models are the same. The goal here is to show that the proposed method can reveal the location of hidden faults in all 3 base models regardless of reservoir model heterogeneity and the extent of uncertainty in permeability distribution.

5.2.1 OLYMPUS Reservoir Description

The OLYMPUS models contains predominantly oil and water. The oil is undersaturated over the duration of the simulation period. Each of the OLYMPUS models consists of 118 x 118 x 16 grid blocks with grid dimensions of 50 m x 50 m x 3 m in the X, Y and Z direction respectively. Also, each model contains only 192,750 active grid blocks. A total of 5 non-sealing faults (represented by thick white lines in Figure 5-11) are present in each model. The ensemble (Figure 5-11, Figure 5-12 and Figure 5-13) contains two main zones. The top zone contains fluvial channel sands firmly implanted in floodplain shales. On the other hand, the bottom zone consists of alternating layers of coarse, medium and fine sands. Both zones are separated by an impermeable shale layer. In the ensemble, reservoir permeability varies from 0.05 mD to 1000 mD while reservoir porosity ranges from 1% to 30%. Horizontal permeability is slightly isotropic in the ensemble while the vertical permeability which is deduced from the horizontal permeability is reduced by a factor of 0.1 (i.e. $K_x \approx K_y$; $K_z = 0.1K_x$).

In the ensemble, the initial reservoir pressure is set at 205 bar and the depth of the oil-water contact exist at 2092 metres. 4 oil-water relative permeability regions exist each in the ensemble according to the defined reservoir zones. Oil and water viscosities in the

ensemble are set at 3.2 cP and 0.4 cP respectively. 7 injectors exist each in the ensemble at the same locations and they each inject water at a rate of 300 m^3/day. Also, a total of 11 producers exist each in the ensemble which are liquid-rate-controlled (LRAT-controlled). Each producer produces 350 m^3/day of oil and water. The total production period is 14 years in the ensemble. The true model is formulated from one of the ensemble (see Figure 5-11). In the true model, 3 additional faults of sealing nature (represented by thick black lines in Figure 5-11) are added to the reservoir model. In all 3 base models, information about the newly added sealing faults are completely omitted. Numerical-noise-free simulator results for the true model is defined as measured data.

The main goal of this test is to reveal the location of these 3 newly added sealing faults in all 3 base models and study the impact of uncertainties in permeability distribution on the proposed method. For easier referencing, each base model are described subsequently as BM-1, BM-2 and BM-3 respectively. BM is an acronym for "base model" which is used henceforth in this section. BM-1 refers to the base model resulting from omitting fault information for the 3 newly added sealing faults in Figure 5-11. Since BM-1 is generated from Figure 5-11 which is the true model, BM-1 is simply Figure 5-11 without the 3 newly added sealing faults. BM-2 and BM-3 are presented in Figure 5-12 and Figure 5-13 respectively.

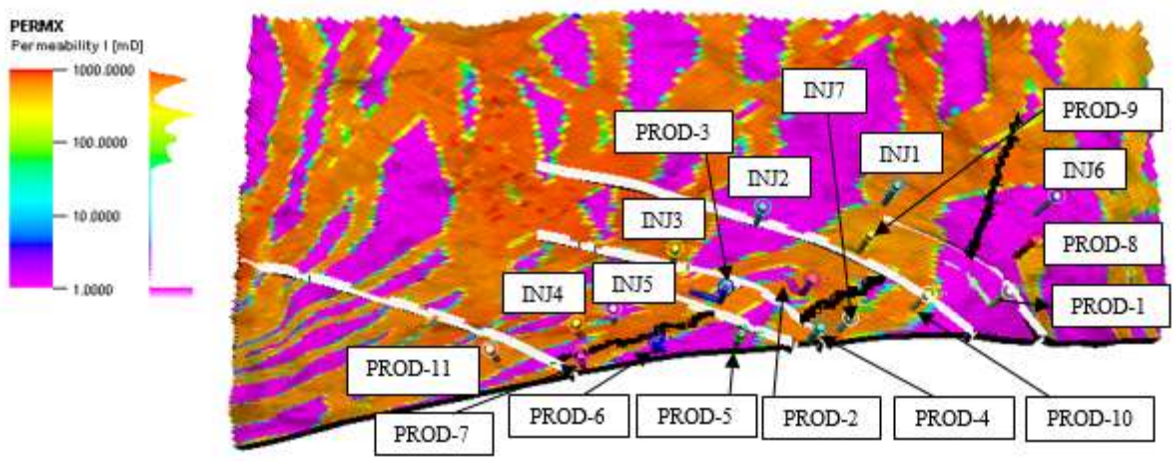

Figure 5-11: Heterogeneous model capturing braided channels and faults in the true model (2nd layer).

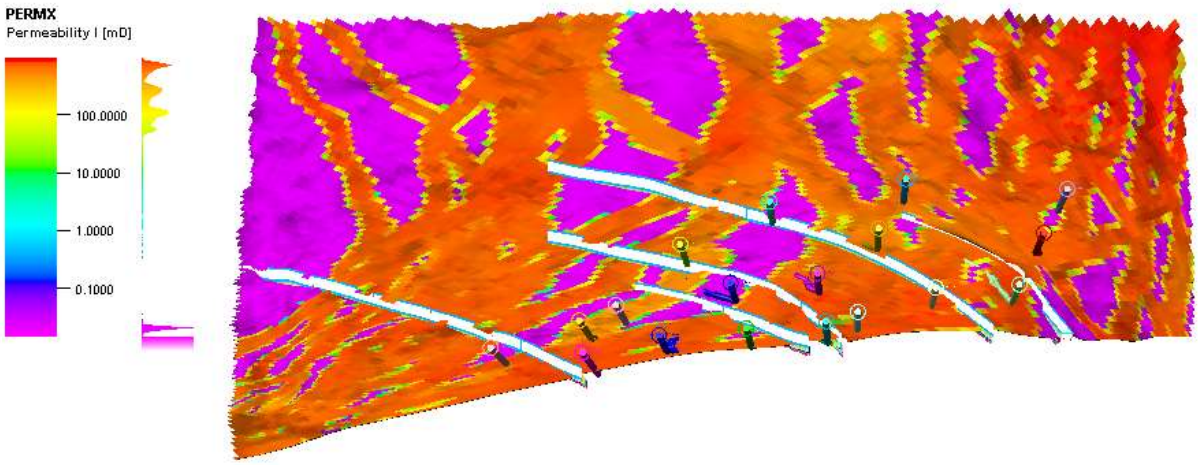

Figure 5-12: BM-2 (2nd layer).

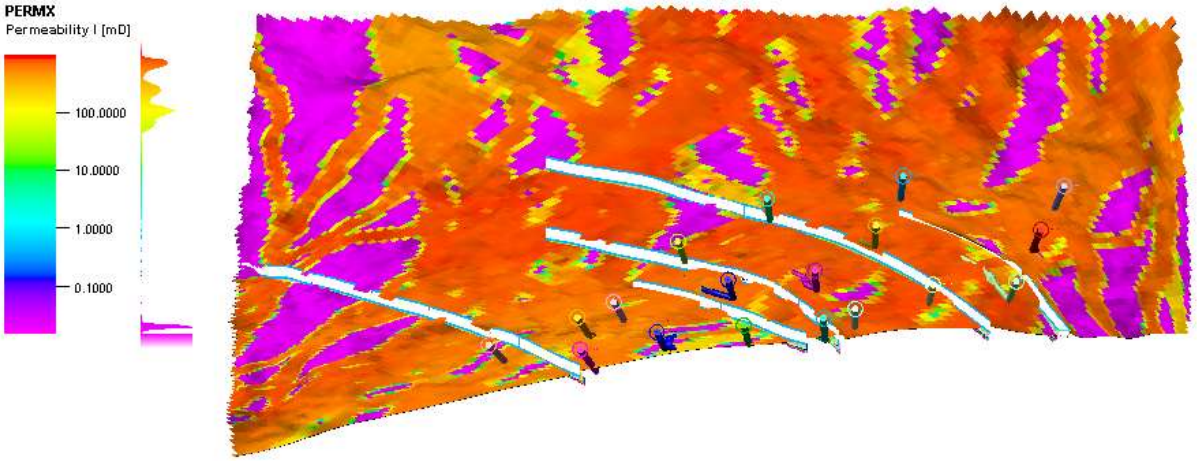

Figure 5-13: BM-3 (2nd layer).

5.2.2 Unconstrained History Matching (UHM) on the Ensemble of Base Models

Prior to the commencement of UHM on BM-1, BM-2 and BM-3 using the adjoint method, horizontal permeabilities (K_x and K_y) which are defined as model parameters are specified in an unconstrained manner (0.0 < K_x, K_y < 1000 mD). K_x and K_y are defined solely as model parameters because we want to reveal hidden faults (See Table 4-17). Also, the specified model responses which intend to fit to their corresponding measured data are well oil production rate (WOPR) in m³/day, well water-cut (WWCT) and well bottom-hole flowing pressure (WBHP) in bar. In addition, the initial assumptions employed prior to performing UHM are:

1. No prior information about the presence of hidden faults.
2. A single base model is assumed to be less than "satisfactory" thus leading to the generation of geostatistical ensemble (i.e. BM-1, BM-2 and BM-3).
3. Core data is available for each well hence changes to grid block permeability values in each well is not permitted.

For each base model, a total of 100 iterations were executed in an attempt to find an optimal solution as shown in Figure 5-14, Figure 5-15 and Figure 5-16 for BM-1, BM-2 and BM-3 respectively. This is so because μ_{K_x,K_y}, the step sizes for K_x and K_y, were set to 10 mD^2 for the ensemble. As shown in Figure 5-14, in the early stage of UHM performed on BM-1, Q is reduced significantly over the first 30 iterations. As the points at each iteration of $\nabla_x Q$ approaches the neighbourhood of minimum Q, the rate of error reduction slows down as expected. The 97th iteration was selected as the best-case in Figure 5-14 because it delivered the lowest Q with an overall model error reduction value of 80%.

In Figure 5-15, the progression of Q over a total of 100 iterations is very much different from what was observed in Figure 5-14. The overall model error in BM-2 prior to the commencement of UHM is 5 times more than that in BM-1. This is mainly as a result of the difference in permeability distribution. The omission of the 3 sealing faults also contributes to the recorded huge model error in BM-2. Compared to the steep decrease in overall model error experienced with BM-1, a rather slow decrease in overall model error was observed for UHM performed on BM-2 for the first 40 iterations. Subsequent iterations showed a somewhat steep decrease in model error to a minimum Q. The 100th iteration is selected as the best-case in Figure 5-15 because it delivered the lowest Q with an overall model error reduction value of 43%. As one would expect, it is very much possible to further reduce the overall model error Q by running more iterations.

Compared to Figures 5-14 and Figure 5-15, in Figure 5-16, the overall model error for BM-3 prior to the initiation of UHM is less than that for BM-2 but also 5 times greater than the overall model error recorded for BM-1. These difference in overall model error values can also be ascribed to the differences in permeability distribution and the impact of the omitted 3 sealing faults in each base model. As seen in Figure 5-16, a steep and continuous sharp drop in overall model error Q is observed for UHM performed on BM-3 all through the 100 iterations. The 100th iteration is selected as the best-case in Figure 5-16 because it delivered the lowest Q with an overall model error reduction value of 78%. Certainly, it is also very much possible to further reduce the overall model error Q by running more iterations until the objective function curve (the Q-curve) flattens out to a constant value (e.g. Figure 5-14). At this point, there is little or no room for improvement of the reservoir model.

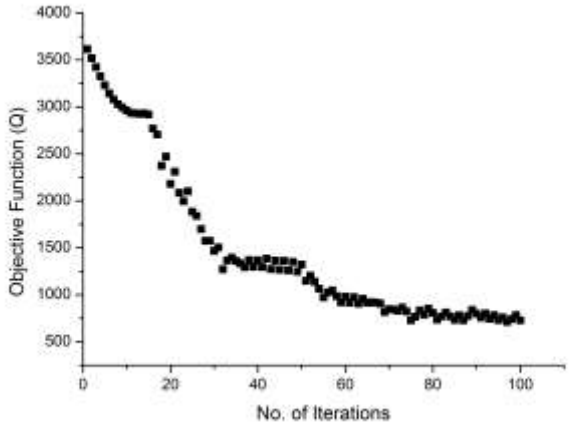

Figure 5-14: Progression of the objective function vs. no. of iterations for BM-1.

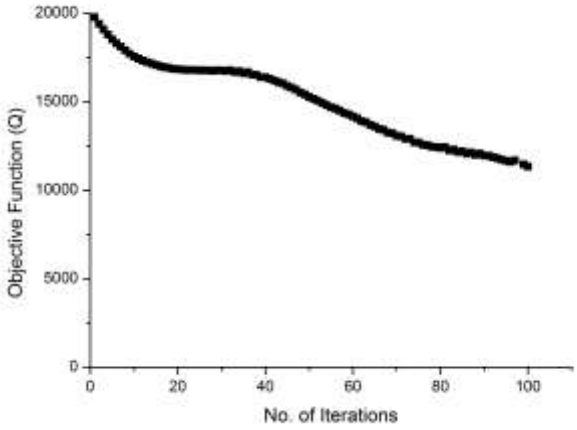

Figure 5-15: Progression of the objective function vs. no. of iterations for BM-2.

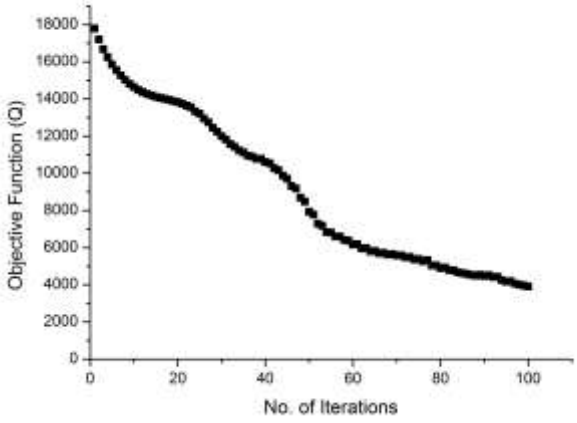

Figure 5-16: Progression of the objective function vs. no. of iterations for BM-3.

Here, R-squared values are also used to describe the match quality of model responses. An R-squared value equal to or greater than 97% describes model responses with excellent history-match results. On the other hand, an R-squared value less than 97%

describes model responses with satisfactory or poor history-match results. The R-squared values generated for each base model prior to performing UHM are presented in Table 5-7, Table 5-8 and Table 5-9 respectively. Judging by the intensity of red-coloured R-squared values for the model responses for each base model, it is obvious that BM-1 is the most satisfactory base model. This is true since the difference between BM-1 and the true model is simply the omission of the 3 sealing faults.

Table 5-7: R-squared values for BM-1 prior to performing UHM.

Well Name	WBHP	WWCT	WOPR
PROD-1	100.0%	99.6%	99.3%
PROD-2	99.7%	48.2%	99.5%
PROD-3	100.0%	99.5%	99.4%
PROD-4	99.9%	98.7%	98.8%
PROD-5	99.9%	98.5%	98.6%
PROD-6	99.3%	98.2%	99.1%
PROD-7	90.0%	96.1%	94.6%
PROD-8	100.0%	97.9%	98.1%
PROD-9	100.0%	99.8%	99.9%
PROD-10	100.0%	99.0%	98.9%
PROD-11	100.0%	98.9%	99.9%
INJ-1	99.9%	—	—
INJ-2	99.9%	—	—
INJ-3	99.9%	—	—
INJ-4	99.4%	—	—
INJ-5	99.9%	—	—
INJ-6	99.9%	—	—
INJ-7	99.9%	—	—
$R^2 \geq 97\%$; $R^2 < 97\%$			

Table 5-8: R-squared values for BM-2 prior to performing UHM.

Well Name	WBHP	WWCT	WOPR
PROD-1	94.2%	90.6%	86.4%
PROD-2	97.8%	46.8%	98.7%
PROD-3	97.5%	95.9%	96.1%
PROD-4	97.4%	97.8%	97.9%
PROD-5	97.1%	97.6%	99.0%
PROD-6	99.1%	97.3%	97.7%
PROD-7	98.2%	95.7%	99.7%
PROD-8	98.0%	97.7%	97.2%
PROD-9	97.6%	98.0%	98.3%

PROD-10	98.5%	95.2%	98.6%
PROD-11	99.5%	94.1%	96.2%
INJ-1	98.5%	—	—
INJ-2	96.2%	—	—
INJ-3	97.9%	—	—
INJ-4	95.3%	—	—
INJ-5	98.7%	—	—
INJ-6	97.0%	—	—
INJ-7	97.2%	—	—
$R^2 \geq 97\%$; $R^2 < 97\%$			

Table 5-9: R-squared values for BM-3 prior to performing UHM.

Well Name	WBHP	WWCT	WOPR
PROD-1	99.7%	90.7%	97.4%
PROD-2	99.8%	86.4%	98.8%
PROD-3	99.6%	99.0%	98.6%
PROD-4	99.1%	91.1%	98.1%
PROD-5	99.3%	91.6%	96.6%
PROD-6	98.0%	99.6%	97.7%
PROD-7	97.9%	97.2%	96.7%
PROD-8	95.4%	95.5%	85.1%
PROD-9	99.8%	96.1%	96.8%
PROD-10	99.7%	97.4%	96.7%
PROD-11	100.0%	96.2%	97.2%
INJ-1	99.2%	—	—
INJ-2	98.2%	—	—
INJ-3	99.7%	—	—
INJ-4	96.4%	—	—
INJ-5	95.9%	—	—
INJ-6	97.7%	—	—
INJ-7	99.3%	—	—
$R^2 \geq 97\%$; $R^2 < 97\%$			

Best-case results obtained from UHM performed on BM-1, BM-2 and BM-3 are presented in Table 5-10, Figure 5-11 and Figure 5-12 respectively. In all base models, a considerable improvement in the history-match quality of all model responses can be observed. Besides the reduction in the number of R-squared values less than 97%, noticeable improvements in R-squared values greater than or equal to 97% can also be observed. This proves that by performing UHM on one or more base models concurrently, it is possible to match unmatchable model responses that may prove difficult to match using the CHM

procedure. It is important to mention that specifying the weight values of model responses is crucial in aiding the adjoint method to focus more on model responses with the highest mismatch. In cases where the R-squared values for most model responses show no improvement whatsoever after performing UHM, one can be certain that the base model is a very poor representation of the subsurface reservoir in question.

Table 5-10: R-squared values for UHM results for BM-1.

Well Name	WBHP	WWCT	WOPR
PROD-1	100.0%	98.7%	99.7%
PROD-2	100.0%	97.0%	99.8%
PROD-3	100.0%	99.6%	99.6%
PROD-4	100.0%	99.9%	100.0%
PROD-5	100.0%	99.7%	99.9%
PROD-6	100.0%	98.5%	98.7%
PROD-7	100.0%	95.9%	99.1%
PROD-8	100.0%	98.3%	98.3%
PROD-9	100.0%	98.6%	99.8%
PROD-10	100.0%	99.6%	99.8%
PROD-11	100.0%	99.3%	99.9%
INJ-1	99.9%	—	—
INJ-2	99.9%	—	—
INJ-3	99.9%	—	—
INJ-4	99.9%	—	—
INJ-5	100.0%	—	—
INJ-6	100.0%	—	—
INJ-7	100.0%	—	—
$R^2 \geq 97\%$; $R^2 < 97\%$			

Table 5-11: R-squared values for UHM results for BM-2.

Well Name	WBHP	WWCT	WOPR
PROD-1	95.1%	88.2%	94.8%
PROD-2	99.9%	70.5%	99.8%
PROD-3	99.7%	96.4%	97.0%
PROD-4	99.9%	97.5%	98.8%
PROD-5	99.9%	98.8%	99.7%
PROD-6	99.8%	97.0%	97.1%
PROD-7	99.6%	96.5%	99.2%
PROD-8	99.9%	97.1%	97.6%
PROD-9	99.9%	97.3%	98.7%
PROD-10	99.9%	98.9%	98.9%

PROD-11	100.0%	93.8%	96.3%
INJ-1	99.4%	—	—
INJ-2	99.9%	—	—
INJ-3	99.5%	—	—
INJ-4	99.9%	—	—
INJ-5	99.9%	—	—
INJ-6	98.6%	—	—
INJ-7	99.9%	—	—
$R^2 \geq 97\%$; $R^2 < 97\%$			

Table 5-12: R-squared values for UHM results for BM-3.

Well Name	WBHP	WWCT	WOPR
PROD-1	99.8%	88.5%	99.7%
PROD-2	99.9%	94.7%	99.7%
PROD-3	100.0%	98.2%	98.2%
PROD-4	99.8%	95.8%	98.3%
PROD-5	100.0%	98.8%	98.6%
PROD-6	99.8%	97.7%	97.2%
PROD-7	99.9%	97.8%	99.2%
PROD-8	99.9%	97.1%	97.2%
PROD-9	100.0%	97.0%	98.0%
PROD-10	99.9%	98.7%	97.9%
PROD-11	100.0%	95.8%	97.0%
INJ-1	99.8%	—	—
INJ-2	99.9%	—	—
INJ-3	99.9%	—	—
INJ-4	99.9%	—	—
INJ-5	99.5%	—	—
INJ-6	99.6%	—	—
INJ-7	99.8%	—	—
$R^2 \geq 97\%$; $R^2 < 97\%$			

5.2.2.1 Detecting Hidden Faults using the Fault Detection Algorithm

In order to reveal the location and approximate shape of all 3 sealing faults in each base model, the fault detection algorithm is utilized. The first part of the fault detection algorithm is used to generate the permeability ratio map. The permeability ratio maps generated for the best-case results from UHM performed on BM-1, BM-2 and BM-3 are presented in Figure 5-17, Figure 5-18 and Figure 5-19 respectively. The variation in permeability ratio values (from ≤ 0.0001 to > 1000) is as a result of existing reservoir

heterogeneity. Regions with permeability ratio values of 1.0 experience no change in permeability over the entire iterative process. The second part of the fault detection algorithm is used to generate the fault indicator map from the permeability ratio map. The fault indicator map generated for each base model is presented in Figure 5-20, Figure 5-21 and Figure 5-22 respectively.

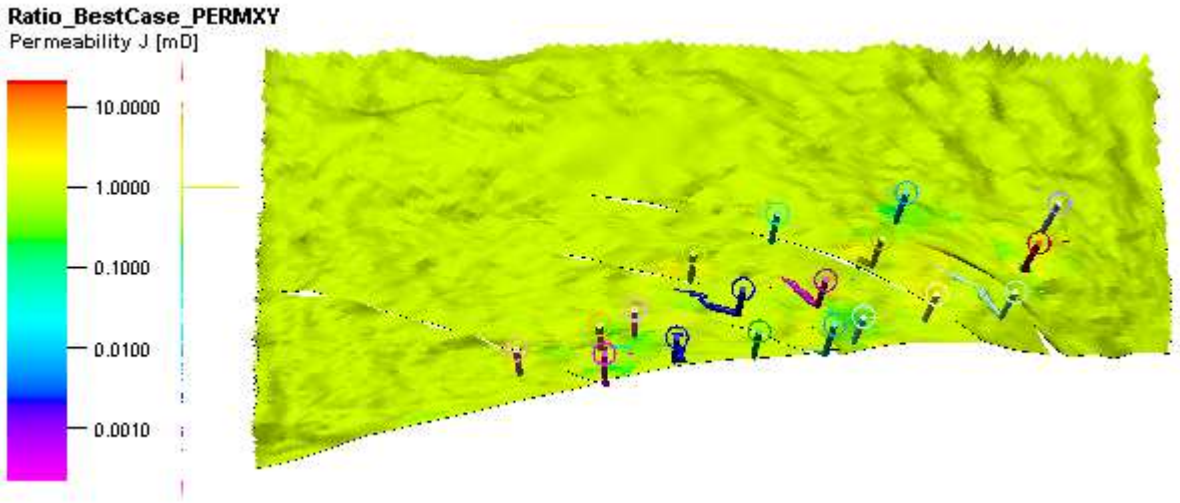

Figure 5-17: Permeability ratio map generated for the best-case result (the 97th iteration) from UHM performed on BM-1 (2nd layer).

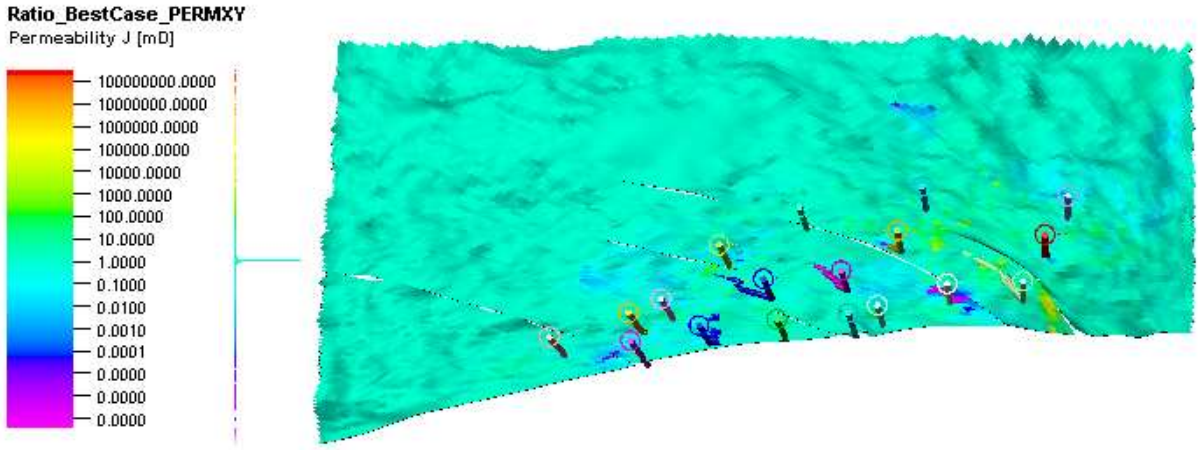

Figure 5-18: Permeability ratio map generated for the best-case result (the 100th iteration) from UHM performed on BM-2 (2nd layer).

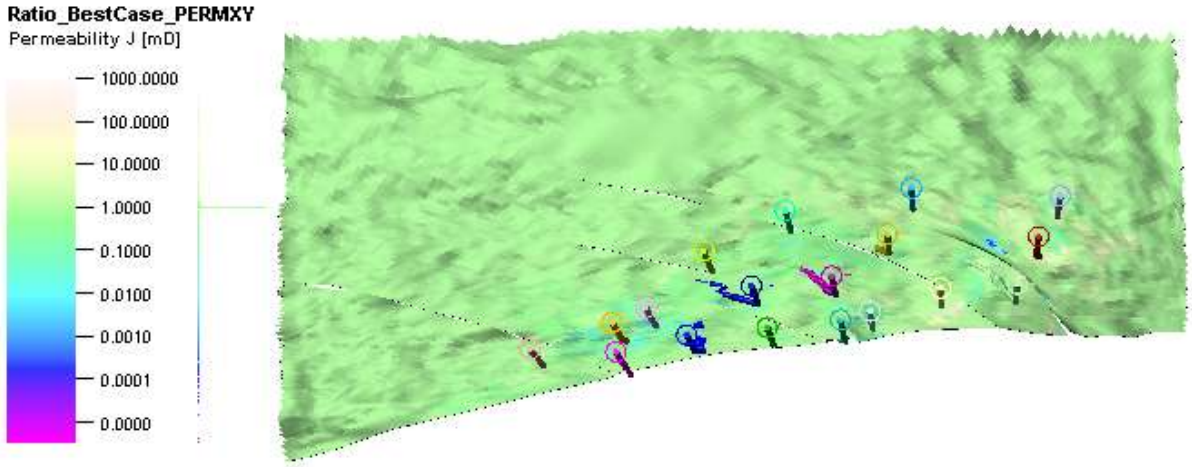

Figure 5-19: Permeability ratio map generated for the best-case result (the 100th iteration) from UHM performed on BM-3 (2nd layer).

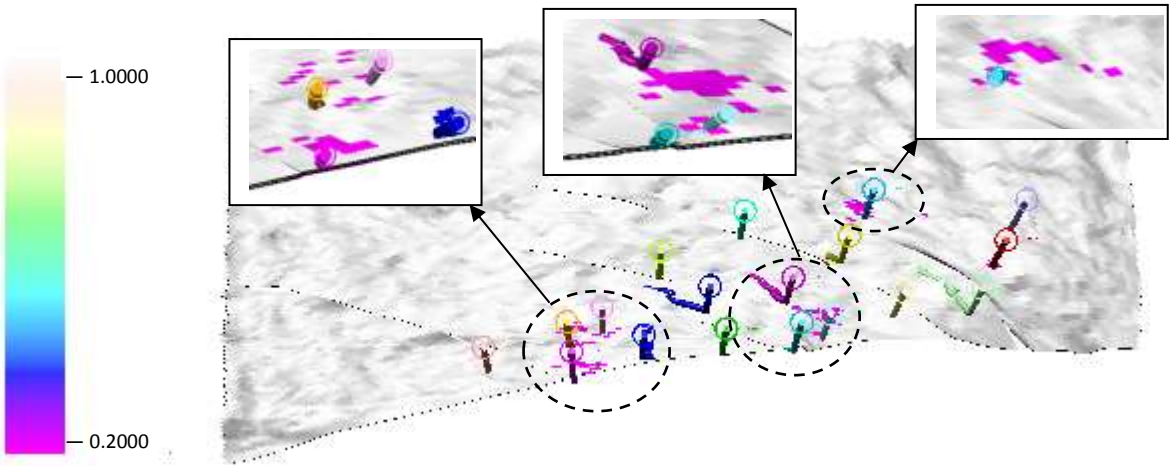

Figure 5-20: Fault indicator map generated from the permeability ratio map at γ_{fault} = 0.2 for BM-1 (2nd layer).

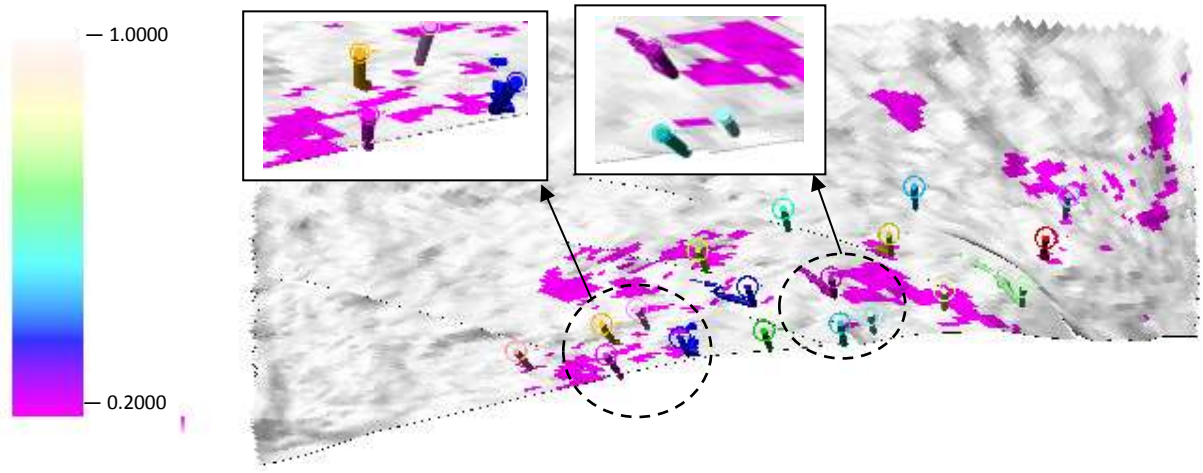

Figure 5-21: Fault indicator map generated from the permeability ratio map at γ_{fault} = 0.2 for BM-2 (2nd layer).

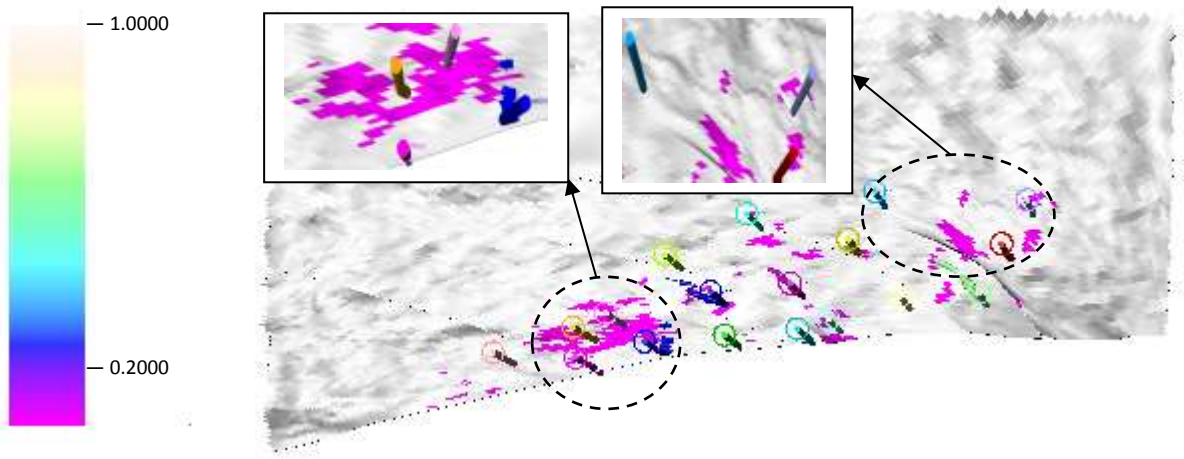

Figure 5-22: Fault indicator map generated from the permeability ratio map at γ_{fault} = 0.2 for BM-3 (2nd layer).

Our goal is to compare the location and shape of the revealed faults in each base model with the 3 sealing faults in the true model. The purple-coloured grids in each fault indicator map have values equal to 0.2 indicating an 80% reduction in each base model K_x and K_y values. The threshold value that reveals the location of the hidden faults is γ_{fault} = 0.2. Compared to Figure 5-20 where purple-coloured grids are concentrated only around wells where the sealing faults are omitted, one can see that the intensity of purple-coloured grids in Figure 5-21 and Figure 5-22 extends beyond the neighbourhood of wells where the sealing faults exists. This is simply because the initial permeability in BM-2 and BM-3 are completely different from the true permeability distribution in BM-1. If the reader recalls vividly, the main difference between BM-1 and the true model used for generating measured data is the omission of the 3 sealing faults. These extra regions of purple-coloured grids in BM-2 and BM-3 outside areas where the sealing faults exists are

meant to compensate for these differences in permeability. In other words, UHM performed on BM-2 and BM-3 also tries to recreate the true permeability distribution while simultaneously revealing the potential location and shape of hidden faults.

One crucial point to mention is that tight simulator solver settings (as discussed in Section 4.8) were set prior to performing UHM in order to eliminate numerical noise from the Jacobians ($\nabla_y f^T, \nabla_{K_x} f^T$ & $\nabla_{K_y} f^T$) generated by the numerical reservoir simulator. This approach ensures accurate computation of the adjoint variables (λ) and sensitivities ($\nabla_{K_x} J$ & $\nabla_{K_y} J$).

5.2.2.2 Estimating Fault Shapes using the Fault Shape Detection Algorithm

The fault shape detection algorithm is applied in order to estimate the shape of the revealed faults from the fault indicator maps generated in Figure 5-20, Figure 5-21 and Figure 5-22 respectively. Using Figure 5-20, Figure 5-21 and Figure 5-22 as an input images for the fault shape detection algorithm, the estimated fault shapes in form of fault lines are presented in Figure 5-23, Figure 5-24 and Figure 5-25 respectively. The improved model for BM-1 is designed taking this estimated fault shapes into account.

Figure 5-23: Estimated fault shapes for BM-1 using the fault shape detection algorithm.

Some of the estimated fault shapes in BM-2 and BM-3 are not really faults. Rather, they are by-product of the differences in permeability distribution between the true model and BM-2 and BM-3. These estimated fault shapes outside well-dominated regions are not taken into account in the development of the improved models for BM-2 and BM-3 respectively. In Figure 5-23, Figure 5-24 and Figure 5-25, the estimated fault shapes appears small because the input images (the fault indicator maps) were rescaled.

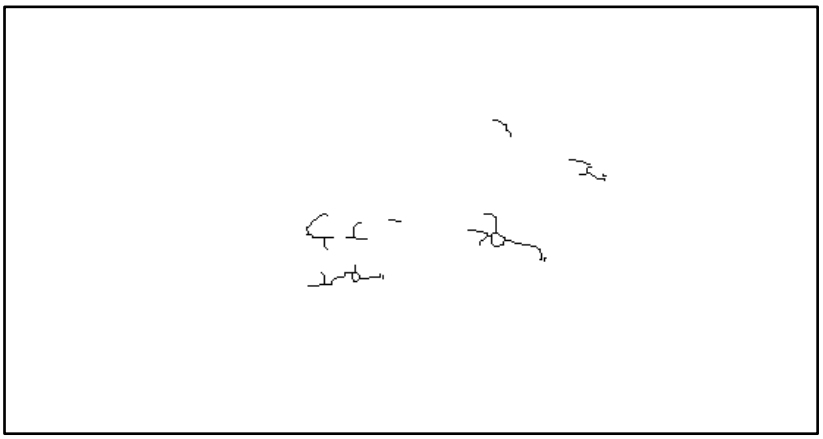

Figure 5-24: Estimated fault shapes for BM-2 using the fault shape detection algorithm.

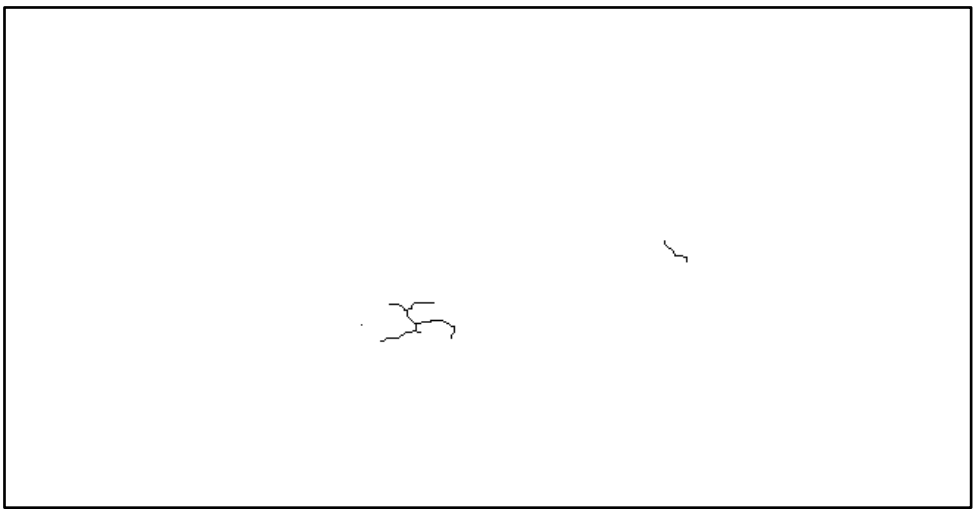

Figure 5-25: Estimated fault shapes for BM-3 using the fault shape detection algorithm.

5.2.2.3 Implementing Revealed Faults into the Base Model Ensemble

Before implementing the revealed faults back into the base model ensemble, it is important to show the 3 sealing faults (in thick black lines) in the true model and identify which wells are mostly influenced by these sealing faults. In Figure 5-26, a top view of the reservoir showing the location of wells and faults is presented. In the bottom-left portion of the reservoir, the two slanted producers (PROD-5 and PROD-6 coloured in green and blue respectively) are drilled through one of the sealing fault meaning that production from these wells are only slightly hampered by the sealing fault. For easier referencing, we will refer to the 3 sealing faults in Figure 5-26 from left to right as SFLT-1, SFLT-2 and SFLT-3 respectively. Also, for the purpose of simplicity in referencing, we describe each improved model as IM-BM-1, IM-BM-2 and IM-BM-3 respectively. IM is an acronym for "improved model".

Based on Figure 5-23, the shape of the revealed faults in IM-BM-1 is presented in Figure 5-27. The shape of the revealed faults in IM-BM-1 is different from faults SFLT-1, SFLT-

2 and SFLT-3 because of the nature of the permeability distribution in BM-1. Some portion of the faults SFLT-1, SFLT-2 and SFLT-3 either runs through areas of extremely low permeability or are located in the proximity of areas with extremely low permeability. In Figure 5-11, the purple-coloured regions have permeabilities of 1 mD and the orange-coloured regions have permeabilities ranging from 650 - 800 mD. PROD-5 and PROD-6 was sidetracked from a low permeability region through fault SFLT-1 into a high permeability region as slanted wells. Since PROD-5 and PROD-6 were not affected by the fault SFLT-1, the proposed method assumes that no hidden fault exists in that region.

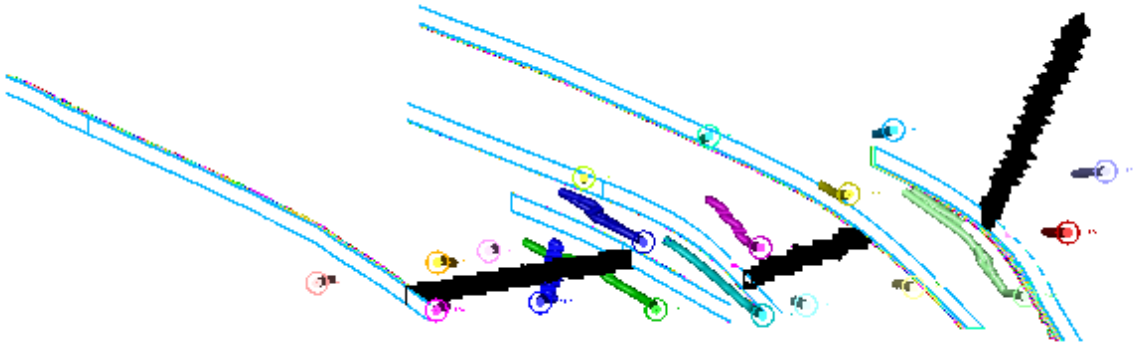

Figure 5-26: Top view of the true model showing wells and location of the 3 sealing faults (in thick black lines).

Also, as seen in Figure 5-11, a weak connection exists between INJ4 and PROD-7 and this is evident from the low permeability region acting as a flow barrier between them. The strongest inter-well connection (based on high permeability connecting them) exists between INJ5 and PROD-7 and since the fault SFLT-1 isolates them, the proposed method revealed faults that significantly reduces connectivity between INJ5 and PROD-7. Another interesting observation is that the revealed fault close to INJ5 only isolates INJ5 from PROD-7 but allows communication with portions of PROD-5 and PROD-6 drilled through fault SFLT-1.

The location and shape of the revealed fault existing between INJ7 and PROD-2 is also slightly different from the true fault SFLT-2. This is so because in BM-1 (see Figure 5-11), SFLT-2 is located in the proximity of areas with extremely low permeability (purple-coloured regions with permeabilities of 1 mD). Considering the fact that these low permeability regions already acts as a flow barrier, the proposed method assumes that no hidden fault exists in these regions. The same explanation applies for the low permeability region slightly isolating PROD-2 from INJ7. The revealed fault is located midway between the two low permeability regions in order to isolate INJ7 from PROD-2. The location and shape of the revealed fault existing between INJ1 and PROD-8 is not revealed precisely in BM-1 because half of the entire length of fault SFLT-3 lies in low permeability regions while the other half lies in high permeability regions (see Figure 5-11). The portion of the fault that lies in the low permeability region and isolates INJ1 from PROD-8 is not revealed by the proposed method because the low permeability

region already acts as a flow barrier. The portion of the fault that lies in high permeability region is revealed although the location is incorrect. This is so because injector-injector interactions are not taking into account by the proposed method.

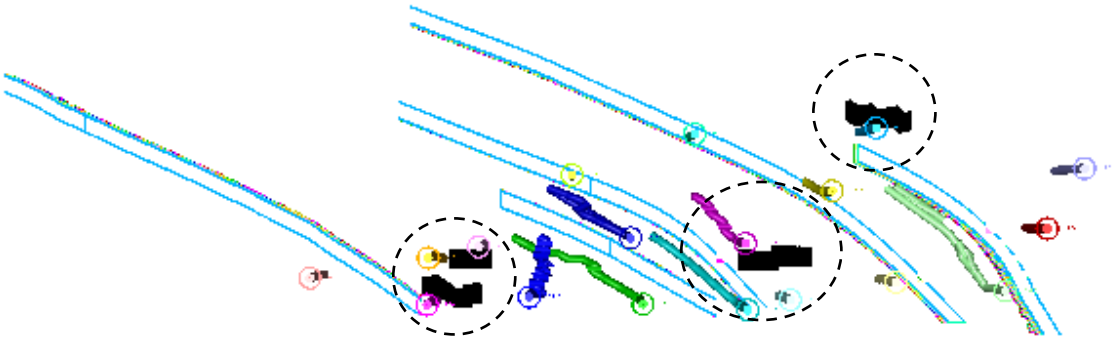

Figure 5-27: Revealed faults in IM-BM-1. The revealed fault locations are captured by the inserted dashed circles.

As seen in Figure 5-28, the shape and location of the revealed faults in IM-BM-2 are very much similar to SFLT-1 and SFLT-2. Similar to the revealed faults in IM-BM-1, PROD-5 and PROD-6 are not isolated from INJ5 and INJ6 because both slanted producers were drilled through SFLT-1 (see Figure 5-26). The location and shape of the revealed fault existing between INJ7 and PROD-2 is similar to SFLT-2 but incomplete. The location of SFLT-3 was not revealed in IM-BM-2.

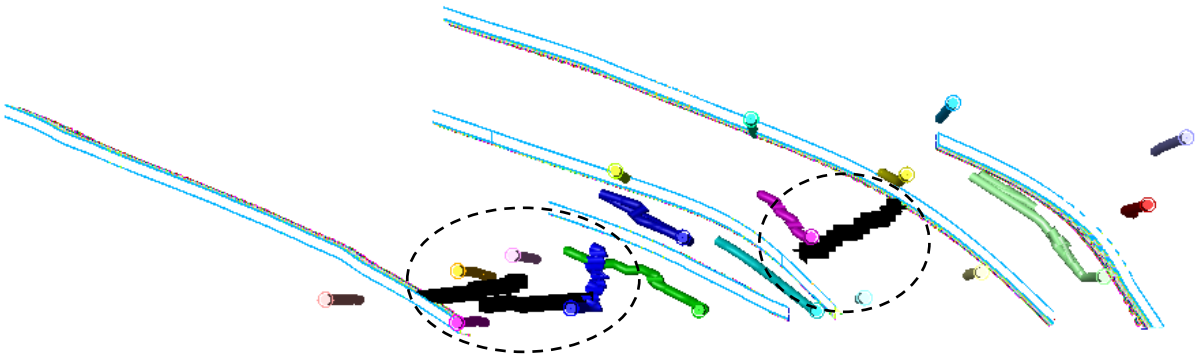

Figure 5-28: Revealed faults in IM-BM-2. The revealed fault locations are captured by the inserted dashed circles.

In Figure 5-29, the shape and location of the revealed faults in IM-BM-3 are very much similar to SFLT-1 and SFLT-3. Similar to the revealed faults in IM-BM-1 and IM-BM-2, PROD-5 and PROD-6 are not fully isolated from INJ4 and INJ5 because both slanted producers were drilled through SFLT-1 (see Figure 5-26). The location of SFLT-2 was not revealed in IM-BM-3. The location and shape of the revealed fault existing between

INJ1 and PROD-8 is similar to SFLT-3 but incomplete. This is because injector-injector interactions are not considered by the proposed method.

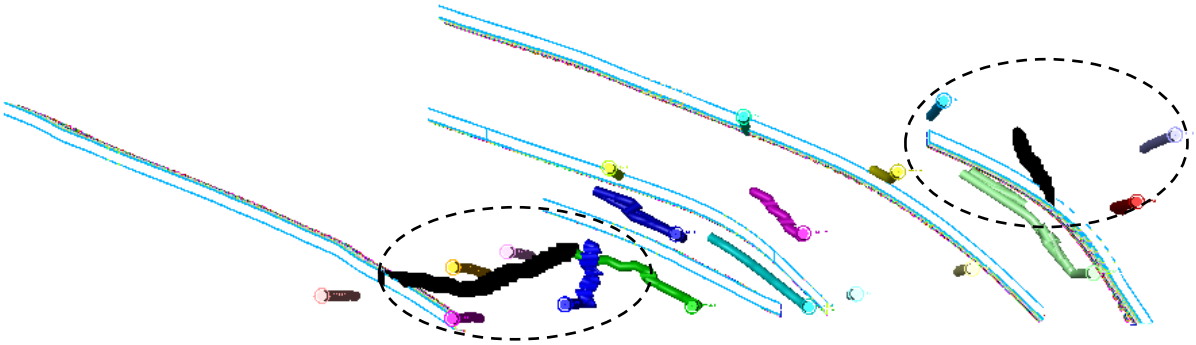

Figure 5-29: Revealed faults in IM-BM-3. The revealed fault locations are captured by the inserted dashed circles.

5.2.3 Constrained History Matching (CHM) on Improved Models

CHM using the adjoint method is performed on all 3 improved models with the transmissibility multipliers across the revealed faults (MULTFLTs) and permeability in all three directions defined solely as model parameters for each improved model. The improved model is the new base model containing information about the revealed faults as shown in Figure 5-27, Figure 5-28 and Figure 5-29 respectively. The uncertainty limits for the transmissibility multipliers across the revealed faults (MULTFLTs) are within the ranges of 0.0 and 1.0. The horizontal and vertical permeability uncertainty limits are constrained to the original range of each respective model.

Unlike the UHM process, a total of 40 iterations were executed each for CHM performed on IM-BM-1, IM-BM-2 and IM-BM-3 in an attempt to reach an optimal Q. This is so because the step sizes, μ_{K_x,K_y} = 30 mD^2, is utilized. Figure 5-30, Figure 5-31 and Figure 5-32 presents the objective function progression with increasing number of iterations from UHM to CHM. The CHM performed on all improved models commenced from the 101th iteration indicated by the red circle in Figure 5-30, Figure 5-31 and Figure 5-32 respectively. The initial transmissibility multipliers across the revealed faults is set at 0.2 for IM-BM-1, IM-BM-2 and IM-BM-3. This is based on using the heuristic approach which forms the third part of the fault detection algorithm discussed in Section 4.4.1.

In Figure 5-30, Figure 5-31 and Figure 5-32, it can be seen that when the revealed faults are introduced into BM-1, BM-2 and BM-3, the model error increases again in IM-BM-1, IM-BM-2 and IM-BM-3 although it is not as large as the initial model errors in BM-1, BM-2 and BM-3. This behaviour is expected as the UHM best-case permeability arrays exhibits permeability reductions in other regions of the model that were excluded by the definition of a threshold value (γ_{fault}). Also, with the use of a threshold value to narrow down on potential fault locations, regions with permeability reductions outside the potential locations of the 3 sealing faults were completely ignored. Another possible

reason for this behaviour can be attributed to the inferred transmissibility multipliers across the revealed faults (MULTFLTs) which may not be entirely accurate. In Figure 5-30, the 137th iteration was selected as our best-case since it delivered the lowest Q with an overall model error reduction value of 71%.

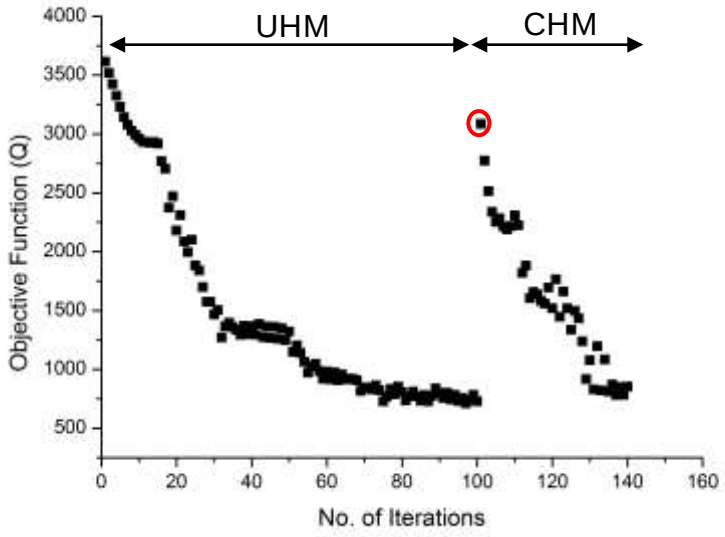

Figure 5-30: Objective function (Q) vs. number of iterations for UHM performed on BM-1 and CHM performed on IM-BM-1.

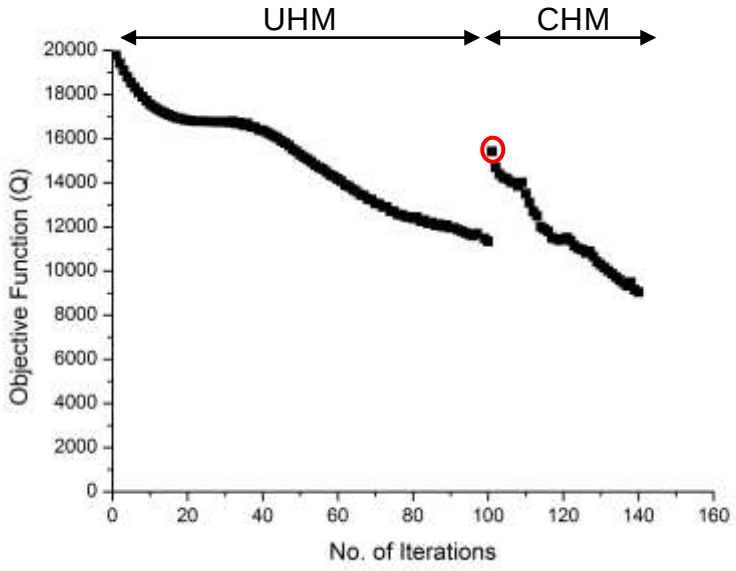

Figure 5-31: Objective function (Q) vs. number of iterations for UHM performed on BM-2 and CHM performed on IM-BM-2.

In Figure 5-31, the 140th iteration was selected as our best-case since it delivered the lowest Q with an overall model error reduction value of 41%. In Figure 5-32, the 139th iteration was selected as our best-case since it delivered the lowest Q with an overall model error reduction value of 81%.

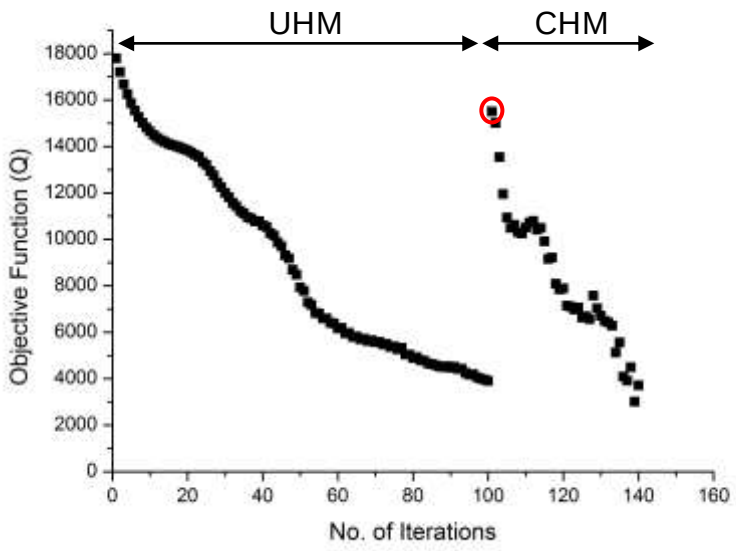

Figure 5-32: Objective function (Q) vs. number of iterations for UHM performed on BM-3 and CHM performed on IM-BM-3.

Best-case results obtained from CHM performed on all 3 improved models are presented in Table 5-13, Table 5-14 and Table 5-15 respectively. In all 3 improved models, a substantial improvement in the match quality of all model responses can be observed when compared to their respective initial base model (i.e. BM-1, BM-2 and BM-3) which was shown earlier in Table 5-7, Table 5-8 and Table 5-9 respectively. The improvements in model responses recorded for all 3 improved models can be attributed to the correct determination of MULTFLTs for all revealed faults via CHM. Naturally, the modification of the field permeability in all three directions played a significant role as well.

Table 5-13: R-squared values for CHM results for IM-BM-1.

Well Name	WBHP	WWCT	WOPR
PROD-1	100.0%	98.4%	99.6%
PROD-2	100.0%	95.2%	99.9%
PROD-3	100.0%	99.1%	99.1%
PROD-4	100.0%	99.9%	99.8%
PROD-5	100.0%	99.9%	99.9%
PROD-6	99.9%	98.6%	98.8%
PROD-7	99.9%	97.0%	99.2%
PROD-8	100.0%	98.7%	98.7%
PROD-9	100.0%	97.8%	99.7%
PROD-10	100.0%	99.2%	99.8%
PROD-11	100.0%	97.4%	99.7%
INJ-1	99.9%	—	—
INJ-2	99.9%	—	—
INJ-3	99.9%	—	—

INJ-4	99.9%	—	—
INJ-5	100.0%	—	—
INJ-6	99.9%	—	—
INJ-7	100.0%	—	—
$R^2 \geq 97\%$; $R^2 < 97\%$			

Table 5-14: R-squared values for CHM results for IM-BM-2.

Well Name	WBHP	WWCT	WOPR
PROD-1	97.2%	92.4%	94.8%
PROD-2	100.0%	85.1%	99.7%
PROD-3	99.8%	97.1%	97.4%
PROD-4	99.9%	97.5%	98.6%
PROD-5	100.0%	99.0%	99.5%
PROD-6	100.0%	97.4%	97.6%
PROD-7	99.8%	97.9%	99.7%
PROD-8	100.0%	97.3%	98.0%
PROD-9	99.9%	97.7%	99.0%
PROD-10	99.9%	99.1%	99.5%
PROD-11	100.0%	94.1%	96.6%
INJ-1	99.6%	—	—
INJ-2	100.0%	—	—
INJ-3	99.7%	—	—
INJ-4	99.9%	—	—
INJ-5	100.0%	—	—
INJ-6	99.5%	—	—
INJ-7	99.9%	—	—
$R^2 \geq 97\%$; $R^2 < 97\%$			

Table 5-15: R-squared values for CHM results for IM-BM-3.

Well Name	WBHP	WWCT	WOPR
PROD-1	99.9%	88.2%	99.8%
PROD-2	99.9%	95.7%	99.8%
PROD-3	99.9%	98.5%	98.9%
PROD-4	99.7%	96.4%	98.6%
PROD-5	99.7%	98.6%	97.8%
PROD-6	99.6%	97.9%	97.3%
PROD-7	99.8%	98.0%	99.4%
PROD-8	99.9%	97.5%	97.1%
PROD-9	100.0%	97.4%	97.7%
PROD-10	99.9%	97.7%	98.6%
PROD-11	100.0%	97.0%	97.2%
INJ-1	99.6%	—	—
INJ-2	99.8%	—	—
INJ-3	99.7%	—	—
INJ-4	99.6%	—	—
INJ-5	99.1%	—	—
INJ-6	99.3%	—	—
INJ-7	99.6%	—	—
$R^2 \geq 97\%$; $R^2 < 97\%$			

Chapter 6

> "Facts are always required to draw conclusions and make serious decisions"
>
> Sunday Adelaja (1967-Present)

6. Conclusions and Future Work

6.1 Conclusions

The main goal of this thesis was to develop a method for improving reservoir characterization using the adjoint method applied in history matching. The proposed method was evaluated with synthetic and real field reservoir simulation models of various dimensions, reservoir heterogeneity, well architecture and well number. Single and multiple base model scenarios were also evaluated in this thesis. This chapter summarizes the main contributions of this thesis, major key findings and recommendations for future investigations.

6.1.1 Main Contributions

The research work conducted in this study for a 3-year period involved the development and application of a method for improving reservoir characterization in reservoir simulation models using the adjoint method. In this context, the main contributions of this research work can be summarized as follows:

a. A detailed and coherent literature review on history matching and methods for improving reservoir characterization in reservoir models.
b. Development of an adjoint-based reservoir characterization improvement workflow.
c. Formulation of various reservoir feature detection algorithms that can be applied to best-case permeability and/or porosity arrays obtained from UHM to reveal the location, shape and other essential properties of hidden reservoir features.

d. The development of a modified Canny edge-detection method and a fault shape detection algorithm for improving the performance of the developed method.
e. Discussing the potential of revealing hidden reservoir features from adjoint-derived sensitivities obtained from UHM.
f. Presentation of a proposed catalogue for revealing hidden reservoir features that highlights key model parameters that are instrumental in revealing these features.
g. Comparison of the performance of the developed method with the most prominent state-of-the-art methods.
h. Studying the effect of numerical and production noise on the developed method.
i. Analysing the benefits associated with performing CHM and UHM.

6.1.2 Major Key Findings

Based on the research work conducted in this research project, the following points can be viewed as conclusions for this research:

a. The developed method outperforms other methods existing in literature in the sense that it can reveal the approximate location and shape of hidden reservoir features per reservoir layer in any reservoir model. Other prominent methods existing in literature infer the presence of hidden reservoir features using a single "connectivity map" which is assumed to be representative of all reservoir layers present.
b. The developed method is capable of handling reservoir models experiencing changes in flow patterns over time. In addition, the developed method is not negatively impacted by evaluated injection strategies and well architectures.
c. The capability of the developed method in revealing certain types of reservoir features during UHM is heavily dependent on the model parameters defined.
d. Assessing the effect of production noise showed that errors in measured data greater than ±15% can adversely affect the performance of the developed method.
e. Numerical noise have a detrimental impact on the performance of the developed method. Using "default" rather than "tight" simulator solver settings can inevitably lead to the degradation of convergence performance. At worst, convergence to an optimal solution may not be achieved.
f. The benefits that comes with performing UHM are enormous in the sense that it is the main step in revealing hidden reservoir features in reservoir simulation model. Also, the adjoint method applied in UHM is a powerful and effective method for computing first-order derivatives of the objective function with respect to model parameters like permeability, porosity etc. at grid block level. There are very few methods out there that can efficiently compute such Jacobians at grid block level.
g. Irrespective of the extent of uncertainty in permeability distributions, the developed method can be used to reveal hidden reservoir features/improve reservoir characterization in a single base model or an ensemble of base models.

6.2 Recommendations for Future Work

The following areas are suggested for future investigations:

- The use of an optimization algorithm like the Levenburg-Marquardt (LM) for performing model parameter updates will speed up the process of finding the global minima with fewer iterations. The LM algorithm is an integration of the steepest descent algorithm (linear convergence) and the Gauss-Newton algorithm (quadratic convergence). This allows the LM algorithm to find the global minima much faster. Also, the LM algorithm does not get stuck in a local minima (stagnation region) like the steepest descent algorithm. One drawback of the LM algorithm lies in the fact that it needs both the Jacobians (for the steepest descent) and the Hessians (for the Gauss-Newton) in order to function effectively.
- Threshold values were used to reveal hidden faults, channels etc. using reservoir feature indicator maps. The determination of the range of threshold values that reveals certain types of reservoir features was achieved through laborious in-house tests using reservoir simulation models of various dimensions, reservoir heterogeneity and well number. The developed reservoir feature detection algorithms are simple and effective but they could be made a lot more effective by finding a way to mathematically determine the threshold value for each reservoir feature to be revealed. As an alternative, supervised learning algorithms or deep learning methods can be applied directly to best-case permeability and/or porosity arrays obtained from UHM to reveal faults, channels etc.
- For the most part of this thesis work, hidden reservoir features in reservoir simulation models were revealed from best-case permeability and/or porosity arrays obtained from UHM. The equivalent adjoint-derived sensitivities for permeability and/or porosity were rarely used. This is simply because it is very challenging to determine physical parameters like the permeability value of a revealed channel from an adjoint-derived sensitivity for permeability. More work can be done to explore ways of determining physical parameters from the adjoint-derived sensitivities.
- The effectiveness of the developed method should also be evaluated with more complex reservoir simulation models like fractured reservoir models in revealing hidden fractures, reservoir simulation models with enhanced oil recovery methods and so on. Also, further evaluations with geothermal reservoir simulation models in estimating the correct reservoir heterogeneity and improving reservoir characterization in geothermal energy systems should be performed.

Bibliography

[1] Energy Information Agency, "Annual Energy Outlook," United States, 2019.

[2] International Energy Agency (IEA), "World Energy Outlook," London, UK, 2018.

[3] M. Kelkar and G. Perez, Applied Geostatistics for Reservoir Characterization, Richardson, Texas: Society of Petroleum Engineers Inc., 2002.

[4] K. I. Ochie and O. J. Rotimi, "Geostatistics - Kriging and Co-Kriging Methods in Reservoir Characterization of Hydrocarbon Rock Deposits," in *Society of Petroleum Engineers*, Lagos, 2018.

[5] T. Lo and A. Bemsawi, "Reservoir Characterization With Sequential Gaussian Simulation Constrained By Diffraction Tomography," in *Society of Exploration Geophysicists*, California, 1994.

[6] P. An and W. M. Moon, "Reservoir Characterization Using Feedforward Neural Networks," in *Society of Exploration Geophysicists*, Washington, DC, 1993.

[7] F. J. Lucia, C. Kerans and J. Jennings, "Carbonate Reservoir Characterization," *SPE Journal,* vol. 55, no. 06, pp. 70-72, 2003.

[8] S. B. Reymond, L. Soenneland and A. Strudley, "Mapping Reservoir Saturation with Seismic Resolution to Improve Reservoir Model," in *Society of Petroleum Engineers (SPE-57259-MS)*, Kuala Lumpur, Malaysia, 1999.

[9] M. Munka and J. Papay, 4D Numerical Modeling of Petroleum Reservoir Recovery, Budapest: Akademiai Kiado, 2001.

[10] M. Carlson, Practical Reservoir Simulation, Tulsa: PennWell Corporation, 2006.

[11] A. L. Morosov and D. J. Schiozer, "Field-Development Process Revealing Uncertainty-Assessment Pitfalls," in *Society of Petroleum Engineers (SPE-180094-PA)*, Vienna, Austria, 2016.

[12] H. B. Crichlow, Modern Reservoir Engineering: A Simulation Approach, Michigan: Prentice-Hall, 1977.

[13] C. C. Mattax and R. L. Dalton, Reservoir Simulation, Richardson, TX: Society of Petroleum Engineers, 1990.

[14] D. S. Oliver, A. C. Reynolds and N. Liu, Inverse Theory for Petroleum Reservoir Characterization and History Matching, New York: Cambridge University Press, 2008.

[15] C. Ozgen and J. R. Gilman, Reservoir Simulation: History Matching and Forecasting, USA: Society of Petroleum Engineers, 2013.

[16] W. D. Kruger, "Determinig Areal Permeability Distribution by Calculations," in *Society of Petroleum Engineers (SPE-1580-G-PA)*, Denver, USA, 1960.

[17] K. H. Coats and J. R. Dempsey, "A New Technique for Determining Reservoir Description from Field Performance Data," in *Society of Petroleum Engineers (SPE-2344-PA)*, Houston, Texas, USA, 1968.

[18] G. E. Slater and E. J. Durrer, "Adjustment of Reservoir Simulation Models To Match Field Performance," in *Society of Petroleum Engineers (SPE-2983-PA)*, Houston, USA, 1970.

[19] L. Thomas, L. J. Hellums and G. M. Reheis, "A Nonlinear Automatic History Matching Technique for Reservoir Simulation Models," in *Society of Petroleum Engineers (SPE-3475-PA)*, New Orleans, USA, 1971.

[20] G. Chavent and M. Dupuy, "History Matching by Use of Optimal Theory," in *Society of Petroleum Engineers (SPE-4627-PA)*, Las Vegas, Nevada, USA, 1973.

[21] W. H. Chen, G. R. Gavalas, J. H. Seinfeld and M. L. Wasserman, "A New Algorithm for Automatic History Matching," in *Society of Petroleum Engineers (SPE-4545-PA)*, Las Vegas, Nevada, USA, 1973.

[22] E. L. Dougherty and D. Khairkhah, "History Matching of Gas Simulation Models Usng Optimal Control Theory," in *Society of Petroleum Engineers (SPE-5371-MS)*, California, USA, 1975.

[23] G. R. Gavalas and J. H. Seinfield, "Reservoir History Matching by Bayesian Estimation," in *Society of Petroleum Engineers (SPE-5740-PA)*, Los Angeles, USA, 1976.

[24] K. Pruess, O. Weres, R. Schroeder, R. Marconcini and G. Neri, "History Match Simulation of Serrazzano Geothermal Reservoir," in *Society of Petroleum Engineers (SPE-9276-MS)*, Dallas, Texas, USA, 1980.

[25] A. T. Watson and W. J. Lee, "A New Algorithm for Automatic History Matching Production Data," in *Society of Petroleum Engineers (SPE-15228-MS)*, Louisville, Kentucky, USA, 1986.

[26] M. D. Zuber, W. K. Sawyer, R. A. Schraufnagel and V. A. Kuuskraa, "The Use of Simulation and History Matching To Determine Critical Coalbed Methane Reservoir Properties," in *Society of Petroleum Engineers (SPE-16420-MS)*, Denver, Colorado, USA, 1987.

[27] A. J. Watkins, R. G. Parish and A. D. Modine, "A Stochastic Role for Engineering Input to Reservoir History Matching," in *Society of Petroleum Engineers (SPE-23738-MS)*, Caracas, Venezuela, 1992.

[28] E. Damsleth, A. Hage and R. Volden, "Maximum Information at Minimum Cost: A North Sea Field Development Study With an Experimental Design," *Society of Petroleum Engineers - Journal of Petroleum Technology (SPE-23139-PA),* vol. 44, no. 12, pp. 1350-1356, 1992.

[29] S. D. Mohaghegh, F. Abdulla, M. Abdou, R. Gaskari and M. Maysami, "Smart Proxy: An Innovative Reservoir Management Tool; Case Study of a Giant Mature Oilfield in the UAE," in *Society of Petroleum Engineers (SPE-177829-MS)*, Abu Dhabi, UAE, 2015.

[30] K. Tyler, T. Svanes and S. Omdal, "Faster History Matching and Uncertainty in Predicted Production Profiles with Stochastic Modeling," in *Society of Exploration Geophysicists (SEG-1994-0264)*, Los Angeles, California, USA, 1994.

[31] M. K. Sen, A. Datta-Gupta, P. L. Stoffa, L. W. Lake and G. A. Pope, "Stochastic Reservoir Modeling Using Simulated Annealing and Genetic Algorithms," *Society of Petroleum Engineers - Journal of Petroleum Technology (SPE-24754-PA),* vol. 10, no. 01, pp. 49-55, 1995.

[32] C. E. Romero, J. N. Carter, R. W. Zimmerman and A. C. Gringarten, "Improved Reservoir Characterization Through Evolutionary Computation," in *Society of Petroleum Engineers (SPE-62942-MS)*, Dallas, Texas, USA, 2000.

[33] P. J. Ballester and J. N. Carter, "A Parallel Real-Coded Genetic Algorithm for History Matching and Its Application to a Real Petroleum Reservoir," *Journal of Petroleum Science & Engineering,* vol. 59, no. 3-4, pp. 157-168, 2007.

[34] R. W. Schulze-Riegert, J. K. Axmann, O. Haase, D. T. Rian and Y. -L. You, "Evolutionary Algorithms Applied to History Matching of Complex Reservoirs," *SPE Reservoir Evaluation & Engineering,* vol. 5, no. 02, pp. 163-173, 2002.

[35] L. Mohamed, M. Christie and V. Demyanov, "Comparison of Stochastic Sampling Algorithms for Uncertainty Quantification," in *Society of Petroleum Engineers (SPE-119139-MS)*, The Woodlands, Texas, USA, 2009.

[36] S. H. Sousa, "Scatter Search Metaheuristic Applied to the History-Matching Problem," in *Society of Petroleum Engineers (SPE-113610-STU)*, Anaheim, California, USA, 2007.

[37] N. Liu and D. S. Oliver, "Critical Evaluation of the Ensemble Kalman Filter on History Matching of Geological Facies," *SPE Reservoir Evaluation & Engineering,* vol. 8, no. 06, pp. 470-477, 2005.

[38] G. Naevdal, L. M. Johnson, S. I. Aanonsen and E. H. Vefring, "Reservoir Monitoring and Continuous Model Updating Using Ensemble Kalman Filter," *SPE Journal (SPE-84372-PA),* vol. 10, no. 01, pp. 66-74, 2005.

[39] A. Bianco, A. Cominelli, L. Dovera, G. Naevdal and B. Valles, "History Matchingand Production Forecast Uncertainty by Means of the Ensemble Kalman Filter: A Real Field Application," in *Society of Petroleum Engineers (SPE-107161-MS)*, London, UK, 2007.

[40] R. Schulze-Riegert, F. Chataigner, N. Kueck, O. Pajonk, J. Baffoe, I. Ajala, D. Awofodu and H. Almuallim, "Strategic Scope of Alternative Optimization Methods in History Matching and Prediction Workflows," in *Society of Petroleum Engineers (SPE-164337-MS)*, Manama, Bahrain, 2013.

[41] S. D. Mohaghegh, "Quantifying Uncertainties Associated With Reservoir Simulation Studies Using Surrogate Reservoir Models," in *Society of Petroleum Engineers (SPE-102492-MS)*, San Antonio, Texas, USA, 2006.

[42] D. I. Zubarev, "Pros and Cons of Applying Proxy-Models as a Substitute for Full Reservoir Simulations," in *Society of Petroleum Engineers (SPE-124815-MS)*, New Orleans, Louisiana, USA, 2009.

[43] G. Gao, G. Li and A. C. Reynolds, "A Stochastic Optimization Algorithm for Automatic History Matching," in *Society of Petroleum Engineers (SPE-90065-MS)*, Houston, Texas, USA, 2004.

[44] M. M. Rafiee, "Model Selection and Uniqueness Analysis for Reservoir History Matching," TU Freiberg, Dissertation, Freiberg, 2011.

[45] H. Almuallim, K. Edwards and L. Ganzer, "History-Matching With Sensitivity-Based Parameter Modifications at Grid-Block Level," in *Society of Petroleum Engineers (SPE-131627-MS)*, Barcelona, Spain, 2010.

[46] I. Ajala, L. Ganzer, R. Schulze-Riegert and H. Almuallim, "Adjoint Method Used in History Matching and Optimization Workflows," in *DGMK/OGEW-Frühjahrstagung*, Celle, Germany, 2012.

[47] R. H. Lind, O. Allottai, A. M. Gaaim and H. Almuallim, "Computer Assisted History Matching - A Field Example," in *Society of Petroleum Engineers (SPE-165979-MS)*, Abu Dhabi, UAE, 2013.

[48] R. Schulze-Riegert, M. Nwakile, S. Skripin and Y. Willen, "Scalability and Performance Efficiency of History Matching Workflows using MCMC and Adoint Techniques Applied to the Norne North Sea Reservoir Case Study," in *Society of Petroleum Engineers (SPE-180106-MS)*, Vienna, Austria, 2016.

[49] I. Ajala, R. Haekal, R. Schulze-Riegert and L. Ganzer, "History Matching of Trasient Pressure Build-up in a Simulation Model Using Adjoint Method," in *DGMK/OGEW-Frühjahrstagung*, Celle, Germany, 2013.

[50] I. Ajala, H. Almuallim, L. Ganzer and R. Schulze-Riegert, "Derivative of Transient Pressure Build-up as an Objective Function Parameter in an Adjoint Based History Matching Tool (SenEx)," in *DGMK/OGEW-Frühjahrstagung*, Celle, Germany, 2014.

[51] R. Rwechungura, M. Dadashpour and J. Kleppe, "Advanced History Matching Techniques Reviewed," in *Society of Petroleum Engineers (SPE-142497-MS)*, Manama, Bahrain, 2011.

[52] F. E. Jansen and M. G. Kelkar, "Exploratory Data Analysis of Production Data," in *Society of Petroleum Engineers (SPE)*, Midland, Texas, USA, 1996.

[53] K. J. Heffer, R. J. Fox, C. A. McGill and N. C. Koutsabeloulis, "Novel Techniques Show Links between Reservoir Flow Directionality, Earth Stress and Geomechanical Changes in Mature Waterfloods," *SPE Journal,* vol. 2, pp. 91-98, 1997.

[54] F. E. Jansen and M. G. Kelkar, "Application of Wavelets to Production Data in Describing Inter-Well Relationships," in *Society of Petroleum Engineers (SPE)*, San Antonio, Texas, USA, 1997.

[55] M. N. Panda and A. K. Chopra, "An Integrated Approach to Estimate Well Interactions," in *Society of Petroleum Engineers (SPE)*, New Delhi, India, 1998.

[56] A. Albertoni and L. W. Lake, "Inferring Interwell Connectivity Only From Well-Rate Fluctuations in Waterfloods," *SPE Reservoir Evaluation & Engineering,* vol. 6, no. 01, pp. 6-16, 2003.

[57] A. A. Yousef, L. W. Lake and J. L. Jensen, "Analysis and Interpretation of Interwell Connectivity From Production and Injection Rate Fluctuations Using a

Capacitance Model," in *Society of Petroleum Engineers (SPE-99998-MS)*, Oklahoma, USA, 2006.

[58] M. Sayarpour, "Development and Application of Capacitance-Resistive Models to Water/CO2 Flood," University of Texas at Austin (Dissertation), Texas, USA, 2008.

[59] D. Kaviani, P. P. Valko and J. L. Jensen, "Application of the Multiwell Productivity Index-Based Method to Evaluate Interwell Connectivity," in *Society of Petroleum Engineers (SPE-129965-MS)*, Oklahoma, USA, 2010.

[60] R. G. Gherabati, H. Zhang and C. D. White, "A Large Scale Network To Obtain Interwell Formation Characteristics," in *Society of Petroleum Engineers (SPE-153386-MS)*, California, USA, 2012.

[61] K. J. Heffer, R. J. Fox, C. A. McGill and N. C. Koutsabeloulis, "Novel Techniques Show Links between Reservoir Flow Directionality, Earth Stress, Fault Structure and Geomechanical Changes in Mature Waterfloods," *SPE Journal,* vol. 2, no. 02, pp. 91-98, 1997.

[62] F. E. Jansen and M. G. Kelkar, "Application of Wavelets to Production Data in Describing Inter-Well Relationships," in *Society of Petroleum Engineers (SPE-38876-MS)*, San Antonio, Texas, USA, 1997.

[63] C. Tian and R. N. Horne, "Inferring Interwell Connectivity Using Production Data," in *Society of Petroleum Engineers (SPE-181556-MS)*, Dubai, UAE, 2016.

[64] Z. Guo and A. C. Reynolds, "A Physics-Based Data-Driven Model for History-Matching, Prediction and Characterization of Waterflooding Performance," in *Society of Petroleum Engineers (SPE-182660-PA)*, Texas, USA, 2017.

[65] H. Zhao, Z. Kang, X. Zhang, H. Sun, L. Cao and A. C. Reynolds, "INSIM: A Data-Driven Model for History Matching and Prediction for Waterflooding Monitoring and Management with a Field Application," in *Society of Petroleum Engineers (SPE-173213-MS)*, Houston, Texas, USA, 2015.

[66] T. J. Spanos, V. De La Cruz, J. Hube and R. C. Sharma, "An Analysis of Buckley-Leverett Theory," *Journal of Canadian Petroleum Technology,* no. 25, pp. 71-75, 1986.

[67] K. -A. Lie and R. Juanes, "A front-tracking method for the simulation of three-phase flow in porous media," *Computational Geosciences,* no. 9, pp. 29-59, 2005.

[68] A. A. Emerick and A. C. Reynolds, "History-Matching Production and Seismic Data in a Real Field Case Using the Ensemble Smoother With Multiple Data

Assimilation," in *Society of Petroleum Engineers (SPE-163675-MS)*, The Woodlands, Texas, USA, 2013.

[69] D. D. Awofodu, L. Ganzer and H. Almuallim, "An Evaluation of Grid-block-based Optimization Methods Applied to History Matching Workflows," *OIL GAS European Magazine,* pp. OG1-OG6, December 2016.

[70] R. L. Plackett and J. P. Burmann, "The design of optimum multifactorial experiments," *Biometrika,* vol. 4, no. 33, pp. 305-325, 1946.

[71] N. Hansen and S. Kern, "Evaluating the CMA Evolution Strategy on Multimodal Test Functions," *Lecture Notes in Computer Science,* no. 3242, pp. 282-291, 2004.

[72] D. I. Zubarev, "Pros and Cons of Applying Proxy-Models as a Substitute for Full Reservoir Simulations," in *Society of Petroleum Engineers (SPE-124815-MS)*, New Orleans, Louisiana, USA, 2009.

[73] E. A. Breitenbach, D. H. Thurnau and H. K. Van Poolen, "The Fluid Flow Simulation Equations," in *Society of Petroleum Engineers (SPE-2020-MS)*, Dallas, Texas, USA, 1968.

[74] B. Adi, "A Newton-Raphson method for the solution of systems of equations," *Journal of Mathematical Analysis and Application,* no. 15, pp. 243-252, 1966.

[75] E. Farkas, "Linearization Techniques of Reservoir-Simulation Equations: Fully Implicit Cases," *SPE Journal,* vol. 4, no. 3, pp. 316-323, 1998.

[76] A. Fichter, H. -P. Bunge and H. Igel, "The adjoint method in seismology," *Physics of the Earth and Planetary Interiors,* no. 157, pp. 86-104, 2006.

[77] F. Zhang, J. A. Skjervheim, A. C. Reynolds and D. S. Oliver, "Automatic history matching in a Bayesian framework, example applications," in *Society of Petroleum Engineers (SPE-84461-MS)*, Denver, USA, 2003.

[78] I. Ajala, Adjoint Method in History Matching of Numerical Reservoir Models - A Simplified Computer Assisted Approach, Clausthal-Zellerfeld: Clausthal University of Technology, 2016.

[79] A. Cauchy, "Methode generale pour la resolution des systemes d'equations simultanees," *C. R. Acad. Sci.,* no. 25, pp. 536-538, 1847.

[80] R. Li, "Conditioning geostatistical models to three-dimensional three-phase flow production data by automatic history matching," University of Tulsa, Dissertation, Tulsa, 2001.

[81] H. Ngodock, M. Carrier and S. Smith, "Weak and Strong Constraints Variational Data Assimilation with the NCOM - 4DVAR in the Agulhas Region Using the Representer Method," *Monthly Weather Review,* vol. 5, no. 145, pp. 1755-1764, 2017.

[82] J. Canny, "A Computational Approach to Edge Detection," *IEEE Transaction on Pattern Analysis and Machine Intelligence,* vol. 8, no. 6, pp. 679-698, 1986.

[83] "The Minitab Blog," Minitab, 30 05 2013. [Online]. Available: blog.minitab.com. [Accessed 30 09 2019].

[84] D. D. Awofodu, L. Ganzer and H. Almuallim, "Revealing Hidden Reservoir Features During History Matching Using An Adjoint Method," in *16th European Conference on the Mathematics of Oil Recovery (EAGE ECMOR XVI)*, Barcelona, Spain, 2018.

[85] R. Wanderley de Holanda, E. Gildin and J. L. Jensen, "Improved Waterflooding Analysis Using the Capacitance-Resistance Model Within a Control Systems Framework," in *Society of Petroleum Engineers (SPE-177106-MS)*, Quito, Ecuador, 2015.

[86] X. Liang, L. W. Lake, T. F. Edgar, A. Yousef, M. Sayarpour and D. Weber, "Optimization of Oil Production Based On A Capacitance Model Of Production And Injection Rates," in *Society of Petroleum Engineers (SPE-107713-MS)*, Dallas, Texas, USA, 2007.

[87] A. P. Nguyen, J. S. Kim, L. W. Lake, T. F. Edgar and B. Haynes, "Integrated Capacitance Resistive Model for Reservoir Characterization in Primary and Secondary Recovery," in *Society of Petroleum Engineers (SPE-147344-MS)*, Denver, Colorado, USA, 2011.

[88] F. Cao, H. Luo and L. W. Lake, "Development of a Fully Coupled Two-phase Flow Based Capacitance Resistance Model (CRM)," in *Society of Petroleum Engineers (SPE-169485-MS)*, Tulsa, Oklahoma, USA, 2014.

[89] M. Sayarpour, E. Zuluaga, C. S. Kabir and L. W. Lake, "The use of capacitance-resistance models for rapid estimation of waterflood performance and optimization," *Journal of Petroleum Science and Engineering,* vol. 69, pp. 227-238, 2009.

[90] A. Yrigoyen, L. Saputelli, C. Chacon and J. Chegin, "Identifying Cost-Effective Waterflooding Optimization Opportunities in Mature Reservoirs from Data Driven Analytics," in *Society of Petroleum Engineers (SPE-187300-MS)*, San Antonio, Texas, USA, 2017.

[91] D. D. Awofodu, L. Ganzer and H. Almuallim, "Enhancing Reservoir Understanding in Mature Fields: Adjoint-State Method Applied to a Semi-Synthetic Model," in *Society of Petroleum Engineers (SPE-184951-MS)*, Salvador, Bahia, Brazil, 2017.

[92] F. Roggero, O. Lerat, D. Y. Ding, P. Berthet, C. Bordenave, F. Lefeuvre and P. Perfetti, "History Matching of Production and 4D Seismic Data: Application to the Girassol Field, Offshore Angola," *Oil & Gas Science and Technology - Rev. IFP Energies nouvelles,* vol. 67, pp. 237-262, 2012.

[93] F. J. T. Floris, M. D. Bush, M. Cuypers, F. Roggero and A. -R. Syversveen, "Methods for Quantifying the Uncertainty of Production Forecasts: A Comparative Study," *Petroleum Geoscience,* no. 7, pp. 87-96, 2001.

[94] H. Almuallim, L. Ganzer, H. Uematsu, S. Bellah and V. Virlan, "Advanced Assisted History Matching of a Large Mature Oil Field Based on a Huge Number of Grid-Block Level Parameters and Saturation Functions," in *Society of Petroleum Engineers (SPE-192780-MS)*, Abu Dhabi, UAE, 2018.

[95] Z. Guo, C. Chen, G. Gao and J. Vink, "Applying Support Vector Regression to Reduce the Effect of Numerical Noise and Enhance the Performance of History Matching," in *Society of Petroleum Engineers (SPE-187430-MS)*, San Antonio, Texas, USA, 2017.

[96] J. J. More and S. M. Wild, "Estimating computational noise," *SIAM Journal on Scientific Computing,* vol. 33, no. 3, pp. 1292-1314, 2011.

[97] D. Awofodu, L. Ganzer, H. Almuallim and J. Schellinger, "An Adjoint-based Method for Improving Reservoir Characterization during History Matching," *OIL GAS European Magazine,* vol. 45, no. 3, pp. OG126-OG135, 2019.

[98] A. Wilson, "Uncertainty Quantification for History-Matching Problems," *Journal of Petroleum Technology,* vol. 69, no. 04, pp. 90-92, 2017.

[99] G. Gao, J. C. Vink, C. Chen, M. Tarrahi and Y. El Khamra, "Uncertainty Quantification for History Matching Problems With Multiple Best Matches Using a Distributed Gauss-Netwon Method," in *Society of Petroleum Engineers (SPE-181611-MS)*, Dubai, UAE, 2016.

[100] R. M. Fonseca, C. R. Geel and O. Leeuwenburgh, "Description of OLYMPUS reservoir model for optimization challenge," TNO, The Hague, Netherlands, 2017.

Appendix A

Improved MEPO-tSenEx Command Scripting

```
::modified version 15.10.2018

::running SenEx v2.0.36 before now

:: Define SenEx version to run

set SENEXROOT=C:\Program Files\SenEx\SenEx_v2.0.47

set PATH=%SENEXROOT%;%PATH%

set MODEL_NAME=SENEX_MODEL

ECHO %MODEL_NAME%

tsenex createproject %MEPO_WORKDIR% Eclipse100

COPY %MEPO_WORKDIR%..\SenexFiles\SetUp1 %MEPO_WORKDIR%SetUps\

COPY %MEPO_WORKDIR%..\SenexFiles\ModelSummary.dat %MEPO_WORKDIR%

COPY %MEPO_WORKDIR%..\SenexFiles\CoreyParameters.dat %MEPO_WORKDIR%

COPY %MEPO_WORKDIR%..\SenexFiles\CoreyRanges.dat %MEPO_WORKDIR%

MD %MEPO_WORKDIR%BaseCase

COPY %MEPO_WORKDIR%..\SenexFiles\ModelSummary.dat %MEPO_WORKDIR%BaseCase\

COPY %MEPO_WORKDIR%..\SenexFiles\CoreyParameters.dat %MEPO_WORKDIR%BaseCase\

tsenex addcase %MEPO_WORKDIR% %MEPO_WORKDIR%%MODEL_NAME%.DATA None

tsenex importcase %MEPO_WORKDIR% Case_0

::Doesn't seem to help much

::Add uncertainty or mask array into the mix

::COPY %MEPO_WORKDIR%..\SenexFiles\UncertaintyArray_Case2.dat
%MEPO_WORKDIR%Arrays\

::Corey parameters and ranges

COPY %MEPO_WORKDIR%..\SenexFiles\CoreyParameters.dat
%MEPO_WORKDIR%Case_0\SensitivityDir\

COPY %MEPO_WORKDIR%..\SenexFiles\CoreyRanges.dat
%MEPO_WORKDIR%Case_0\SensitivityDir\

tsenex EvaluateOF %MEPO_WORKDIR% Case_0 SetUp1

tsenex computesensitivity %MEPO_WORKDIR% Case_0 SetUp1

::introduce locality option (no well grouping)
```

```
::COPY %MEPO_WORKDIR%..\SenexFiles\WellGrouping.dat
%MEPO_WORKDIR%Case_0\SensitivityDir\

tsenex CreateDefaultPropertyConstraints %MEPO_WORKDIR% Case_0

::Section works fine

if exist "%MEPO_WORKDIR%..\SenexFiles\PropertyConstraintsPermx.dat" goto q

if not exist "%MEPO_WORKDIR%..\SenexFiles\PropertyConstraintsPermx.dat" goto p

:p

COPY %MEPO_WORKDIR%Case_0\SensitivityDir\PropertyConstraintsPor.dat
%MEPO_WORKDIR%..\SenexFiles

COPY %MEPO_WORKDIR%Case_0\SensitivityDir\PropertyConstraintsPermx.dat
%MEPO_WORKDIR%..\SenexFiles

COPY %MEPO_WORKDIR%Case_0\SensitivityDir\PropertyConstraintsPermy.dat
%MEPO_WORKDIR%..\SenexFiles

COPY %MEPO_WORKDIR%Case_0\SensitivityDir\PropertyConstraintsPermz.dat
%MEPO_WORKDIR%..\SenexFiles

:q

COPY %MEPO_WORKDIR%..\SenexFiles\PropertyConstraintsPermx.dat
%MEPO_WORKDIR%Case_0\SensitivityDir\

COPY %MEPO_WORKDIR%..\SenexFiles\PropertyConstraintsPermy.dat
%MEPO_WORKDIR%Case_0\SensitivityDir\

COPY %MEPO_WORKDIR%..\SenexFiles\PropertyConstraintsPermz.dat
%MEPO_WORKDIR%Case_0\SensitivityDir\

COPY %MEPO_WORKDIR%..\SenexFiles\PropertyConstraintsPor.dat
%MEPO_WORKDIR%Case_0\SensitivityDir\

::COPY %MEPO_WORKDIR%..\SenexFiles\PropertyConstraintsInitWater.dat
%MEPO_WORKDIR%Case_0\SensitivityDir\

::COPY %MEPO_WORKDIR%..\SenexFiles\PropertyConstraintsInitGas.dat
%MEPO_WORKDIR%Case_0\SensitivityDir\

tsenex exportnewarraysandsensitivities %MEPO_WORKDIR% Case_0 SetUp1
%MEPO_WORKDIR%..\SenexFiles %MODEL_NAME%

::export sensitivities for perm and poro

COPY
%MEPO_WORKDIR%Case_0\SensitivityDir\SensitivityResults_SetUp1\upscaledPermXSensitivity.vo
l %MEPO_WORKDIR%..\SenexFiles
```

```
COPY
%MEPO_WORKDIR%Case_0\SensitivityDir\SensitivityResults_SetUp1\upscaledPermYSensitivity.vo
l %MEPO_WORKDIR%..\SenexFiles

COPY
%MEPO_WORKDIR%Case_0\SensitivityDir\SensitivityResults_SetUp1\upscaledPermZSensitivity.vol
%MEPO_WORKDIR%..\SenexFiles

COPY
%MEPO_WORKDIR%Case_0\SensitivityDir\SensitivityResults_SetUp1\upscaledPorSensitivity.vol
%MEPO_WORKDIR%..\SenexFiles

::export Adjoint Lagrangian variables (Lambda)

::Look out for defined "noiseFactor"

COPY %MEPO_WORKDIR%Case_0\SensitivityDir\LinearSolver.out
%MEPO_WORKDIR%..\SenexFiles

EXIT
```

Appendix B

MATLAB Code for Interpreting Adjoint-derived Sensitivities

```
% Read an .inc File
file='D:\ITE300_Modified\MSW_VS_CRM\MEPO_5_Inj_4_Prod\SENEX_MODEL_HetK_ConPh
i_SPE182660_Ly5_NN\BestCase\upscaledPermYSensitivity_Mod.INC'
breakOn='/'

function [ A ] = ReadSensInc( file,breakOn)
%ReadInc Reads .Inc File to Vektor
%  Function reads the .inc file specified within file line by line
% If the first character in a line is not a number the line is skipped
% If the line contains a character defined by breakOn,reading is stopped
%
% Example:
%
% file='C:\...\TutorialCase_2017-07-
31_ID_225\SenEx_Proj1\Sim1\1\SENEX_CASE_SENEX_PERMX.INC';
% breakOn='\'
fid = fopen(file);
tline = fgetl(fid);
i=1;
while ischar(tline)
    if(isempty(str2num(tline)==1))
        tline = fgetl(fid);
        continue
    end
    if(findstr(tline,breakOn))
        break
    end
    A(i,:)=strsplit(tline);
    tline = fgetl(fid);
    i=i+1;
end
fclose(fid);

end

A=str2double(ReadSensInc(file,breakOn))

function [ F ] = cGrid( Xval,Yval,Zval,FProp)
%cGrid create out of a vector by an inc file a rectangular grid by storing
%them into a (x*y*z) * 4 Matrix
%   FProp=Vektor
F=zeros(Xval*Yval*Zval,4);
i=1;
for(z=1:Zval)
    for(y=1:Yval)
        for(x=1:Xval)
            F(i,:)=[x,y,z,FProp(i)];
```

```
            i=i+1;
        end
    end
end



end

F=cGrid(20,20,5,A)

%f1 = figure;
%f2 = figure;
%% Surf a Layer
Xval=20;
Yval=20;
Zval=5;

Layer=3;
idx=find(F(:,3)==Layer);
[X,Y] = meshgrid(1:Xval,1:Yval);
FLayer=[F(idx,1),F(idx,2),F(idx,4)];
Z=reshape(FLayer(:,3),[Yval,Xval])

%figure(f1)
%surf(X,Y,Z);

x = [1:Xval];                % Random data
y = [1:Yval];
C = Z %[0 1 2 3 ; 1 2 3 4 ; 2 3 4 5];
xSplit = diff(x)/2;              % Find edge points
ySplit = diff(y)/2;
xEdges = [x(1)-xSplit(1) x(2:end)-xSplit x(end)+xSplit(end)];
yEdges = [y(1)-ySplit(1) y(2:end)-ySplit y(end)+ySplit(end)];
[XGrid, YGrid] = meshgrid(xEdges,yEdges);
YGrid = flipud(YGrid);           % To match expected behavior
C = [[C zeros(size(C,1),1)] ; zeros(1,size(C,2)+1)];% Last row/col ignored
%surf(XGrid,YGrid,C);
pcolor(XGrid,YGrid,C)
%hold on                         % Plot original data points
%[X,Y] = meshgrid(x,y);
%Y = flipud(Y);
%plot(X,Y,'or')
```

Appendix C

MATLAB Code for the modified Canny Edge-detection method

```
% Read image file and display it
file='D:\ITE300_Modified\MATLAB_CODE_MSW\Channel_Type1_NoGrid.PNG'

% Canny edge detection method
x = imread ('Channel_Type1_NoGrid.PNG')

% Convert to grey scale
%m1 = rgb2gray(x);

% Convert to BW image
%level = 0.6
m1 = im2bw(x,0.6)

% Remove small objects from BW image
m1 = bwareaopen(m1,1000);
%imshow(BW);

x1 = edge(m1, 'canny');
x2 = edge(m1, 'sobel');

% Sobel edge detection method
m2 = double(m1);
% Sobel operator
f1=[-1 -2 1;0 0 0;1 2 -1];
[r,c] = size(m1);
for q1=1:(r-3);
for p1=1:(c-3);
    m1 = m2(q1:(q1+2),p1:(p1+2));
    res=f1.*m1;
    f(q1,p1)=sum(sum(res));
end
end
%subplot(2,2,1);
%imshow(f);
%imshow(~x2);
%title('Sobel filter');
%subplot(2,2,2);

imshow(~x1);
%title('BW Image of Input Image');
```

MATLAB Code for the fault shape detection algorithm

```
% Read image file and display it
file='Fault_13.PNG';
% number of grid blocks used for image scaling
n=20

I = imread (file);
figure
imshow(I);
s=size(I)
scaleFactor=n/s(1)
I = imresize(I,scaleFactor);

% Convert to grayscale image
Igray = rgb2gray(I);
% level = graythresh(Igray)
% we use a user-selected threshold here but algorithms exists too
% however they can lead to failures

BW = imbinarize(Igray,0.3);

% Remove small objects from BW image
%BW = bwareaopen(BW,68);

BW = bwmorph(BW,'fill');
BW = imresize(BW,1/scaleFactor);
I=imresize(I,1/scaleFactor);

BW3 = bwmorph(BW,'skel',Inf);
B = bwmorph(BW3, 'branchpoints');
E = bwmorph(BW3, 'endpoints');

[y,x] = find(E);
B_loc = find(B);
Dmask = false(size(BW3));
for k = 1:numel(x)
    D = bwdistgeodesic(BW3,x(k),y(k));
    distanceToBranchPt = min(D(B_loc));
    Dmask(D < distanceToBranchPt) =true;
end
skelD = BW3 - Dmask;

% skelD = imresize(skelD,10);
figure
imshow(skelD);
hold all;
```